Exploring intermolecular interactions through Coupled Cluster, Density Functional, and Multireference Symmetry-Adapted Perturbation Theories

by

Daniel George Aulbach Smith

A dissertation submitted to the Graduate Faculty of
Auburn University
in partial fulfillment of the
requirements for the Degree of
Doctor of Philosophy

Auburn, Alabama
December 12, 2015

Keywords: quantum chemistry, intermolecular interactions, symmetry-adapted perturbation theory

Approved by

Konrad Patkowski, Chair, Assistant Professor of Chemistry and Biochemistry
Vincent Ortiz, Ruth W. Molette Professor of Chemistry and Biochemistry
Orlando Acevedo, Associate Professor of Chemistry and Biochemistry
Rik Blumenthal, Associate Professor of Chemistry and Biochemistry
Allen Landers, Howard Carr Professor of Department of Physics

Abstract

Intermolecular interactions are computed at successively lower levels of theory to establish the relative accuracy of each level. A set of 21 small molecules was first computed using the CCSDT(Q) level of theory to establish the post-CCSD(T) uncertainty of approximately 3%. Methane and CO_2 bound to a series of polycyclic aromatic hydrocarbons (PAHs) are then computed using a variety of tools to approximate the CCSD(T)/CBS interaction energy, the MP2/CBS+ΔCCSD(T)-F12avg/aDZ method demonstrated a mean error of just 2% from benchmark results. The accuracy of a set of dispersion including DFT methods is explored for methane and CO_2 bound to curved coronene systems. While these DFT methods exhibited mean errors of 5-15% at the van der Waals minima their error at shorter ranges rose dramatically. In order to mitigate these short-range errors, the damping parameters of the DFT-D3 method were refitted to a large database of 8,299 intermolecular interactions. It was found that through refitting the average error of the DFT-D3 methods was reduced by 10-50%, the greatest reduction in error came from the largest DFT-D3 outliers. The resulting refitted DFT-D3 method is more accurate and the error is less variable with respect to the choice of underlying DFT functional and damping form. In addition, symmetry-adapted perturbation theory (SAPT) will be extended to multiconfigurational self-consistent field (MCSCF) wavefunctions. To this end, optimization techniques for MCSCF wavefunctions are detailed and density-fitting is introduced into these equations to reduce their overall cost.

Acknowledgments

There are many folks who have helped me during this time. First and foremost, I would like to thank Dr. Konrad Patkowski for being a wonderful advisor. Even though I was your first student, and you were a new advisor, you let me have the space to grow in my own directions. I will always be grateful for your tutelage, knowledge, and passion. I very much look forward to seeing the continuation of your work.

I would also like to thank my committee: Dr. Vincent Ortiz who gave me historical perspectives in quantum chemistry, Dr. Rik Blumenthal for an abundance of thermodynamical knowledge, and Dr. Orlando Acevedo who gave me insight into how to transition my ideas to larger molecular scales.

I am also deeply indebted to Dr. David Sherrill and his group for teaching me how to collaborate and interact with others within my field. In particular, Dr. Lori Burns, Dr. Rob Parrish, and Dr. Jerome Gonthier of the Sherrill group have been the very best of associates and I will be forever thankful for their camaraderie.

Finally, I would like to thank Dr. Jamie Kinsley and VBK for being an unending source of encouragement and companionship.

It has certainly been an interesting journey, thank you all for being a part of it.

Table of Contents

List of Figures

List of Tables

Chapter 1

Introduction

Through quantum mechanics we are able to explore many aspects of chemistry and seek answers that are not currently possible to obtain through macroscale experiments. Here we will focus on the accurate elucidation of intermolecular interactions. These intermolecular interactions dictate many aspects of chemistry such as drug binding,[2–4] freezing and melting point temperatures of molecular materials,[5,6] reaction pathways,[7–9] and astrophysical phenomena.[10,11]

Of particular interest to our group are noncovalent interactions (NCI) between small molecules and carbon nanostructures; these interactions have been the subject of many experimental and theoretical studies.[12–21] Specifically, this research will focus on methane and carbon dioxide physisorption onto carbon nanotubes due to the proposed applications of nanotubes for methane storage,[22,23] C-H bond activation in organic synthesis,[24,25] CO_2 sequestration,[19,26–30] and molecular sieves to separate CO_2 from flue gases.[31–33] As we explore these systems we will observe how the fundamental understanding of these systems contributes to the vast body of NCI knowledge.

1.1 Computation of Noncovalent Interactions

There are two approaches to the computation of the interaction energy (IE) between two molecules: the supermolecular and perturbative methodologies. The supermolecular approach to the computation of noncovalent interaction energies is simply the energy of the dimer minus the energy of each monomer,

$$E_{\text{interaction}}^{\text{method}} = E_{\text{dimer}}^{\text{method}} - E_{\text{monomer A}}^{\text{method}} - E_{\text{monomer B}}^{\text{method}} \tag{1.1}$$

This approach is often utilized as it is valid for any methodology that returns molecular energies. As it is quite difficult to obtain absolute energies for a given monomer or complex the supermolecular approach is often criticized as working due to large cancellation of errors. While this comment is likely valid for approaches that are not systematically improvable, care needs to be taken for methods that are. For these systematically improvable methods, a more accurate way of describing this outcome is that higher order effects contribute less to the overall interaction energy. As most methodologies scale as some power of the system size, the supermolecular approach requires much more computational effort for the computation of the dimer than for each of the monomers.

A second approach to the computation of noncovalent interaction energies is through a perturbation theory. While there are many perturbation theories, the most popular form is Symmetry-Adapted Perturbation Theory (SAPT).[34] SAPT breaks the interaction energy down into four fundamental forces which comprise all intermolecular interactions.

- Exchange:

  Directly arising from the Pauli exclusion principle, exchange is the primary repulsive force in intermolecular interactions. The exchange energy decays as $e^{-\alpha r}$. This is often computed with the S^2 approximation where only interchanges of particle pairs are considered – compared to the S^∞ approach, where all possible interchanges are considered.

- Electrostatics:

  Long range electrostatics can be computed through the permanent multipole moments of each monomer; however, this approximation breaks down at short-range. At these shorter ranges the leading effects of electrostatic interactions are computed by simply accounting for all possible charge-charge interactions between the monomers. In SAPT, electrostatics are computed as the sum of the following terms: the electron repulsion between the two monomers, the attraction of electrons on monomer A to the nuclei of monomer B, the attraction of electrons on monomer B to the nuclei of monomer A, and finally the nuclei–nuclei repulsion from monomers A and B.

- Induction:

  The electronic relaxation of one monomer in response to the electric field of another. This can be computed to a high precision by continuously relaxing each monomer in the response to the other. However, induction is typically only computed as the relaxation of each monomer in response to the electric field generated by the reference electronic state of the other monomer.

- Dispersion:

  Instantaneous multipole-multipole interaction arising from the fluctuations of the electronic density on each monomer. Dispersion is one of the most computationally demanding forces to compute as it is a purely dynamical electron correlation effect. This also means dispersion is the only force that is not at least partially captured by mean-field theories. Fortunately, at long-range the dispersion interaction acquires the following straightforward form,

  $$E_{disp} = -\frac{C_6}{r^6} - \frac{C_8}{r^8} - \frac{C_{10}}{r^{10}} - ... \tag{1.2}$$

  At shorter distances the dispersion energy is damped due to overlap effects between monomers.

Throughout this introduction the methane and water dimers will be used as quintessential examples for NCI. The global minimum water and methane geometries were taken from the S22 database[35] and interaction energy curves were created by moving the monomers along the axis connecting their center of masses. Example wavefunction (CCSD(T)[36]) and SAPT (SAPT2+3[37]) methods are shown for these dimers in Figure 1.1. As can be seen, the total SAPT and CCSD(T) interaction energies only deviate by a few percent from each other throughout the entire potential energy curve. However, the SAPT data is significantly more illuminating in terms of the interaction itself.

Figure 1.1: CCSD(T)/(aTZ,aQZ) and SAPT2+3/aTZ data for the water and methane dimers.

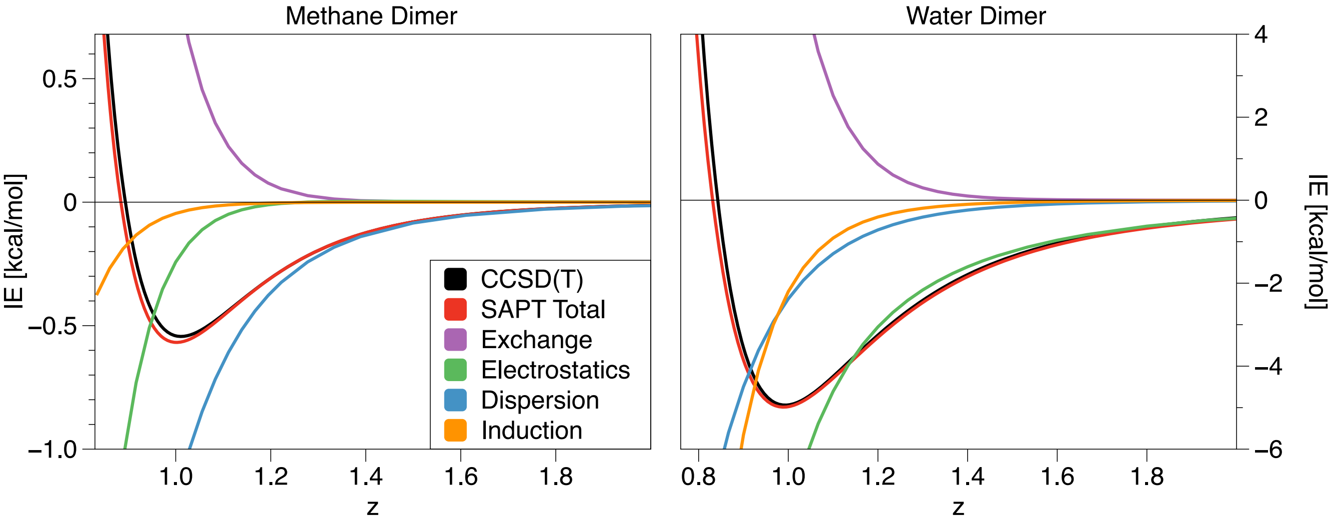

In the methane dimer we can see that dispersion is the dominant attractive force; however, electrostatics plays a large role around the minimum and induction comes into play on the repulsive wall. For the water dimer we see that electrostatics in the form of a hydrogen bond is the primary attractive force. At the same time, induction and dispersion forces play large roles at the minimum and shorter distances. From typical descriptions of hydrogen bonds the strength of the dispersion term is somewhat surprising, demonstrating the usefulness of computations that elucidate the breakdown of the interaction energy. Through SAPT we are able to describe the interaction in more physical detail while simultaneously capturing the total interaction energy accurately.

1.2 Wavefunction Theory for Noncovalent Interactions

The most accurate computation of the interaction energy between two atoms or molecules comes from full Configuration Interaction (FCI) theory.[38–41] However, the factorial scaling of this method limits accurate calculations to approximately 8 electrons. A more computationally tractable approach that has been described as the ”gold-standard” of computational chemistry is the coupled cluster approach with singles and doubles with the inclusion of perturbative triples [CCSD(T)].[36] The ”gold standard” title for the CCSD(T) approach comes from the high accuracy (roughly 3% or better for noncovalent interactions);[42–44] however, the cost (N^7 scaling, applicable up to approximately 25 heavy atoms) is quite limiting with respect to system size. The accuracy of the CCSD(T) method will be explored in Chapter 2.

To increase the applicability of wavefunction theory more approximate methods that scale like N^4 to N^6 must be utilized. Most popular among these is second-order Møller-Plesset perturbation theory (MP2). While MP2's description of hydrogen bonded complexes,[45] such as the water dimer, is quite accurate, dispersion-bound systems are over bound by 20–40%.[46–48] To correct the over-binding of dispersion scaling parallel- and antiparallel-spin contributions have been proposed such as the SCS-MP2[49,50] and SCS(MI)-MP2.[51] However, both methods of scaling the different spin cases of MP2 lead to somewhat sporadic errors and while they improve mean accuracy across a variety of tests cases, significant outliers still remain.[52]

As there is not currently a wavefunction method that gives the accuracy of CCSD(T) at a lower cost,[52] we will end our discussion on wavefunction based methods. Suffice to say that this is a very active area of research and there are many promising approaches on the horizon. However, this dissertation will primarily focus on the accuracy of DFT methods as these methods can be utilized for systems many times the size of even the lowest cost wavefunction method. A thorough review on the behavior of current wavefunction methods can be found in Ref. 53.

1.3 Density Functional Theory for Noncovalent Interactions

Density Functional Theory (DFT) is often turned to when wavefunction based methods prove to be too costly for systems of interest. The many flavors of DFT functionals are often classified in tiers popularized by Perdew's Jacob's Ladder.[54] The bottom rung begins with the local density approximation (LDA) theory and consecutively adds more wavefunction-based quantities or higher derivatives of the density into the functional. The rungs considered here are the Generalized Gradient Approximation (GGA), which utilizes pure Kohn-Sham (KS) orbitals and their gradient, hybrid-GGA functionals which include a portion of exact (SCF) exchange, and finally double-hybrid functionals, that include a portion of the MP2 correlation energy as computed with KS orbitals. Of these three different types only the double-hybrid functionals include long-range correlation; therefore, any GGA or hybrid-GGA is lacking in dispersion.

Instead of climbing Jacob's Ladder and adding more physics to improve results, there are a class of so-called interaction-optimized functionals, which attempt to optimize the various empirical coefficients for a given DFT method to CCSD(T) or experimental quantities.[55–57] This approach is highly successful as long as the molecules in question are similar to those in the training set. However, it has been shown that these results are over-fitted and the accuracy of the method is not guaranteed for a diverse set of quantities.[58] In addition, these functionals are still inherently local and the asymptotic behavior between two non-polar molecules will decrease exponentially instead of the correct $1/r^6$ asymptotic behavior.

The behavior of the GGA (BLYP[59,60]), hybrid-GGA (B3LYP[61,62]), double-hybrid (B2PLYP[63]), and interaction-optimized (M05-2X[55]) functionals is given in Figure 1.2. For the methane dimer it can be seen that the GGA, hybrid-GGA, and double-hybrid functionals are always too repulsive and only the double-hybrid functional is ever attractive at long-range. The double-hybrid functional, unlike the GGA and hybrid-GGA does include a partial description of dispersion through the fractional inclusion of MP2 correlation. While this does decrease the repulsiveness of the functional it is clearly not sufficient to capture

Figure 1.2: CCSD(T)/(aTZ,aQZ) in addition to the BLYP, B3LYP, B2PLYP, and M05-2X functionals in the QZVP basis for the water and methane dimers.

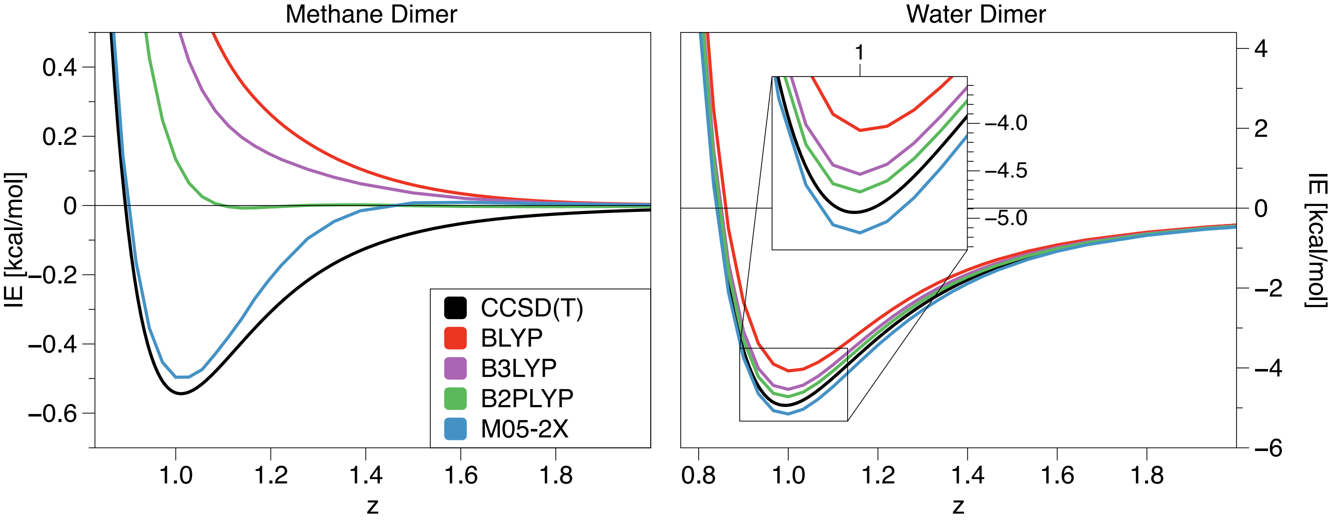

the interaction energy accurately alone. The interaction-optimized functional does represent the interaction energy at the minimum quite well; however as mentioned it does not have the correct long-range behavior and goes to zero at long-range like e^{-r} instead of $1/r^6$. In addition, we can see that the M05-2X functional is actually positive at long-range like its non-dispersion including counterparts. On the other hand the water dimer is primarily dominated by electrostatics and the performance of each functional is quite good.

Dispersion can be added to the base functional in a pairwise manner such as the dispersion corrections of Grimme *et al.*,[64,65] the atom-in-a-molecule dispersion expansion resulting from the Hirshfeld partitioning of electron density,[66] the exchange-hole dipole moment (XDM) approach by Becke and Johnson,[67] the dDsC modification by Steinmann and Corminboeuf,[68] or through the use of explicitly nonlocal van der Waals correlation functionals.[69,70] These approaches are computed similarly and each can be formulated like the following

$$E_{\text{disp}} = -\sum_{A>B}\sum_{n=6,8,\ldots} f_{damp}(r)\frac{C_n^{AB}}{r_{AB}^n} \tag{1.3}$$

The differences between the methods are illuminated in the computation of the coefficients (C_n^{AB}), the form of the damping term ($f_{damp}(r)$), and whether A and B are atoms or regions of electronic density. These methods accurately capture asymptotic behavior to within approximately 10% or better;[65] however, their accuracy at short to medium range depends heavily on the empirically defined damping form.

Figure 1.3: CCSD(T)/(aTZ,aQZ) in addition to the BLYP-D3, B3LYP-D3, B2PLYP-D3, and M05-2X-D3 functionals in the QZVP basis for the water and methane dimers.

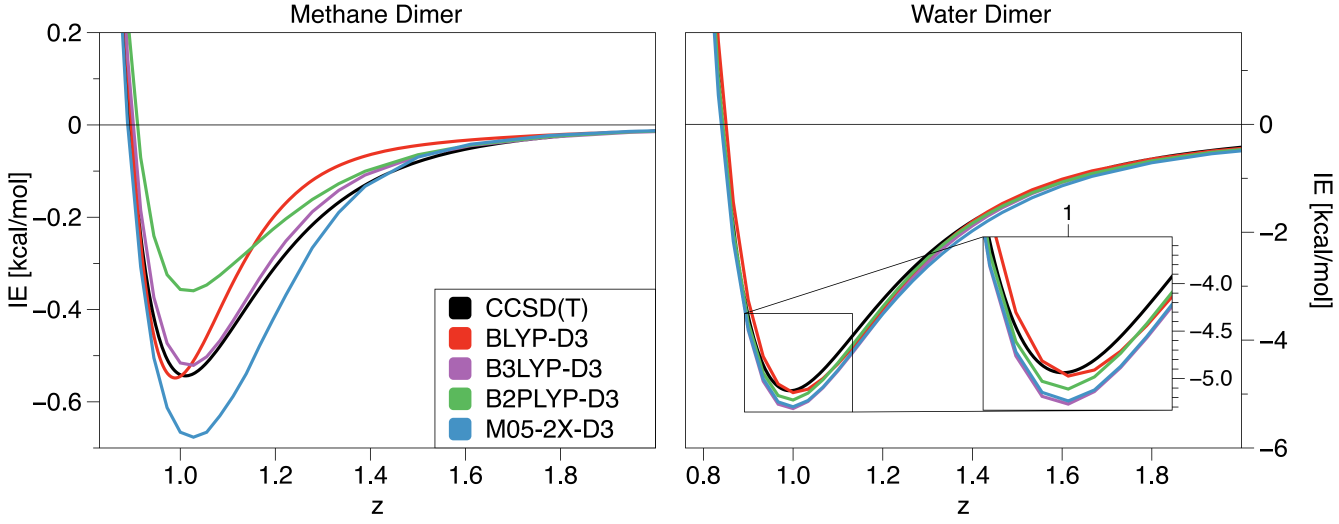

The DFT functionals shown in Figure 1.2 are augmented with Grimme's -D3 dispersion expression and shown in Figure 1.3. For the methane dimer it can be seen that the interaction energy is overall quite improved for non-interaction-optimized functionals. The M05-2X functional's minimum is now too deep; however, the correct asymptotic behavior is recovered. The primary issue with the DFT-D3 method is that while the results can be quite good, for example, the B3LYP-D3 method shown here, the results can be somewhat sporadic. The B2PLYP-D3 functional theoretically should have the best performance as it represents the most advanced functional shown; however, here it is the worst performer. For the water dimer the SAPT results of Figure 1.1 show the attractive components of the interaction energy are comprised of 20% dispersion at the minimum. Therefore, it should not be surprising that the inclusion of a dispersion term improves the accuracy of these methods for the water dimer as well.

Like the methane and water dimer, large scale benchmarking for a variety of dispersion including functionals shows somewhat mixed results. While overall accuracy for these dispersion including functionals is quite impressive, with average errors at the van der Waals minimum geometries down to about 0.2 kcal/mol in some cases;[71] however, these methods can have large outliers and do not always exhibit systematic accuracy across a range of distances.[71–73] This makes DFT-D methods an active area of research and the accuracy and understanding of these methods will be explored in Chapters 4 and 5.

1.4 The one-electron basis

As the wavefunction cannot be computed exactly, we will approximate the exact wavefunction in a given basis set. In many ways we can view basis sets as fitting functions. For variational methods, the more flexibility the method has, the lower the overall energy will be. To examine the effect of this on intermolecular computations let us examine two possible methods of computing the interaction energy. The first is where we compute the energy of the dimer and monomers in their respective basis sets

$$E_{int} = E_{AB}^{AB} - E_{A}^{A} - E_{B}^{B} \tag{1.4}$$

where subscripts denote the molecular geometries and superscripts denote the basis set. The dimer in the above energy expression will have more flexibility than each of the monomers. Therefore, the energy of the dimer compared to the monomers will be relatively too low, this results in an interaction energy that is too deep when compared to the complete basis set (CBS) limit.

The Boys and Bernardi counterpoise (CP) approach[74,75] aims to remove this error by computing all energies in the same basis set

$$E_{int} = E_{AB}^{AB} - E_{A}^{AB} - E_{B}^{AB} \tag{1.5}$$

Now each monomer has more flexibility than the dimer leading to interaction energies that are too positive compared to the CBS limit. As such, the CP correction does not fix the fundamental flexibility issue.

Figure 1.4: CP (solid) and nonCP (dashed) corrected MP2 values in a series of Dunning basis for the water and methane dimers.

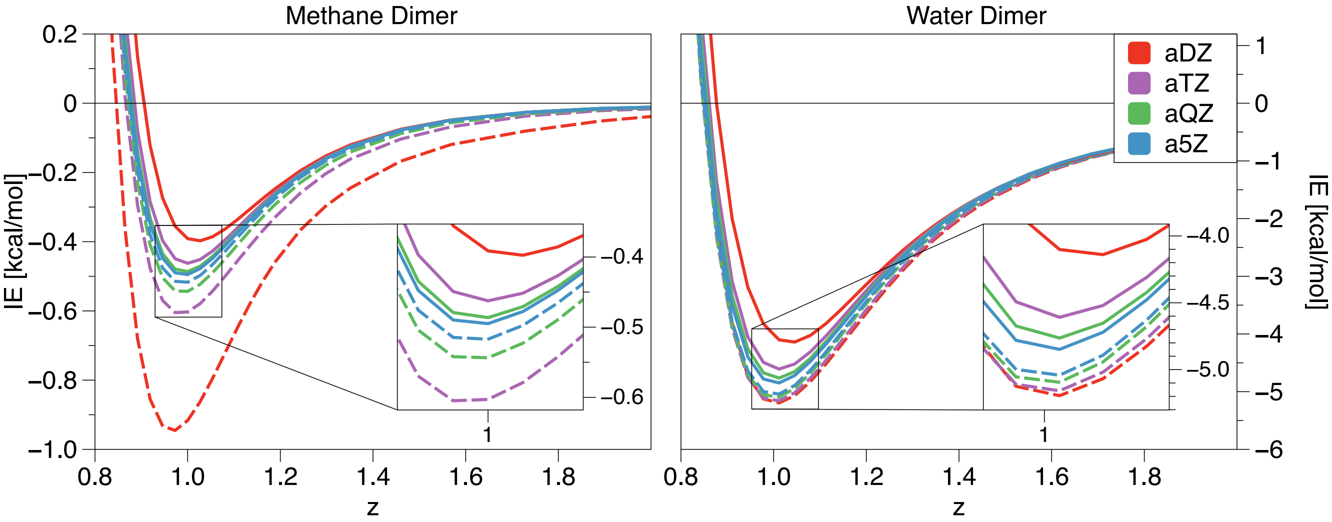

As can be seen in Figure 1.4, the CP correction is greatly beneficial for the methane dimer where the nonCP aDZ results are too deep by a factor of two. For the water dimer we see the same trend of nonCP being too negative and CP being too positive; however, the nonCP results are slightly more converged on a per basis trend than the CP results. This demonstrates that the CP correction can either help or hurt depending on the type of system in consideration. In terms of countering the worst absolute or relative errors it is advantageous to CP correct all results, thus unless otherwise indicated all results shown will be CP corrected.

In this work we will make extensive use of the Dunning correlation-consistent bases cc-pVXZ≡XZ and aug-cc-pVXZ≡aXZ ($X = D$, T, Q,...)[76,77] These correlation-consistent bases were developed specifically so that the correlation energy converges at roughly a constant X^{-3} rate; therefore, this constant rate can be used to approximate the CBS limit,[78]

$$E_{\infty}^{corr} \approx \frac{E_{X}^{corr} X^3 - E_{Y}^{corr} Y^3}{X^3 - Y^3} \tag{1.6}$$

where X and Y refer to the cardinal numbers of each basis. The notation $method/(basis1, basis2)$ denotes that the correlation energy has been obtained from the values in bases ($basis1$) and ($basis2$) using the standard X^{-3} extrapolation. As SCF energy converges at an exponential rate, the SCF energy is simply taken from the larger of the two basis sets and not extrapolated.

In addition to the Dunning series, the Turbomole def2 series of basis sets were employed.[79] These are SVP, TZVP, and QZVP which roughly correlate in size to cc-pVDZ, cc-pVTZ, and cc-pVQZ, respectively. These bases are generally employed for DFT methods as the auxiliary density-fitting basis for Coulomb integrals is of a fixed size for all def2 basis sets. This leads to a reduced computation time when employing the density fitting approximation in comparison to their Dunning counterparts, especially for the large QZVP basis.

1.5 Databases

The geometries and energies found in this work have been organized into four separate databases and are taken from Appendices B, C, and D.

1.5.1 Nanotube Fragments

Nanotubes can come in a range of chiralities; however, we choose the zigzag $(k, 0)$ and armchair (k, k) nanotubes for simplicity.[12] Where k roughly represents the number of fused benzene rings around the circumference of the nanotube.

As full carbon nanotubes cannot be computed with conventional wavefunction theory, very large nanotube fragments will first be generated using the TUBEGEN program[80] and more manageable fragments that emulate the parent nanotube will then be sliced from these super fragments. These slices are then capped with hydrogen atoms to make PAH-like structures. C_n fragments will be hexagonal pieces of the carbon nanotube where n represents the number of successive peri-fused benzene ring layers, i.e., benzene (C_0), coronene (C_1), circumcoronene (C_2), etc. The C_1 fragment is also referred to as "curved coronene" and the language "(5,0) curved coronene" would represent a coronene sized fragment cut out of a (5,0) nanotube. The nanotube can also be sliced perpendicular to its primary axis into full toroidal fragments denoted T_n. The width is determined so that the corresponding C_n fragment is a subset of the full toroidal T_n fragment as shown in Figure 1.5.

Figure 1.5: A representation of both C_n (red) and T_n (teal) model fragments cut from a (12,0) carbon nanotube.

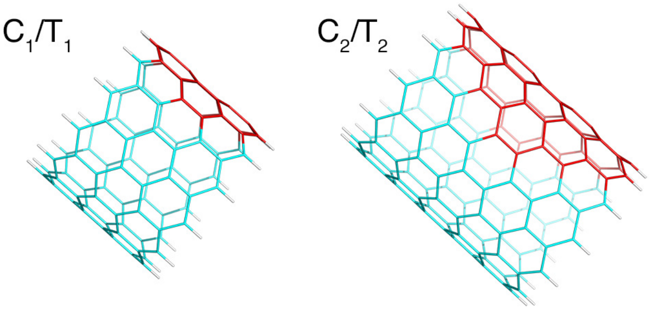

1.5.2 Methane–PAH

Geometries of methane bound to PAH's the size of benzene through pyrene come from Appendix B. The individual geometries will be denoted nC where n represents the number of methane hydrogens pointing towards the PAH surface.

Figure 1.6: The three coordinations of the methane bound to PAH's the size of benzene through pyrene. Adapted from Appendix B.

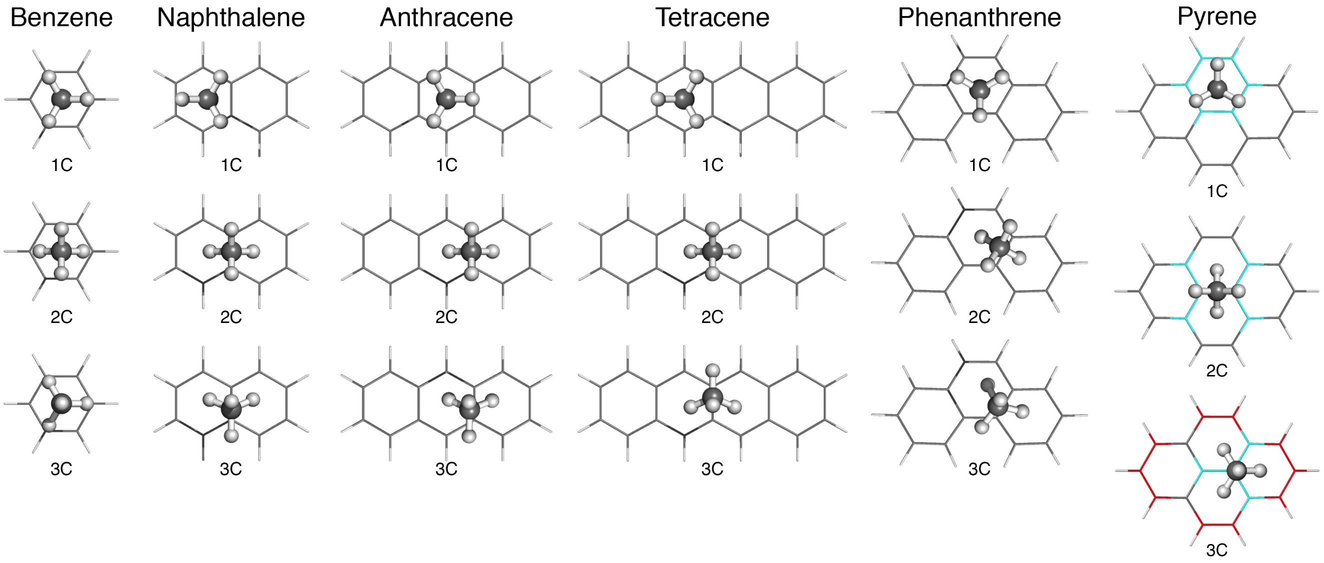

For each of the eighteen minima shown in Fig. 1.7, fifteen additional geometries were created by altering the distance between the methane center of mass and the plane of the PAH. The range of distances was chosen as $z = 0.8$ to 2.4 to emulate a complete 1-dimensional potential energy curve. The reduced distance z is defined as $z = \frac{R}{R_{eq}}$, R is the distance between two monomers, and R_{eq} is the minimum separation on a 1-dimensional energy curve. This results in 270 separate geometries with a benchmark level of theory of MP2/(aQZ, a5Z) + ΔCCSD(T)/aDZ or higher.

1.5.3 Methane–Curved Coronene

The methane–curved coronene dataset comes from Appendix C and comprises of methane bound to curved coronene. Five representative nanotubes, (5,5), (7,0), (9,0), (12,0), and (5000,0) where (5000,0) represents flat graphene, were first chosen. The minima for the (12,0) curved coronene complex are shown in Figure 1.7. This produces a total of 30 minimum geometries, the interior geometries for the (5000,0) nanotube were removed due to symmetry, resulting in a total 27 minimum geometries.

Figure 1.7: 1C, 2C, and 3C interior and exterior minima locations for the methane–(12,0) curved coronene complex. Adapted from Appendix C.

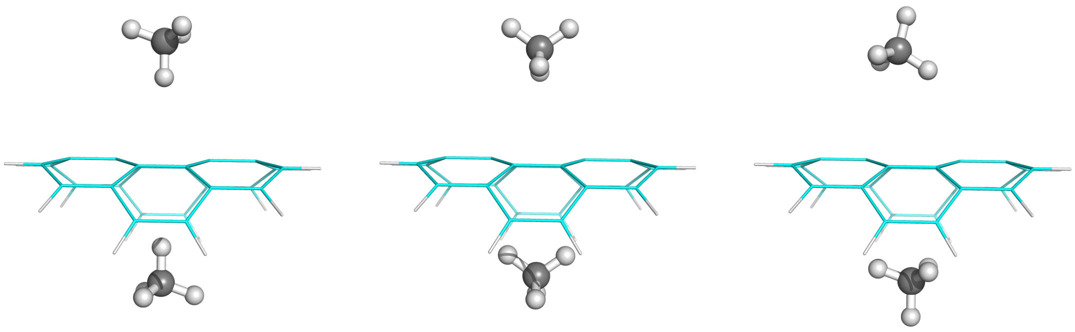

In Appendix C additional geometries were created by choosing $z = 0.9$, 1.0, 1.2, 1.4 for a total of 108 geometries. Since this publication[73] it was discovered that an additional point at $z = 0.8$ was crucial for the description of interactions shorter than the minima. This point was subsequently computed bringing the total to 135 methane–curved coronene geometries. Therefore, all statistics given in this dissertation will differ slightly compared to the values found in Ref. 73. The benchmark level of theory is MP2/(aTZ, aQZ) + ΔCCSD(T)/laDZ (cf. Section 3.1.3).

1.5.4 CO_2–PAH

For the CO_2 bound to benzene, naphthalene, and pyrene the dataset comes from Appendix D. The global minimum for each PAH is where the CO_2 molecule is parallel to the

Figure 1.8: Minimum geometries for the CO_2–PAH complexes. Adapted from Appendix D.

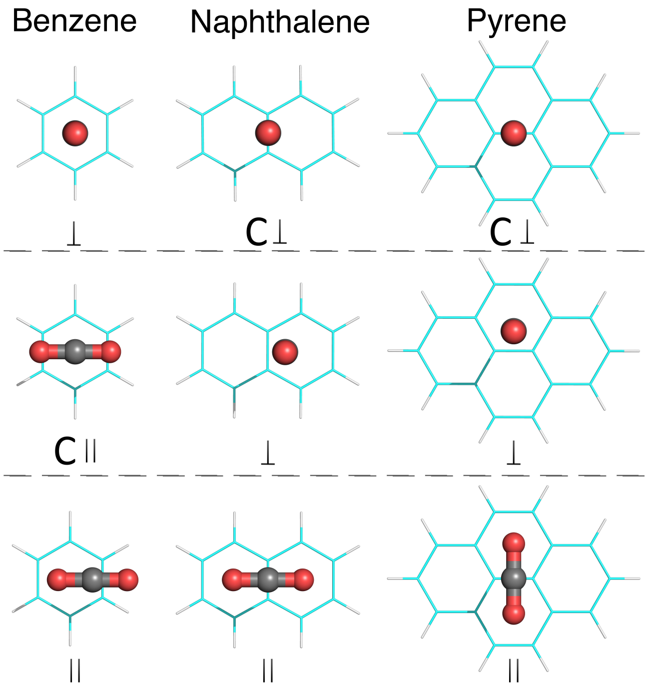

PAH surface, these geometries will be denoted parallel or ‖. Unlike the methane–PAH systems there are no other local minima to add angular diversity to the dataset. Instead, a geometry where the CO_2 molecule is perpendicular to the PAH will be denoted as perpendicular or ⊥. We will also consider an additional high-symmetry C_{2v} geometry where the CO_2 molecule is located over the center of the PAH: these orientations will be labeled as Centered or abbreviated as C. All nine structures can be found in Figure 1.8. The three ‖ and three ⊥ C_{2v} structures had their z distances expanded to: 0.8, 0.9, 1.0, 1.2, 1.4, 1.6, 1.8, 2.0, and 2.5 resulting in a total of 54 geometries. The benchmark level of theory is MP2/(aTZ, aQZ) + ΔCCSD(T)-F12avg/aDZ (cf. Section 3.3).

1.5.5 CO_2–Curved Coronene

The CO_2–curved coronene dataset contains CO_2 with coronene curved to mimic (5,5), (6,6), (7,7), (8,0), (10,0), and (12,0) carbon nanotubes along with flat graphene and comes

Figure 1.9: Minimum geometries for the CO_2–curved coronene complexes. The global minimum for $\parallel$ CO_2 on zigzag nanotubes is shown with transparency. The opaque C_s minimum was utilized for computational efficiency. Adapted from Appendix D.

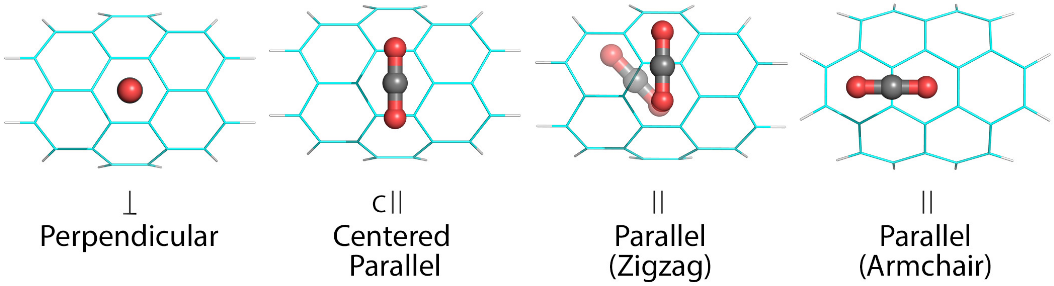

from Appendix D. Again, the minima were always in a $\parallel$ position where the center of the carbon dioxide molecule was centered over a carbon-carbon bond. To explore the angular space a C_{2v} centered (C) $\parallel$ orientation was created along with a $\perp$ orientation directly in the center of the coronene molecule. These minima were then expanded for a $z = 0.8$, 0.9, 1.0, 1.2, and 1.4, resulting in a total of 195 geometries. The benchmark level of theory is MP2/(aTZ, aQZ) + ΔCCSD(T)-F12avg/laDZ.

1.6 Statistics

In quantum chemistry the two most used statistics are unsigned error (UE),

$$\text{UE} = |E - E_{\text{ref}}| \tag{1.7}$$

and unsigned relative error (URE)

$$\text{URE} = \left(\left| \frac{E - E_{\text{ref}}}{E_{\text{ref}}} \right| \right) \cdot 100\%, \tag{1.8}$$

These quantities are usually computed on sets of points that comprise databases and then the mean (MURE), median (MeURE), or max (maxURE) are taken. However, UE-based quantities work well only if the database has reference values that are similar in magnitude and URE-based quantities only work well if there are no reference values close to zero. In addition, the root mean square (RMS) of each quantity can be taken

$$RMS = \sqrt{\frac{1}{n}\sum_{i}^{n}\chi_i^2} \tag{1.9}$$

where χ can represent an individual UE or URE.

It should be noted that the definition of R can vary; however, it is most commonly defined as the center of mass distance between two monomers. The language short-range will refer to distances shorter than the minima and long-range will refer to distances corresponding to the minima and longer for this work.

In Fig 1.10 the UE and URE is presented for four different cases of potential energy curves. Errors in the top panel are built specifically to be even in UE and URE respectively, while errors on the bottom panel represent more realistic cases. As can be seen, the UE has difficulty describing short and long distances where the energy is either very small or very large, respectively. The URE describes the entire PES well except for where the repulsive wall crosses zero, unless the method and reference cross zero at the exact same point the URE quantity will suffer singularity issues.

The issues with URE can be circumvented by simply neglecting small values close to zero on the repulsive wall; however, the PES can cross zero multiple times at short and long-ranges and it is not always clear which points should be removed. As in the case of Appendix D a weighted unsigned relative error (wURE) was utilized that effectively caps the denominator at short-range,

$$\text{wURE} = \left(\left|\frac{E - E_{\text{ref}}}{E_{\text{weight}}}\right|\right) \cdot 100\%, \quad E_{\text{weight}} = \begin{cases} |E_{\text{ref}}| & z \geq z_{\min} \\ \max\{|E_{\text{ref}}|, E_{\text{mask}}\} & z < z_{\min} \end{cases} \tag{1.10}$$

Figure 1.10: A comparison of UE and URE for four different potential energy curves.

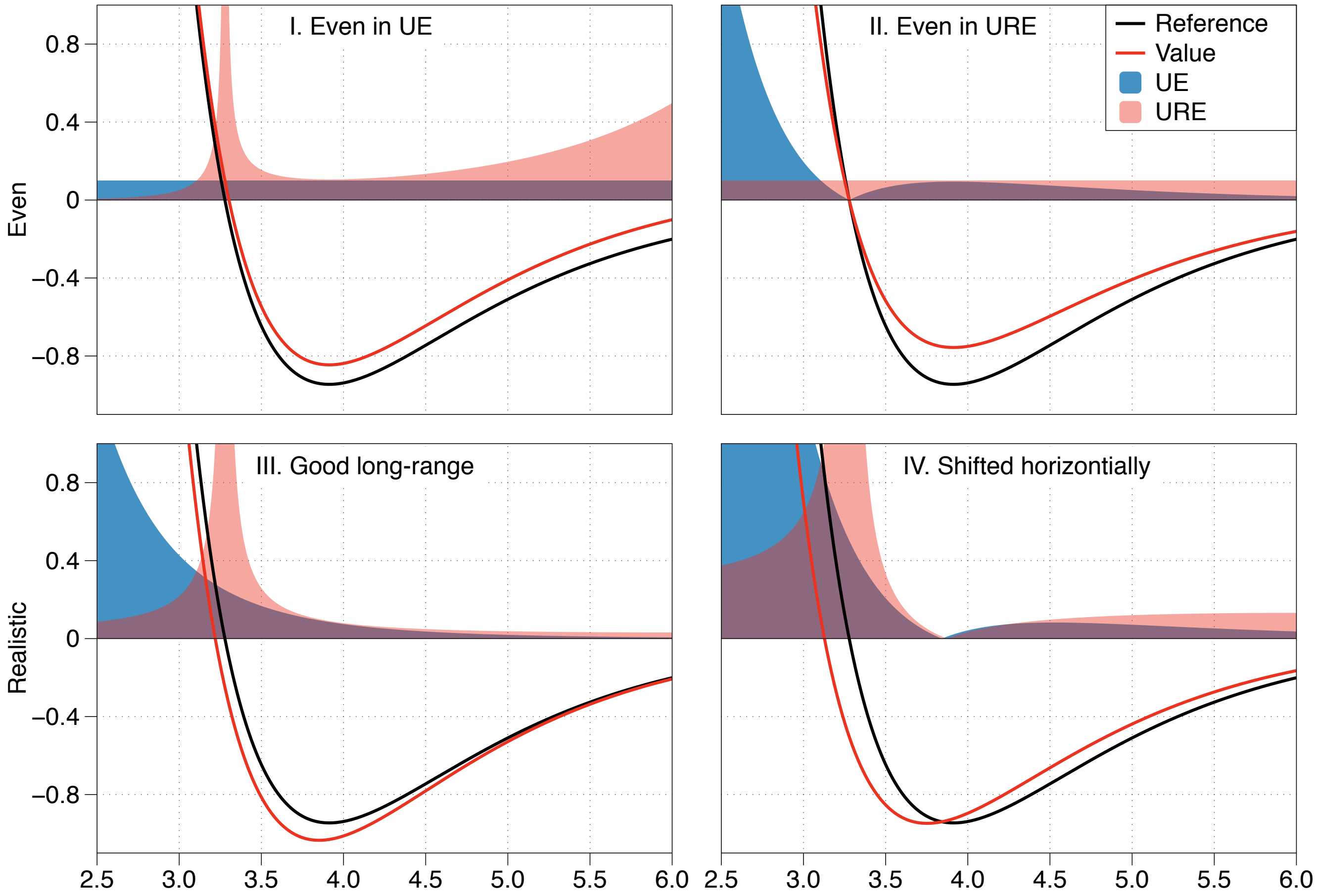

wURE works well when the database has PESs of similar equilibrium distance and magnitude, the error with respect to distance is well understood, and the PES does not cross zero at long-range. For this work a E_{mask} of 2.0 kcal/mol, as in Appendix D, was chosen for all systems.

For more heterogeneous datasets, the overall form of wMURE was later expanded to capped unsigned relative error (CURE),

$$\text{CURE} = \left(\left| \frac{E - E_{\text{ref}}}{E_{\text{weight}}} \right| \right) \cdot 100\%, \quad E_{\text{weight}} = \max \left\{ |E_{\text{ref}}|, \frac{\xi |E_{\text{ref-eq}}|}{z^3} \right\} \tag{1.11}$$

For this work a ξ value of 0.2 is employed. The denominator capping has now been completely generalized, the dependence on $E_{\mathrm{ref-eq}}$ allows for variable capping based on well depth and the dependence on z allows capping at both short and long-ranges. This allows all curves in large and diverse datasets to be treated equally. For datasets where $E_{\mathrm{ref-eq}}$ and z are unknown, the CURE weighting function can be defaulted back to a wURE-like quantity.

1.7 Notation

There exist many ways to label and describe quantum chemistry theories. In this section the quantities and indices used will be defined and outlined. Generalized multidimensional arrays will be referred to as ”tensors” and two dimensional arrays will be referred to as ”matrices”.

1.7.1 Einstein summation notation

The generalized Einstein summation notation will be employed where repeated indices on the right hand side (RHS) that do not appear on left hand side (LHS) are assumed to be summed over. A matrix-matrix multiplication example:

$$\text{Conventional} : C_{ij} = \sum_k A_{ik} B_{kj} \tag{1.12}$$

$$\text{Einstein summation} : C_{ij} = A_{ik} B_{kj} \tag{1.13}$$

an outer product example

$$C_{ikj} = A_{ik} B_{kj} \tag{1.14}$$

1.7.2 Indices

The following notation will be adhered to throughout this dissertation. Occasionally indices will be redefined, but it should be clear in the context what the alternate meaning is.

• General atomic orbitals	$\mu, \nu, \lambda, \sigma$
• Inactive (doubly occupied) molecular orbitals	i, j, k, l
• Active (partially occupied) molecular orbitals	t, u, v, w, x, y
• Unoccupied (virtual) molecular orbitals	a, b, c, d
• General index molecular orbitals	p, q, r, s, m, n, o
• Auxiliary basis	P, Q, R, S

1.7.3 Operators

Operators used in the second quantization formalism.

• Creation operator	$a_p^\dagger$
• Annihilation operator	a_p
• Single excitation operator	$\hat{E}_{pq} = a_p^\dagger a_q = a_{p\alpha}^\dagger a_{q\alpha} + a_{p\beta}^\dagger a_{q\beta}$
• Two-electron excitation operator	$e_{pqrs} = \hat{E}_{pq}\hat{E}_{rs} - \delta_{pr}\hat{E}_{qs}$

1.7.4 Tensors

Common matrices and tensors utilized in this work.

• Core Hamiltonian matrix	H_{pq}
• Molecular orbital coefficient matrix	$C_{p\mu}$
• Overlap matrix	$S_{\mu\nu}$
• SCF one-particle density matrix	D_{pq}

- CI active one-particle density matrix $\langle 0|\hat{E}_{tu}|0\rangle = \gamma_{tu}$
- CI active two-particle density matrix $\langle 0|e_{tuvw}|0\rangle = \Gamma_{tuvw}$
- CI active transition density matrix $\gamma^{i}_{tu} = \langle 0|\hat{E}_{tu}|i\rangle$ or $\Gamma^{i}_{tuvw} = \langle 0|\hat{e}_{tuvw}|i\rangle$
- Atomic-orbital two-electron integral $g_{\mu\nu\lambda\sigma} = \int \mu(\mathbf{r}_1)\nu(\mathbf{r}_1)\frac{1}{r_{12}}\lambda(\mathbf{r}_2)\sigma(\mathbf{r}_2)d^3\mathbf{r}_1 d^3\mathbf{r}_2$
- Molecular-orbital two-electron integral $g_{pqrs} = C_{p\mu}C_{q\nu}g_{\mu\nu\lambda\sigma}C_{r\lambda}C_{s\sigma}$
- Density-fitted tensor $(pq|A)$

1.8 Outline

The accuracy of the CCSD(T) method along with the basis set convergence of several post-CCSD(T) methods will be illuminated in Chapter 2. After the accuracy of the CCSD(T)/CBS method itself is established, we will turn our attention to the accurate computation of this quantity through explicitly correlated and composite based methods in Chapter 3. More approximate DFT methods will then be compared to benchmark CCSD(T) computations in Chapter 4. Chapter 5 will then detail the problems of the DFT-D3 method that arose in Chapter 4 along with possible solutions. Chapters 2 through 5 reorganize and summarize the pertinent points of the five papers that are submitted in partial fulfillment of this dissertation:

(Appendix A) Smith, D.G.A.; Jankowski, P.; Slawik, M.; Witek, H.A.; Patkowski, K. *Basis Set Convergence of the Post-CCSD(T) Contribution to Noncovalent Interaction Energies* J. Chem. Theory Comput. **2014**, *10*, 3140.

(Appendix B) Smith, D.G.A.; Patkowski, K. *Interactions between Methane and Polycyclic Aromatic Hydrocarbons: A High Accuracy Benchmark Study* J. Chem. Theory Comput., **2013**, *9*, 370.

(Appendix C) Smith, D.G.A.; Patkowski, K. *Toward an Accurate Description of Methane Physisorption on Carbon Nanotubes* J. Phys. Chem. C **2014**, *118*, 544.

(Appendix D) Smith, D.G.A.; Patkowski, K. *Benchmarking the CO_2 Adsorption Energy on Carbon Nanotubes* J. Phys. Chem. C **2015**, *119*, 4934.

(Appendix E) Smith, D.G.A.; Burns, L.A.; Patkowski, K.; Sherrill C. D. *Limits of accuracy of the -D3 dispersion correction to Density Functional Theory at all length scales* – in preperation.

Through the course of deriving Multi-Reference Symmetry-Adapted Perturbation Theory (MRSAPT) it was realized that a more flexible MCSCF program than is currently available was required to adequately describe all parts of MRSAPT. To this end, a new MCSCF program was implemented in the PSI4[81] quantum chemistry package and Chapter 6 will detail the specifics of this program. The current work on MRSAPT is then summarized in Chapter 7.

Chapter 2

Accuracy of the CCSD(T) method for noncovalent interactions

In this section we will summarize the most important findings of Ref. 42 found in Appendix A.

The accuracy of the CCSD(T) method is difficult to determine as the cost of computing less approximate methods is intractable for all but the smallest systems. However, the inexorable increase of computational power and improved algorithm design slowly allows post-CCSD(T) methods to be computed for complexes of increasing size.

Let us first turn our attention to a description of Coupled-Cluster (CC) theory. As there exists a litany of reviews that cover CC derivation, implementation, and meaning in great detail[82–84] let us instead give a brief overview of the method. CC theory uses the exponentiated $\hat{T}$ excitation operator

$$\hat{T} = \hat{T}_1 + \hat{T}_2 + \hat{T}_3 + ... \tag{2.1}$$

where the subscript denotes the number of electrons each operator will excite. The idea is that we can reproduce the exact wavefunction Ψ as combinations of excitations of our reference wavefunction Φ_0, $\Psi = e^{\hat{T}}\Phi_0$. As the cost of computing the CC expansion is equal to N^{2n+2}, where N is the number of basis functions and n is the largest excitation, it is often convenient to limit the overall number of excitations. This leads to a hierarchy of CC methods, e.g., $\hat{T} \equiv \hat{T}_1 + \hat{T}_2 \rightarrow$ CCSD. Where "S", "D", T", "Q", ... represents singles ($\hat{T}_1$), doubles ($\hat{T}_2$), triples ($\hat{T}_3$), quadruples ($\hat{T}_4$), etc. When the number of excitations n equals the number of electrons in the system, then the CC method is equivalent to FCI, e.g., for a four electron system CCSDTQ $\equiv$ FCI.

The CC method produces a set of non-linear equations that must be solved iteratively. If CCn is computed iteratively, CC$(n+1)$ can be computed perturbatively. This leads to the popular CCSD(T) method where CCSD is computed iteratively to convergence and (T) is then computed perturbatively.

2.1 Previous work on post-CCSD(T) accuracy

Computations of post-CCSD(T) interaction energies have typically been limited to four electron systems such as He–He,[85] He–H_2,[86] and H_2–H_2.[87] While these computations are quite illuminating and show that the overall post-CCSD(T) contribution (FCI - CCSD(T)) is no more than 4% of the total interaction energy, such systems typically exhibit different convergence properties than more conventional, biologically relevant molecules.

Recently, Hobza and collaborators completed several studies that explored the CCSDT,[88] CCSDT(Q),[89,90] and CCSDTQ[91,92] energies on the A24 database.[43,44,93] The A24 database contains small complexes for which very computationally demanding computations can be run routinely. However, the basis set utilized for post-CCSD(T) computations was 6-31G**(0.25, 0.15). These results should be taken with caution as this basis can yield corrections with either the incorrect sign or the incorrect magnitude.[42] Fortunately, it was previously shown that CCSDT(Q) is converged with respect to the CC level to 0.5 cm^{-1} or better.[43,94–96] In addition, CCSDT results are typically worse than CCSD(T) making CCSDT(Q) required to improve the interaction energy.

2.2 Basis set convergence of the CCSDT and CCSDT(Q) corrections

A dataset of 21 small complexes was created for which CCSDT(Q) could be computed in the aTZ basis to ensure both the correct sign and relative magnitude of the correction was obtained. The largest complex in this database was the methane dimer for which the CCSDT(Q)/aTZ computation required over five CPU years to complete. This database was then divided into 4-valence-electron, nonpolar-nonpolar, polar-nonpolar, and polar-polar complexes. The language 4-valence-electron systems is utilized to encompass systems where freezing the core electrons also results in 4-electron systems such as the lithium hydride dimer.

Figure 2.1: Performance of different basis sets in the recovery of the $\delta_{\mathrm{T+(Q)}}$ benchmark (computed as a sum of the δ_{T} and $\delta_{\mathrm{(Q)}}$ benchmarks obtained in separate extrapolations) displayed as MURE, the black lines denote MeURE. Adapted from Appendix A.

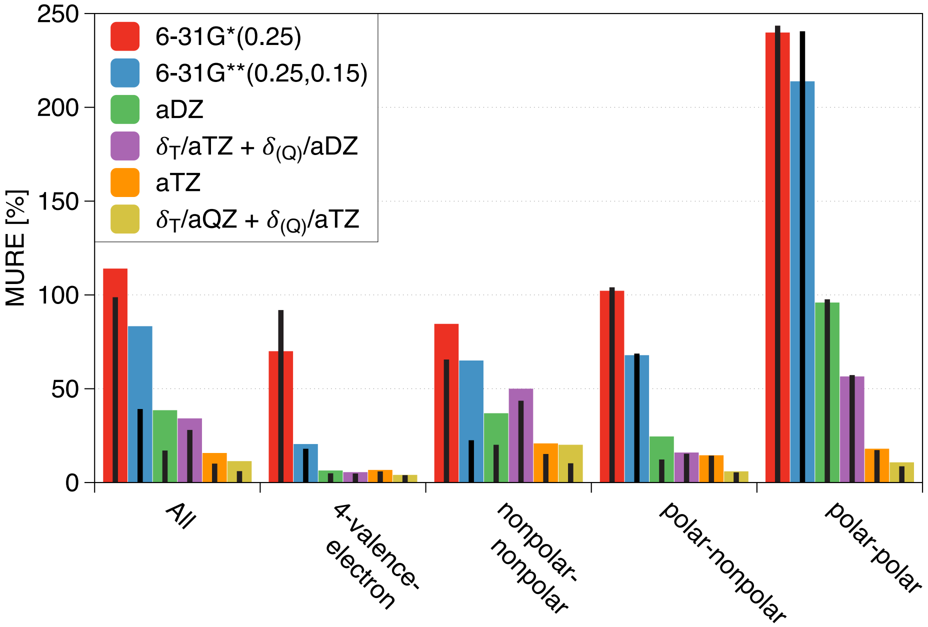

The $\delta_{\mathrm{T}} \equiv$ CCSDT - CCSD(T) and $\delta_{\mathrm{(Q)}} \equiv$ CCSDT(Q) - CCSDT interaction energy contributions were computed for all 21 complexes in basis sets ranging up to a6Z for the smallest complexes. The relative error for $\delta_{\mathrm{T+(Q)}} \equiv \delta_{\mathrm{T}} + \delta_{\mathrm{(Q)}}$ compared to the best $\delta_{\mathrm{T+(Q)}}$ estimate is shown in Figure 2.1. As can be seen, the small 6-31G*(0.25) and 6-31G**(0.25, 0.15) basis sets employed by Hobza and collaborators[43] can have MURE's over 100%. This means that, on the average, the computation of this correction in these small basis sets is more harmful than helpful, stressing the need for adequate basis sets utilized in these corrections.

Figure 2.1 also demonstrates that basis set conclusions cannot be made on 4-valence-electron systems alone and that the behavior of larger complexes is not consistent with these very small systems. For the aDZ basis the worst basis errors come from the polar-polar complexes; however, for these complexes the $\delta_{\mathrm{T+(Q)}}$ term has the smallest relative effect, amounting to less than 0.3% of the total interaction energy. Neglecting the polar-polar systems, the aDZ $\delta_{\mathrm{T+(Q)}}$ error is at worst 37% on the average, and 21% for aTZ. While the aTZ basis is recommended to compute these corrections, this is not always possible and the aDZ basis will give a reasonable description of the corrections. The δ_{T} and $\delta_{\mathrm{(Q)}}$ contributions can be computed in different basis sets; however, as seen in Fig 2.1, utilizing separate basis sets is not always beneficial and typically does not justify the additional computational expense.

2.3 Relative magnitude of the post-CCSD(T) contribution

To examine how large these contributions are compared to the CCSD(T) interaction energy, the best estimates for the δ_{T}, $\delta_{\mathrm{(Q)}}$, $\delta_{\mathrm{T+(Q)}}$, and δ_{Q} interaction energies are shown in Figure 2.2. Again, the 4-valence-electron systems are outliers with the largest $\delta_{\mathrm{T+(Q)}}$ contributions of between 3 and 4%. In general, the contribution of the $\delta_{\mathrm{T+(Q)}}$ correction is less than 2% with the only outlier besides the 4-valence-electron systems being the H_2–CO complex. This small relative magnitude of the $\delta_{\mathrm{T+(Q)}}$ contribution does rely on a cancellation between δ_{T} and $\delta_{\mathrm{(Q)}}$. The largest cancellation occurs with the two configurations of the N_2 dimer utilized which are the two lines furthest from zero for the δ_{T}, $\delta_{\mathrm{(Q)}}$, and δ_{Q} corrections. This is likely due to the fact that this is the only complex where each monomer has a triple bond, which leads to a total of eight electrons in π orbitals (four on each monomer); δ_{Q} is the first CC method that includes four excitations from the ground state in the iterative equations. However, for all other complexes the δ_{Q} is less than 0.1% of the CCSD(T) energy, further confirming that effects post-CCSDT(Q) are negligible for all but the most precise computations.

Figure 2.2: The δ_{T}, $\delta_{(\mathrm{Q})}$, $\delta_{\mathrm{T}+(\mathrm{Q})}$, and δ_{Q} interaction energy contributions as percentages of the CCSD(T)/CBS interaction energy. The four-valence-electron, nonpolar-nonpolar, polar-nonpolar, and polar-polar dimers are represented by green, blue, orange, and red symbols, respectively. The dots represent the *unsigned* averages of the individual values, with the black dot showing the unsigned average for all complexes. Adapted from Appendix A.

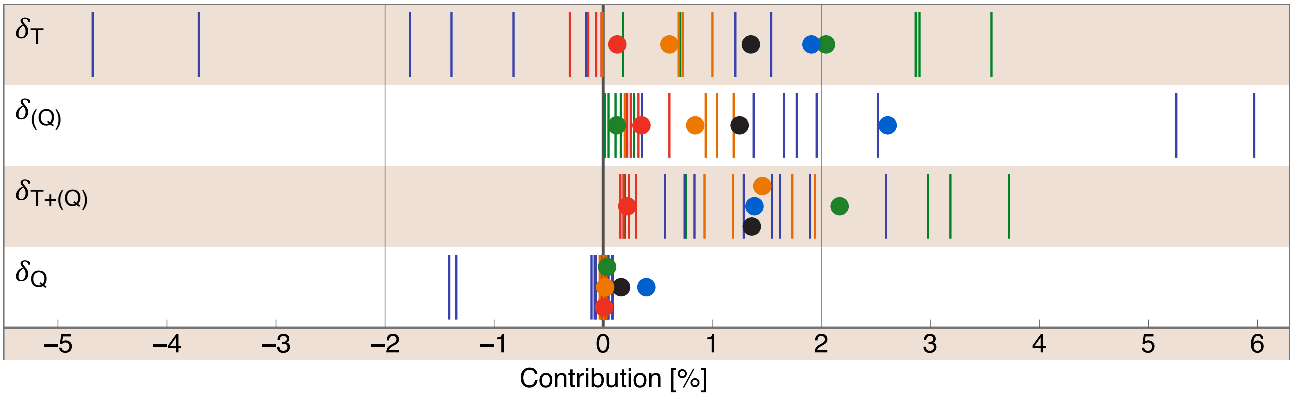

2.4 Conclusions

It is shown that the post-CCSD(T) contributions should not be computed in small 6-31G*(0.25) or 6-31G**(0.25, 0.15) basis sets and doing so will often be harmful to the overall accuracy of the computation. The post-CCSD(T) contributions should be computed in at least the aDZ basis set and when possible, the aTZ basis. While the aDZ basis set can still lead to incorrect signs for several systems, it improves the overall estimation of the interaction energy on the average. The post-CCSD(T) contributions only comprise 2-3% of the total interaction energy for typical complexes.

These post-CCSD(T) contributions are currently programmed quite naively, often being automatically implemented. While such implementations can produce results, their computational efficiency is quite low. As these contributions become a more important part of research, better algorithmic improvements rather than more computational power are likely to lead to the ability to compute post-CCSD(T) corrections for larger systems.

Chapter 3

Obtaining the CCSD(T)/CBS limit for noncovalent interaction energies

In this section we will summarize the most important CCSD(T) benchmark findings of Ref. 42 and 97, found in Appendices B and D, respectively.

As we have now established the accuracy of the CCSD(T)/CBS approach, we will now turn our attention to the accurate computation of this limit. We have previously stated that CCSD(T) calculations are limited to approximately 25 heavy atoms; however, this is a rather convenient idiom and the real restriction is the size of the basis set. Routine CCSD(T) calculations, that is those without the utilization of prestige level supercomputers, are currently limited to approximately 500-800 basis functions depending on molecular symmetry. With this limitation in mind, our CCSD(T) calculations on 25 heavy atoms are now limited to the aDZ basis set. However, a simple computation of CCSD(T)/aDZ would be fairly inaccurate compared to CCSD(T)/CBS. To this end, a number of approximations and schemes have been created to obtain this limit with small basis sets. These are outlined below.

3.1 Pragmatic computations of the CCSD(T)/CBS limit

3.1.1 Explicitly correlated CCSD(T)-F12 methods

Explicitly correlated CCSD(T) methods aim to improve the slow convergence of conventional CCSD(T) methods by targeting the source of the slow basis set convergence, the electron-electron cusp.[98–100] Conventional one-electron basis sets reproduce this cusp slowly resulting in their comparably slow convergence. Explicitly including terms between pairs of electrons greatly enhances the convergence rate; however, inclusion of these terms exactly would dramatically increase the cost of the overall computation. A series of *Ansätze* (or approximations), combined with density-fitting, has enabled the cost of these explicitly correlated approaches to be reduced to roughly the cost of conventional CCSD(T) itself. While there are many *Ansätze* we will focus on the CCSD(T)-F12a and CCSD(T)-F12b approaches.[101,102]

Inclusion of explicitly correlated terms has been derived for the (T) term; however, it is much more computationally demanding than conventional (T) even with the inclusion of density-fitting.[103] Instead, CCSD(T)-F12 denotes, somewhat confusingly, that the CCSD equations have included explicitly correlated terms and the (T) term is then computed without an explicit inclusion of explicitly correlated terms. The lack of the explicitly correlated (T) term can be partially solved by scaling this term by the ratio between the MP2-F12 (explicitly correlated MP2) and MP2 correlation energies like

$$\Delta E^{(\mathrm{T}^{**})} = \Delta E^{(\mathrm{T})} \cdot \frac{E_{\mathrm{corr}}^{\mathrm{MP2-F12}}}{E_{\mathrm{corr}}^{\mathrm{MP2}}}, \tag{3.1}$$

where $\Delta E^{(\mathrm{T})} = E^{\mathrm{CCSD(T)-F12}} - E^{\mathrm{CCSD-F12}}$ and $E_{\mathrm{corr}}^{\mathrm{MP2-F12}}$ is the MP2-F12 correlation energy. If the scaling factor is determined separately for each part of CP computation, the resulting interaction energy is not guaranteed to be size consistent, as such the scaling factor for the dimer is used for all parts of the CP computation.[104,105]

Based on previous experience with the CCSD(T)-F12 method, the CCSD(T)-F12a and CCSD(T**)-F12b combinations of scaling and *Ansätze* provide the best accuracy compared to the CCSD(T)/CBS limit.[97,106,107]

3.1.2 Composite based CCSD(T)/CBS approximations

The idea of delta corrections similar to $\delta_{\mathrm{T+(Q)}}$ of the previous section can be applied once more to CCSD(T)

$$\begin{aligned} E_{\mathrm{CBS}}^{\mathrm{CCSD(T)}} &\approx E_{\mathrm{CBS}}^{\mathrm{MP2}} + \Delta E_{\mathrm{a}X\mathrm{Z}}^{\mathrm{CCSD(T)}}, & (3.2) \\ \Delta E_{\mathrm{a}X\mathrm{Z}}^{\mathrm{CCSD(T)}} &= E_{\mathrm{a}X\mathrm{Z}}^{\mathrm{CCSD(T)}} - E_{\mathrm{a}X\mathrm{Z}}^{\mathrm{MP2}} & (3.3) \end{aligned}$$

It should be noted that for a single basis set this is exact, i.e., CCSD(T)/aDZ = MP2/aDZ + ΔCCSD(T)/aDZ. The underlying assumption behind this approximation is that the MP2 energy comprises a very large portion of the overall CCSD(T)/CBS correlation energy (typically 50-70%) for an individual monomer and the ΔCCSD(T) term converges much faster than CCSD(T) itself.

Inspection of the CCSD correlation energy equations shows that the second term is identical to MP2 correlation energy

$$E_{\text{corr}}^{\text{CCSD}} = F_i^a T_i^a + \tfrac{1}{4} I_{ij}^{ab} T_{ij}^{ab} + \tfrac{1}{2} I_{ij}^{ab} T_i^a T_j^b \tag{3.4}$$

$$E_{\text{corr}}^{\text{MP2}} = \tfrac{1}{4} I_{ij}^{ab} \tilde{T}_{ij}^{ab}, \quad \tilde{T}_{ij}^{ab} = I_{ij}^{ab} / (\epsilon_i + \epsilon_j - \epsilon_a - \epsilon_b) \tag{3.5}$$

where I denotes the spin-orbital MO two-electron tensor, F the Fock matrix, ϵ the orbital energies, and T either the T_1 or T_2 amplitudes. In MP2 the $\tilde{T}_2$ amplitude is fixed at the approximation shown, while in CCSD the T_2 amplitude is iterated to convergence. However, in CCSD the first guess to the T_2 amplitude is typically taken as the approximate $\tilde{T}_2$ amplitude shown in the MP2 equation.

MP2 can routinely be computed in a much larger basis than CCSD(T) as MP2 scales like N^5 compared to the N^7 scaling of CCSD(T). This method can also be used in conjunction with explicitly correlated CCSD(T) methods, as we will see in the next section this combination works particularly well.

3.1.3 The local-aug-cc-pVXZ basis

For the largest CCSD(T) computations considered here, either CO_2 or methane bound to curved coronene, the aDZ basis can be cost limiting and suffer convergence problems due to linear dependencies. Fortunately, these systems have a very specific motif where the small molecule is almost always over the center of the curved coronene meaning that there are many atoms relatively far away from the small molecule which will contribute less to the overall interaction energy. To this end, the full set of diffuse functions is pruned so that the small molecule always uses the full augmented basis while only carbon atoms close to the small molecule on the curved coronene use diffuse basis functions and all other carbons and hydrogens utilize the non-augmented counterpart. For the particular case of the local-aXZ (laXZ) basis sets, the closest six carbon atoms have diffuse functions (symmetric carbons are also augmented occasionally resulting in more augmented carbon atoms). This pruning results in a truncation of the basis set size by approximately 30%, removes the worst linear dependencies of the basis set, and the overall computational cost is reduced by a factor of 5-10 depending on molecular symmetry.

It should be noted that in Appendix B the diffuse functions on the PAH were present on any carbon atom within 2.1 Å from the projection of the methane carbon atom on the PAH plane. This definition was subsequently refined in later publications and the closest six atoms should always be utilized as the definition of laXZ.

3.2 Example: Methane–PAH

The global minimum of the methane–benzene complex[35, 108–110] was explored in great detail by computing a series of MP2, MP2-F12, CCSD(T), and CCSD(T)-F12 interaction energies in the largest bases currently possible, these results are shown in Table 3.1. While this table is very information dense, it gives an overview of the general behavior of MP2, CCSD(T), composite, and explicitly correlated methods. Beginning with MP2 we can give a MP2/CBS value of 1.794±0.001 kcal/mol by observation of the large MP2/(aQZ, a5Z) and MP2-F12/(aQZ, a5Z) extrapolations. Examining the conventional and explicitly correlated MP2 methods in the aDZ basis set, we can see that the basis set incompleteness error for MP2/aDZ is 0.316 kcal/mol while for MP2-F12/aDZ the error is just 0.049 kcal/mol, thus demonstrating the accelerated convergence for explicitly correlated methods. However, for (aTZ, aQZ) and (aQZ,a5Z) extrapolations the MP2 energy is virtually converged for both conventional and explicitly correlated computations. As the MP2-F12 computations can take considerably longer for large basis sets, conventional MP2 calculations followed by CBS extrapolations are utilized for all subsequent MP2 values.

Table 3.1: Different estimates of the benzene-methane interaction energy at the global-minimum 1C configuration. Columns denote the aXZ basis that the computation utilized. The rows marked "ext." display the CBS-extrapolated results where the values in the "X" column were obtained using the $(X-1, X)$ extrapolation. Values are in kcal/mol. Adapted from Appendix B.

Method	D	T	Q	5
MP2	-1.478	-1.691	-1.754	-1.774
ext.		-1.777	-1.795	-1.793
MP2-F12	-1.745	-1.785	-1.792	-1.794
ext.		-1.802	-1.795	-1.795
CCSD(T)	-1.156	-1.357	-1.407	
CCSD(T)/$(X-1, X)$		-1.438	-1.440	
MP2/(Q,5)+ΔCCSD(T)/aXZ	-1.468	-1.455	-1.445	
MP2/(Q,5)+ΔCCSD(T)/$(X-1, X)$		-1.449	-1.437	
CCSD(T)-F12a	-1.393	-1.431	-1.434	
CCSD(T)-F12a/$(X-1, X)$		-1.449	-1.435	
MP2-F12/(aQZ,a5Z)+ΔCCSD(T)-F12a/aXZ	-1.436	-1.436	-1.434	
MP2-F12/(aQZ,a5Z)+ΔCCSD(T)-F12a/$(X-1, X)$		-1.436	-1.433	
CCSD(T**)-F12b	-1.351	-1.415	-1.426	
CCSD(T**)-F12b/$(X-1, X)$		-1.448	-1.434	
MP2-F12/(aQZ,a5Z)+ΔCCSD(T**)-F12b/aXZ	-1.450	-1.439	-1.435	
MP2-F12/(aQZ,a5Z)+ΔCCSD(T**)-F12b/$(X-1, X)$		-1.435	-1.432	

We can place the CCSD(T)/CBS interaction energy at 1.433±0.002 kcal/mol by examining our largest CCSD(T) extrapolations and composite methods. Taking the conventional CCSD(T) results, we can see that a plain CCSD(T)/aDZ computation of the interaction energy is off by 19% compared to CCSD(T)/CBS. However, taking MP2/(aQZ, a5Z) + ΔCCSD(T)/aDZ, this difference is just 2%. With explicitly correlated CCSD(T)-F12a/aDZ and CCSD(T**)-F12b/aDZ the energy differs by just 3% and 6%, respectively. Again, this demonstrates the enhanced convergence behavior for explicitly correlated approaches, but also demonstrates that these methods by themselves are not more accurate than composite based approaches. Combining explicitly correlated methods with the composite approach yields errors of 0.2% and 1.2% for MP2-F12/(aQZ, a5Z) + ΔCCSD(T)-F12a/aDZ and MP2-F12/(aQZ, a5Z) + ΔCCSD(T**)-F12b/aDZ, respectively. Thus, the best estimate combines the composite and explicitly correlated approaches.

Figure 3.1: Differences between the benchmark MP2/(aQZ,a5Z)+ΔCCSD(T**)-F12b/(aDZ,aTZ) interaction energy and other CCSD(T)/CBS estimates for the 3C methane–naphthalene complex. Adapted from Appendix B.

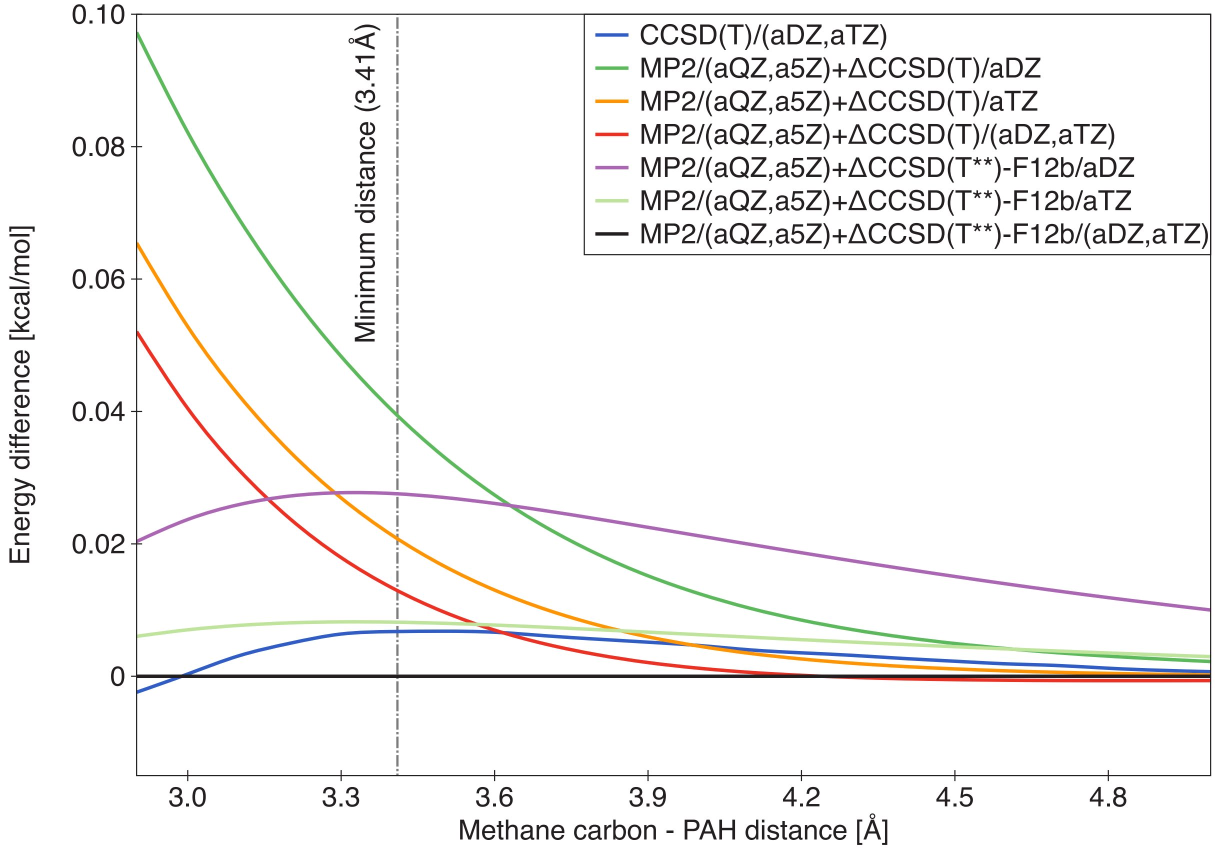

To expand this analysis to both shorter and longer ranges than the minima, the 3C methane–naphthalene complex curve was computed utilizing the largest basis possible. The energy differences compared to MP2/(aQZ,a5Z)+ΔCCSD(T**)-F12b/(aDZ,aTZ) are shown in Figure 3.1. As can be seen, the trends in CCSD(T)/CBS estimates at the minimum are identical to those of the 1C methane–benzene complex. However, at distances longer than the minima the MP2/(aQZ,a5Z)+ΔCCSD(T**)-F12b/aDZ results are worse than the conventional MP2/(aQZ,a5Z)+ΔCCSD(T)/aDZ. This error likely occurs from the density fitting approximations that the CCSD(T)-F12 methods utilize. Conversely, at short-range the MP2/(aQZ,a5Z)+ΔCCSD(T**)-F12b/aDZ results are significantly better than their conventional counterpart. As the two monomers are pressed closer together, the accurate capture of the electron-electron cusp is of utmost importance as demonstrated by the explicitly correlated ΔCCSD(T) approach.

Overall these errors are very small, the 3C methane–naphthalene interaction energy at the minimum is -2.119 kcal/mol leading to an error of just 2% for the most approximate method, MP2/(aQZ,a5Z)+ΔCCSD(T)/aDZ. The slight decrease in absolute accuracy at long-range of the MP2/(aQZ,a5Z)+ΔCCSD(T**)-F12b/aDZ method is concerning as the energies in the region are smaller, thus the relative error is much larger. In comparison to short-range where the energies are overall much larger the relative error is much smaller making the MP2/(aQZ,a5Z)+ΔCCSD(T)/aDZ method the best overall choice for this dataset.

To explore the effect of choosing the laDZ basis over aDZ, a series of computations in partially augmented basis sets were run. Basis sets known as "calendar" denote basis sets created by Truhlar and coworkers[111] which uniformly remove diffuse functions from all atoms. Here we will use the calendar basis set jun-DZ where "d" diffuse functions have been removed from all atoms in addition to all diffuse functions on hydrogen atoms. We will also utilize the heavy-aDZ≡jul-DZ sets where all of the diffuse functions on hydrogens have been removed and the heavy'-aDZ basis set where only the diffuse functions on PAH hydrogens have been removed. It should be noted that for the aDZ, heavy'-aDZ, and local-aDZ basis sets the methane molecule always retains all diffuse functions.

The MP2 and ΔCCSD(T) results have been compiled in Table 3.2. First examining the heavy'-aDZ compared to the heavy-aDZ basis, it is apparent that diffuse functions on the methane molecule help considerably for all configurations except for 2C methane–pyrene compared to the full aDZ result. Comparing jun-DZ and local-aDZ it is clear that the local

Table 3.2: The MP2 and ΔCCSD(T) contributions to methane–pyrene and methane–coronene interaction energies (in kcal/mol) computed using different partially augmented basis sets. A blank space signifies that the CCSD expansion failed to converge due to linear dependencies in the basis set. The size of the laDZ basis set is slightly different for different coordinations. Thus, a range of values is listed. Adapted from Appendix B.

	methane–pyrene				methane–coronene			
Basis	Size	1C	2C	3C	Size	1C	2C	3C
			MP2					
DZ	308	-1.157	-1.484	-1.630	430	-1.493	-1.746	-1.897
local-aDZ	369-387	-2.166	-2.741	-3.046	491-509	-2.603	-3.069	-3.362
jun-DZ	376	-1.613	-2.073	-2.331	530	-2.057	-2.428	-2.693
heavy-aDZ	461	-2.128	-2.836	-3.028	655	-2.595	-3.051	-3.381
heavy'-aDZ	477	-2.221	-2.688	-3.218	671	-2.687	-3.186	-3.559
aDZ	517	-2.227	-2.853	-3.229	719	-2.691	-3.192	-3.565
			ΔCCSD(T)					
DZ	308	0.581	0.718	0.815	430	0.767	0.868	0.953
local-aDZ	369-387	0.656	0.835	0.957	491-509	0.881	1.005	1.115
jun-DZ	376	0.614	0.771	0.886	530	0.818	0.948	1.037
heavy-aDZ	461	0.675	0.851	0.974	655			
heavy'-aDZ	477	0.660	0.838	0.963	671			
aDZ	517	0.658	0.836	0.962	719			

augmentation scheme is superior in terms of the number of basis functions cut and the relative accuracy of each contribution. While the reduction in basis from aDZ to laDZ for the MP2 correlation energy results in a penalty of approximately 4% compared to the full aDZ result, the ΔCCSD(T) correction differs by less than one percent. We conclude that the reduction of the ΔCCSD(T) correction to the laDZ basis in comparison to the aDZ basis does not seriously impact the overall interaction energy while providing numerous benefits.

3.3 Example: CO_2–PAH

For the CO_2–PAH systems an expansive series of computations was carried out for the minimum geometries similar to the previous section. Where possible, the ΔCCSD(T) correction was computed in basis sets as large as aTZ. When aTZ computations are possible, the uncertainty of this benchmark is estimated as

$$\begin{aligned}\sigma &= |\text{MP2(aQZ, a5Z)} - \text{MP2/(aTZ, aQZ)}| \\ &\quad +|\Delta\text{CCSD(T)-F12avg/a}X\text{Z} - \Delta\text{CCSD(T)-F12avg/(a}(X{-}1)\text{Z, a}X\text{Z)}|. \qquad (3.6)\end{aligned}$$

where ΔCCSD(T)-F12avg will represent the average between ΔCCSD(T)-F12a and ΔCCSD(T**)-F12b terms. It was previously noted that full aDZ computations are not possible for coronene due to linear dependencies; however, curving the coronene molecule removes these linear dependencies allowing full aDZ computations to be run.

Figure 3.2: Differences between various CCSD(T)/CBS interaction energy estimates for the CO_2–PAH minima, with the ΔCCSD(T) term computed in the aDZ (solid lines) and laDZ (dashed lines) bases. If the benchmark cannot be calculated in at least the aTZ basis, the MP2/(aQZ,a5Z)+ΔCCSD(T)-F12avg/aDZ method was taken as the zero line and no uncertainty was assigned. Uncertainties (the range in blue) were computed as in Eq. 3.6 where $X = Q$ for the C_{2v} CO_2–benzene complexes and $X = T$ for all other complexes. The numbers along the horizontal axis give benchmark interaction energies in kcal/mol. Adapted from Appendix D.

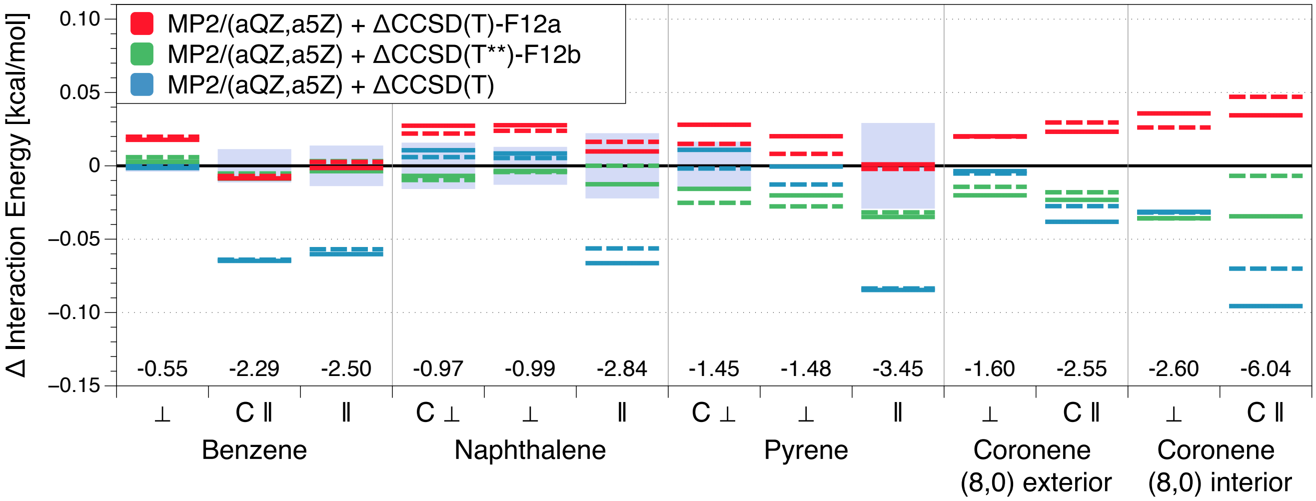

The resulting benchmarks are shown in Figure 3.2. Comparing the ΔCCSD(T) correction computed in the aDZ and laDZ basis sets again demonstrates that the laDZ basis set is a very worthwhile approximation over aDZ. The worst case scenario is the interior C

$\|$ CO$_2$–(8,0) curved coronene complex which deviates from the full aDZ basis by just 0.04 kcal/mol. This increase in absolute difference compared to other results that differ by just 0.01 kcal/mol on average is offset by the deepening of the minima. In absolute terms it makes sense that this is the worst performer as more carbon atoms are close to the CO$_2$ molecule. In other words, the worst case scenario for the laDZ basis differs by just 0.6% compared to the full aDZ result. Where error bars are available, the MP2/(aQZ,a5Z)+ΔCCSD(T)-F12/aDZ results typically fall within them; however, the MP2/(aQZ,a5Z)+ΔCCSD(T)/aDZ values are systematically too deep for the $\|$ configurations. It is not possible to determine if MP2/(aQZ,a5Z)+ΔCCSD(T)-F12a/aDZ or MP2/(aQZ,a5Z)+ΔCCSD(T**)-F12b/aDZ is more accurate. Therefore, the benchmark value for the test set will simply be the average between the two, denoted MP2/(aQZ,a5Z)+ΔCCSD(T)-F12avg/aDZ.

Figure 3.3: Comparison of the conventional and explicitly correlated composite MP2/CBS+ΔCCSD(T) schemes for the $\|$ CO$_2$–naphthalene (benchmark: MP2/(aQZ,a5Z) + ΔCCSD(T)-F12avg/aTZ) and $\|$ CO$_2$–pyrene (benchmark: MP2/(aQZ,a5Z) + ΔCCSD(T)-F12avg/laTZ) complexes. Solid lines represent the ΔCCSD(T) correction in the aDZ basis set while the dashed lines represent ΔCCSD(T) in the laDZ basis set. The blue region is the uncertainty range of the benchmark. Adapted from Appendix D.

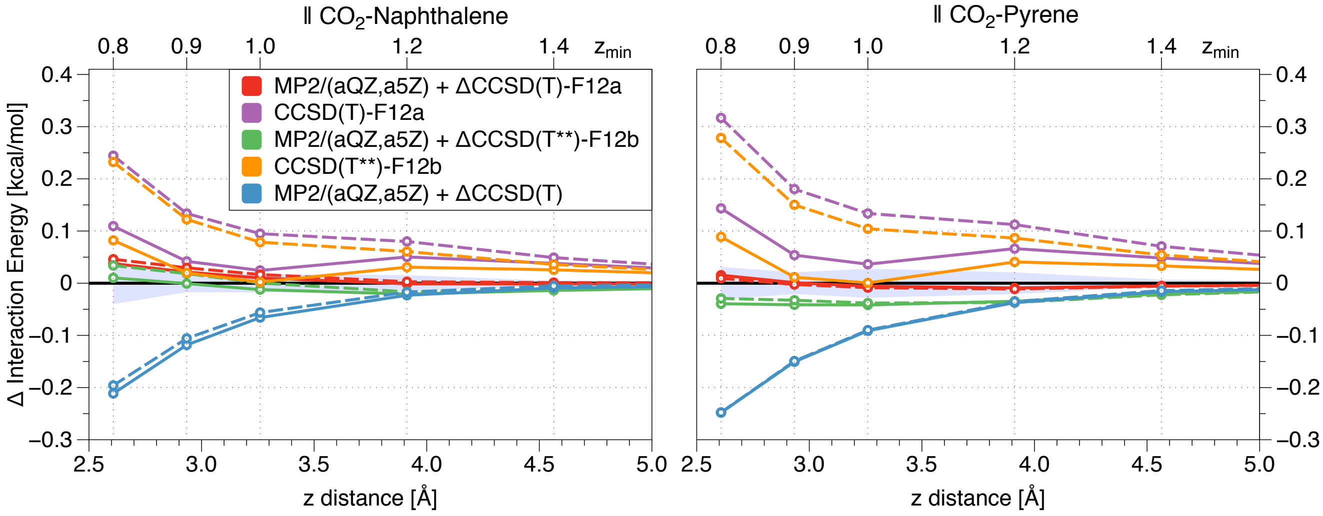

The accuracy as a function of intermonomer distance is again explored in Figure 3.3. First examining the CCSD(T)-F12 computations in the aDZ basis, we can observe that the accuracy is overall quite good; however, the reduction to the laDZ basis set significantly impacts the overall accuracy. Comparison of the composite approach paired with either the aDZ or laDZ basis shows little deviation demonstrating that the laDZ basis, when paired with the composite approach, is sufficient at all distances. Again, at short-range the conventional ΔCCSD(T) approach begins to deviate strongly while the accuracy of the explicitly correlated ΔCCSD(T) remains quite good. Unlike in the methane–PAH study, the long-range accuracy of the ΔCCSD(T) method does not deviate strongly.

3.4 Conclusions

In this chapter we have demonstrated different methodologies to obtain accurate CCSD(T)/CBS results. When we limit ourselves to CCSD(T)/aDZ due to computational limitations, it is crucial to use the explicitly correlated methods, composite approach, or both simultaneously. We have demonstrated the breakdown of conventional small-basis CCSD(T) at short-range and a single system where CCSD(T)-F12 results are worse than CCSD(T) at long-range. However, it should be noted that in both cases the errors are relatively minimal, roughly equal to the effects of the post-CCSD(T) corrections. As a general guideline the MP2/CBS+ΔCCSD(T)-F12avg/aDZ result represents the best method. When the basis set and post-CCSD(T) errors are combined, we arrive at a conservative accuracy of approximately 5%.

Chapter 4

Assessment of DFT approaches

While the composite CCSD(T) approach is remarkably accurate, routine computations are limited to systems with approximately 25 heavy atoms. To continue to larger systems, lower rank approximations are required such as DFT. However, the number of DFT approaches is virtually limitless, especially when different combinations of basis set, dispersion expression, and base functional are considered. For example let us consider a situation where we utilize three different basis sets (aDZ, aTZ, aQZ), with and without the CP correction, combined with the five Grimme's -D dispersion corrections (-D2,[64] -D3,[65] -D3-E$^{(3)}$, -D3(BJ),[112] -D3(BJ)-E$^{(3)}$), and eight functionals B2PLYP, B3LYP, BLYP, LC-ωPBE,[113] PBE0,[114,115] PBE,[116] B97,[64] and BP86.[59,117] This results in 240 distinct possible combinations of DFT methods. All of these combinations contain some of the proper physics involved and thus will give at least reasonable results; at the same time blindly benchmarking all 240 combinations will eventually yield a functional form that produces near CCSD(T)/CBS quality results.

Unlike wavefunction based methods, converging to the basis-limit is not guaranteed to improve a given functional. In order to limit the possible DFT combinations the analysis presented here will rely on CP corrected computations in the largest basis available to maintain results near the basis-limit. Consistently computing DFT methods at the basis-limit removes the largest variability with respect to the interaction energy and reduces the number of possible DFT-D combinations considered from 240 to 40.

4.1 Methane–PAH and methane–curved coronene systems

The methane–PAH and methane–curved coronene datasets have been reanalyzed from Appendix B and C to provide a consistent description across all datasets. It should be noted again that the methane–curved coronene dataset has been extended to $z = 0.8$, thus the statistics shown in the figures below will not match those of Appendix C. The best DFT-D combinations are shown in Figure 4.1.

Figure 4.1: Performance of each density functional in the QZVP basis combined with the best atom-pairwise dispersion term. The large gray bars represent the overall wMURE, the smaller red and blue bars represent short-range and long-range wMURE, respectively. LC and DH correspond to long-range corrected (range separated) and double-hybrid functionals, respectively. The target accuracy level of 5% has been shaded in yellow.

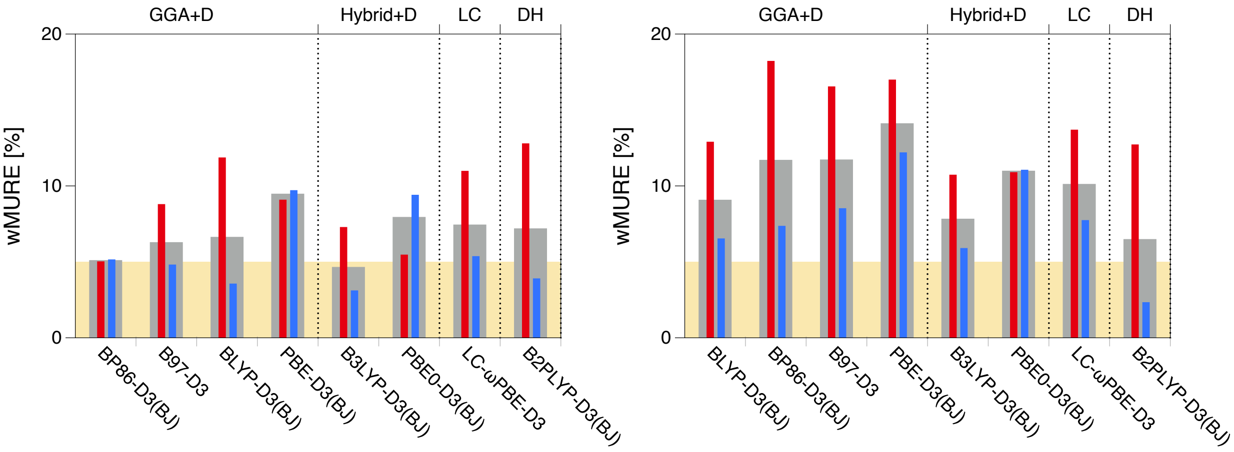

(a) Methane–PAH dataset.

(b) Methane–curved coronene dataset.

First examining the methane–PAH dataset, we can see that the DFT-D methods work well overall with wMURE values between 5 and 9%. Considering the accuracy of the benchmark is approximately 5%, this is quite impressive. For the methane–curved coronene dataset, we can see that the errors roughly double for the majority of the functionals considered here, in particular the error at short-range increases significantly. From this figure we observe that benchmarking statistics for small PAH's does not always match the curved coronene systems. For example, take the BP86-D3(BJ) method which is the best GGA-D for the methane–PAH complexes with errors of 5% for both short and long-range. However, for the methane–curved coronene systems we see these errors grow rapidly to 18 and 7%, respectively. This inconsistency is common for DFT-D methods and exemplifies the reason why careful benchmarking is required before blindly using DFT-D as a substitute for CCSD(T).

These large accuracy swings are somewhat mitigated by using hybrid and double hybrid functionals. For example, take the B3LYP-D3(BJ) method whose performance only decreases by 3% between the methane-PAH and methane–curved coronene datasets. The double hybrid B2PLYP-D3(BJ) error actually improves by 1% on the average between the methane–PAH and methane–curved coronene datasets.

4.2 Carbon dioxide–PAH and carbon dioxide–curved coronene systems

The following was adapted from Appendix D.

Following a similar path to the last section, the wMURE of various DFT-D variants is shown in Figure 4.2 for the CO_2–PAH dataset. As can be seen, the performance at long-range remains quite good with errors between 4 and 10%. However, the short-range error degrades significantly with errors of up to 46%, this is quite surprising as the worst error for the methane–PAH dataset at short-range was 13%. It should be noted again that the nature of the wMURE statistic prevents singularities from causing such errors and similar increases of error at short-range can all be seen in MUE as well. Also, this short-range region is either still in the van der Waals well or no more than 5 kcal/mol on the repulsive wall, thus this short-range region is still quite important to an accurate description of the overall energy surface. The double hybrid and non-local functionals again contain the short-range error somewhat with performance of 11-12%.

Due to the poor performance of DFT-D methods on the CO_2–PAH dataset, the list of possible dispersion including variants was greatly extended for the CO_2–curved coronene

Figure 4.2: Performance of each density functional in the QZVP basis combined with the best atom-pairwise dispersion term for the CO_2–PAH dataset. The large gray bars represent the overall wMURE, the smaller red and blue bars represent short-range and long-range wMURE, respectively. LC and DH correspond to long-range corrected (range separated) and double-hybrid functionals, respectively. The target accuracy level of 5% has been shaded in yellow.

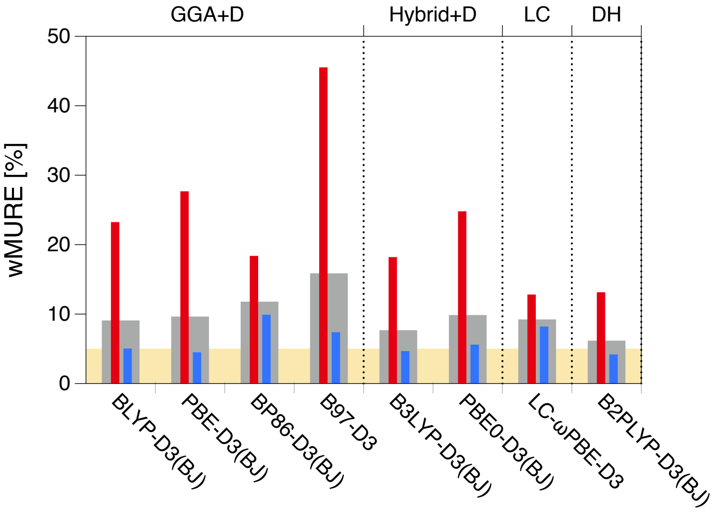

system. In addition to the DFT-D method, interaction optimized functionals (M05-2X, M06-2X, dlDF-D_{as},[118] and ωB97X-D[56]), the dDsC method, and the non-local VV10 method were also included. These methods were chosen as they are current popular choices for dispersion including functionals. The resulting wMURE for the CO_2–curved coronene dataset can be found in Figure 4.3.

As can be seen, the poor performance at short-range for DFT-D methods extends to the CO_2–curved coronene dataset similar to the CO_2–PAH dataset. The addition of the dDsC, interaction-optimized and NL functionals does not appear to significantly improve upon the short-range errors and can make the error much worse as seen by the BLYP-dDsC/TZVP and ωB97X-D/aTZ functionals. However, it should be mentioned that long-range performance is overall quite excellent with errors often around 10%. As before the LC,

Figure 4.3: Performance of each density functional in the largest basis set computed combined with the best atom-pairwise dispersion term (if applicable). The large gray bars represent the overall wMURE, the smaller red and blue bars represent short-range and long-range wMURE, respectively. LC, NL, and DH correspond to long-range corrected (range separated), non-local, and double-hybrid functionals, respectively. The target accuracy level of 5% has been shaded in yellow. Adapted from Appendix D.

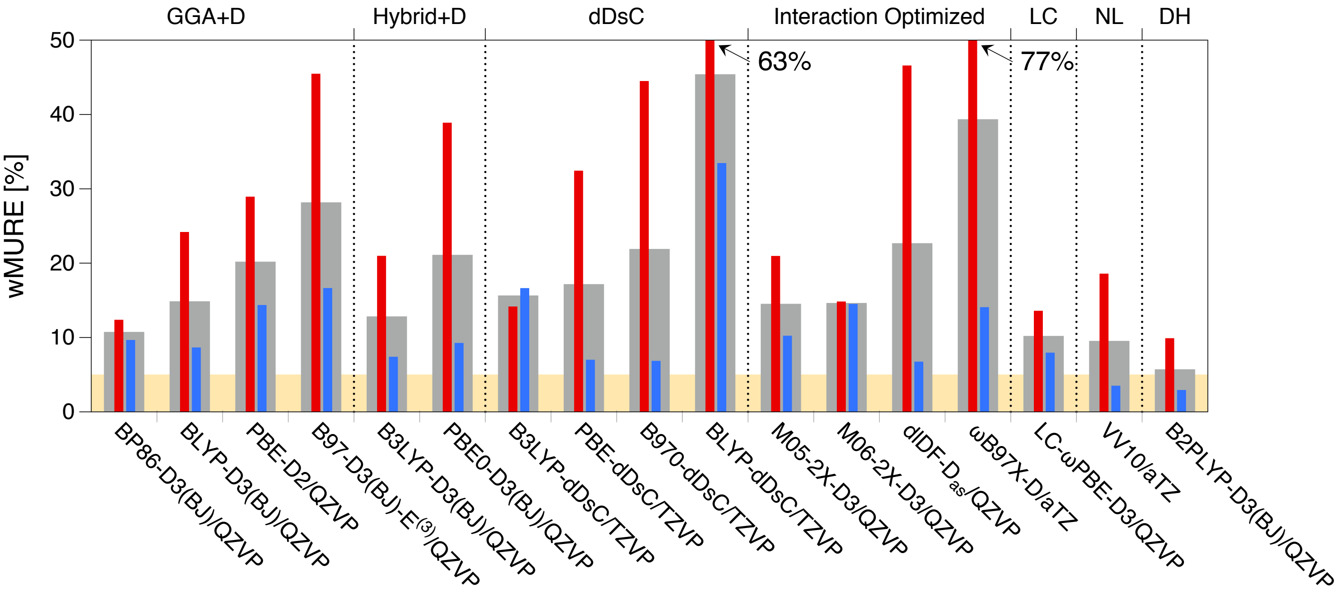

NL, and DH functionals do make reasonable improvements over normal GGA and hybrid-GGA functionals at short-range. The dDsC and interaction optimized functionals do not appear to be an improvement over normal GGA or hybrid-GGA functionals.

4.3 Conclusions

DFT is the primary methodology turned to when conventional wavefunction approaches prove too expensive. Therefore, each functional rung will be discussed in detail with respect to its cost.

- Double-Hybrid Functionals

  The sole double-hybrid functional tried, B2PLYP, should be combined with the -D3(BJ) dispersion term. This functional had a performance of approximately 10%

for all datasets utilized making it the best overall functional. However, if we return to the methane-methane interaction curve of Figure 1.3, we see that this performance is not always systematic. In addition, as with all methods that utilize some portion of MP2, this method scales like N^5. As such, this method will face steep competition against non-empirical MP2 based methods such as SCS(MI)-MP2 and MP2C.[52,119]

- Range-separated Functionals

  The LC-ωPBE-D3 functional also had consistent performance of around 10%. While this method formally scales like N^4, the computation of the range-separated exchange integrals means that this functional will be more costly to compute compared to conventional hybrid-GGA's such as B3LYP.

- Hybrid-GGA and GGA Functionals

  These method are of utmost interest for applications to large molecules as they scale like N^3 (GGA) and N^4 (hybrid-GGA). While the performance of GGA and hybrid-GGA functionals is overall quite excellent for the methane–PAH and methane–curved coronene datasets, the performance on the CO_2–PAH and CO_2–curved coronene datasets varies greatly. Therefore, these methods should be used with caution.

On the whole, the DFT-D methods perform quite reasonably at the van der Waals minimum and longer distances. However, the accuracy at short-range is consistently worse and can vary dramatically depending on the type of complex under consideration. Higher rung functionals do offset this error and appear to be more accurate overall; however, their cost begins to reach approximate wavefunction methods that may be more accurate for a wider range of interaction archetypes.

Chapter 5

Improved damping parameters for the DFT-D3 approach

As seen in the previous chapter, the issue with DFT-D3 methods is not in the asymptotic region, but at short to medium ranges. This chapter will focus on the damping forms utilized in the -D3 approach in addition to possible solutions.

5.1 Medium-range correlation in Density Functional Theory

A variety of DFT functionals have been plotted for the methane dimer without any dispersion correction, shown in Figure 5.1. As can be seen, several of the functionals do have a slight van der Waals well for this complex; this is often referred to as medium-range correlation.[120] For the M05-2X and M06-2X functionals we can see that while they do not explicitly include long-range correlation, their interaction energies near the minimum position are quite good. This is achieved by fitting various empirical coefficients within the DFT functional and causing the careful balance between exchange and correlation in the DFT functionals to lean toward the attractive correlation contribution. As can be seen, this either leaves medium-range correlation deficient (M05-2X) or provides strangely shaped interaction curves (M06-2X).

The fundamental problem with DFT theory for NCI is often said to be the lack of dispersion. To put this in context, SAPT interaction energies without the dispersion terms have been also plotted in Figure 5.1. While it can be argued that SAPT is not the only decomposition of interaction energies available, this gives us a reasonable expectation of what a ”dispersionless” DFT functional should look like. The B3LYP, BLYP, and BP86 functionals are missing correlation components above and beyond what SAPT dispersion provides while all other functionals provide some ”dispersion”. The word ”dispersion” is in quotes as the

Figure 5.1: Various DFT functionals computed for the methane dimer in the QZVP basis set along with benchmark (CCSD(T)/(aTZ,aQZ)) energies and SAPT - E_{Disp} (SAPT2+3/aTZ without the E^{20}_{Disp}, $E^{(21)}_{\mathrm{Disp}}$, $E^{(22)}_{\mathrm{Disp}}$, $E^{(20)}_{\mathrm{Exch-Disp}}$, $E^{(30)}_{\mathrm{Disp}}$, $E^{(30)}_{\mathrm{Exch-Disp}}$, $E^{(30)}_{\mathrm{Ind-Disp}}$, or $E^{(30)}_{\mathrm{Exch-Ind-Disp}}$ terms).

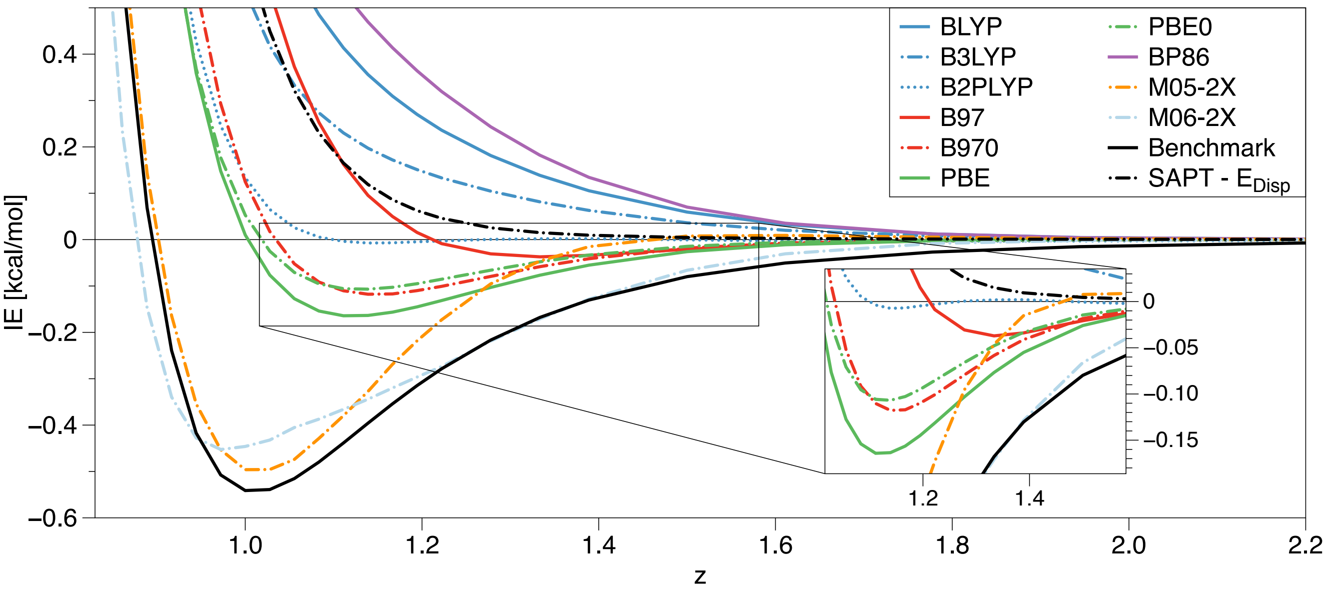

nature of correlation in DFT theory is not rigorous and all missing attractive components in the NCI context have been widely deemed "dispersion". Notably, the definition of DFT "dispersion" is different for every functional leading to the requirement that the damping parameters in the DFT-D3 methods also need to be different for every functional.

5.2 Refitting damping parameters to the CO_2–curved coronene dataset

The following was adapted from Appendix D.

The original -D3 damping parameters were fitted to just 130 datapoints.[65] Importantly, this dataset contained no points on potential energy curves shorter than the minima. As the amount of damping at short-range is particularly sensitive to the damping parameters, the poor short-range results demonstrated in the previous chapter are quite understandable.

To attempt to correct this situation, the damping parameters are refitted explicitly to the CO_2–curved coronene test set.

Three damping forms were considered, including the so-called "zero damping" or Chai-Head-Gordon (CHG) damping form[56,65]

$$E_{\mathrm{disp}}^{\mathrm{CHG}} = -\frac{1}{2}\sum_{A\neq B}\sum_{n=6,8} s_n \frac{C_n^{AB}}{r_{AB}^n}\frac{1}{1+6(r_{AB}/(s_{r,n}R_0^{AB}))^{-\alpha_n}}, \tag{5.1}$$

which has two parameters s_8 and $s_{r,6}$ (the $s_{r,8}$ values are held constant at 1). The α_n parameters are set to 14 and 16 for α_6 and α_8, respectively, and not adjusted.

The Becke-Johnson (BJ) damping[121,122] with three parameters s_8, α_1, and α_2 is

$$E_{\mathrm{disp}}^{\mathrm{BJ}} = -\frac{1}{2}\sum_{A\neq B}\sum_{n=6,8} s_n \frac{C_n^{AB}}{r_{AB}^n + (\alpha_1 \cdot R_0^{AB} + \alpha_2)^n} \tag{5.2}$$

The Tang and Toennies (TT)[123] damping with two parameters s_8 and d_{TT} has the form

$$E_{\mathrm{disp}}^{\mathrm{TT}} = -\frac{1}{2}\sum_{A\neq B}\sum_{n=6,8} s_n \frac{C_n^{AB}}{r_{AB}^n} f_{TT,n-1}\left(\frac{r_{AB}\cdot d_{TT}}{R_0^{AB}}\right) \tag{5.3}$$

$$f_{TT,n}(x) = 1 - e^{-x}\sum_{m=0}^{n}\frac{x^m}{m!} \tag{5.4}$$

While the TT damping form is not historically used for DFT-D3 damping, it has been used to great success in many analytical energy surfaces.[10] In addition, the CHG damping is often criticized due to the fact that the damping expression goes to zero at short-range, which is quite unphysical compared to BJ damping which converges to a non-zero value. The TT damping is therefore not computed as $f_{TT,n}$ which would also go to zero at short-range, but instead as $f_{TT,n-1}$ so that it converges to a non-zero value at short-range. The R_0^{AB} value for the CHG and TT damping comes from the original -D3 work,[65] while for BJ damping the R_0^{AB} value is computed as $R_0^{AB} = \sqrt{\frac{C_8^{AB}}{C_6^{AB}}}$.

It should be briefly noted that the dominant long-range contribution comes from C_6 and thus if the s_6 parameter has any value except for unity, the long-range behavior would be quite skewed. Thus, the s_6 parameters is not fit, but held at a unity for all functionals except for B2PLYP. For B2PLYP s_6 is kept at 0.64 to avoid double counting as this functional contains a fraction of long-range correlation.[65] The fitting of s_8 is generally less worrisome as the C_8 contribution happens to go to zero roughly in the region where medium-range correlation also fades. This appears to be a beneficial happenstance and no physical meaning is ascribed to this phenomenon.

The DFT-D3 damping parameters were then fitted to the 195 datapoints in the CO_2–curved coronene dataset, the results obtained with refitted damping parameters will be tagged "-refit". The performance of the refitted and original damping parameters is shown in Figure 5.2. As the statistics are shown on the fitting set itself, the accuracy must improve. What is quite surprising is the magnitude of the improvement for several functionals. In the case of PBE and PBE0 the functionals before refitting are among the worst performers due to their short-range errors of 39-60%; however, after refitting this is reduced to 5-7% for both CHG and BJ damping. The improvement is so great that PBE-D3(BJ)$_{\text{refit}}$ is now the best GGA functional for this dataset.

However, it should be noted that this level of improvement is not seen for every functional. In particular, the improved damping parameters for LC-ωPBE have a very small effect meaning the original damping parameters are nearly optimal for this dataset. The lack of improvement is quite interesting as, before refitting, LC-ωPBE was one of the best overall functionals, but after refitting it is among the worst. Nevertheless, refitting the damping parameters improves all short-range results except for the HFPBE-D3(BJ) method. Before refitting, the B97-D3 and PBE-D3 functionals were tied for worst short-range performance with a wMURE of 60%; however, after refitting, the worst performer for CHG damping was B97-D3$_{\text{refit}}$ at 22% and for BJ damping LC-ωPBE-D3(BJ)$_{\text{refit}}$ at 12%. Overall, the radical

Figure 5.2: The performance of various DFT functionals before and after refitting for the CO_2–curved coronene dataset. Adapted from Appendix D.

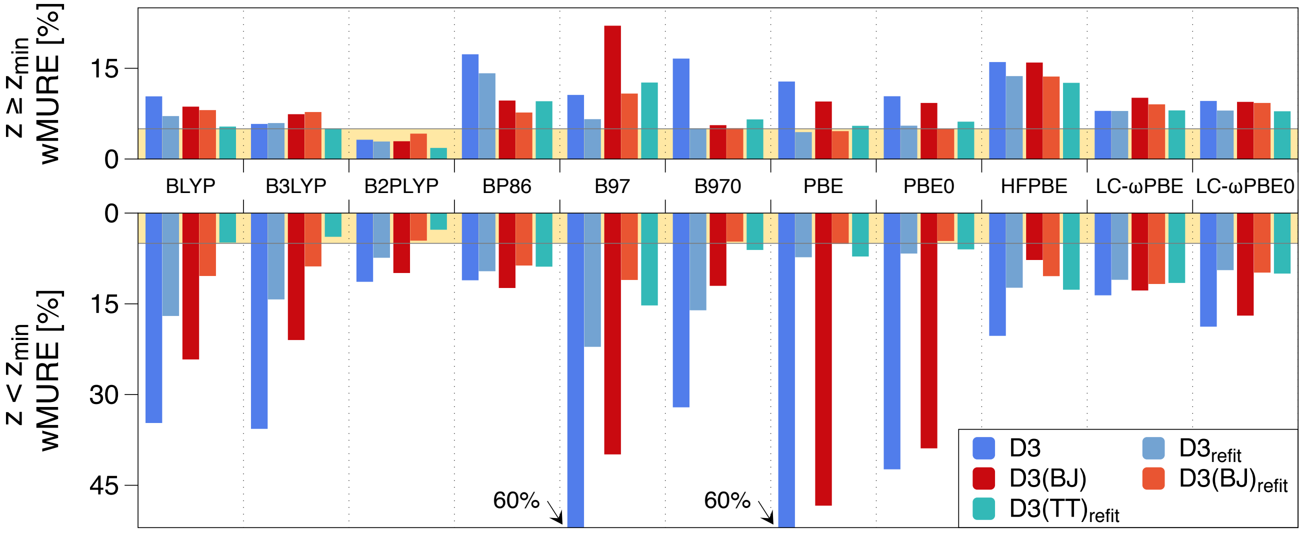

performance increase by fitting two (CHG damping) or three parameters (BJ damping) for 195 datapoints is clear.

The performance of PBE-D3$_{refit}$ was plotted for each point in Figure 5.3 to demonstrate the consistency of the refitting. As can be seen, the performance is fairly consistent across all datapoints with the worst error being 15% wMURE, only 3 times the average. This is in stark comparison to the PBE-D3 method which has outliers in excess of 100% wMURE.

To examine the transferability of these damping parameters, the parameters were tried on the S22x5[72] and S66x8[124] datasets, the performance is shown in Table 5.1. The S22x5 and S66x8 datasets are a diverse set of biologically relevant molecules that are widely used in NCI research to examine the accuracy of various approximate methods. For CHG damping, the refitting to the CO_2–curved coronene data neither universally makes the performance better or worse. On the other hand, refitting for the BJ damping typically makes the results much worse, with the only exception of the B2PLYP-D3(BJ) method in which the performance actually improves very slightly. For TT damping there are no original damping parameters to

Figure 5.3: The performance of PBE-D3 before and after refitting in the QZVP basis. The 195 points in the CO_2–curved coronene dataset have been sorted to mimic a potential energy curve. Adapted from Appendix D.

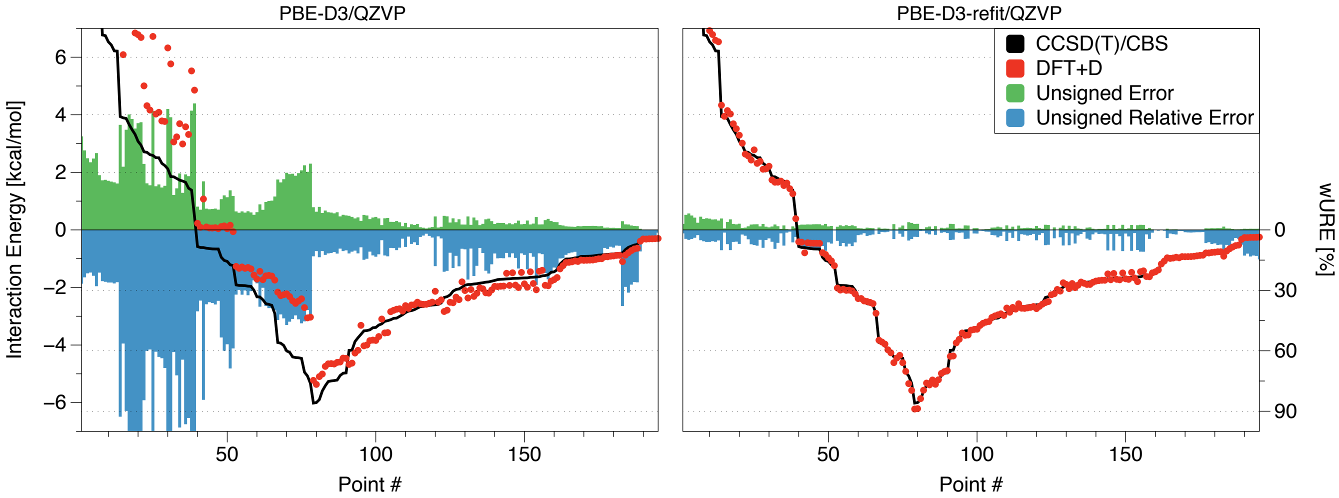

compare to; however, the results can be described as average. Interestingly, the exception for TT damping is again the B2PLYP functional whose performance is roughly on par with the CHG and BJ damping forms. A possible explanation for this is that the B2PLYP functional contains more physics than any other functional in Table 5.1 and hence may be more stable with respect to transferability.

5.3 Comprehensive refitting of the DFT-D3 parameters

This section was adapted from Appendix E.

The improved DFT-D3 damping parameters for the CO_2–curved coronene dataset are quite useful for this particular type of complexes and will certainly be utilized in the future. The unique benefit here is the relative stability in statistics for the S22x5 and S66x8 dataset for the CHG damping. This strongly suggests that the general damping coefficients may improved by fitting to a larger dataset than the original damping parameters were fitted to.

Table 5.1: Mean unsigned relative errors (in percent) for different density functionals augmented by the original and refitted atom-pairwise dispersion corrections, averaged over the combined S22x5 and S66x8 datasets. The QZVP basis set and CP correction were used for all DFT calculations. Adapted from Appendix D.

Functional	-D3	-D3$_{\text{refit}}$	-D3(BJ)	-D3(BJ)$_{\text{refit}}$	-D3(TT)$_{\text{refit}}$
BLYP	10.7	9.1	6.8	29.0	13.4
B3LYP	10.5	10.3	4.9	28.1	14.9
B2PLYP	7.9	5.9	6.8	6.7	7.0
BP86	13.6	12.0	12.4	68.3	13.3
B97D	9.1	11.2	13.4	40.4	18.7
B970	9.9	13.7	6.4	31.3	21.5
PBE	15.9	14.1	10.8	33.9	20.1
PBE0	13.4	13.3	9.6	42.3	17.4
HFPBE	18.0	17.2	15.1	28.6	21.6
LC-ωPBE	6.3	8.1	7.7	21.2	10.8
LC-ωPBE0	7.9	9.7	5.7	23.3	12.7

If this is the case, the DFT-D3 method can be improved to produce more accurate results greatly increasing its applicability and reliability.

To explore this possibility, a large variety of benchmark datasets for NCI was collected into a single large database. For this large database, NCI datapoints must be of the "silver standard" (or better) quality of Ref. 52 (≈5% accuracy) and databases that contain potential curves must contain one positive point on the repulsive wall at short-range and extend past the minima to long-range. Surprisingly, these criteria were somewhat difficult to obtain and many of the current benchmark sets in the literature required either extension to shorter ranges or an improvement of the benchmark values. It should be noted that for this section, the methane–PAH and methane–curved coronene datasets have been combined and labeled methane–PAH, similarly, the CO_2–PAH and CO_2–curved coronene sets were combined and labeled CO_2–PAH. The databases used are shown in Table 5.2.

For the CO_2–curved coronene refitting (Section 5.2), the training and validation sets were the same, this was acceptable because we were only concerned with the accuracy of that

Table 5.2: Datasets utilized in the training and validation sets. Adapted from Appendix E.

Database	**Points**	**Curves**	**Largest**[6]	**Reference**	**Description**
Training	**1526**	**114**			
$CO_2 \cdot$ PAH	249	45	27	97	CO_2 with PAHs the size of benzene through coronene and curved coronene
HBC6[2]	118	6	6	105, 125	dissociation curves of doubly hydrogen-bonded bimolecular complexes
NBC10ext[2]	195	10	12	71, 105	dissociation curves of dispersion-bound bimolecular complexes
S22×7[2,3]	154	22	19	127	dissociation curves for a balanced mix of hydrogen bonded and dispersion bonded complexes
SSI500	500	[1]	20	128	a subset of 500 molecules from SSI
X31×10[4]	310	31	18	129	dissociation curves of organic halides, halohydrides, and halogens
Validation	**6773**	**148**			
ACHC	54	6	19	130	rise, twist, slide, shift, roll, and tilt of adenine:cytosine nucleobase step
BBI	100	[1]	10	128	peptide backbone-backbone complexes
$C_2H_4 \cdot$ PAH	75	15	26	131	ethene with curved coronene
$CH_4 \cdot$ PAH[2]	405	45	25	48, 73	methane with PAHs the size of benzene through coronene and curved coronene
$CO_2 \cdot$ NPHAC	96	16	27	132	CO_2 with nitrogen-doped polyheterocyclic aromatic compounds (N-PHAC)
S66×10[2]	660	66	16	124	dissociation curves for a balanced mix of biomolecule NCI bonding motifs
SSI	[5]2873	[1]	21	128	peptide sidechain-sidechain complexes
Water2510	2510	[1]	2	133–135	water PES

[1] Database does not contain curves.

[2] Database was extended to shorter ranges.

[3] Database was recomputed at a higher level of theory.

[4] The X40×10 database with iodine containing complexes removed.

[5] SSI contains 3380 bimolecular complexes. The stated figure is less 500 from the SSI500 fitting subset and 7 for which GGA functionals do not reliably converge.

[6] Largest refers to the largest number of heavy atoms in the dataset.

particular system. However, for a general refit of damping parameters, statistics computed on the fitting database itself does not convey how transferable the refitted damping parameters are. Therefore, the master database was split into training and validation sets which contain 1,526 and 6,773 datapoints, respectively. In comparison, the original -D3 parameters were fit to 130 datapoints, of those 72 were intermolecular interactions and 66 of those were from the S22 and S22+ (S22x7, z=1.0, 1.2, 1.4) datasets. The remaining 58 training datapoints consisted of thermochemical data and are not considered here.

In order to ensure the diversity of intermolecular interactions, ternary diagrams, which show the ratio between the electrostatic, induction, and dispersion SAPT components, were computed and shown in Figure 5.4.[136] The term "minima cross sections" refers to databases where the interaction energy curves were expanded radially from minimum configurations, these comprise all datasets except for SSI, BBI, and Water2510. As can be seen, the "minima

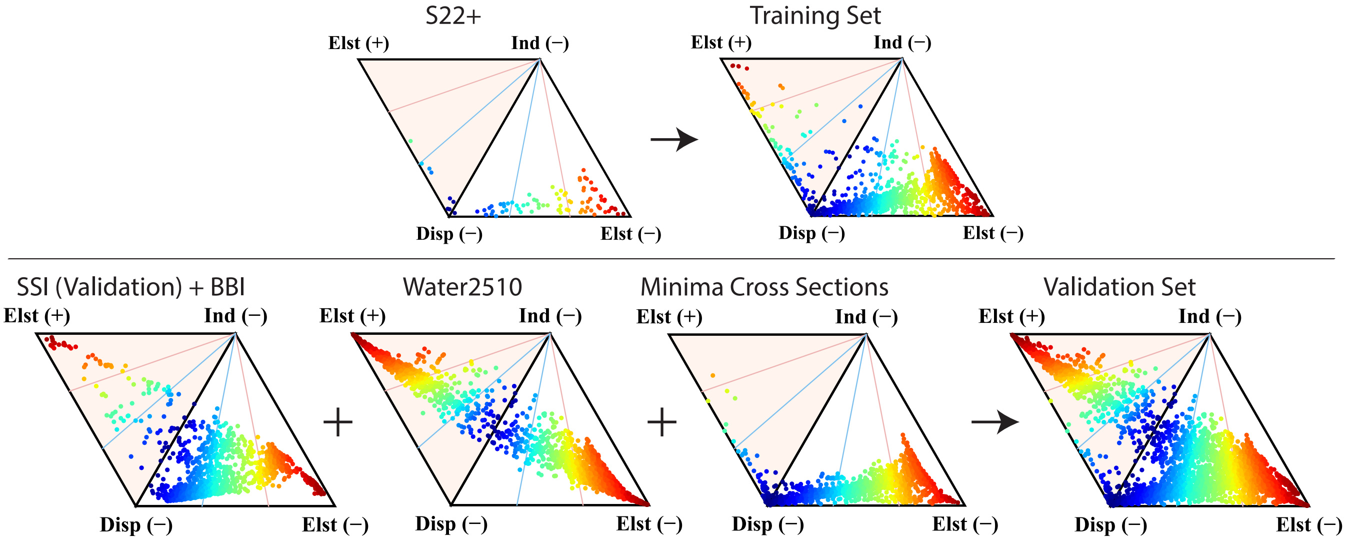

Figure 5.4: Top Panel: Ternary diagram comparison between the original -D3 fitting set and the current fitting set. Bottom Panel: Ternary diagram breakdown of the three major categories of points included in the validation set. Adapted from Appendix E.

cross sections" databases only cover a small portion of the ternary diagram. This stresses the importance of fully exploring the angular space, especially for biologically relevant interactions.

An examination of the current CHG and BJ damping forms show that CHG has two parameters while BJ has three. To give equal flexibility to both damping forms, the β parameter is added to the CHG expression

$$E_{\text{disp}}^{\text{CHG}} = -\frac{1}{2}\sum_{A\neq B}\sum_{n=6,8} s_n \frac{C_n^{AB}}{r_{AB}^n} \frac{1}{1+6(r_{AB}/(s_{r,n}R_0^{AB})+R_0^{AB}\beta)^{-\alpha_n}}, \tag{5.5}$$

and will be denoted "-D3^3".

For overall statistics, each dataset is weighted equally to avoid implicit weighting due to the number of points in each dataset, the exception is that the SSI (or SSI500) dataset always counts as $\frac{1}{3}$ of the overall statistic. This is done due to the fact that the SSI dataset contains a much more diverse and important set than any other single database. The DFT-D3 damping parameters were then fitted to the training set using a RMS CURE quantity (Eq. 1.9): the resulting refitted parameters will be denoted with a "M" for modified.

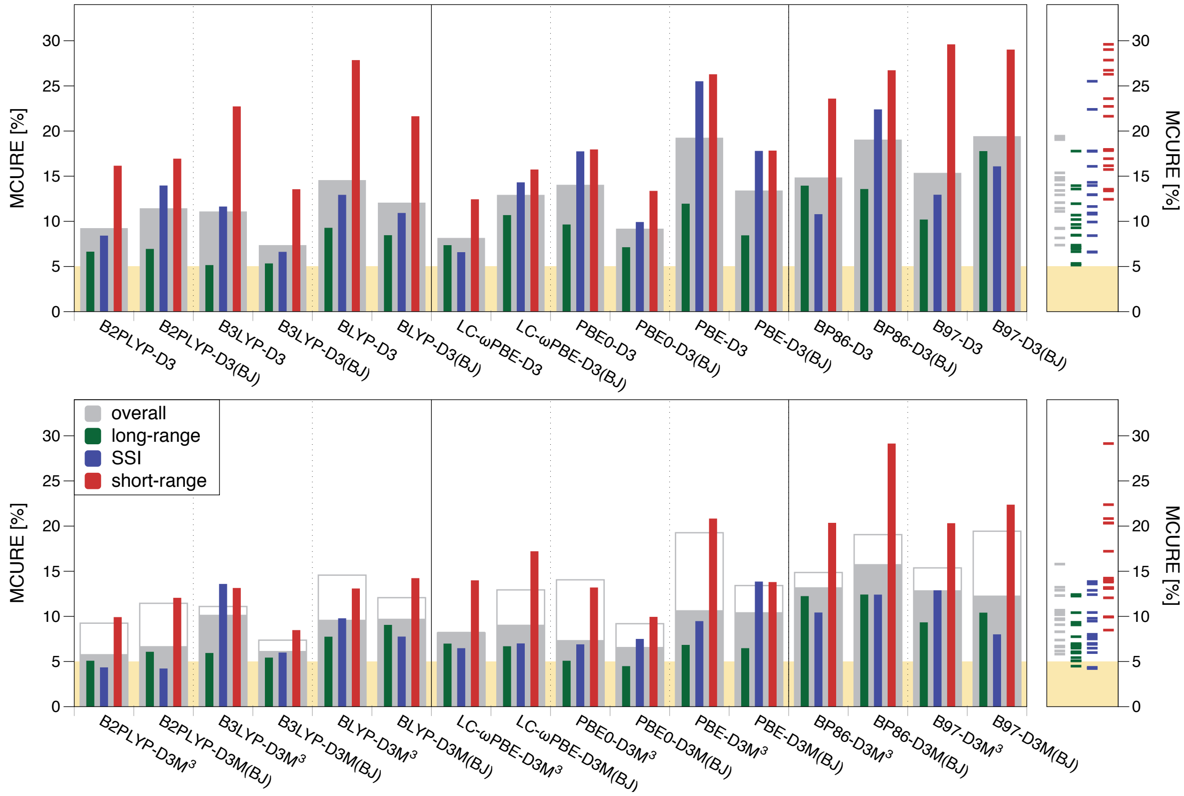

Figure 5.5: Top Panel: All functionals utilizing the original damping parameters. Bottom Panel: All functionals utilizing the new damping parameters, the light grey outlines represent the MCURE of the original damping parameters. The right hand panels give the spread of MCURE values for all functionals. All statistics are shown for the validation set. Adapted from Appendix E.

The original and refitted DFT-D3 statistics for a range of functionals are shown in Figure 5.5. First, examining the original parameters, it is apparent that short-range accuracy problems are not localized to the CO_2–PAH dataset, but are instead fairly systematic. As can be seen, the overall MCURE for the validation set improves after refitting for every single functional except for LC-ωPBE-D3M^3 whose MCURE statistic does not change. The largest improvements again come from the popular PBE-D3 method whose overall MCURE went from 19% to 10%, the majority of this improvement comes from the SSI dataset and at short-range. This radical improvement is not seen for all functionals, for example the B3LYP-D3 refitted only improved the overall MCURE by 1%; importantly, the majority of this improvements comes from short-range which goes from 23% to 13% MCURE.

As shown, refitting can greatly enhance the performance of DFT-D3 methods; however, the performance degradation at short-range cannot fully be ameliorated by refitting alone. These refitted parameters likely represent the most accurate general damping parameters possible for DFT-D3 and effectively places a limit on the performance of the current damping forms. As shown in Appendix E, more complex damping forms are not likely to improve the overall performance on the DFT-D3 method and other approaches need to be explored. Nevertheless, the new damping parameters do improve the overall accuracy of the DFT-D3 method and partially reduce the large variation in DFT-D performance. Overall, the top performing B3LYP-D3M(BJ) method is recommended for all NCI computations if CCSD(T)-based benchmarks are not available.

Chapter 6

Density-Fitted Multi-Configurational Self Consistent Field

Multi-Configurational Self Consistent Field (MCSCF) is a methodology that combines aspects of SCF and CI. In this chapter we will present optimization techniques for MCSCF wavefunctions and the application of density fitted two-electron integrals to reduce the overall cost of this method. Both the SCF and CI methods will be briefly summarized and the pieces pertinent to MCSCF optimization will be highlighted.

6.1 Self Consistent Field

Here we will focus on a variant of SCF known as restricted Hartree-Fock (RHF) where the α and β orbitals are equal denoting a closed-shell molecule with all paired electrons. The usage of RHF over generalized SCF is done both for simplicity and the fact that the SCF-like indices in MCSCF are effectively RHF indices. To begin, let us start with the AO Fock matrix, which is represented as[41, 137]

$$F_{\mu\nu} = H_{\mu\nu} + 2g_{\mu\nu\lambda\sigma}D_{\lambda\sigma} - g_{\mu\lambda\nu\sigma}D_{\lambda\sigma} \tag{6.1}$$

and the one-particle RHF density matrix D is computed from the orbitals C (assumed real).

$$D_{\lambda\sigma} = C_{i\sigma}C_{i\lambda} \tag{6.2}$$

It should be noted that if D is converted to the MO basis, we have a diagonal matrix of ones up to the number of occupied indices and zero thereafter

$$D_{pq} = \begin{pmatrix} 1_{ii} & 0 \\ 0 & 0 \end{pmatrix} \tag{6.3}$$

This is specifically noted as a generalized density matrix would have two across the diagonal to represent two electrons

$$\gamma_{pq} = \begin{pmatrix} 2_{ii} & 0 \\ 0 & 0 \end{pmatrix} \tag{6.4}$$

This factor of two is instead absorbed into the RHF equations to simplify the expressions and to be consistent with RHF equations typically found in reference texts.

The total RHF energy can be expressed as a sum of the electronic and Born-Oppenheimer (BO) nuclear energies

$$E^{RHF} = E^{RHF}_{electronic} + E^{BO}_{nuclear} \tag{6.5}$$

$$E^{RHF}_{electronic} = (F_{\mu\nu} + H_{\mu\nu})D_{\mu\nu} \tag{6.6}$$

$$E^{BO}_{nuclear} = \sum_{i>j} \frac{Z_i Z_j}{r_{ij}} \tag{6.7}$$

where Z_i is the nuclear charge of atom i.

Examining these equations, it is clear that the most computationally demanding portions are the convolution of the density matrix with the two-electron integral tensor. Therefore, it is often convenient to define the following quantities

$$J[D_{\lambda\sigma}]_{\mu\nu} = g_{\mu\nu\lambda\sigma} D_{\lambda\sigma} \tag{6.8}$$

$$K[D_{\lambda\sigma}]_{\mu\nu} = g_{\mu\lambda\nu\sigma} D_{\lambda\sigma} \tag{6.9}$$

The resulting J and K matrices are often called the Coulomb and Exchange matrices, respectively. Often quantum chemistry programs have very efficient routines to compute these equations, thus utilizing these routines is of the utmost importance.

6.1.1 Density-fitted Coulomb and Exchange algorithms

With density fitting[138–141] the two-electron integrals are represented by the following

$$g_{\mu\nu\lambda\sigma} \approx (\widetilde{\mu\nu|P})[J^{-1}]_{PQ}(\widetilde{Q|\lambda\sigma}) \tag{6.10}$$

where the Coulomb metric $[J]_{PQ}$ and the three center overlap integral $(\widetilde{Q|\lambda\sigma})$ are define as

$$[J]_{PQ} = \int P(\mathbf{r}_1)\frac{1}{\mathbf{r}_{12}}Q(\mathbf{r}_2)d^3\mathbf{r}_1 d^3\mathbf{r}_2 \tag{6.11}$$

$$(\widetilde{Q|\lambda\sigma}) = \int Q(\mathbf{r}_1)\frac{1}{r_{12}}\lambda(\mathbf{r}_2)\sigma(\mathbf{r}_2)d^3\mathbf{r}_1 d^3\mathbf{r}_2 \tag{6.12}$$

To simplify the density fitting notation, the inverse Coulomb metric is typically folded into the three center overlap tensor

$$(P|\lambda\sigma) = [J^{-\frac{1}{2}}]_{PQ}(\widetilde{Q|\lambda\sigma}) \tag{6.13}$$

$$g_{\mu\nu\lambda\sigma} \approx (\mu\nu|P)(P|\lambda\sigma) \tag{6.14}$$

The Coulomb matrix can then be computed in $\mathcal{O}(\mathrm{N}^2\mathrm{N}_{aux})$ operations:

$$\chi_P = (P|\lambda\sigma)D_{\lambda\sigma} \tag{6.15}$$

$$J[D_{\lambda\sigma}]_{\mu\nu} = (\mu\nu|P)\chi_P \tag{6.16}$$

The Exchange matrix can be computed in $\mathcal{O}(\mathrm{N}^3\mathrm{N}_{aux})$ operations:

$$\zeta_{P\nu\lambda} = (P|\nu\sigma)D_{\lambda\sigma} \tag{6.17}$$

$$K[D_{\lambda\sigma}]_{\mu\nu} = (\mu\lambda|P)\zeta_{P\nu\lambda} \tag{6.18}$$

however, considering the form of the density matrix, we can reduce this to $\mathcal{O}(p\mathrm{N}^2\mathrm{N}_{aux})$

$$D_{\lambda\sigma} = C_{p\sigma}C_{p\lambda} \tag{6.19}$$

$$\zeta^1_{P\mu p} = (\mu\sigma|P)C_{p\sigma} \tag{6.20}$$

$$\zeta^2_{P\nu p} = (P|\nu\lambda)C_{p\lambda} \tag{6.21}$$

$$K[D_{\lambda\sigma}]_{\mu\nu} = \zeta^1_{P\mu p}\zeta^2_{P\nu p} \tag{6.22}$$

where p is a generalized MO index that can span any space. This technique is especially beneficial when p is an inactive or active index as these are typically small relative to the full N space. It should be noted that Eqs. 6.19-6.22 pertain to the generalized case where $C_{p\sigma} \neq C_{p\lambda}$, if both C matrices are identical, only one ζ intermediate needs to be built. The $C_{p\sigma} \neq C_{p\lambda}$ case often arises in MCSCF theory when either rotated, transition, or generalized density matrices are used.

Computation of the Coulomb and Exchange matrices through conventional means costs N^4, here we see that Coulomb builds are rank reduced, but Exchange builds are of the same rank. The real benefit of density-fitted integrals for K builds comes from data locality and data storage. As N_{aux} is typically twice the size of N, we can imagine a case with 3000 AO basis functions. Conventional 4-index two-electron integrals would use 81 TB if the 8-fold symmetry of the tensor is exploited, on the other hand, the 3-index density-fitted tensor would only take up 216 GB if the 2-fold symmetry is exploited, a reduction of 375 fold.

6.1.2 Roothaan Equations

The SCF equations are often solved through the Roothan equations,[137] shown in matrix formalism

$$\mathbf{FC} = \mathbf{SC}\epsilon \tag{6.23}$$

This is a pseudo-eigenvalue equation. At every iteration we need to solve for the coefficients **C** that diagonalize the Fock matrix. An ideal world would produce AO orbitals that are orthogonal, unfortunately, as demonstrated by non-diagonal overlap matrices, this is not the case. To overcome this problem, a orthonormalized Fock matrix is diagonalized instead, shown in matrix formalism

$$\mathbf{A} = \mathbf{S}^{-1/2} \tag{6.24}$$

$$\mathbf{F}' = \mathbf{A}^T\mathbf{FA} \tag{6.25}$$

$$\mathbf{F}'\mathbf{C}' = \mathbf{C}'\epsilon \tag{6.26}$$

$$\mathbf{C} = \mathbf{AC}' \tag{6.27}$$

At every iteration we construct our Fock matrix from the previous orbitals ($\mathbf{C}_{n-1}$) and compute new orbitals ($\mathbf{C}_n$) until convergence is reached.

For the rest of this section, the "physicist's water molecule" (O-H = 1.1Å, ∠ HOH = 104°) will be utilized in the cc-pVDZ basis set for illustrating convergence patterns. A pure iterative diagonalization approach is shown in Fig. 6.1. As can be seen, the convergence for this simple molecule is quite slow and the next sections will detail convergence acceleration.

6.1.3 Direct Inversion of the Iterative Subspace convergence acceleration

Direct Inversion of the Iterative Subspace (DIIS) is often used for convergence acceleration[142] of SCF wavefunctions. For iterative diagonalization, we discard all previous guess

Figure 6.1: A RHF computation of "physicist's water molecule" starting with a core Hamiltonian guess in the cc-pVDZ basis set. dE is the energy difference between iterations and dRMS is the root mean square of the orbital gradient.

```
RHF Iteration   1: Energy = -68.98003273414295   dE = -6.898E+01   dRMS = 1.165E-01
RHF Iteration   2: Energy = -69.64725442845806   dE = -6.672E-01   dRMS = 1.074E-01
RHF Iteration   3: Energy = -72.84030309363035   dE = -3.193E+00   dRMS = 1.039E-01
RHF Iteration   4: Energy = -72.89488390650019   dE = -5.458E-02   dRMS = 8.660E-02
RHF Iteration   5: Energy = -74.12078064688371   dE = -1.225E+00   dRMS = 8.646E-02
RHF Iteration   6: Energy = -74.86718194576882   dE = -7.464E-01   dRMS = 6.528E-02
RHF Iteration   7: Energy = -75.41490878039029   dE = -5.477E-01   dRMS = 5.216E-02
...
RHF Iteration  22: Energy = -75.98979285429830   dE = -3.768E-06   dRMS = 1.188E-04
RHF Iteration  23: Energy = -75.98979450314014   dE = -1.648E-06   dRMS = 7.860E-05
RHF Iteration  24: Energy = -75.98979522446778   dE = -7.213E-07   dRMS = 5.198E-05
```

vectors (orbitals) and generate completely new guess vectors at each iteration. DIIS keeps previous guess vectors and builds the best guess as a linear combination of all previous guess vectors.

For the explanation of DIIS, we will break with all conventional terminology to stress that this is a linear algebra technique that is widely applicable to many problems besides SCF, as we will see in the next several sections. Let us assume that we have generated several state vectors (s) with a series of complementary error vectors (r) through some iterative method.

For DIIS to be applicable, we assume that both the next residual and the next state vector can be built as a linear combination of previous guess vectors with coefficients c.

$$s_{i+1} = \sum_i^n c_i s_i \tag{6.28}$$

$$r_{i+1} = \sum_i^n c_i r_i \tag{6.29}$$

$$\sum_i^n c_i = 1 \tag{6.30}$$

Therefore, we want to select the coefficients in a manner that minimizes the norm of the residual

$$r_{i+1} \cdot r_{i+1} = \sum_{ij}^{n} c_i c_j (r_i \cdot r_j) \tag{6.31}$$

This can be solved through the following matrix equations

$$\begin{bmatrix} B_{11} & B_{12} & ... & B_{1n} & -1 \\ B_{21} & B_{22} & ... & B_{2n} & -1 \\ ... & ... & ... & ... & ... \\ B_{n1} & B_{n2} & ... & B_{nn} & -1 \\ -1 & -1 & ... & -1 & 0 \end{bmatrix} \begin{bmatrix} c_1 \\ c_2 \\ ... \\ c_n \\ \lambda \end{bmatrix} = \begin{bmatrix} 0 \\ 0 \\ ... \\ 0 \\ -1 \end{bmatrix} \tag{6.32}$$

where B is a matrix of inner products between error vectors

$$B_{ij} = (r_i \cdot r_j) \tag{6.33}$$

and λ is value of the Lagrange multiplier. It should be noted that often our error vectors are in effect tensors, e.g., $F_{\mu\nu}$, and the norm is computed as the generalized inner product between tensors.

For SCF, the state vector is always the Fock matrix and the error vector is typically the orthonormalized orbital gradient expressed in a AO matrix formalism,

$$\mathrm{r}_{\mu\nu} = (\mathbf{A}^{\mathrm{T}}(\mathbf{FDS} - \mathbf{SDF})\mathbf{A})_{\mu\nu} \tag{6.34}$$

The procedure for applying DIIS to SCF at every iteration is therefore:

1. Compute the Fock (s_n) matrix using $\mathbf{C}_n$ orbitals
2. Construct the AO gradient (r_n)
3. Obtain the DIIS Fock guess (s_{DIIS})

4. Obtain $\mathbf{C}_{n+1}$ orbitals by diagonalizing the DIIS Fock guess (s_{DIIS})

This procedure is iterated until the desired convergence thresholds are reached.

Figure 6.2: A RHF computation of "physicist's water molecule" starting with a core Hamiltonian guess in the cc-pVDZ basis set utilizing DIIS convergence.

```
RHF Iteration   1: Energy = -68.98003273414295   dE = -6.898E+01   dRMS = 1.165E-01
RHF Iteration   2: Energy = -69.64725442845806   dE = -6.672E-01   dRMS = 1.074E-01 DIIS
RHF Iteration   3: Energy = -75.79192914624532   dE = -6.144E+00   dRMS = 2.892E-02 DIIS
RHF Iteration   4: Energy = -75.97218922804181   dE = -1.802E-01   dRMS = 7.564E-03 DIIS
RHF Iteration   5: Energy = -75.98936905846086   dE = -1.717E-02   dRMS = 8.749E-04 DIIS
RHF Iteration   6: Energy = -75.98971633493079   dE = -3.472E-04   dRMS = 5.356E-04 DIIS
RHF Iteration   7: Energy = -75.98979323982247   dE = -7.690E-05   dRMS = 6.212E-05 DIIS
RHF Iteration   8: Energy = -75.98979567508871   dE = -2.435E-06   dRMS = 1.972E-05 DIIS
RHF Iteration   9: Energy = -75.98979578301157   dE = -1.079E-07   dRMS = 1.727E-06 DIIS
```

The DIIS convergence procedure is then applied to the "physicist's water molecule" in Fig. 6.2. It should be noted that while DIIS can be utilized on every iteration, the results are equal to pure diagonalization until two error vectors have been constructed. Therefore, the first iteration which benefits from DIIS acceleration is iteration three. As can be seen, roughly the same energy convergence is obtained in 9 iterations compared to 24 iterations without DIIS. The cost of DIIS itself is negligible; however, the cost of building the gradient is on the order of N^3, which is still much less than the Coulomb and Exchange matrix builds.

6.1.4 Second-order orbital optimization

Diagonalization builds completely new orbitals at every iteration; an alternative is to construct new orbitals by rotating the orbitals of the previous iteration. This is often called second-order optimization and, if done exactly, the convergence will be quadratic with respect to the MO gradient,[143] e.g., $\text{grad}_{pq}^{n+1} \approx (\text{grad}_{pq}^{n})^2$. As a consequence of the quadratic convergence, the second-order procedure can only be started once all elements of the gradient in the MO basis are less than one, else the error will increase.

The overall goal is to find an orbital rotation matrix, $\boldsymbol{\kappa}$, that satisfies the following set of linear equations:

$$\mathbf{E}^{(2)}\boldsymbol{\kappa} = -\mathbf{E}^{(1)} \tag{6.35}$$

where $\mathbf{E}^{(2)}$ is our orbital Hessian and $\mathbf{E}^{(1)}$ is the orbital gradient. The $\boldsymbol{\kappa}$ matrix is a antisymmetric matrix of non-redundant rotations that describes the unitary transformation $\mathbf{U}$

$$\mathbf{U} = e^{\boldsymbol{\kappa}} \tag{6.36}$$

$$\mathbf{C}_{n+1} = \mathbf{C}_n\mathbf{U} \tag{6.37}$$

Rotations within a given space (inactive or virtual for SCF) are redundant: the only non-redundant orbital rotations for SCF are the inactive-virtual ones.

The orbital gradient can be written as

$$\mathrm{E}^{(1)}_{pq} = 2(F_{pq} - F_{qp}) \tag{6.38}$$

where F is our generalized Fock matrix[143]

$$F_{in} = 2({}^{A}F_{in} + {}^{I}F_{in}) \tag{6.39}$$

$$F_{vn} = {}^{I}F_{nw}\gamma_{vw} + Q_{vn}, \quad Q_{vn} = \Gamma_{vwxy}g_{nwxy} \tag{6.40}$$

$$F_{an} = 0 \tag{6.41}$$

and the Active (${}^{A}F$) and Inactive (${}^{I}F$) Fock matrices are defined as

$${}^{I}F_{pq} = H_{pq} + 2g_{pqrs}D_{rs} - g_{prqs}D_{rs} \tag{6.42}$$

$${}^{A}F_{pq} = \gamma_{tu}(g_{pqtu} - \frac{1}{2}g_{ptuq}) \tag{6.43}$$

In the case of RHF, the Inactive Fock matrix is identical to the AO Fock matrix given in Eq. 6.1, this equation can be rewritten considering the special form of the RHF density matrix with MO indices

$$^{I}F_{pq} = H_{pq} + 2g_{pqii} - g_{piqi} \tag{6.44}$$

The orbital Hessian can be built explicitly; however, this matrix is quite large and it is typically sufficient to know the product of the Hessian with a given vector. To do so, we will introduce the rotated Hamiltonian

$$\hat{H}^{\kappa} = h^{\kappa}_{pq}\gamma_{pq} + g^{\kappa}_{pqrs}\Gamma_{pqrs} \tag{6.45}$$

and the one-index transformed integrals

$$h^{\kappa}_{pq} = (\kappa_{po}h_{oq} + \kappa_{qo}h_{po}) \tag{6.46}$$

$$g^{\kappa}_{pqrs} = (\kappa_{po}g_{oqrs} + \kappa_{qo}g_{pors} + \kappa_{ro}g_{pqos} + \kappa_{so}g_{pqro}) \tag{6.47}$$

Applying this Hamiltonian to our SCF wavefunction results in a rotated Fock matrix (F^{κ}) where all one- and two-electron integrals have been replaced by their respective one-index transformed counterparts. This rotated Fock matrix is the Hessian vector product ($\mathbf{E}^{(2)}\boldsymbol{\kappa}$) and can be substituted for the LHS of Eq. 6.35:

$$2(F^{\kappa}_{pq} - F^{\kappa}_{qp}) = -2(F_{pq} - F_{qp}) \tag{6.48}$$

Considering the special structure of the generalized Fock matrix for RHF calculations (only inactive-virtual rotations are non-redundant and F_{ai} is zero), we can write our set of linear equations for the last time as

$$-4^{I}F^{\kappa}_{ia} = 4^{I}F_{ia} \tag{6.49}$$

which must be solved iteratively. As shown below, this is the most computationally efficient form of these equations. For demonstration purposes, the ${}^{I}F^{\kappa}_{ia}$ tensor need not be contracted with $\boldsymbol{\kappa}$ to yield iterative form shown in Eq. 6.49. Instead, the full 4-index orbital Hessian can be constructed and Eq. 6.35 can then be solved exactly. However, when solved exactly, the cost of inverting the full orbital Hessian is o^3v^3, unless o is very small, we have effectively changed the cost of SCF from N^4 to N^6, or roughly the cost of CCSD. Solving either Eq. 6.35 or Eq. 6.49 will be denoted second-order SCF (SOSCF).

Figure 6.3: A RHF computation of "physicist's water molecule" starting with a core Hamiltonian guess in the cc-pVDZ basis set utilizing DIIS and SOSCF convergence. For the SOSCF step, the Eq. 6.35 has been solved exactly by inverting the full orbital Hessian. The right most abbreviations indicate the type of step taken in each iteration.

```
RHF Iteration   1: Energy = -68.98003273414295   dE = -6.898E+01   dRMS = 1.165E-01
RHF Iteration   2: Energy = -69.64725442845806   dE = -6.672E-01   dRMS = 1.074E-01 DIIS
RHF Iteration   3: Energy = -75.79192914624532   dE = -6.144E+00   dRMS = 2.892E-02 DIIS
RHF Iteration   4: Energy = -75.97218922804181   dE = -1.802E-01   dRMS = 7.564E-03 DIIS
RHF Iteration   5: Energy = -75.98973929215161   dE = -1.755E-02   dRMS = 3.049E-04 SOSCF
RHF Iteration   6: Energy = -75.98979578473095   dE = -5.649E-05   dRMS = 1.231E-06 SOSCF
RHF Iteration   7: Energy = -75.98979578551825   dE = -7.873E-10   dRMS = 1.901E-11 SOSCF
RHF Iteration   8: Energy = -75.98979578551835   dE = -9.948E-14   dRMS = 2.395E-15 SOSCF
```

Returning to our "physicist's water molecule", the convergence pattern for SOSCF is demonstrated in Fig. 6.3. We can observe that three regular DIIS steps were required before all elements of the gradient were less than one. The RHF wavefunction is then converged to within machine precision in terms of energy and density within 4 SOSCF iterations. SOSCF is quite beneficial in terms of the number of iterations, but is not currently competitive in terms of cost.

Let us return our attention to Eq. 6.49 and to the implementation of an efficient rotated Inactive Fock (${}^{I}F^{\kappa}$) build

$$ {}^{I}F^{\kappa}_{mn} = h^{\kappa}_{mn} + 2g^{\kappa}_{mnii} - g^{\kappa}_{miin} \tag{6.50} $$

Inserting our equations for one-index transformed integrals, we obtain

$$\begin{aligned}
{}^{I}F^{\kappa}_{mn} =&(\kappa_{mp}h_{pn} + \kappa_{np}h_{mp})+\\
&2(\kappa_{mo}g_{onii} + \kappa_{no}g_{moii} + \kappa_{io}g_{mnoi} + \kappa_{io}g_{mnio})-\\
&(\kappa_{mo}g_{oiin} + \kappa_{io}g_{moin} + \kappa_{io}g_{mion} + \kappa_{no}g_{miio}) \qquad (6.51)
\end{aligned}$$

Simplifying and collecting these terms yields

$$ {}^{I}F^{\kappa}_{mn} = ({}^{I}F_{mp}\kappa_{np} + {}^{I}F_{pn}\kappa_{mp}) + \kappa_{ip}(4g_{mnip} - g_{mpin} - g_{npim}) \qquad (6.52)$$

which can be computed using conventional AO-based J and K routines:

$$\begin{aligned}
\vartheta_{\lambda\sigma} =&C_{i\lambda}\kappa_{ip}C_{p\sigma} \qquad (6.53)\\
{}^{I}F^{\kappa}_{mn} =&({}^{I}F_{mp}\kappa_{np} + {}^{I}F_{pn}\kappa_{mp})\\
&+ C_{m\mu}(4J[\vartheta_{\lambda\sigma}]_{\mu\nu} - K[\vartheta_{\lambda\sigma}]_{\mu\nu} - K[\vartheta_{\lambda\sigma}]_{\nu\mu})C_{n\nu} \qquad (6.54)
\end{aligned}$$

The cost of solving Eq. 6.49 is now N^4 when the left hand side is computed from Eq. 6.54 and each iteration of Eq. 6.49 (often called a microiteration) is equivalent to the cost of a normal RHF iteration. The term macroiteration refers to a step in which the overall SCF energy is computed, this step collects all Fock builds, microiterations, and orbital rotations.

Our "physicist's water molecule" was again optimized using iterative SOSCF in Fig. 6.4. We observe that while the convergence is significantly faster than for the DIIS acceleration alone, the overall convergence is much slower than when Eq. 6.49 was solved exactly. This is due to the fact that the number of microiterations used is insufficient to solve Eq. 6.49 exactly. More microiterations can be utilized, but a balance between macro- and microiterations must be computationally efficient. However, it should be noted that even though each microiteration of SOSCF is equivalent to the cost of a normal RHF step, the overall computational effort expended for SOSCF is generally greater than the DIIS methods for a

Figure 6.4: A RHF computation of ”physicist’s water molecule” starting with a core Hamiltonian guess in the cc-pVDZ basis set utilizing DIIS and SOSCF convergence. For the SOSCF step, Eq. 6.49 has been solved iteratively through a conjugate gradient method limited to four microiterations. The rightmost abbreviations indicate the type of step taken on each iteration.

```
RHF Iteration   1: Energy = -68.98003273414295   dE = -6.898E+01   dRMS = 1.165E-01
RHF Iteration   2: Energy = -69.64725442845806   dE = -6.672E-01   dRMS = 1.074E-01 DIIS
RHF Iteration   3: Energy = -75.79192914624532   dE = -6.144E+00   dRMS = 2.892E-02 DIIS
RHF Iteration   4: Energy = -75.97218922804181   dE = -1.802E-01   dRMS = 7.564E-03 DIIS
RHF Iteration   5: Energy = -75.98970327666461   dE = -1.751E-02   dRMS = 5.908E-04 SOSCF
RHF Iteration   6: Energy = -75.98979576713703   dE = -9.249E-05   dRMS = 8.777E-06 SOSCF
RHF Iteration   7: Energy = -75.98979578513478   dE = -1.799E-08   dRMS = 8.237E-07 SOSCF
RHF Iteration   8: Energy = -75.98979578551806   dE = -3.832E-10   dRMS = 1.648E-08 SOSCF
```

given convergence criterion. SOSCF should therefore only be utilized for difficult to converge SCF cases.

6.2 Configuration Interaction

The CI wavefunction is built from a linear combination of excitations, $\Psi = \sum\limits_I c_I \Phi_I$, where I represents all possible excitations from the ground state and $\mathbf{c}$ is the coupling coefficient. Unlike CC theory which relies on the exponential operator e^T to choose excitations, CI excitations are restricted simply by the number of excitations out of the reference state.

CI theory can be solved by the following matrix equation

$$\mathbf{Hc} = E\mathbf{c} \tag{6.55}$$

where $\mathbf{H}$ is our Hamiltonian $\mathbf{H} = \langle \Phi_I | \hat{H} | \Phi_J \rangle$ and $\mathbf{c}$ is our vector of coupling coefficients $\mathbf{c} = |C\rangle = \sum\limits_I c_I |I\rangle$. This is similar to SCF, where instead of expanding our basis in terms of atomic orbitals, we are now expanding our basis in terms of Slater determinants. While CI can be solved exactly by diagonalizing the Hamiltonian, this is almost always too computationally demanding. Instead, trial vectors $\mathbf{c}$ are generated and optimized through various means not detailed here. See Ref.143 for further reading. Hamiltonian trial vector products can be computed as $\boldsymbol{\sigma} = \mathbf{Hc}$.

Importantly, the complexity of CI can be hidden inside generalized density matrices:

$$\gamma_{pq} = \langle 0|\hat{E}_{pq}|0\rangle = \sum_{IJ} c_I c_J \gamma_{pq}^{IJ} \tag{6.56}$$

$$\Gamma_{pqrs} = \langle 0|\hat{e}_{pqrs}|0\rangle = \sum_{IJ} c_I c_J \Gamma_{pqrs}^{IJ} \tag{6.57}$$

where $|0\rangle$ is the reference CI vector. These density matrices lead to a simple expression of the CI energy

$$E_{CI} = \gamma_{pq} h_{pq} + \frac{1}{2}\Gamma_{pqrs} g_{pqrs} \tag{6.58}$$

Full CI (FCI) will be the focus of the current work where all possible excitations are included in the determinant basis. The number of FCI determinants scales like the following binomial function where N is the number of orbitals and n is the number of electrons:

$$N_{det} = \begin{pmatrix} N \\ n_\alpha \end{pmatrix} \begin{pmatrix} N \\ n_\beta \end{pmatrix} \tag{6.59}$$

where n_α and n_β are the number of alpha and beta electrons, respectively. CI computations can routinely be run on approximately ten million determinants. The number of orbitals and electrons in a FCI computation is typically denoted (n, N), where n is the number of electrons and N is the number of orbitals. For example, a (14e,14o) FCI computation would result in 11E^6 determinants and be fairly routine. However, a (16e,16o) (166E^6 determinants) would be quite expensive and (18e,18o) (2,364E^6 determinants) would be difficult to impossible. This puts a hard cap on the size of the FCI computations. It should be noted that FCI computations where $n \approx$N are most closely associated with MCSCF-like computations and general FCI calculations are usually of type $n \ll$N. Density-fitting is not able to reduce the computation time of CI: density-fitted CI simply means that the g_{pqrs} tensor is formed using density-fitted quantities.

6.3 Multiconfigurational Self Consistent Field

To extend CI out to large multireference molecules, the orbitals are partitioned between inactive orbitals (SCF-like) and active orbitals (CI-like). To be explicit in how MCSCF combines both SCF and CI, let us examine a hybrid one-particle density matrix

$$\gamma = \begin{pmatrix} 2_{ii} & 0 \\ 0 & \gamma_{tu} \end{pmatrix} \tag{6.60}$$

where the diagonal factor of two represents our SCF-like density elements and the γ represents our (non-diagonal) CI density in the active space.

As SCF can only describe a single state, and the orbitals from an SCF computation are therefore optimized to this state, they are likely inadequate to describe a fully multireference system. Therefore, we need to optimize both the $\mathbf{c}$ (CI vector) and $\boldsymbol{\kappa}$ (orbital rotation vector) simultaneously leading to the MCSCF parameters

$$\boldsymbol{\lambda} = \begin{pmatrix} \mathbf{c} \\ \boldsymbol{\kappa} \end{pmatrix} \tag{6.61}$$

For $\boldsymbol{\kappa}$ there are four types of non-redundant rotations, inactive-active, inactive-vitrual, active-active, and active-virtual. When the CI expansion is equal to active-space FCI in a MCSCF wavefunction (known specifically as complete active space SCF (CASSCF)), the active-active rotations are redundant and can safely be neglected.

The best $\boldsymbol{\lambda}$ vector at every iteration can be computed by solving the following set of linear equations

$$\mathbf{E}^{(2)}\boldsymbol{\lambda} = -\mathbf{E}^{(1)} \tag{6.62}$$

where $\mathbf{E}^{(1)}$ and $\mathbf{E}^{(2)}$ are the gradient vector and Hessian matrix, respectively.

6.3.1 MCSCF Gradient

The gradient vector, $\mathbf{E}^{(1)}$, can be rewritten in block form

$$\mathbf{E}^{(1)} = \begin{pmatrix} {}^{c}\mathbf{E}^{(1)} \\ {}^{o}\mathbf{E}^{(1)} \end{pmatrix} \tag{6.63}$$

The CI gradient can be defined as

$${}^{c}\mathrm{E}_i^{(1)} = 2\langle i|\hat{H}|0\rangle - 2C_i^{(0)}E^0 = 2\sum_{tu}\gamma_{tu}^{i}\,{}^{I}F_{tu} + \sum_{tuvw}\Gamma_{tuvw}^{i}g_{tuvw} - 2C_i^{(0)}(E^{(0)} - {}^{I}E) \tag{6.64}$$

$${}^{I}E = \sum_i (h_{ii} + {}^{I}F_{ii}) \tag{6.65}$$

It should be noted that $\langle i|\hat{H}|0\rangle$ can be obtained from a canonical CI sigma vector computation: $\boldsymbol{\sigma} = \mathbf{Hc}$.

The orbital gradient is identical to that of the SCF equations

$${}^{o}\mathrm{E}_{pq}^{(1)} = 2(F_{pq} - F_{qp}) \tag{6.66}$$

In MCSCF theory, this is occasionally denoted the Lagrangian.

The generalized Fock matrix can again be written as

$$F_{ip} = 2({}^{I}F_{pi} + {}^{A}F_{pi}) \tag{6.67}$$

$$F_{tp} = \gamma_{pu}h_{tu} + Q_{pt}, \quad Q_{pt} = \Gamma_{tuvw}g_{puvw} \tag{6.68}$$

$$F_{ap} = 0 \tag{6.69}$$

Recalling the definition of Active (${}^{A}F$) and Inactive (${}^{I}F$) Fock matrices

$${}^{I}F_{pq} = H_{pq} + 2g_{pqkl}D_{kl} - g_{pkql}D_{kl} \tag{6.70}$$

$$ {}^{A}F_{pq} = \gamma_{tu}(g_{pqtu} - \frac{1}{2}g_{ptuq}) \tag{6.71} $$

these matrices can be computed using normal J and K builds

$$ D_{\lambda\sigma} = C_{i\lambda}C_{i\sigma} \tag{6.72} $$

$$ {}^{I}F_{pq} = H_{pq} + C_{p\mu}(2J[D_{\lambda\sigma}]_{\mu\nu} - K[D_{\lambda\sigma}]_{\mu\nu})C_{q\nu} \tag{6.73} $$

$$ \gamma_{\lambda\sigma} = C_{t\lambda}\gamma_{tu}C_{u\sigma} \tag{6.74} $$

$$ {}^{A}F_{pq} = C_{p\mu}(J[\gamma_{\lambda\sigma}]_{\mu\nu} - \frac{1}{2}K[\gamma_{\lambda\sigma}]_{\mu\nu})C_{q\nu} \tag{6.75} $$

For MCSCF scalings, we make the assumption that a reasonably sized CI space is picked and the orbital part will dominate the overall cost considerations. In addition, we make the assumption that a^2<N (a is the size of the active space) which is reasonable for typical MCSCF calculations. It should be noted that if a^2>N, the cost of the orbital part will be quite negligible due to the upper bounds of the size of a in the previous section.

The Q matrix is the first quantity for which typical J or K builds are not suitable and the explicit form of the density-fitting needs to be shown. It should be noted that while the Q matrix can be computed with J builds,[144] this technique is typically not recommended due to the prefactor of this methodology growing as the square of the active space size. The computation of this term through conventional means would cost $\mathcal{O}(a^4\mathrm{N})$ which is effectively negligible; however, the formation of the g_{puvw} tensor would have a leading cost of $\mathcal{O}(a\mathrm{N}^4)$. Nevertheless, building Q through explicit use of density-fitted tensors is quite simple at the cost of $\mathcal{O}(a^2\mathrm{N}\mathrm{N}_{aux})$:

$$ \chi_{tuQ} = \Gamma_{tuvw}(Q|vw) \tag{6.76} $$

$$ Q_{pt} = (pu|Q)\chi_{tuQ} \tag{6.77} $$

While this scaling is N^5, the reliance on the active indices being very small means that this contraction is usually of negligible time. The transformation of the $(Q|vw)$ tensor scales like $\mathcal{O}(a\mathrm{N}^2\mathrm{N}_{aux})$ demonstrating that the real benefit here is the reduction in overall scaling of the two-electron integral transformation.

6.3.2 MCSCF Hessian

The MCSCF Hessian has the overall form

$$\mathbf{E}^{(2)} = \mathbf{K}^{(2)} - \bar{\mathbf{E}}^{(1)}\boldsymbol{\zeta}^{(0)^T} - \boldsymbol{\zeta}^{(0)}\bar{\mathbf{E}}^{(1)^T} \tag{6.78}$$

with rank 1

$$\bar{\mathbf{E}}^{(1)} = \begin{pmatrix} {}^{c}\mathbf{E}^{(1)} \\ 2{}^{o}\mathbf{E}^{(1)} \end{pmatrix} ; \boldsymbol{\zeta}^{(0)} = \begin{pmatrix} \mathbf{C}^0 \\ 0 \end{pmatrix} \tag{6.79}$$

and rank 2 contributions

$$\mathbf{K}^{(2)} = \begin{pmatrix} {}^{cc}\mathbf{K}^{(2)}_{i,j} & {}^{co}\mathbf{K}^{(2)}_{i,rs} \\ {}^{oc}\mathbf{K}^{(2)}_{pq,j} & {}^{oo}\mathbf{K}^{(2)}_{pq,rs} \end{pmatrix} \tag{6.80}$$

Rather than explicitly building the Hessian, we will instead focus on Hessian trial vector products

$$\begin{pmatrix} {}^{c}\boldsymbol{\sigma} \\ {}^{o}\boldsymbol{\sigma} \end{pmatrix} = \begin{pmatrix} {}^{cc}\mathbf{K}^{(2)}_{i,j} & {}^{co}\mathbf{K}^{(2)}_{i,rs} \\ {}^{oc}\mathbf{K}^{(2)}_{pq,j} & {}^{oo}\mathbf{K}^{(2)}_{pq,rs} \end{pmatrix} \begin{pmatrix} \mathbf{c} \\ \boldsymbol{\kappa} \end{pmatrix} = \begin{pmatrix} {}^{cc}\mathbf{K}^{(2)}\ \mathbf{c} \ + \ {}^{co}\mathbf{K}^{(2)}\ \boldsymbol{\kappa} \\ {}^{oc}\mathbf{K}^{(2)}\ \mathbf{c} \ + \ {}^{oo}\mathbf{K}^{(2)}\ \boldsymbol{\kappa} \end{pmatrix} \tag{6.81}$$

For each element we obtain:

$$[{}^{cc}\mathbf{K}^{(2)}\ \mathbf{c}]_i = 2\langle i|\hat{H} - E^{(0)}|\mathbf{c}\rangle \tag{6.82}$$

$$[{}^{co}\mathbf{K}^{(2)}\ \boldsymbol{\kappa}]_i = 2\langle i|\hat{H}^{\kappa}|0\rangle \tag{6.83}$$

$$[{}^{oc}\mathbf{K}^{(2)}\ \mathbf{c}]_{pq} = \langle 0|[E^{-}_{pq}, \hat{H}]|\mathbf{c}\rangle + \langle \mathbf{c}|[E^{-}_{pq}, \hat{H}]|0\rangle \tag{6.84}$$

$$[{}^{oo}\mathbf{K}^{(2)}\ \boldsymbol{\kappa}]_{pq} = \langle 0|[E^{-}_{pq}, \hat{H}^{\kappa}]|0\rangle + ([{}^{o}\mathbf{E}^{(1)}, \boldsymbol{\kappa}])_{pq} \tag{6.85}$$

where $\mathrm{E}^{-}_{pq} = \hat{E}_{pq} - \hat{E}_{qp}$. Careful examination of the first two terms shows that they can be built from standard CI σ vector computations where for the second term the rotated integrals need to be substituted for the regular integrals. The last two terms can be built similar to the rotated Fock builds (F^{κ}) of Eq. 6.54. The $[{}^{oo}\mathrm{K}^{(2)}\ \boldsymbol{\kappa}]_{pq}$ block can be written simply as

$$[{}^{oo}\mathrm{K}^{(2)}\ \boldsymbol{\kappa}]_{pq} = F^{\kappa}_{pq} + F_{pr}\kappa_{qr} - F_{rq}\kappa_{pr} \tag{6.86}$$

The $[{}^{oc}\mathrm{K}^{(2)}\ \mathbf{c}]_{pq}$ term can also be built through rotated Fock builds; however, the transition density matrices must be used

$$\gamma^{\mathbf{c}}_{pq} = \langle 0|\hat{E}_{pq}|\mathbf{c}\rangle \tag{6.87}$$

$$\Gamma^{\mathbf{c}}_{pqrs} = \langle 0|\hat{e}_{pqrs}|\mathbf{c}\rangle \tag{6.88}$$

If $|\mathbf{c}\rangle$ is equivalent to the current reference state, $|0\rangle$, we obtain the normal CI density matrices. Therefore, $\langle 0|[E^{-}_{pq}, \hat{H}]|\mathbf{c}\rangle$ is simply the generalized Fock matrix with transition density matrices.

We have previously shown how to build the rotated Inactive Fock matrix through J and K matrices in Eq. 6.54. The rotated Active Fock matrix can be rewritten using similar techniques:

$${}^{A}F^{\kappa}_{mn} = \sum_{p}({}^{A}F_{mp}\kappa_{np} + {}^{A}F_{pn}\kappa_{mp}) + \sum_{vwp}\gamma_{vw}\kappa_{wp}(2g_{mnvp} - \frac{1}{2}g_{mpvn} - \frac{1}{2}g_{npvm}) \tag{6.89}$$

and rewritten through J and K matrices

$$\vartheta_{\lambda\sigma} = C_{v\lambda}\gamma_{vw}\kappa_{wp}C_{p\sigma} \tag{6.90}$$

$$\begin{aligned} {}^{A}F^{\kappa}_{mn} =& \sum_{p}({}^{A}F_{mp}\kappa_{np} + {}^{A}F_{pn}\kappa_{mp}) + \\ & C_{m\mu}(2J[\vartheta_{\lambda\sigma}]_{\mu\nu} - \frac{1}{2}K[\vartheta_{\lambda\sigma}]_{\mu\nu} - \frac{1}{2}K[\vartheta_{\lambda\sigma}]_{\nu\mu})C_{n\nu} \end{aligned} \tag{6.91}$$

The last required term of the rotated Fock matrix is the rotated Q matrix

$$Q^{\kappa}_{vm} = \Gamma_{vwxy}(\kappa_{mo}g_{owxy} + \kappa_{wo}g_{moxy} + \kappa_{xo}g_{mwoy} + \kappa_{yo}g_{mwxo}) \tag{6.92}$$

Examining the above equation shows a scaling of $\mathcal{O}(a^3\mathrm{N}^2)$, again as the size of the active index is typically quite small, this is fairly negligible. However, as with the computation of the Q_{vm} matrix, the leading cost is not with the term itself, but the transformation of the g_{owxy} tensor, $\mathcal{O}(a\mathrm{N}^4)$. Through the use of density-fitting, the cost of this term is only $\mathcal{O}(a\mathrm{N}^2\mathrm{N}_{aux})$; however, the transformation of the required $(mo|Q)$ tensor is $\mathcal{O}(\mathrm{N}^3\mathrm{N}_{aux})$. While the scaling of the density-fitted and conventional MO transformations appear to be roughly equal on paper (due to $\mathrm{N}_{aux} \approx 2\mathrm{N}$), the real benefit is again the vast reduction in the size of quantities involved.

6.3.3 Approximate orbital Hessian

As the computation of the exact orbital Hessian in the previous subsection is relatively costly an approximate Hessian can be employed. In addition, the approximate orbital Hessian is typically chosen to be diagonal and no iterations are required to solve the Hessian vector equations. In this particular case we will use the approximate Hessian of Gordon and collaborators[145] which is defined as follows

$$H_{ia,ia} = 4({}^{I}F_{aa} + {}^{A}F_{aa}) - 4({}^{I}F_{ii} + {}^{A}F_{ii}) \tag{6.93}$$

$$H_{ta,ta} = 2\gamma_{tt}{}^{I}F_{aa} - 2\gamma_{tu}{}^{I}F_{tu} - 2\Gamma_{tuvw}g_{tuvw} + 2\gamma_{tt}{}^{A}F_{aa} \tag{6.94}$$

$$\begin{aligned} H_{it,it} =& 4({}^{I}F_{tt} + {}^{A}F_{tt}) - 4({}^{I}F_{ii} + {}^{A}F_{ii}) + 2\gamma_{tt}{}^{I}F_{ii} \\ & - 2\gamma_{tu}{}^{I}F_{tu} - 2\Gamma_{tuvw}g_{tuvw} + 2\gamma_{tt}{}^{A}F_{ii} \end{aligned} \tag{6.95}$$

Once the generalized Fock matrix is built for use in the MCSCF orbital gradient, the above approximate Hessian is of negligible cost.

6.4 MCSCF optimization examples

In this section we will demonstrate several different ways to optimize the MCSCF wavefunction. In general, MCSCF optimization is broken down into one-step and two-step approaches. One-step refers to solving Eq. 6.62 fully at each macroiteration. Two-step updates the CI and orbital vectors independently of each other by assuming the orbital-CI coupling blocks of the MCSCF Hessian are zero; for each macroiteration, the CI vector is first optimized followed by an orbital update. The two-step method is widely implemented as it is computationally simple compared to one-step and the orbital and CI methods are disconnected. This allows many orbital and CI approximations to be mixed together with little theoretical or programmatic effort.

Figure 6.5: A (6*e*, 6o) CASSCF computation of the triplet methylene molecule in the cc-pVDZ basis. The CI vector is optimized fully at every iteration and the orbitals are updated through the approximate Hessian of Eq. 6.93.

```
                             Energy             dE          dRMS
DF-MCSCF Iter  1:  -38.92805625506162   -7.064e-03   2.624e-03
DF-MCSCF Iter  2:  -38.94892541392244   -2.086e-02   5.120e-03
DF-MCSCF Iter  3:  -38.95815470936352   -9.229e-03   2.620e-03
DF-MCSCF Iter  4:  -38.95983274315701   -1.678e-03   1.198e-03
...
DF-MCSCF Iter 14:  -38.96050382683669   -3.068e-07   3.290e-05
DF-MCSCF Iter 15:  -38.96050397567139   -1.488e-07   2.283e-05
DF-MCSCF Iter 16:  -38.96050404789300   -7.222e-08   1.584e-05
```

The triplet methylene (CH_2) (C-H = 1.1Å, ∠ HCH = 133°) molecule in the cc-pVDZ basis with a (6*e*, 6o) active space (i.e., only the 1*s* orbital of the carbon atom is inactive) will be used in example calculations. To begin, let us solve Eq. 6.62 in a two-step fashion where the CI vector is optimized at every iteration followed by an orbital update using the approximate orbital Hessian: this is demonstrated in Fig. 6.5. We observe that the convergence is quite slow, especially in comparison to SCF.

To accelerate the convergence, DIIS can be used once again with error and state vectors

$$r_n = \boldsymbol{\kappa}_n \tag{6.96}$$

$$s_n = \boldsymbol{\kappa}_n + s_{n-1} \tag{6.97}$$

The resulting s_{n+1} is therefore a $\boldsymbol{\kappa}$ for the orbitals of the original reference state

$$\mathbf{C}_{n+1} = \mathbf{C}_0 e^{s_{n+1}} \tag{6.98}$$

It should be noted that when DIIS is applied in this way, the MCSCF wavefunction should be relatively converged to ensure that the assumption that κ is a reasonable approximation to the error vector, is valid. Therefore, the DIIS procedure is typically not started until several approximate MCSCF steps have been taken. The DIIS procedure is shown for triplet methylene in Fig. 6.6. Roughly the same convergence criteria can be accomplished in 9 steps as opposed to 16 steps without DIIS.

Figure 6.6: A (6*e*, 6o) CASSCF computation of the triplet methylene molecule in the cc-pVDZ basis. The CI vector is optimized fully at every iteration and the orbitals are updated through the approximate Hessian of Eq. 6.93 with DIIS extrapolation starting on iteration four.

```
                           Energy             dE          dRMS
DF-MCSCF Iter  1:  -38.92805625506162   -7.064e-03   2.624e-03
DF-MCSCF Iter  2:  -38.94892541392244   -2.086e-02   5.120e-03
DF-MCSCF Iter  3:  -38.95815470936358   -9.229e-03   2.620e-03
DF-MCSCF Iter  4:  -38.95983274315691   -1.678e-03   1.198e-03
DF-MCSCF Iter  5:  -38.96025602909073   -4.232e-04   7.596e-04 DIIS
DF-MCSCF Iter  6:  -38.96047551306498   -2.194e-04   4.533e-04 DIIS
DF-MCSCF Iter  7:  -38.96050334465582   -2.783e-05   1.093e-04 DIIS
DF-MCSCF Iter  8:  -38.96050406482120   -7.201e-07   4.357e-05 DIIS
DF-MCSCF Iter  9:  -38.96050411065154   -4.583e-08   1.927e-05 DIIS
```

The orbital-orbital part of the Hessian can be solved iteratively at every macroiteration and the results are shown in Fig. 6.7. As can be seen, this provides roughly the same convergence as using an approximate diagonal Hessian with DIIS acceleration. This can be understood as orbital-CI coupling blocks, while small, are not completely negligible and the small perturbation they provide is critical to obtain quadratic convergence. In some difficult cases solving the orbital-orbital block iteratively does accelerate convergence; however, in most examples a simple two-step method with orbital updates through an approximate Hessian performs equally well.

Figure 6.7: A (6*e*, 6o) CASSCF computation of the triplet methylene molecule in the cc-pVDZ basis. The CI vector is optimized fully at every iteration and the orbitals are updated through the approximate Hessian of Eq. 6.93 with DIIS extrapolation starting on iteration four. SOMCSCF represents solving the orbital-orbital update of Eq. 6.62, without the orbital-CI coupling block, iteratively.

```
                           Energy             dE          dRMS
DF-MCSCF Iter  1:  -38.92805625506168   -7.064e-03   2.624e-03
DF-MCSCF Iter  2:  -38.94892541392238   -2.086e-02   5.120e-03
DF-MCSCF Iter  3:  -38.95815470936356   -9.229e-03   2.620e-03
DF-MCSCF Iter  4:  -38.95983274315695   -1.678e-03   1.198e-03
DF-MCSCF Iter  5:  -38.96025602909057   -4.232e-04   7.596e-04 DIIS
DF-MCSCF Iter  6:  -38.96048414379979   -2.281e-04   3.482e-04 SOMCSCF
DF-MCSCF Iter  7:  -38.96050154195560   -1.739e-05   1.149e-04 SOMCSCF
DF-MCSCF Iter  8:  -38.96050372971953   -2.187e-06   4.095e-05 SOMCSCF
DF-MCSCF Iter  9:  -38.96050405645276   -3.267e-07   1.474e-05 SOMCSCF
DF-MCSCF Iter 10:  -38.96050410677239   -5.031e-08   5.615e-06 SOMCSCF
```

The PSI4 implementation of the one-step MCSCF procedure has not yet been completed and a one-step example will be given using the MOLPRO package.[146] It should be noted that MOLPRO does not have DF-MCSCF and thus conventional MCSCF was computed. Previous density-fitted MCSCF examples were shown, resulting in a small difference in the energy given by each programming package. However, the energies agree to within the convergence criterion when conventional MCSCF is requested of the PSI4 package. A one-step methylene convergence example is shown in Fig. 6.8 demonstrating the rapid convergence of full one-step methods. It should be noted that the MOLPRO package uses approximate updates in the microiterations, and any comparison of the number of iterations here is likely not valid. Instead, the point of Fig. 6.8 is simply to demonstrate that when the orbital-CI coupling blocks are included in the MCSCF Hessian, full quadratic convergence can be obtained.

Figure 6.8: A (6*e*, 6o) CASSCF computation of the triplet methylene molecule in the cc-pVDZ starting. Eq. 6.62 is solved at every macroiteration as implemented in the MOLPRO package and described by Knowles and coworkers.[1] The MOLPRO output has been reformatted to mimic the rest of this section, within printing limitations.

```
                    Energy         dE         dRMS
MCSCF Iter  1:  -38.92871989   -3.156e-02   2.769e-02
MCSCF Iter  2:  -38.96018877   -3.146e-02   1.000e-08 SOMCSCF
MCSCF Iter  3:  -38.96051679   -3.280e-04   0.000e-00 SOMCSCF
MCSCF Iter  4:  -38.96051679    0.000e-00   0.000e-00 SOMCSCF
```

6.5 Conclusions

The MCSCF Hessian and gradient formulas have been presented along with descriptions of how various approximations to the Hessian effect MCSCF convergence. A new MCSCF routine that is capable of computing both conventional and density-fitted MCSCF energies has been implemented in the PSI4 package. This new MCSCF routine makes heavy use of the highly optimized J and K builders inside PSI4 to reduce both the computational time and overall complexity.

Timings for the conventional and density-fitted approximate Hessian steps are shown in Figure 6.9. For conventional algorithms, the transformation scales like $\mathcal{O}(a\mathrm{N}^4)$ and the gradient like $\mathcal{O}(\mathrm{N}^4)$ and for density-fitted algorithms the transformation scales like $\mathcal{O}(a\mathrm{N}^2\mathrm{N}_{aux})$ and the gradient like $\mathcal{O}((i+a)\mathrm{N}^2\mathrm{N}_{aux})$. As can be seen, the density-fitted version is overall 4.6 times faster than the conventional version at 756 basis functions. In addition, the reduced scaling of the density-fitted J and Kbuilders can be seen after 400 basis functions as $(i+a)\ll\mathrm{N}$ in this regime. It should be noted that the density-fitted transformation is not yet optimal and further work is underway to reduce this cost. A paper detailing the cost

Figure 6.9: A comparison of the integral transformation and gradient build times for density-fitted (dashed lines) and conventional (solid lines) routines in the PSI4 package. An example benzene molecule was utilized with a (6*e*, 12o) active space resulting in 18 inactive orbitals. It should be noted that as the basis set is increased, the only change is in the number of virtual orbitals. Each computation was run on four AMD Opteron cores.

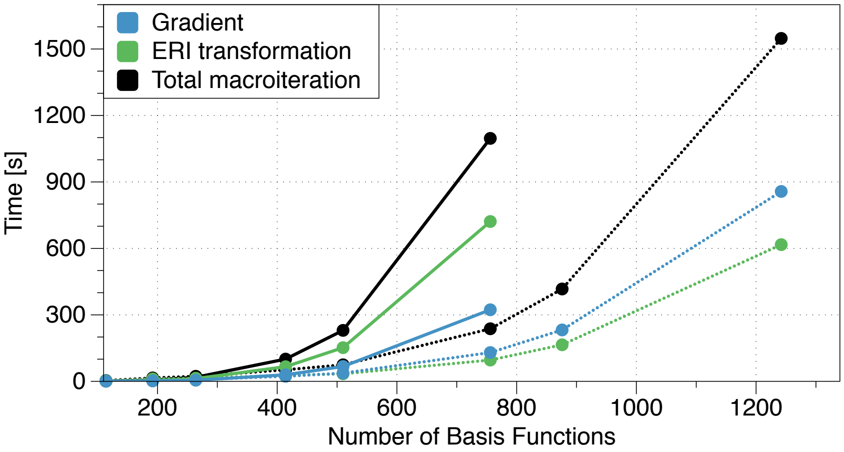

and benefits of one and two step MCSCF along with either density-fitted or conventional two-electron integrals is currently planned and will be forthcoming.

Chapter 7

Multi-Reference Symmetry-Adapted Perturbation Theory

Many of the molecules under consideration fall under the single-reference category and can be computed using conventional single-reference methods as detailed in Chapters 1-5. However, there are many molecules of interest that do not fall into this category and require multireference approaches. For example, in atmospheric chemistry the singlet oxygen molecule, OH radical, and NO radical all have a fair amount of multireference character making conventional computations unsuitable.[147–150] In addition, our group is interested in CO_2 sequestration for which metal-organic frameworks (MOFs) have been suggested due to their excellent CO_2 adsorption capabilities.[151,152] The metal centers of the MOFs make them inherently multireference in nature. Therefore, in this Chapter we will describe preliminary work into extending the SAPT methodology to systems described by CASSCF reference wavefunctions. It is not yet verified if these equations are valid for general MCSCF wavefunctions.

7.1 MRSAPT notation

We will first start with the 4-index intermolecular operator $\tilde{v}$ which is fundamental to all terms in SAPT theory

$$\tilde{v}_{pr}^{qs} = g_{pqrs} + (v_A)_{rs} S_{pq}/N_A + (v_B)_{pq} S_{rs}/N_B + V_0 S_{pq} S_{rs}/N_A N_B \tag{7.1}$$

where S are the standard overlap integrals, $(v_X)_{pq}$ is the one-electron potential integral of monomer X, V_0 the constant nuclear repulsion term, and N_X is the number of electrons in monomer X. In addition, we will use the γ^{Xs} and Γ^{Xs} density matrices where X again represents the monomer and s represents the spin. When s is not present, this will denote the spin summed density matrix.

Previously, when multiple indices of the same type were used, subsequent letters of the alphabet denoted separate indices, i.e., S_{ij}. For SAPT theory, we will utilize subsequent letters to denote monomers and the $'$ symbol to denote multiple indices of the same type, i.e., $S_{ii'}$. Therefore, indices i, t, and a will denote indices of monomer A and j, u, and b will denote indices on monomer B.

7.2 Electrostatics and Exchange

We will begin with first order electrostatics and exchange as they can be computed entirely from the ground state and will be among the simplest terms considered here. The first order electrostatic term can be written as follows

$$E^{(10)}_{\text{elst}} = \langle V \rangle = 4\tilde{v}^{ij}_{ij} + 2\gamma^{A}_{t't}\tilde{v}^{tj}_{t'j} + 2\gamma^{B}_{u'u}\tilde{v}^{iu}_{iu'} + \gamma^{A}_{t't}\gamma^{B}_{u'u}\tilde{v}^{tu}_{t'u'} \tag{7.2}$$

The benefits of writing the formula in this way are multiple. First, we gain insight by breaking down the $E^{(10)}_{\text{elst}}$ energy and partitioning this energy into the inactive–inactive, active A–inactive B, inactive A–active B, and active–active electrostatics. In addition, this is currently the most general SAPT formula available and can describe interactions between SCF-SCF, SCF-CASSCF, and CASSCF-CASSCF wavefunctions where, if any t or u index is zero, the term simply vanishes. Finally, if we again assume that the active space is relatively small compared to the size of the inactive space, this partitioning allows us to use current SAPT routines to compute the $\tilde{v}^{ij}_{ij}$ term very efficiently and any terms containing two or more active indices will deal with relatively small tensors and be amenable to naive implementations.

The $E^{(10)}_{\text{exch}}$ correction in the single exchange approximation can be formulated in a similar manner and is shown below:

$$E^{(10)}_{\text{exch}} = \langle VP \rangle - \langle V \rangle \langle P \rangle \tag{7.3}$$

$$\langle P \rangle = -2S_{ij}S_{ij} - \gamma^{A}_{t't}S_{jt'}S_{jt} - \gamma^{B}_{u'u}S_{iu'}S_{iu} - \gamma^{A\alpha}_{t't}\gamma^{B\alpha}_{u'u}S_{tu'}S_{t'u} - \gamma^{A\beta}_{t't}\gamma^{B\beta}_{u'u}S_{tu'}S_{t'u} \tag{7.4}$$

$$\begin{aligned}
\langle VP \rangle = {} & -4.0\tilde{\upsilon}^{i'i}_{i'j}S_{ij} - 8\tilde{\upsilon}^{i'j'}_{i'j'}S_{ij}S_{ij} + 4\tilde{\upsilon}^{i'j}_{i'j'}S_{ij}S_{ij'} + 2\tilde{\upsilon}^{ii}_{i'j}S_{i'j} + 4\tilde{\upsilon}^{ij'}_{i'j'}S_{i'j}S_{ij} \\
& - 2\tilde{\upsilon}^{ij}_{i'j'}S_{i'j}S_{ij'} - 2\tilde{\upsilon}^{ii}_{jj} - 4\tilde{\upsilon}^{ij'}_{jj'}S_{ij} + 2\tilde{\upsilon}^{ij}_{jj'}S_{ij'} - 2\gamma^{B}_{uu'}\tilde{\upsilon}^{i'i}_{i'u'}S_{iu} \\
& - 4\gamma^{B}_{uu'}\tilde{\upsilon}^{i'j}_{i'j}S_{iu}S_{iu'} + 2\gamma^{B}_{uu'}\tilde{\upsilon}^{i'j}_{i'u'}S_{ij}S_{iu} + 2\gamma^{B}_{uu'}\tilde{\upsilon}^{i'j}_{i'u}S_{ij}S_{iu'} - 4\gamma^{B}_{uu'}\tilde{\upsilon}^{i'u}_{i'u'}S_{ij}S_{ij} \\
& + \gamma^{B}_{uu'}\tilde{\upsilon}^{ii}_{i'u'}S_{i'u} + 2\gamma^{B}_{uu'}\tilde{\upsilon}^{ij}_{i'j}S_{i'u}S_{iu'} - \gamma^{B}_{uu'}\tilde{\upsilon}^{ij}_{i'u'}S_{i'u}S_{ij} - \gamma^{B}_{uu'}\tilde{\upsilon}^{ij}_{i'u}S_{i'j}S_{iu'} \\
& + 2\gamma^{B}_{uu'}\tilde{\upsilon}^{iu}_{i'u'}S_{i'j}S_{ij} + \gamma^{B}_{uu'}\tilde{\upsilon}^{ij}_{ju}S_{iu'} - 2\gamma^{B}_{uu'}\tilde{\upsilon}^{iu}_{ju'}S_{ij} - \gamma^{B}_{uu'}\tilde{\upsilon}^{ii}_{uu'} - 2\gamma^{B}_{uu'}\tilde{\upsilon}^{ij}_{uj}S_{iu'} \\
& + \gamma^{B}_{uu'}\tilde{\upsilon}^{ij}_{uu'}S_{ij} - 2\Gamma^{B}_{uu'u''u'''}\tilde{\upsilon}^{i'u}_{i'u'}S_{iu''}S_{iu'''} + \Gamma^{B}_{uu'u''u'''}\tilde{\upsilon}^{iu}_{i'u'}S_{i'u''}S_{iu'''} \\
& - \Gamma^{B}_{uu'u''u'''}\tilde{\upsilon}^{iu}_{u''u'}S_{iu'''} - 4\gamma^{A\alpha}_{tt'}\gamma^{B\alpha}_{uu'}\tilde{\upsilon}^{ij}_{ij}S_{t'u}S_{tu'} + 2\gamma^{A\alpha}_{tt'}\gamma^{B\alpha}_{uu'}\tilde{\upsilon}^{ij}_{iu'}S_{t'u}S_{tj} \\
& + 2\gamma^{A\alpha}_{tt'}\gamma^{B\alpha}_{uu'}\tilde{\upsilon}^{ij}_{iu}S_{t'j}S_{tu'} - 2\gamma^{A\alpha}_{tt'}\gamma^{B\alpha}_{uu'}\tilde{\upsilon}^{it}_{iu'}S_{t'u} + 2\gamma^{A\alpha}_{tt'}\gamma^{B\alpha}_{uu'}\tilde{\upsilon}^{ij}_{t'j}S_{iu}S_{tu'} \\
& - \gamma^{A\alpha}_{tt'}\gamma^{B\alpha}_{uu'}\tilde{\upsilon}^{ij}_{t'u'}S_{iu}S_{tj} - \gamma^{A\alpha}_{tt'}\gamma^{B\alpha}_{uu'}\tilde{\upsilon}^{ij}_{t'u}S_{ij}S_{tu'} + \gamma^{A\alpha}_{tt'}\gamma^{B\alpha}_{uu'}\tilde{\upsilon}^{it}_{t'u'}S_{iu} \\
& + \gamma^{A\alpha}_{tt'}\gamma^{B\alpha}_{uu'}\tilde{\upsilon}^{ii}_{tu'}S_{t'u} + 2\gamma^{A\alpha}_{tt'}\gamma^{B\alpha}_{uu'}\tilde{\upsilon}^{ij}_{tj}S_{iu'}S_{t'u} - \gamma^{A\alpha}_{tt'}\gamma^{B\alpha}_{uu'}\tilde{\upsilon}^{ij}_{tu'}S_{ij}S_{t'u} \\
& - \gamma^{A\alpha}_{tt'}\gamma^{B\alpha}_{uu'}\tilde{\upsilon}^{ij}_{tu}S_{iu'}S_{t'j} + \gamma^{A\alpha}_{tt'}\gamma^{B\alpha}_{uu'}\tilde{\upsilon}^{jj}_{t'u}S_{tu'} - 2\gamma^{A\alpha}_{tt'}\gamma^{B\alpha}_{uu'}\tilde{\upsilon}^{t'j}_{uj}S_{tu'} \\
& + \gamma^{A\alpha}_{tt'}\gamma^{B\alpha}_{uu'}\tilde{\upsilon}^{t'j}_{uu'}S_{tj} - \gamma^{A\alpha}_{tt'}\gamma^{B\alpha}_{uu'}\tilde{\upsilon}^{t't}_{uu'} - 2\gamma^{A\alpha}_{tt'}\Gamma^{B\alpha\alpha+\beta\alpha}_{uu'u''u'''}\tilde{\upsilon}^{iu}_{iu'}S_{t'u''}S_{tu'''} \\
& + \gamma^{A\alpha}_{tt'}\Gamma^{B\alpha\alpha+\beta\alpha}_{uu'u''u'''}\tilde{\upsilon}^{iu}_{t'u'}S_{iu''}S_{tu'''} + \gamma^{A\alpha}_{tt'}\Gamma^{B\alpha\alpha+\beta\alpha}_{uu'u''u'''}\tilde{\upsilon}^{iu}_{tu'}S_{iu'''}S_{t'u''} \\
& - \gamma^{A\alpha}_{tt'}\Gamma^{B\alpha\alpha+\beta\alpha}_{uu'u''u'''}\tilde{\upsilon}^{t'u}_{u''u'}S_{tu'''} - 4\gamma^{A\beta}_{tt'}\gamma^{B\beta}_{uu'}\tilde{\upsilon}^{ij}_{ij}S_{t'u}S_{tu'} \\
& + 2\gamma^{A\beta}_{tt'}\gamma^{B\beta}_{uu'}\tilde{\upsilon}^{ij}_{iu'}S_{t'u}S_{tj} + 2\gamma^{A\beta}_{tt'}\gamma^{B\beta}_{uu'}\tilde{\upsilon}^{ij}_{iu}S_{t'j}S_{tu'} - 2\gamma^{A\beta}_{tt'}\gamma^{B\beta}_{uu'}\tilde{\upsilon}^{it}_{iu'}S_{t'u} \\
& + 2\gamma^{A\beta}_{tt'}\gamma^{B\beta}_{uu'}\tilde{\upsilon}^{ij}_{t'j}S_{iu}S_{tu'} - \gamma^{A\beta}_{tt'}\gamma^{B\beta}_{uu'}\tilde{\upsilon}^{ij}_{t'u'}S_{iu}S_{tj} - \gamma^{A\beta}_{tt'}\gamma^{B\beta}_{uu'}\tilde{\upsilon}^{ij}_{t'u}S_{ij}S_{tu'} \\
& + \gamma^{A\beta}_{tt'}\gamma^{B\beta}_{uu'}\tilde{\upsilon}^{it}_{t'u'}S_{iu} + \gamma^{A\beta}_{tt'}\gamma^{B\beta}_{uu'}\tilde{\upsilon}^{ii}_{tu'}S_{t'u} + 2\gamma^{A\beta}_{tt'}\gamma^{B\beta}_{uu'}\tilde{\upsilon}^{ij}_{tj}S_{iu'}S_{t'u}
\end{aligned}$$

$$
\begin{aligned}
&- \gamma^{A\beta}_{tt'}\gamma^{B\beta}_{uu'}\tilde{\upsilon}^{ij}_{tu'}S_{ij}S_{t'u} - \gamma^{A\beta}_{tt'}\gamma^{B\beta}_{uu'}\tilde{\upsilon}^{ij}_{tu}S_{iu'}S_{t'j} + \gamma^{A\beta}_{tt'}\gamma^{B\beta}_{uu'}\tilde{\upsilon}^{jj}_{t'u}S_{tu'} \\
&- 2\gamma^{A\beta}_{tt'}\gamma^{B\beta}_{uu'}\tilde{\upsilon}^{t'j}_{uj}S_{tu'} + \gamma^{A\beta}_{tt'}\gamma^{B\beta}_{uu'}\tilde{\upsilon}^{t'j}_{uu'}S_{tj} - \gamma^{A\beta}_{tt'}\gamma^{B\beta}_{uu'}\tilde{\upsilon}^{t't}_{uu'} \\
&- 2\gamma^{A\beta}_{tt'}\Gamma^{B\alpha\beta+\beta\beta}_{uu'u''u'''}\tilde{\upsilon}^{iu}_{iu'}S_{t'u''}S_{tu'''} + \gamma^{A\beta}_{tt'}\Gamma^{B\alpha\beta+\beta\beta}_{uu'u''u'''}\tilde{\upsilon}^{iu}_{t'u'}S_{iu''}S_{tu'''} \\
&+ \gamma^{A\beta}_{tt'}\Gamma^{B\alpha\beta+\beta\beta}_{uu'u''u'''}\tilde{\upsilon}^{iu}_{tu'}S_{iu'''}S_{t'u''} - \gamma^{A\beta}_{tt'}\Gamma^{B\alpha\beta+\beta\beta}_{uu'u''u'''}\tilde{\upsilon}^{t'u}_{u''u'}S_{tu'''} \\
&- 4\gamma^{A}_{tt'}\tilde{\upsilon}^{ij'}_{ij'}S_{t'j}S_{tj} + 2\gamma^{A}_{tt'}\tilde{\upsilon}^{ij}_{ij'}S_{t'j}S_{tj'} - 2\gamma^{A}_{tt'}\tilde{\upsilon}^{ij}_{it}S_{t'j} \\
&+ 2\gamma^{A}_{tt'}\tilde{\upsilon}^{ij'}_{t'j'}S_{ij}S_{tj} - \gamma^{A}_{tt'}\tilde{\upsilon}^{ij}_{t'j'}S_{ij}S_{tj'} + \gamma^{A}_{tt'}\tilde{\upsilon}^{ij}_{t't}S_{ij} \\
&+ \gamma^{A}_{tt'}\tilde{\upsilon}^{ii}_{tj}S_{t'j} + 2\gamma^{A}_{tt'}\tilde{\upsilon}^{ij'}_{tj'}S_{ij}S_{t'j} - \gamma^{A}_{tt'}\tilde{\upsilon}^{ij}_{tj'}S_{ij'}S_{t'j} \\
&- 2\gamma^{A}_{tt'}\tilde{\upsilon}^{jj'}_{t'j'}S_{tj} + \gamma^{A}_{tt'}\tilde{\upsilon}^{jj}_{t'j'}S_{tj'} - \gamma^{A}_{tt'}\tilde{\upsilon}^{jj}_{t't} \\
&- 2\gamma^{A}_{tt'}\tilde{\upsilon}^{ti}_{t'j}S_{ij} - 4\gamma^{A}_{tt'}\tilde{\upsilon}^{tj'}_{t'j'}S_{ij}S_{ij} + 2\gamma^{A}_{tt'}\tilde{\upsilon}^{tj}_{t'j'}S_{ij}S_{ij'} \\
&- 2\gamma^{A}_{tt'}\gamma^{B}_{uu'}\tilde{\upsilon}^{iu}_{iu'}S_{t'j}S_{tj} + \gamma^{A}_{tt'}\gamma^{B}_{uu'}\tilde{\upsilon}^{iu}_{t'u'}S_{ij}S_{tj} + \gamma^{A}_{tt'}\gamma^{B}_{uu'}\tilde{\upsilon}^{iu}_{tu'}S_{ij}S_{t'j} \\
&- \gamma^{A}_{tt'}\gamma^{B}_{uu'}\tilde{\upsilon}^{ju}_{t'u'}S_{tj} - \gamma^{A}_{tt'}\gamma^{B}_{uu'}\tilde{\upsilon}^{ti}_{t'u'}S_{iu} - 2\gamma^{A}_{tt'}\gamma^{B}_{uu'}\tilde{\upsilon}^{tj}_{t'j}S_{iu}S_{iu'} \\
&+ \gamma^{A}_{tt'}\gamma^{B}_{uu'}\tilde{\upsilon}^{tj}_{t'u'}S_{ij}S_{iu} + \gamma^{A}_{tt'}\gamma^{B}_{uu'}\tilde{\upsilon}^{tj}_{t'u}S_{ij}S_{iu'} - 2\gamma^{A}_{tt'}\gamma^{B}_{uu'}\tilde{\upsilon}^{tu}_{t'u'}S_{ij}S_{ij} \\
&- \gamma^{A}_{tt'}\Gamma^{B}_{uu'u''u'''}\tilde{\upsilon}^{tu}_{t'u'}S_{iu''}S_{iu'''} - 2\Gamma^{A\alpha\alpha+\beta\alpha}_{tt't''t'''}\gamma^{B\alpha}_{uu'}\tilde{\upsilon}^{tj}_{t'j}S_{t'''u}S_{t''u'} \\
&+ \Gamma^{A\alpha\alpha+\beta\alpha}_{tt't''t'''}\gamma^{B\alpha}_{uu'}\tilde{\upsilon}^{tj}_{t'u'}S_{t'''u}S_{t''j} + \Gamma^{A\alpha\alpha+\beta\alpha}_{tt't''t'''}\gamma^{B\alpha}_{uu'}\tilde{\upsilon}^{tj}_{t'u}S_{t'''j}S_{t''u'} \\
&- \Gamma^{A\alpha\alpha+\beta\alpha}_{tt't''t'''}\gamma^{B\alpha}_{uu'}\tilde{\upsilon}^{tt''}_{t'u'}S_{t'''u} - \Gamma^{A\alpha\alpha+\beta\alpha}_{tt't''t'''}\Gamma^{B\alpha\alpha+\beta\alpha}_{uu'u''u'''}\tilde{\upsilon}^{tu}_{t'u'}S_{t'''u''}S_{t''u'''} \\
&- 2\Gamma^{A\alpha\beta+\beta\beta}_{tt't''t'''}\gamma^{B\beta}_{uu'}\tilde{\upsilon}^{tj}_{t'j}S_{t'''u}S_{t''u'} + \Gamma^{A\alpha\beta+\beta\beta}_{tt't''t'''}\gamma^{B\beta}_{uu'}\tilde{\upsilon}^{tj}_{t'u'}S_{t'''u}S_{t''j} \\
&+ \Gamma^{A\alpha\beta+\beta\beta}_{tt't''t'''}\gamma^{B\beta}_{uu'}\tilde{\upsilon}^{tj}_{t'u}S_{t'''j}S_{t''u'} - \Gamma^{A\alpha\beta+\beta\beta}_{tt't''t'''}\gamma^{B\beta}_{uu'}\tilde{\upsilon}^{tt''}_{t'u'}S_{t'''u} \\
&- \Gamma^{A\alpha\beta+\beta\beta}_{tt't''t'''}\Gamma^{B\alpha\beta+\beta\beta}_{uu'u''u'''}\tilde{\upsilon}^{tu}_{t'u'}S_{t'''u''}S_{t''u'''} - 2\Gamma^{A}_{tt't''t'''}\tilde{\upsilon}^{tj'}_{t'j'}S_{t'''j}S_{t''j} \\
&+ \Gamma^{A}_{tt't''t'''}\tilde{\upsilon}^{tj}_{t'j'}S_{t'''j}S_{t''j'} - \Gamma^{A}_{tt't''t'''}\tilde{\upsilon}^{tj}_{t't''}S_{t'''j} - \Gamma^{A}_{tt't''t'''}\gamma^{B}_{uu'}\tilde{\upsilon}^{tu}_{t'u'}S_{t'''j}S_{t''j}
\end{aligned}
\tag{7.5}
$$

We observe that while the number of diagrams in this term is quite large, the vast majority contain one or more active indices again indicating that naive implementations can be utilized. Therefore, much of $E^{(10)}_{\text{exch}}$ can be implemented with automatic code generation techniques with little loss in performance. It should be noted that this particular form requires all unpaired electrons to have the same spin, in other words, only the high-spin state of the dimer can be recovered. We have recently derived the $E^{(10)}_{\text{exch}}$ correction in the single exchange approximation for arbitrary dimer spin-states between restricted open-shell HF (ROHF) based wavefunctions and work is underway to extend this to CASSCF based wavefunctions.

7.3 Induction and Dispersion

Second-order induction and dispersion, unlike electrostatics and exchange, cannot be computed from the ground-state wavefunction. Instead, we will use the response-function method of computing the second-order dispersion and induction energy which is given by the generalized Casimir-Polder formula[153]

$$E^{(2)}_{disp} = -\frac{1}{2\pi}\int_0^\infty \int\int\int\int \alpha^A(\mathbf{r}_1,\mathbf{r}_2|i\omega)\alpha^B(\mathbf{r}_3,\mathbf{r}_4|i\omega)\frac{1}{r_{13}}\frac{1}{r_{24}}d\mathbf{r}_1 d\mathbf{r}_2 d\mathbf{r}_3 d\mathbf{r}_4 d\omega \tag{7.6}$$

where $\alpha^X(\mathbf{r}_1,\mathbf{r}_2|\omega)$ are the frequency dependent density susceptibilities (FDDS) of monomer X, at a given frequency ω. This approach has been quite successful in computing the $E^{(2)}_{disp}$ energy between monomers described by SCF, DFT, RPA, and CC wavefunctions.[154–157]

The FDDSs are density-density response functions:

$$\alpha^X(\mathbf{r}_1,\mathbf{r}_2|\omega) = \langle\langle\hat{\rho}(\mathbf{r}_1);\hat{\rho}(\mathbf{r}_2)\rangle\rangle_\omega \tag{7.7}$$

Where $\hat{\rho}(\mathbf{r})$ is our electron-density operator:

$$\hat{\rho}(\mathbf{r}) = \phi_p\phi_q\hat{E}_{pq} \tag{7.8}$$

and ϕ_p is our set of orthonormal orbitals. We can now expand the FDDS in terms of an orbital basis:

$$\alpha^X(\mathbf{r}_1,\mathbf{r}_2|\omega) = \Pi^{pr}_{qs}(\omega)\phi_p(\mathbf{r}_1)\phi_q(\mathbf{r}_1)\phi_r(\mathbf{r}_2)\phi_s(\mathbf{r}_2) \tag{7.9}$$

Thus, $E^{(2)}_{disp}$ in the orbital basis is

$$E^{(2)}_{disp} = -\frac{1}{2\pi} g_{klmn} g_{k'l'm'n'} \int_0^\infty \Pi^{kk'}_{ll'}(i\omega)\Pi^{mm'}_{nn'}(i\omega)\mathrm{d}\omega \tag{7.10}$$

where k and l are general indices on monomer A and m and n are general indices on monomer B. Only combinations of k and l (m and n) that need to be considered are the non-redundant pairs.

Returning our focus to the computation of FDDS's, we will employ the general perturbation notation A and B instead of the $\hat{E}$ operators:

$$\langle\langle A; B\rangle\rangle_\omega = \langle\langle \hat{E}_{pq}; \hat{E}_{rs}\rangle\rangle_\omega \tag{7.11}$$

To begin, we first need to solve the MCSCF linear equations[158, 159]

$$(\mathbf{E}^{[2]} - \omega\mathbf{S}^{[2]})\boldsymbol{\beta}^B = \mathbf{V}^{[1]}_B \tag{7.12}$$

where $\mathbf{E}^{[2]}$ is the electronic Hessian, $\mathbf{S}^{[2]}$ is the metric matrix, $\boldsymbol{\beta}^B$ collects the CI and orbital rotation vectors

$$\boldsymbol{\beta}^B = \begin{pmatrix} \mathbf{c}^B \\ \boldsymbol{\kappa}^B \\ \mathbf{c}^{-B^*} \\ \boldsymbol{\kappa}^{-B^*} \end{pmatrix} \tag{7.13}$$

and $\mathbf{V}_B^{[1]}$ is our perturbation which, in the case of $B = \hat{E}_{pq}$,

$$\mathbf{V}_{\hat{E}_{pq}}^{[1]} = \begin{pmatrix} -\boldsymbol{\gamma} \\ \mathbf{d} \\ -\boldsymbol{\gamma}^\dagger \\ \mathbf{d}^\dagger \end{pmatrix} \tag{7.14}$$

$$d_{rs} = \delta_{ps}\gamma_{rq} - \delta_{rq}\gamma_{ps} \tag{7.15}$$

$$\gamma_i = \langle 0|\hat{E}_{pq}|i\rangle \tag{7.16}$$

where for d_{rs} the rs pair is again limited to non-redundant rotations. It should be noted that the presence of the complex conjugate (*) and conjugate transpose (†) are required to ensure the time-dependent equations are symmetric.[158] In direct response to this, the electronic Hessian of Chapter 6 is only a part of the electronic Hessian presented here, full equations can be found in Ref. 158. To remove the difficultly of working with complex values, the MCSCF linear equations can be reformulated as a pair of linear equations that contain no complex components.[160]

The term $\langle\langle A; B\rangle\rangle_\omega$ can then be computed as

$$\langle\langle A; B\rangle\rangle_\omega = -i\beta_\omega^{-B^\dagger}\mathbf{V}_A^{[1]} \tag{7.17}$$

The final MCSCF FDDSs can then be computed as

$$\Pi_{ll'}^{kk'}(\omega) = \langle\langle \hat{E}_{kl}; \hat{E}_{k'l'}\rangle\rangle_\omega = -i\beta_\omega^{-\hat{E}_{kl}^\dagger}\mathbf{V}_{\hat{E}_{k'l'}}^{[1]} \tag{7.18}$$

The ω range is normally integrated over by transforming the range $\omega \in [0, \infty]$ to $t \in [-1, 1]$ by

$$\omega = 0.3\frac{t-1}{t+1} \tag{7.19}$$

followed by an n-point Gauss-Legendre quadrature.

As can be seen, the formulas themselves are quite straightforward and the majority of quantities involved can be computed as described in Chapter 6. However, the number of linear equations to be solved is equal to the number of non-redundant orbital rotations which can be quite large.

The $E^{(2)}_{ind}$ energy in this formalism can be computed as follows:[34]

$$E^{(2),B\to A}_{ind} = -\frac{1}{2}(\omega_B)^k_l(\omega_B)^{k'}_{l'}\Pi^{kk'}_{ll'}(0) \tag{7.20}$$

where $(\omega_B)^k_l$ is the unperturbed electrostatic potential of monomer B. The total $E^{(2)}_{ind}$ correction can be computed as $E^{(2),B\to A}_{ind} + E^{(2),A\to B}_{ind}$.

7.4 Conclusions

A general formula for the $E^{(10)}_{\text{exch}}$ and $E^{(10)}_{\text{elst}}$ energies between two CASSCF wavefunctions has been presented. In addition, the expressions for $E^{(20)}_{\text{disp}}$ and $E^{(20)}_{\text{ind}}$ have been formulated, but not fully derived. Work on the derivation and implementation of these formulas is currently in progress.

Bibliography

[1] H.-J. Werner and P. J. Knowles, J. Chem. Phys. **82**, 5053 (1985).

[2] R. M. Parrish, T. M. Parker, and C. D. Sherrill, J. Chem. Theory Comput. **10**, 4417 (2014).

[3] D. L. Mobley, A. P. Graves, J. D. Chodera, A. C. McReynolds, B. K. Shoichet, and K. A. Dill, Journal of Molecular Biology **371**, 1118 (2007).

[4] J. C. Faver, M. L. Benson, X. He, B. P. Roberts, B. Wang, M. S. Marshall, M. R. Kennedy, C. D. Sherrill, and K. M. Merz Jr., J. Chem. Theory Comput. **7**, 790 (2011).

[5] F. Paesani and G. A. Voth, J. Phys. Chem. B **113**, 5702 (2009).

[6] A. Aguado and M. F. Jarrold, Annu. Rev. Phys. Chem. **62**, 151 (2011).

[7] L.-P. Wang, A. Titov, R. McGibbon, F. Liu, V. S. Pande, and T. J. Martínez, Nature Chemistry **6**, 1 (2014).

[8] D. Townsend, S. A. Lahankar, S. K. Lee, S. D. Chambreau, A. G. Suits, X. Zhang, J. Rheinecker, L. B. Harding, and J. M. Bowman, Science **306**, 1158 (2004).

[9] F. Nattino, H. Ueta, H. Chadwick, M. E. van Reijzen, R. D. Beck, B. Jackson, M. C. van Hemert, and G.-J. Kroes, J. Phys. Chem. Lett. **5**, 1294 (2014).

[10] D. G. A. Smith, K. Patkowski, D. Trinh, N. Balakrishnan, T.-G. Lee, R. C. Forrey, B. H. Yang, and P. C. Stancil, J. Phys. Chem. A **118**, 6351 (2014).

[11] S. Quaglioni and P. Navrátil, Phys. Rev. Lett. **101**, 092501 (2008).

[12] D. A. Britz and A. N. Khlobystov, Chem. Soc. Rev. **35**, 637 (2006).

[13] J. Kong, N. R. Franklin, C. W. Zhou, M. G. Chapline, S. Peng, K. J. Cho, and H. J. Dai, Science **287**, 622 (2000).

[14] S. Yang, L. Ouyang, J. M. Phillips, and W. Y. Ching, Phys. Rev. B **73**, 165407 (2006).

[15] L. Huang, L. Zhang, Q. Shao, L. Lu, X. Lu, S. Jiang, and W. Shen, J. Phys. Chem. C **111**, 11912 (2007).

[16] D. R. Kauffman and A. Star, Angew. Chem. Int. Ed. **47**, 6550 (2008).

[17] A. G. Albesa, E. A. Fertitta, and J. L. Vicente, Langmuir **26**, 786 (2010).

[18] E. Voloshina, D. Usvyat, M. Schütz, Y. Dedkov, and B. Paulus, Phys. Chem. Chem. Phys. **13**, 12041 (2011).

[19] Y. Y. Liu and J. Wilcox, Environ. Sci. Technol. **45**, 809 (2011).

[20] S. Zöttl, A. Kaiser, P. Bartl, C. Leidlmair, A. Mauracher, M. Probst, S. Denifl, O. Echt, and P. Scheier, J. Phys. Chem. Lett. **3**, 2598 (2012).

[21] P. Lazar, F. Karlický, P. Jurečka, M. Kocman, E. Otyepková, K. Šafářová, and M. Otyepka, J. Am. Chem. Soc. **135**, 6372 (2013).

[22] D. Cao, X. Zhang, J. Chen, W. Wang, and J. Yun, J. Phys. Chem. B **107**, 13286 (2003).

[23] T. Duren, L. Sarkisov, O. M. Yaghi, and R. Q. Snurr, Langmuir **20**, 2683 (2004).

[24] X. Hu, Z. Zhou, Q. Lin, Y. Wu, and Z. Zhang, Chem. Phys. Lett. **503**, 287 (2011).

[25] D. S. Su, S. Perathoner, and G. Centi, Chem. Rev. **113**, 5782 (2013).

[26] C. Lu, H. Bai, B. Wu, F. Su, and J. F. Hwang, Energy Fuels **22**, 3050 (2008).

[27] A. Samanta, A. Zhao, G. K. H. Shimizu, P. Sarkar, and R. Gupta, Ind. Eng. Chem. Res. **51**, 1438 (2012).

[28] P. Kowalczyk, S. Furmaniak, P. A. Gauden, and A. P. Terzyk, J. Phys. Chem. C **114**, 21465 (2010).

[29] G. P. Lithoxoos, A. Labropoulos, L. D. Peristeras, N. Kanellopoulos, J. Samios, and I. G. Economou, J. Supercrit. Fluid. **55**, 510 (2010).

[30] M. Rahimi, J. K. Singh, D. J. Babu, J. J. Schneider, and F. Müller-Plathe, J. Phys. Chem. C **117**, 13492 (2013).

[31] B. J. Bucior, D.-L. Chen, J. Liu, and J. K. Johnson, J. Phys. Chem. C **116**, 25904 (2012).

[32] H. Liu, V. R. Cooper, S. Dai, and D. Jiang, J. Phys. Chem. Lett. **3**, 3343 (2012).

[33] P. Kowalczyk, Phys. Chem. Chem. Phys. **14**, 2784 (2012).

[34] B. Jeziorski, R. Moszynski, and K. Szalewicz, Chem. Rev. **94**, 1887 (1994).

[35] P. Jurečka, J. Šponer, J. Černý, and P. Hobza, Phys. Chem. Chem. Phys. **8**, 1985 (2006).

[36] K. Raghavachari, G. W. Trucks, J. A. Pople, and M. Head-Gordon, Chem. Phys. Lett. **157**, 479 (1989).

[37] T. M. Parker, L. A. Burns, R. M. Parrish, A. G. Ryno, and C. D. Sherrill, J. Chem. Phys. **140**, 094106 (2014).

[38] J. Paldus, J. Chem. Phys. **61**, 5321 (1974).

[39] C. Eckart, Phys. Rev. **28**, 711 (1926).

[40] J. Olsen, B. O. Roos, P. Jørgensen, and H. J. A. Jensen, J. Chem. Phys. **89**, 2185 (1988).

[41] A. Szabo and N. S. Ostlund, *Modern Quantum Chemistry*, Introduction to Advanced Electronic Structure Theory. Courier Corporation, 1996.

[42] D. G. A. Smith, P. Jankowski, M. Slawik, H. A. Witek, and K. Patkowski, J. Chem. Theory Comput. **10**, 3140 (2014).

[43] L. Šimová, J. Řezáč, and P. Hobza, J. Chem. Theory Comput. **9**, 3420 (2013).

[44] J. Řezáč, L. Šimová, and P. Hobza, J. Chem. Theory Comput. **9**, 364 (2013).

[45] G. S. Tschumper, M. L. Leininger, B. C. Hoffman, E. F. Valeev, H. F. Schaefer, and M. Quack, J. Chem. Phys. **116**, 690 (2002).

[46] C. D. Sherrill, T. Takatani, and E. G. Hohenstein, J. Phys. Chem. A **113**, 10146 (2009).

[47] K. E. Riley, M. Pitoňák, P. Jurečka, and P. Hobza, Chem. Rev. **110**, 5023 (2010).

[48] D. G. A. Smith and K. Patkowski, J. Chem. Theory Comput. **9**, 370 (2013).

[49] S. Grimme, J. Chem. Phys. **118**, 9095 (2003).

[50] J. G. Hill and J. A. Platts, J. Chem. Theory Comput. **3**, 80 (2007).

[51] R. A. DiStasio Jr. and M. Head-Gordon, Mol. Phys. **105**, 1073 (2007).

[52] L. A. Burns, M. S. Marshall, and C. D. Sherrill, J. Chem. Phys. **141**, 234111 (2014).

[53] E. G. Hohenstein and C. D. Sherrill, WIREs Comput. Mol. Sci. **2**, 304 (2011).

[54] J. P. Perdew and K. Schmidt, AIP Conference Proceedings **577**, 1 (2001).

[55] Y. Zhao, N. E. Schultz, and D. G. Truhlar, J. Chem. Theory Comput. **2**, 364 (2006).

[56] J.-D. Chai and M. Head-Gordon, Phys. Chem. Chem. Phys. **10**, 6615 (2008).

[57] Y. Zhao and D. G. Truhlar, Theor. Chem. Acc. **120**, 215 (2008).

[58] N. Mardirossian and M. Head-Gordon, J. Chem. Phys. **140**, 18A527 (2014).

[59] A. D. Becke, Phys. Rev. A **38**, 3098 (1988).

[60] C. Lee, W. Yang, and R. G. Parr, Phys. Rev. B **37**, 785 (1988).

[61] A. D. Becke, J. Chem. Phys. **98**, 5648 (1993).

[62] P. J. Stephens, F. J. Devlin, C. F. Chabalowski, and M. J. Frisch, J. Phys. Chem. **98**, 11623 (1994).

[63] S. Grimme, J. Chem. Phys. **124**, 034108 (2006).

[64] S. Grimme, J. Comput. Chem. **27**, 1787 (2006).

[65] S. Grimme, J. Antony, S. Ehrlich, and H. Krieg, J. Chem. Phys. **132**, 154104 (2010).

[66] A. Tkatchenko and M. Scheffler, Phys. Rev. Lett. **102**, 073005 (2009).

[67] A. D. Becke and E. R. Johnson, J. Chem. Phys. **127**, 124108 (2007).

[68] S. N. Steinmann and C. Corminboeuf, J. Chem. Theory Comput. **7**, 3567 (2011).

[69] M. Dion, H. Rydberg, E. Schröder, D. C. Langreth, and B. I. Lundqvist, Phys. Rev. Lett. **92**, 246401 (2004).

[70] O. A. Vydrov and T. Van Voorhis, J. Chem. Phys. **133**, 244103 (2010).

[71] L. A. Burns, A. Vazquez-Mayagoitia, B. G. Sumpter, and C. D. Sherrill, J. Chem. Phys. **134**, 084107 (2011).

[72] L. Gráfová, M. Pitoňák, J. Řezáč, and P. Hobza, J. Chem. Theory Comput. **6**, 2365 (2010).

[73] D. G. A. Smith and K. Patkowski, J. Phys. Chem. C **118**, 544 (2014).

[74] S. F. Boys and F. Bernardi, Mol. Phys. **19**, 553 (1970).

[75] F. B. van Duijneveldt, J. G. C. M. van Duijneveldt-van de Rijdt, and J. H. van Lenthe, Chem. Rev. **94**, 1873 (1994).

[76] T. H. Dunning Jr., J. Chem. Phys. **90**, 1007 (1989).

[77] R. A. Kendall, T. H. Dunning Jr., and R. J. Harrison, J. Chem. Phys. **96**, 6796 (1992).

[78] A. Halkier, T. Helgaker, P. Jørgensen, W. Klopper, H. Koch, J. Olsen, and A. K. Wilson, Chem. Phys. Lett. **286**, 243 (1998).

[79] F. Weigend and R. Ahlrichs, Phys. Chem. Chem. Phys. **7**, 3297 (2005).

[80] J. T. Frey and D. J. Doren, Tubegen 3.4 (web-interface, http://turin.nss.udel.edu/research/tubegenonline.html), University of Delaware, Newark DE, 2011.

[81] J. M. Turney, A. C. Simmonett, R. M. Parrish, E. G. Hohenstein, F. A. Evangelista, J. T. Fermann, B. J. Mintz, L. A. Burns, J. J. Wilke, M. L. Abrams, N. J. Russ, M. L. Leininger, C. L. Janssen, E. T. Seidl, W. D. Allen, H. F. Schaefer, R. A. King, E. F. Valeev, C. D. Sherrill, and T. D. Crawford, WIREs Comput. Mol. Sci. **2**, 556 (2012).

[82] A. P. Rendell and T. J. Lee, J. Chem. Phys. **101**, 400 (1994).

[83] G. E. Scuseria, C. L. Janssen, and H. F. Schaefer, J. Chem. Phys. **89**, 7382 (1988).

[84] G. D. Purvis III and R. J. Bartlett, J. Chem. Phys. **76**, 1910 (1982).

[85] K. Patkowski, W. Cencek, M. Jeziorska, B. Jeziorski, and K. Szalewicz, J. Phys. Chem. A **111**, 7611 (2007).

[86] B. W. Bakr, D. G. A. Smith, and K. Patkowski, J. Chem. Phys. **139**, 144305 (2013).

[87] K. Patkowski, W. Cencek, P. Jankowski, K. Szalewicz, J. B. Mehl, G. Garberoglio, and A. H. Harvey, J. Chem. Phys. **129**, 094304 (2008).

[88] J. Noga and R. J. Bartlett, J. Chem. Phys. **86**, 7041 (1987).

[89] Y. J. Bomble, J. F. Stanton, M. Kállay, and J. Gauss, J. Chem. Phys. **123**, 054101 (2005).

[90] M. Kállay and J. Gauss, J. Chem. Phys. **123**, 214105 (2005).

[91] N. Oliphant and L. Adamowicz, J. Chem. Phys. **94**, 1229 (1991).

[92] S. A. Kucharski and R. J. Bartlett, Theor. Chim. Acta **80**, 387 (1991).

[93] J. Řezáč and P. Hobza, J. Chem. Theory Comput. **9**, 2151 (2013).

[94] J. Noga, M. Kállay, and P. Valiron, Mol. Phys. **104**, 2337 (2006).

[95] B. Jäger, R. Hellmann, E. Bich, and E. Vogel, Mol. Phys. **107**, 2181 (2009).

[96] K. Patkowski and K. Szalewicz, J. Chem. Phys. **133**, 094304 (2010).

[97] D. G. A. Smith and K. Patkowski, J. Phys. Chem. C **119**, 4934 (2015).

[98] R. T. Pack, J. Chem. Phys. **45**, 556 (1966).

[99] C. Hättig, W. Klopper, A. Köhn, and D. P. Tew, Chem. Rev. **112**, 4 (2012).

[100] L. Kong, F. A. Bischoff, and E. F. Valeev, Chem. Rev. **112**, 75 (2012).

[101] T. B. Adler, G. Knizia, and H.-J. Werner, J. Chem. Phys. **127**, 221106 (2007).

[102] G. Knizia, T. B. Adler, and H.-J. Werner, J. Chem. Phys. **130**, 054104 (2009).

[103] A. Köhn, J. Chem. Phys. **130**, 131101 (2009).

[104] O. Marchetti and H.-J. Werner, J. Phys. Chem. A **113**, 11580 (2009).

[105] M. S. Marshall and C. D. Sherrill, J. Chem. Theory Comput. **7**, 3978 (2011).

[106] K. Patkowski, J. Chem. Phys. **138**, 154101 (2013).

[107] M. S. Marshall, L. A. Burns, and C. D. Sherrill, J. Chem. Phys. **135**, 194102 (2011).

[108] R. Podeszwa, K. Patkowski, and K. Szalewicz, Phys. Chem. Chem. Phys. **12**, 5974 (2010).

[109] T. Takatani, E. G. Hohenstein, M. Malagoli, M. S. Marshall, and C. D. Sherrill, J. Chem. Phys. **132**, 144104 (2010).

[110] C. D. Sherrill, T. Takatani, and E. G. Hohenstein, J. Phys. Chem. A **113**, 10146 (2009).

[111] E. Papajak, J. Zheng, X. Xu, H. R. Leverentz, and D. G. Truhlar, J. Chem. Theory Comput. **7**, 3027 (2011).

[112] S. Grimme, S. Ehrlich, and L. Goerigk, J. Comput. Chem. **32**, 1456 (2011).

[113] O. A. Vydrov and G. E. Scuseria, J. Chem. Phys. **125**, 234109 (2006).

[114] C. Adamo and V. Barone, J. Chem. Phys. **110**, 6158 (1999).

[115] M. Ernzerhof and G. E. Scuseria, J. Chem. Phys. **110**, 5029 (1999).

[116] J. P. Perdew, K. Burke, and M. Ernzerhof, Phys. Rev. Lett. **77**, 3865 (1996).

[117] J. P. Perdew, Phys. Rev. B **33**, 8822 (1986).

[118] K. Pernal, R. Podeszwa, K. Patkowski, and K. Szalewicz, Phys. Rev. Lett. **103**, 263201 (2009).

[119] A. Heßelmann, J. Chem. Phys. **128**, 144112 (2008).

[120] L. Goerigk, J. Phys. Chem. Lett. **6**, 3891 (2015).

[121] E. R. Johnson and A. D. Becke, J. Chem. Phys. **123**, 024101 (2005).

[122] S. Grimme, S. Ehrlich, and L. Goerigk, J. Comput. Chem. **32**, 1456 (2011).

[123] K. T. Tang and J. P. Toennies, J. Chem. Phys. **80**, 3726 (1984).

[124] J. Řezáč, K. E. Riley, and P. Hobza, J. Chem. Theory Comput. **7**, 2427 (2011).

[125] K. S. Thanthiriwatte, E. G. Hohenstein, L. A. Burns, and C. D. Sherrill, J. Chem. Theory Comput. **7**, 88 (2011).

[126] L. A. Burns, Á. Vázquez-Mayagoitia, B. G. Sumpter, and C. D. Sherrill, J. Chem. Phys. **134**, 084107 (2011).

[127] L. Gráfová, M. Pitoňák, J. Řezáč, and P. Hobza, J. Chem. Theory Comput. **6**, 2365 (2010).

[128] J. C. Faver, L. A. Burns, C. D. Sherrill, and K. M. Merz Jr., "Assessing modeling errors with the biomolecular fragment database," *in preparation.*

[129] J. Řezác, K. E. Riley, and P. Hobza, J. Chem. Theory Comput. **8**, 4285 (2012).

[130] T. M. Parker and C. D. Sherrill, J. Chem. Theory Comput. **11**, 4197 (2015).

[131] S. Li and K. Patkowski, unpublished.

[132] S. Li, D. G. A. Smith, and K. Patkowski, Phys. Chem. Chem. Phys. **17**, 16560 (2015).

[133] R. Bukowski, K. Szalewicz, G. C. Groenenboom, and A. van der Avoird, Science **315**, 1249 (2007).

[134] R. Bukowski, K. Szalewicz, G. C. Groenenboom, and A. van der Avoird, J. Chem. Phys. **128**, 094313 (2008).

[135] D. G. A. Smith and K. Patkowski, unpublished.

[136] N. J. Singh, S. K. Min, D. Y. Kim, and K. S. Kim, J. Chem. Theory Comput. **5**, 515 (2009).

[137] I. N. Levine, *Quantum Chemistry.* Prentice-Hall, New Jersey, 5th edition, 2000.

[138] F. Weigend, Phys. Chem. Chem. Phys. **4**, 4285 (2002).

[139] O. Vahtras, J. Almlöf, and M. W. Feyereisen, Chem. Phys. Lett. **213**, 514 (1993).

[140] B. I. Dunlap, J. W. D. Connolly, and J. R. Sabin, J. Chem. Phys. **71**, 3396 (1979).

[141] J. L. Whitten, J. Chem. Phys. **58**, 4496 (1973).

[142] P. Pulay, Chem. Phys. Lett. **73**, 393 (1980).

[143] T. Helgaker, P. Jørgensen, and J. Olsen, *Molecular electronic-structure theory.* John Wiley & Sons Inc, 2000.

[144] E. G. Hohenstein, N. Luehr, I. S. Ufimtsev, and T. J. Martínez, J. Chem. Phys. **142**, 224103 (2015).

[145] G. Chaban, M. W. Schmidt, and M. S. Gordon, Theor. Chem. Acc. **97**, 88 (1997).

[146] H.-J. Werner, P. J. Knowles, G. Knizia, F. R. Manby, M. Schütz, P. Celani, T. Korona, R. Lindh, A. Mitrushenkov, G. Rauhut, K. R. Shamasundar, T. B. Adler, R. D. Amos, A. Bernhardsson, A. Berning, D. L. Cooper, M. J. O. Deegan, A. J. Dobbyn, F. Eckert, E. Goll, C. Hampel, A. Hesselmann, G. Hetzer, T. Hrenar, G. Jansen, C. Köppl, Y. Liu, A. W. Lloyd, R. A. Mata, A. J. May, S. J. McNicholas, W. Meyer, M. E. Mura, A. Nicklass, D. P. O'Neill, P. Palmieri, D. Peng, K. Pflüger, R. Pitzer, M. Reiher, T. Shiozaki, H. Stoll, A. J. Stone, R. Tarroni, T. Thorsteinsson, and M. Wang, Molpro, version 2012.1, a package of ab initio programs, 2012, see http://www.molpro.net (accessed June 2, 2014).

[147] F. Dayou, M. I. Hernández, J. Campos-Martínez, and R. Hernández-Lamoneda, J. Chem. Phys. **132**, 044313 (2010).

[148] D. Feller and E. R. Davidson, J. Chem. Phys. **82**, 4135 (1985).

[149] S. Chattopadhyay, U. S. Mahapatra, and R. K. Chaudhuri, J. Phys. Chem. A **113**, 5972 (2009).

[150] M. Kirste, X. Wang, H. C. Schewe, G. Meijer, K. Liu, A. van der Avoird, L. M. C. Janssen, K. B. Gubbels, G. C. Groenenboom, and S. Y. T. van de Meerakker, Science **338**, 1060 (2012).

[151] A. R. Millward and O. M. Yaghi, J. Am. Chem. Soc. **127**, 17998 (2005).

[152] K. Sumida, D. L. Rogow, J. A. Mason, T. M. McDonald, E. D. Bloch, Z. R. Herm, T.-H. Bae, and J. R. Long, Chem. Rev. **112**, 724 (2012).

[153] H. C. Longuet-Higgins, Disc. Farad. Soc. **40**, 7 (1965).

[154] P. S. Żuchowski, B. Bussery-Honvault, R. Moszynski, and B. Jeziorski, J. Chem. Phys. **119**, 10497 (2003).

[155] R. Bukowski, R. Podeszwa, and K. Szalewicz, Chem. Phys. Lett. **414**, 111 (2005).

[156] A. G. Ioannou, S. M. Colwell, and R. D. Amos, Chem. Phys. Lett. **278**, 278 (1997).

[157] T. Korona and B. Jeziorski, J. Chem. Phys. **128**, 144107 (2008).

[158] T. Helgaker, S. Coriani, P. Jørgensen, K. Kristensen, J. Olsen, and K. Ruud, Chem. Rev. **112**, 543 (2012).

[159] J. Olsen and P. Jørgensen, J. Chem. Phys. **82**, 3235 (1985).

[160] P. Norman, A. Jiemchooroj, and B. E. Sernelius, J. Chem. Phys. **118**, 9167 (2003).

Appendices

Appendix A

Basis Set Convergence of the Post-CCSD(T) Contribution to Noncovalent Interaction Energies

JCTC Journal of Chemical Theory and Computation

Article

pubs.acs.org/JCTC

Basis Set Convergence of the Post-CCSD(T) Contribution to Noncovalent Interaction Energies

Daniel G. A. Smith

Department of Chemistry and Biochemistry, Auburn University, Auburn, Alabama 36849, United States

Piotr Jankowski

Department of Quantum Chemistry, Faculty of Chemistry, Nicolaus Copernicus University, Gagarina 7, 87-100 Toruń, Poland

Michał Slawik and Henryk A. Witek

Department of Applied Chemistry and Institute of Molecular Science, National Chiao Tung University, 1001 Ta-Hsueh Road, Hsinchu 30010, Taiwan

Konrad Patkowski*

Department of Chemistry and Biochemistry, Auburn University, Auburn, Alabama 36849, United States

Ⓢ *Supporting Information*

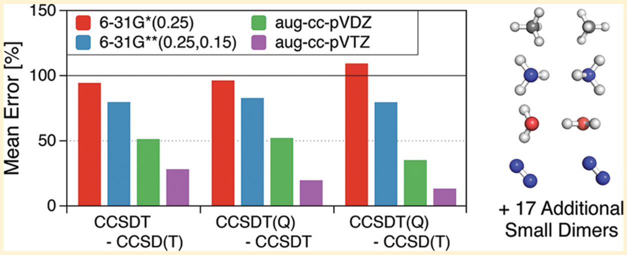

ABSTRACT: We investigated the basis set convergence of high-order coupled-cluster interaction energy contributions for 21 small weakly bound complexes. By performing CCSDT(Q) calculations in at least the aug-cc-pVTZ basis set, and CCSDT calculations in at least aug-cc-pVQZ (aug-cc-pVTZ for one system), we found the convergence to be quite slow. In particular, the 6-31G*(0.25) and 6-31G**(0.25,0.15) bases advocated by Hobza et al. (*J. Chem. Theory Comput.* **2013**, *9*, 2151; *ibid.* **2013**, 9, 3420) are unsuitable for the post-CCSD(T) effects, with average errors for the CCSDT(Q)-CCSD(T) interaction energy contribution of about 80% for 6-31G**(0.25,0.15) and 110% for 6-31G*(0.25). Upgrading the basis set to aug-cc-pVDZ reduces the average error to about 35% and extremely demanding CCSDT(Q)/aug-cc-pVTZ calculations are necessary for further improvement in accuracy. An error cancellation between basis set incompleteness effects at the CCSDT-CCSD(T) and CCSDT(Q)-CCSDT levels occurs for most (but not all) complexes, making it unproductive to carry out CCSDT calculations in a larger basis set than the more demanding CCSDT(Q) calculations. We also found that the frozen natural orbital approximation at the CCSDT and CCSDT(Q) levels works well only if the thresholds for discarding least occupied natural orbitals are very tight (significantly tighter than the thresholds recommended for molecular correlation energies in the original work of Rolik and Kállay, *J. Chem. Phys.* **2011**, *134*, 124111), making the performance gains quite limited. The interaction energy contributions through CCSDT(Q) are both a necessity and a bottleneck in the construction of top-accuracy interaction potentials and further improvements in the efficiency of high-order coupled-cluster calculations will be of great help.

I. INTRODUCTION

The "gold-standard" coupled-cluster approach[1,2] with single, double, and noniterative triple excitations [CCSD(T)][3] has proven immensely successful in generating highly accurate noncovalent interaction energies. In particular, the databases of CCSD(T)-level interaction energies are an extremely valuable tool for the benchmarking and tuning of more approximate methods.[4−8] Due to the increase of the available computational power and the advances in overcoming basis set incompleteness effects at the CCSD(T) level (such as complete-basis-set (CBS) extrapolations,[9,10] bond functions,[11] and explicitly correlated F12 approaches[12,13]), the CCSD(T)/CBS interaction energies can be obtained so precisely that higher-order coupled-cluster excitations can become the leading contribution to the residual errors of interaction energies (along with the corrections for core−core and core−valence correlation, relativistic effects, and post-Born−Oppenheimer terms). Therefore, higher-order coupled-cluster interaction energy contributions, obtained using CCSDT,[14] CCSDT(Q),[15,16] and/or CCSDTQ,[17,18] have

Received: April 22, 2014
Published: June 9, 2014

dx.doi.org/10.1021/ct500347q | *J. Chem. Theory Comput.* 2014, 10, 3140−3150

Table 1. Interaction Energy Contributions (in cm^{-1}) for the He−He, He−H_2, and H_2−H_2 Complexes in Their Respective van der Waals Minimum Geometries

basis set	CCSD(T)	δ_T	$\delta_{(Q)}$	$\delta_{T+(Q)}$	δ_Q
He−He					
6-31G*(0.25)	6.7387	−0.0027	0.0000	−0.0027	0.0000
6-31G**(0.25,0.15)	−1.5310	−0.1273	−0.0073	−0.1346	−0.0036
aDZ	−2.9223	−0.1891	−0.0042	−0.1933	−0.0021
aTZ	−5.7698	−0.2124	−0.0066	−0.2190	−0.0031
aQZ	−6.4344	−0.2124	−0.0074	−0.2198	−0.0034
a5Z	−6.8306	−0.2108	−0.0077	−0.2185	−0.0032
a6Z	−7.1316	−0.2117	−0.0080	−0.2197	−0.0034
He−H_2					
6-31G*(0.25)	10.9419	−0.0120	0.0010	−0.0110	0.0007
6-31G**(0.25,0.15)	−6.2201	−0.2826	−0.0020	−0.2846	0.0008
aDZ	−6.8620	−0.4035	−0.0096	−0.4130	−0.0027
aTZ	−9.1984	−0.4040	−0.0140	−0.4180	−0.0034
aQZ	−9.9053	−0.3947	−0.0159	−0.4106	−0.0036
a5Z	−10.2463	−0.3870	−0.0165	−0.4035	−0.0037
a6Z	−10.4263	−0.3830			
H_2−H_2					
6-31G*(0.25)	28.2768	−0.0747	−0.0238	−0.0985	−0.0144
6-31G**(0.25,0.15)	−22.8972	−0.9264	−0.0736	−1.0000	−0.0342
aDZ	−24.3163	−1.1896	−0.0901	−1.2797	−0.0333
aTZ	−35.0745	−1.2392	−0.1006	−1.3398	−0.0306
aQZ	−37.3259	−1.1885	−0.1059	−1.2944	−0.0307
a5Z	−37.8178	−1.1550	−0.1072	−1.2622	
a6Z	−38.0588	−1.1364			

attracted significant attention in the last year, culminated by the extensive and illuminating studies of Hobza and collaborators.[19−21] These authors have constructed the A24 database of 24 small complexes for which the benchmark interaction energies contain, in addition to an estimate of the CCSD(T)/CBS interaction energy, the corrections due to core−core and core−valence correlation, relativistic effects, and post-CCSD(T) terms. The latter correction was calculated[20] at the CCSDT(Q) level using a 6-31G**(0.25,0.15) basis set. Furthermore, by performing calculations up to CCSDTQP (for the smallest dimers, even full CI), Hobza et al. have shown[21] that the CCSDT(Q) interaction energies are already converged to about 0.5 cm^{-1} or better. This conclusion is in line with earlier observations of a remarkable agreement between the interaction energies predicted by CCSDT(Q) and CCSDTQ.[22−24] On the other hand, the inclusion of full, iterative (CCSDT) triples alone does not provide a consistent improvement over CCSD(T); the inclusion of quadruple excitations at least at the noniterative (Q) level is crucial.[19]

The work of Hobza and collaborators used a small 6-31G**(0.25,0.15) basis for the post-CCSD(T) corrections to make the calculations feasible (only ref 19 presented results in the slightly larger aDZ ≡ aug-cc-pVDZ basis as well). Due to the steep computational scaling of the methods involved (N^8 for CCSDT and N^9 for CCSDT(Q)), it is not possible to obtain fully converged CBS estimates of the post-CCSD(T) contributions except for small four-electron systems (the latter are, however, not quite representative of larger systems as will be shown below). However, there is some compelling evidence that the basis set convergence of the post-CCSD(T) terms is no faster than for the CCSD(T) interaction energy, so that basis sets such as 6-31G**(0.25,0.15) or aDZ are likely inadequate. In particular, for the argon dimer, the δ_T = CCSDT−CCSD(T) and $\delta_{(Q)}$ = CCSDT(Q)−CCSDT contributions to the near-minimum interaction energy, computed in the aDZ basis set, amount to only −4% (that is, the sign is wrong) and 32%, respectively, of the values computed in the largest basis sets feasible, aug-cc-pV(5 + *d*)Z and aug-cc-pV(Q + *d*)Z, respectively.[24]

In view of the slow basis set convergence of δ_T and $\delta_{(Q)}$ for the argon dimer, and of a similar pattern observed for other weakly interacting dimers investigated in our groups,[25,26] we suspect that the largest remaining error in the interaction energies of the A24 database might be due to the, possibly severe, basis set incompleteness effects in δ_T and $\delta_{(Q)}$. On a more fundamental level, we would like to gauge the utility of adding a small-basis CCSDT(Q) correction to the interaction energy and to establish the basis set requirements for an accurate description of this correction. Additionally, as for some systems δ_T and $\delta_{(Q)}$ cancel each other to a large extent, we want to study the basis set convergence of the overall CCSDT(Q)-CCSD(T) contribution and compare it with the properties of δ_T and $\delta_{(Q)}$ separately. As our working hypothesis is that small-basis δ_T and $\delta_{(Q)}$ corrections may be qualitatively inaccurate, we restrict our considerations to small systems for which the CCSDT(Q) calculations in at least the aTZ basis are feasible. For some smaller complexes, we will be able to run CCSDT and CCSDT(Q) in bases as large as a5Z and aQZ, respectively, and for the four-electron systems (where CCSDTQ is equivalent to FCI) still larger basis sets can be utilized even at the CCSDTQ level.

The example dimers considered in this work include nearly all complexes for which post-CCSD(T) interaction energy corrections have been previously computed using any basis set larger than aDZ as well as a number of dimers (e.g., NH_3−NH_3 and CH_4−CH_4) for which such calculations have not been done before. Specifically, we consider the four-electron systems He−He,[27] He−H_2,[28] and H_2−H_2,[29] rare gas dimers Ne−Ne[30] and Ar−Ar,[23,24] the complexes H_2−CO,[25,31] H_2−HCl,[32] He−C_3,[26]

Table 2. Interaction Energy Contributions (in cm^{-1}) for the He−LiH and LiH−LiH Complexes[a]

basis set	CCSD(T)	δ_T	$\delta_{(Q)}$	$\delta_{T+(Q)}$	δ_Q
		He−LiH			
6-31G*(0.25)	−12.718	−0.522	−0.030	−0.552	−0.007
6-31G**(0.25,0.15)	−31.749	−1.157	−0.102	−1.258	−0.041
aDZ	−98.359	−1.063	−0.054	−1.117	−0.025
aTZ	−139.102	−1.120	−0.066	−1.185	−0.028
aQZ	−147.367	−1.105	−0.071	−1.176	−0.029
a5Z	−148.140	−1.080	−0.072	−1.152	
		LiH−LiH			
6-31G*(0.25)	−13872.24	−28.86	−1.08	−29.94	−0.16
6-31G**(0.25,0.15)	−14473.47	−31.54	−0.16	−31.70	0.39
aDZ	−15851.05	−29.48	−1.17	−30.65	−0.21
aTZ	−16689.70	−35.06	−2.51	−37.56	−0.56
aQZ	−16818.09	−33.20	−2.83	−36.03	−0.50
a5Z	−16854.59	−31.94			

[a]The lithium 1*s* core electrons have not been correlated.

Ar−HF,[33−35] Ne−HF, and H_2−HF under investigation in our groups, and the N_2−N_2,[36] H_2O−H_2O,[37] He−LiH, LiH−LiH, Ar−CH_4, HF−HF, NH_3−NH_3, and CH_4−CH_4 dimers. Compared to the post-CCSD(T) interaction energies beyond the aDZ basis available in the literature, to our knowledge, we only exclude the systems with less than four electrons for which FCI calculations are quite straightforward[38,39] and the alkaline earth metal dimers which are four-electron systems within the frozen-core approximation (this approximation, however, works poorly in this case, and the accuracy of the CCSD(T) interaction energies is particularly low; see ref 40 and references therein).

II. COMPUTATIONAL DETAILS

The majority of the calculations are performed at the global-minimum geometries, which are taken from the literature to facilitate comparison with previous studies. For the H_2O−H_2O and N_2−N_2 complexes, where the global minimum has relatively low symmetry, we have performed additional calculations at a more symmetric configuration. The geometries of all studied complexes are described in Table SI in the Supporting Information (which also lists the corresponding Cartesian coordinates). We have employed the 6-31G*(0.25)[41,42] and 6-31G**(0.25,0.15) basis sets popularized by Hobza as well as the singly augmented Dunning sequence a*X*Z, X = D,T,Q,5,6.[43,44] Note that for the second-row atoms (Cl and Ar) the regular a*X*Z sets were used, not the aug-cc-pV($X + d$)Z sets[45] as the latter, while slightly larger, have not shown any consistent improvement for interaction energies. Moreover, the a*X*Z, X = D,T,Q, bases for lithium are the original sets from ref 46 (as listed on the Basis Set Exchange Web site[47]), not the revised sets of ref 48. All interaction energies include the counterpoise (CP) correction for basis set superposition error. Contrary to refs 19−21, which correlated all electrons, our δ_T and $\delta_{(Q)}$ corrections will be obtained within the frozen-core approximation. This approach corresponds to treating the corrections to CCSD(T)/CBS for higher-order excitations and for core−core and core−valence correlation as additive, as implicitly assumed in nearly all studies to date. We have, however, tested this assumption on the "worst-case-scenario" examples involving the LiH molecule (the frozen-core approximation generally works poorly for interactions involving alkali or alkaline earth metals[40]) as well as on the much less critical example of Ne−Ne.

All CCSDT(Q) and CCSDTQ calculations have been carried out using the MRCC program,[49−51] either stand-alone or interfaced to MOLPRO2012.1.[52] The largest CCSDT calculations have used the CFOUR code.[53] For a few systems, we have carried out additional CCSDT and CCSDT(Q) calculations with the virtual orbital space truncated according to occupations of MP2 natural orbitals;[54] see section III.B for details.

III. NUMERICAL RESULTS AND DISCUSSION

The basis set convergence of the δ_T, $\delta_{(Q)}$, and δ_Q = CCSDTQ−CCSDT(Q) contributions to the near-minimum interaction energies of four-electron dimers He−He, He−H_2, and H_2−H_2 is presented in Table 1. The corresponding values of the CCSD(T) interaction energies are shown to illustrate the significance of the post-CCSD(T) contribution.

The first observation from Table 1 affirms that for the four-electron systems quadruple excitations are only of minor importance. At the largest basis sets listed, the $\delta_{(Q)}$ term does not exceed 10% of δ_T, and the correction for full CCSDTQ (equivalent to full CI in this case) is still smaller by a factor of at least 2. While the basis set convergence of $\delta_{(Q)}$ might not be of critical importance for these systems, it is quite slow, with the aDZ value amounting to 54−84% of the a5Z result. Fortunately, the dominating δ_T contribution exhibits faster basis set convergence, with the aDZ basis reproducing 89−105% of the a6Z value. The 6-31G**(0.25,0.15) basis accidentally gives a very good value of $\delta_{(Q)}$ for He−He, but it is quite inaccurate for the remaining two dimers as well as for the dominating δ_T correction, for which the errors are about four times that of aDZ. As could be expected, the still smaller 6-31G*(0.25) basis (equivalent to just 6-31G for hydrogen and helium) is completely unsuitable for dispersion-dominated interactions.

The δ_T, $\delta_{(Q)}$, and δ_Q results for the He−LiH and LiH−LiH dimers are presented in Table 2. As the 1*s* lithium electrons were not correlated (we will examine the all-electron δ_T and $\delta_{(Q)}$ contributions for these systems in section III.C), these are also four-electron systems and even CCSDTQ≡FCI can be computed in reasonably large basis sets. Similar to the other four-electron systems (Table 1), the δ_T effect strongly dominates over $\delta_{(Q)}$ and δ_Q. However, the overall post-CCSD(T) effects are very minor (below 1%) for He−LiH and LiH−LiH and the convergence of the δ_T contribution is generally quite good even though it becomes monotonic only from the aTZ level on. Even the 6-31G**(0.25,0.15) set, while inadequate for the minor $\delta_{(Q)}$ contribution, recovers 98−107% of the a5Z result for δ_T; the 6-31G*(0.25) basis is not much worse for the LiH−LiH complex.

Table 3. Interaction Energy Contributions (in cm^{-1}) for the Ne–Ne, Ar–Ar, and He–C_3 Complexes in Their Respective Global Minima[a]

basis set	CCSD(T)	δ_T	$\delta_{(Q)}$	$\delta_{T+(Q)}$	δ_Q
Ne–Ne					
6-31G*(0.25)	−16.8056	−0.1078	0.1276	0.0199	−0.0129
aDZ	−3.0539	−0.0407	0.0326	−0.0080	−0.0074
aTZ	−16.6713	−0.2694	−0.0269	−0.2963	
aQZ	−22.9583	−0.3728	−0.0704	−0.4432	
a5Z	−25.7525	−0.4072			
Ar–Ar					
6-31G*(0.25)	−12.940	0.005	0.774	0.780	−0.148
aDZ	−24.467	−0.054	−0.547	−0.601	0.104
aTZ	−66.090	0.824	−1.206	−0.382	
aQZ	−81.579	1.052	−1.612	−0.560	
a5Z	−90.097	1.200			
He–C_3					
6-31G*(0.25)	19.023	0.075	−0.139	−0.064	0.007
6-31G**(0.25,0.15)	−12.309	0.084	−0.295	−0.211	0.029
aDZ	−15.499	0.189	−0.579	−0.390	0.021
aTZ	−22.628	0.370	−0.649	−0.279	
aQZ	−24.485	0.432			

[a] The Ar–Ar and He–C_3 results (except for the 6-31G*(0.25) and 6-31G**(0.25,0.15) ones) are taken from Refs 24 and 26, respectively, and most of the Ne–Ne results have been obtained in Ref 30. The 6-31G*(0.25) and 6-31G**(0.25,0.15) bases are identical when no hydrogen or helium atoms are present.

Table 4. Interaction Energy Contributions (in cm^{-1}) for the Ne–HF, Ar–HF, and Ar–CH_4 Complexes in Their Respective Global Minima

basis set	CCSD(T)	δ_T	$\delta_{(Q)}$	$\delta_{T+(Q)}$	δ_Q
Ne–HF					
6-31G*(0.25)	−49.798	−0.054	0.191	0.137	−0.025
6-31G**(0.25,0.15)	−88.120	−0.123	0.102	−0.021	−0.038
aDZ	−55.225	−0.252	−0.303	−0.555	0.028
aTZ	−72.406	−0.928	−0.610	−1.538	
aQZ	−79.262	−0.938	−0.736	−1.674	
a5Z	−86.125	−0.911			
Ar–HF					
6-31G*(0.25)	−21.707	0.488	0.067	0.555	−0.100
6-31G**(0.25,0.15)	−82.679	−0.083	0.030	−0.052	−0.030
aDZ	−94.051	−1.288	−0.849	−2.137	−0.013
aTZ	−185.643	−0.889	−1.977	−2.866	
aQZ	−207.969	−0.477	−2.331	−2.808	
a5Z	−212.617	−0.238			
Ar–CH_4					
6-31G*(0.25)	−22.898	−0.136	0.241	0.105	−0.111
6-31G**(0.25,0.15)	−50.559	−0.469	0.454	−0.015	−0.121
aDZ	−82.669	−0.506	−1.020	−1.526	
aTZ	−119.564	0.522	−1.924	−1.402	
aQZ	−132.986	0.880			

As seen in Table 2, the frozen-core He–LiH and LiH–LiH systems are not particularly demanding when it comes to the basis set selection for the post-CCSD(T) corrections. It is, unfortunately, not the case for most of the larger dimers, as illustrated in Tables 3 (Ne–Ne, Ar–Ar, He–C_3), 4 (Ne–HF, Ar–HF, Ar–CH_4), 5 (H_2–HF, H_2–HCl, H_2–CO), 6 (H_2O–H_2O, N_2–N_2), and 7 (HF–HF, NH_3–NH_3, CH_4–CH_4). In the most extreme cases of the H_2O–H_2O and HF–HF complexes, the aDZ basis either fails to capture the correct sign of the $\delta_{T+(Q)} \equiv \delta_T + \delta_{(Q)}$ sum or underestimates $\delta_{T+(Q)}$ several times, and the 6-31G*(0.25) and 6-31G**(0.25,0.15) bases are still worse. Tables 3–7 also show that the $\delta_{(Q)}$ correction tends to converge from above to a negative CBS result, while the δ_T term can have either sign and mostly approaches its CBS limit from below although the convergence often becomes monotonic only from the aTZ level on.

To facilitate the analysis of the overall performance of different basis sets for δ_T and $\delta_{(Q)}$, we will partition the complexes into four groups as follows.

- *Four-valence-electron dimers*: He–He, He–H_2, H_2–H_2, He–LiH, and LiH–LiH
- *Nonpolar–nonpolar dimers*: Ne–Ne, Ar–Ar, He–C_3, H_2–CO, Ar–CH_4, N_2–N_2 (2 orientations), and CH_4–CH_4
- *Polar–nonpolar dimers*: H_2–HF, H_2–HCl, Ne–HF, Ar–HF

Table 5. Interaction Energy Contributions (in cm^{-1}) for the H_2−HF, H_2−HCl, and H_2−CO Complexes in Their Respective near-Global Minimum Geometries[a]

basis set	CCSD(T)	δ_T	$\delta_{(Q)}$	$\delta_{T+(Q)}$	δ_Q
		H_2−HF			
6-31G*(0.25)	233.239	−0.218	0.242	0.024	−0.128
6-31G**(0.25,0.15)	−93.337	−2.545	0.326	−2.219	−0.105
aDZ	−296.317	−3.612	0.156	−3.456	−0.130
aTZ	−370.023	−3.937	−0.458	−4.395	
aQZ	−387.151	−3.450	−0.646	−4.096	
a5Z	−391.676	−3.181			
		H_2−HCl			
6-31G*(0.25)	118.346	−0.700	−0.026	−0.726	−0.036
6-31G**(0.25,0.15)	−57.089	−2.460	0.182	−2.278	−0.096
aDZ	−122.888	−2.722	−1.123	−3.845	−0.010
aTZ	−183.349	−2.426	−1.774	−4.200	
aQZ	−199.442	−1.927	−1.991	−3.919	
a5Z	−202.779	−1.683			
		H_2−CO			
6-31G*(0.25)	−15.706	−0.842	−0.095	−0.937	−0.109
6-31G**(0.25,0.15)	−89.638	−1.536	−0.532	−2.068	0.021
aDZ	−73.160	−1.850	−0.856	−2.706	−0.045
aTZ	−86.503	−1.469	−1.131	−2.600	
aQZ	−89.257	−1.303	−1.205	−2.508	
a5Z	−90.210	−1.207			

[a] Most of the H_2−CO results were obtained in the course of the work on refs 31 and 25.

Table 6. Interaction Energy Contributions (in cm^{-1}) for the Water and Nitrogen Dimers[a]

basis set	CCSD(T)	δ_T	$\delta_{(Q)}$	$\delta_{T+(Q)}$	δ_Q
		H_2O−H_2O (global minimum)			
6-31G*(0.25)	−1386.50	5.65	−0.71	4.93	−0.08
6-31G**(0.25,0.15)	−1475.05	5.52	−1.50	4.02	0.11
aDZ	−1530.34	2.36	−3.24	−0.88	
aTZ	−1665.60	1.51	−4.95	−3.44	
aQZ	−1726.71	2.02			
		H_2O−H_2O (C_{2v})			
6-31G*(0.25)	−902.55	3.89	1.04	4.93	−0.18
6-31G**(0.25,0.15)	−1021.62	3.75	0.27	4.03	−0.07
aDZ	−1026.27	1.14	−0.73	0.41	−0.08
aTZ	−1107.16	0.30	−2.26	−1.96	
aQZ	−1141.02	0.55	−2.44[b]	−1.89[b]	
		N_2−N_2 (global minimum)			
6-31G*(0.25)	−85.401	2.479	−4.448	−1.969	1.462
aDZ	−79.561	2.855	−4.852	−1.997	
aTZ	−97.162	3.622	−5.456	−1.835	
aQZ	−102.468	3.857			
		N_2−N_2 (D_{2h})			
6-31G*(0.25)	−50.828	1.877	−3.050	−1.173	1.372
aDZ	−49.207	2.294	−3.540	−1.246	1.122
aTZ	−69.069	3.267	−4.391	−1.124	
aQZ	−72.826	3.531			

[a] Each complex is presented in two geometries: the global-minimum one (less symmetric) and a highly symmetric structure that is only a radial minimum. The 6-31G*(0.25) and 6-31G**(0.25,0.15) bases are identical when no hydrogen or helium atoms are present. [b] Result obtained in the FNO approximation (section III.B).

- *Polar−polar dimers*: H_2O−H_2O (2 orientations), HF−HF, and NH_3−NH_3

The first important factor that differentiates between complexes belonging to different groups is the relative importance of the δ_T and $\delta_{(Q)}$ interaction energy contributions compared to the leading CCSD(T) term. There exists ample literature concerning the methodology (basis sets, counterpoise correction or lack thereof, CBS extrapolations, and different explicitly correlated CCSD(T)-F12 variants) of obtaining precise and reliable CCSD(T)/CBS interaction energy estimates,[55−59] and it is not our aim to generate ultra-accurate values of the CCSD(T)/CBS term. Therefore, we will select the most accurate CCSD(T)/CBS benchmark values from the literature if available for a given geometry: if not, we will obtain

Table 7. Interaction Energy Contributions (in cm^{-1}) for the HF, NH_3, and CH_4 Dimers in Their Respective near-Minimum Configurations

basis set	CCSD(T)	δ_T	$\delta_{(Q)}$	$\delta_{T+(Q)}$	δ_Q
		HF−HF			
6-31G*(0.25)	−1316.83	6.17	−0.98	5.18	0.15
6-31G**(0.25,0.15)	−1247.58	9.23	−3.21	6.02	0.32
aDZ	−1391.01	4.52	−2.15	2.37	
aTZ	−1504.08	0.91	−3.48	−2.57	
aQZ	−1576.91	0.52			
		NH_3−NH_3			
6-31G*(0.25)	−791.26	1.13	−1.01	0.12	0.00
6-31G**(0.25,0.15)	−927.82	−0.24	−1.25	−1.49	0.00
aDZ	−928.12	−0.47	−3.72	−4.19	
aTZ	−1050.72	1.56	−5.80	−4.24	
aQZ	−1082.74	2.60			
		CH_4−CH_4			
6-31G*(0.25)	−23.384	−0.124	−0.992	−1.116	−0.043
6-31G**(0.25,0.15)	−102.161	−1.008	−1.170	−2.178	0.124
aDZ	−143.081	−1.403	−1.888	−3.292	
aTZ	−174.241	−0.212	−2.893	−3.105	
aQZ	−181.931				

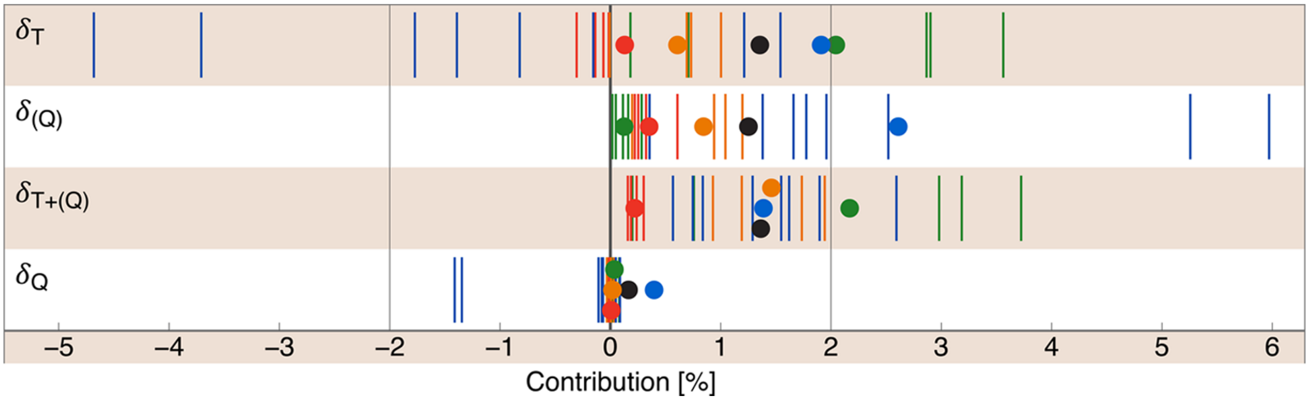

Figure 1. δ_T, $\delta_{(Q)}$, $\delta_{T+(Q)}$, and δ_Q interaction energy contributions as percentages of the CCSD(T)/CBS interaction energy. The four-valence-electron, nonpolar−nonpolar, polar−nonpolar, and polar−polar dimers are represented by green, blue, orange, and red symbols, respectively. The circles represent the *unsigned* averages of the individual values, with the black circle showing the unsigned average for all complexes.

CCSD(T)/CBS estimates by the standard X^{-3} extrapolation[9] of the results computed in the aQZ and a5Z bases (a5Z and a6Z for a few systems). The complete set of benchmark CCSD(T)/CBS interaction energies is listed in Table SI in the Supporting Information.

The values of the δ_T and $\delta_{(Q)}$ corrections, as well as of their $\delta_{T+(Q)}$ sum and of the post-CCSDT(Q) term δ_Q, as percentages of the CCSD(T)/CBS interaction energy are presented in Figure 1. In this figure (its design is inspired by refs 58 and 60), the four-valence-electron, nonpolar−nonpolar, polar−nonpolar, and polar−polar dimers (see the partitioning above) are represented by green, blue, orange, and red symbols, respectively. Note that, as the CCSD(T)/CBS interaction energy is negative, a positive percentage means a negative interaction energy contribution. For individual systems, the actual percentages (positive or negative) are shown: however, all averages pertain to unsigned percentages (in other words, we show the mean unsigned relative deviations of, for example, CCSD(T) + δ_T relative to CCSD(T)). In Figure 1, the values of δ_T and $\delta_{(Q)}$ are chosen as (supposedly) the most accurate estimates of these corrections available from Tables 1−7, that is, the results of the X^{-3} extrapolation using the two largest-X aXZ values (note that the largest X available is typically higher for δ_T than for $\delta_{(Q)}$). In the particular case of the a(D,T)Z extrapolation, it was observed for the CCSD(T)−MP2 interaction energy contribution[61] that the inadequacy of the aDZ basis often makes the extrapolated result inferior to the calculated aTZ value. In order to check whether the similar observation holds for δ_T and $\delta_{(Q)}$, we compared the performance of the a(D,T)Z and aTZ estimates of these corrections to the benchmark values obtained by the a(T,Q)Z extrapolation or higher: this comparison was done on 18 systems (all but CH_4−CH_4, HF−HF, and Ar−HF, excluded for the reasons described below) for δ_T and 13 systems for $\delta_{(Q)}$. For δ_T, the overall accuracy of the a(D,T)Z and aTZ results was about the same (a mean unsigned relative error (MURE) of 25.3% versus 28.3%), however, the a(D,T)Z approach performed much better on the nonpolar−nonpolar dimers (a MURE of 10.6% versus 30.0% for bare aTZ) so we chose the δ_T/a(D,T)Z result as benchmark for the methane dimer (the only complex for which CCSDT/aQZ could not be calculated). In the case of $\delta_{(Q)}$, the extrapolated a(D,T)Z estimates performed significantly better (a MURE of 10.8% versus 24.5% for aTZ) so we adopted the $\delta_{(Q)}$/a(D,T)Z values as benchmarks when larger-basis results are not available. All benchmark estimates of the post-CCSD(T) corrections are listed in Table SII in the Supporting Information. On the average, the δ_T and $\delta_{(Q)}$ effects amount to, respectively, 2.04% and 0.13% for four-valence-electron dimers, 1.91% and 2.61% for nonpolar–nonpolar dimers, 0.61% and 0.84% for polar–nonpolar dimers, 0.13% and 0.35% for polar–polar dimers, and 1.36% and 1.25% overall. The magnitude of the post-CCSD(T) effects can be contrasted with the $\delta_{(T)}$ = CCSD(T)−CCSD interaction energy contribution which amounts, on the average, to 17.4% of the CCSD(T) benchmark (the MP2, CCSD, and $\delta_{(T)}$ interaction energy terms are given in Table SII for completeness). As evident from Figure 1, for the nonpolar–nonpolar dimers the δ_T and $\delta_{(Q)}$ contributions cancel out partially but systematically while for the polar–nonpolar and polar–polar dimers no such cancellation is present. As mentioned above, the δ_T contribution strongly dominates for the four-valence-electron complexes. The benchmark values for the nonperturbative quadruples correction δ_Q were computed in the largest bases available in Tables 1–7 without any extrapolation. As shown in Figure 1, the δ_Q correction is generally very small. The only exceptions are the two geometries of the nitrogen dimer: interactions between triply bonded molecules such as N_2 or CO are known to require particularly high orders of Møller–Plesset perturbation theory (MP*n*) or high-order coupled-cluster excitations.[62] One should note that the same two N_2–N_2 structures are responsible for the largest percentage contributions to δ_T (the two leftmost lines in Figure 1) and $\delta_{(Q)}$ (the two rightmost lines); however, these two terms cancel out to a large extent.

When the δ_T term can be computed in a larger basis than $\delta_{(Q)}$ (which is the case for all complexes but four, cf. Tables 1–7), there are two sensible ways of estimating the benchmark value of the overall $\delta_{T+(Q)}$ contribution: as a sum of the δ_T and $\delta_{(Q)}$ benchmarks (obtained in separate extrapolations) or via a single extrapolation of the $\delta_{T+(Q)}$ term computed in the two largest basis sets for which the $\delta_{(Q)}$ value is available. While the first approach is formally closer to CBS (it includes the δ_T contribution in larger basis sets), the second approach is preferable if any cancellation between the basis set incompleteness errors at the δ_T and $\delta_{(Q)}$ levels occurs. For the 12 complexes for which the CCSDT/a5Z and CCSDT(Q)/aQZ calculations are possible, the single-extrapolation $\delta_{T+(Q)}$/a(T,Q)Z estimate differs from the separate-extrapolations δ_T/a(Q,5)Z + $\delta_{(Q)}$/a(T,Q)Z one by an average of 5.2%. As the results in Tables 1–7 show that the $\delta_{T+(Q)}$ sum exhibits faster basis set convergence than its δ_T and $\delta_{(Q)}$ components for most but not all dimers (in other words, error cancellation is likely but not at all systematic), it is not clear which one of these estimates is more accurate but the difference is minor. For smaller bases, an additional factor is the poor performance of the $\delta_{T+(Q)}$/a(D,T)Z extrapolation—comparison with the a(T,Q)Z (or higher) benchmark data for 13 complexes shows a MURE of 19.9% for $\delta_{T+(Q)}$/a(D,T)Z and 13.5% for $\delta_{T+(Q)}$/aTZ. Therefore, computing the δ_T part from the a(T,Q)Z extrapolation should be highly preferred over either a(D,T)Z or aTZ: not only the basis set is larger but the extrapolation is clearly beneficial. Consequently, we decided to compute our $\delta_{T+(Q)}$ benchmark values, presented in Figure 1, using the separate-extrapolations approach whenever possible (for the methane dimer, we chose the $\delta_{T+(Q)}$/a(D,T)Z value as benchmark).

While, as expected, the overall $\delta_{T+(Q)}$ interaction energy correction is quite minor (0.16% to 3.72% of the CCSD(T)/CBS value, or a maximum of 2.68% if four-valence-electron dimers are neglected), it nevertheless becomes important in top-accuracy calculations. Therefore, one should ask how well the δ_T, $\delta_{(Q)}$, and $\delta_{T+(Q)}$ corrections are recovered (relative to the benchmark values of these terms from Figure 1) when computed in a smaller basis set. To answer this question, we computed the MURE values of the δ_T correction obtained in the 6-31G*(0.25), 6-31G**(0.25,0.15), aDZ, aTZ, and aQZ basis sets, and of the $\delta_{(Q)}$ and $\delta_{T+(Q)}$ terms computed in the 6-31G*(0.25), 6-31G**(0.25,0.15), aDZ, and aTZ basis sets, relative to the benchmark values from Figure 1. The results are presented in Figures 2, 3, and 4 for δ_T, $\delta_{(Q)}$, and $\delta_{T+(Q)}$, respectively. Note that a MURE of over 100%, obtained for some classes of systems at the 6-31G*(0.25) and 6-31G**(0.25,0.15) basis sets, means that it is better to neglect a contribution completely (a 100% error) than to compute it using such a small basis set. It should also be noted that even our largest-basis estimates are in general not converged, as indicated by the overall MURE values of 13.7, 19.2, and 15.8% obtained for δ_T/aQZ, $\delta_{(Q)}$/aTZ, and $\delta_{T+(Q)}$/aTZ, respectively.

There are three systems for which the benchmark δ_T value is particularly close to zero so that the relative errors are greatly

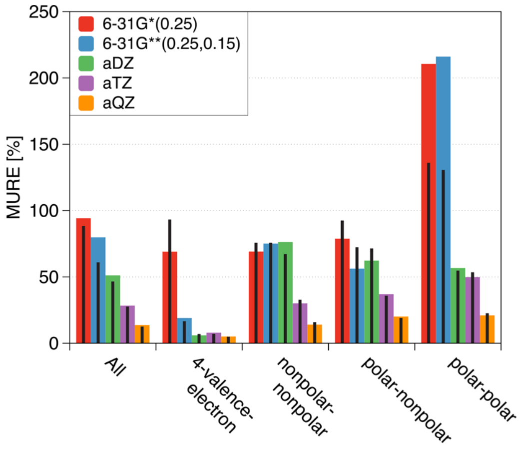

Figure 2. Performance of different basis sets in the recovery of the δ_T benchmark (extrapolated from the two largest-basis results in Tables 1–7) displayed as mean unsigned relative errors (MURE). The black lines represent the median unsigned relative errors (MeURE). The CH_4–CH_4, HF–HF, and Ar–HF complexes are excluded from the MURE and MeURE calculation due to the accidental smallness of the benchmark value (see text for details).

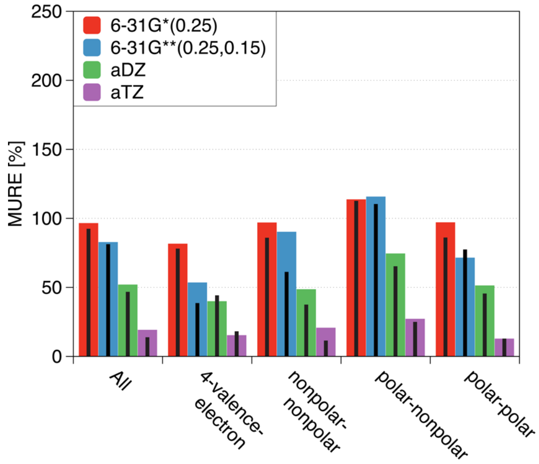

Figure 3. Performance of different basis sets in the recovery of the $\delta_{(Q)}$ benchmark (extrapolated from the two largest-basis results in Tables 1–7) displayed as mean unsigned relative errors (MURE). The black lines represent the median unsigned relative errors (MeURE).

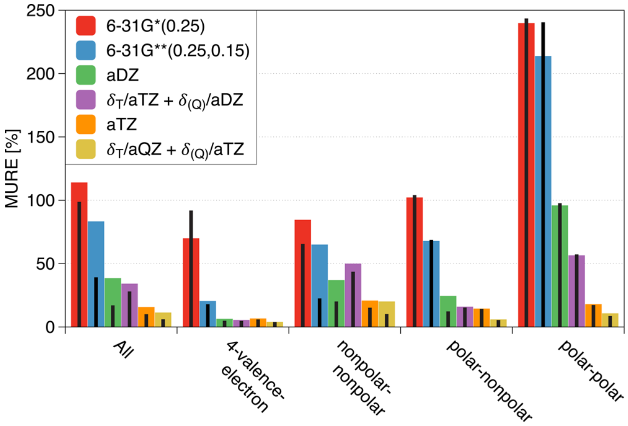

Figure 4. Performance of different basis sets in the recovery of the $\delta_{T+(Q)}$ benchmark (computed as a sum of the δ_T and $\delta_{(Q)}$ benchmarks obtained in separate extrapolations) displayed as mean unsigned relative errors (MURE). The black lines represent the median unsigned relative errors (MeURE).

exaggerated (no similar issues arise for $\delta_{(Q)}$ and $\delta_{T+(Q)}$). These systems are CH_4−CH_4, HF−HF, and Ar−HF, with the two largest-basis computed results, δ_T/a(X−1)Z and δ_T/aXZ, and the extrapolated δ_T/(a(X − 1)Z,aXZ) value amounting to (−1.403,−0.212,0.289) cm^{-1}, respectively, for CH_4−CH_4 (note that the correction is particularly poorly converged in this case because the aQZ value is not available), (0.91,0.52,0.24) cm^{-1} for HF−HF, and (−0.477,−0.238, 0.013) cm^{-1} for Ar−HF. Thus, the unsigned relative errors of even the largest-basis computed results (with respect to the extrapolated value) exceed 100% for these three systems. Therefore, to make the statistics in Figure 2 meaningful, the CH_4−CH_4, HF−HF, and Ar−HF complexes had to be excluded. Even after this exclusion, the 6-31G*(0.25) and 6-31G**(0.25,0.15) bases lead to δ_T errors of over 50% in all cases except the four-valence-electron dimers in the latter set. With the same exception of the four-valence-electron systems, the aDZ basis set is also inadequate for the δ_T term, with the largest errors (excluding the CH_4−CH_4, HF−HF, and Ar−HF complexes) of 144.3, 113.9, and 104.0% obtained for Ar−CH_4, NH_3−NH_3, and Ar−Ar, respectively. The percentage errors are particularly large for the polar−polar dimers: fortunately, these are also the systems where the post-CCSD(T) corrections are least important in relative terms, cf. Figure 1.

For the $\delta_{(Q)}$ contribution (Figure 3), the 6-31G*(0.25) and 6-31G**(0.25,0.15) basis sets give average errors close to 100% while the errors in the aDZ set are around 50%. Notably, the errors of $\delta_{(Q)}$ are quite similar across all classes of systems despite the vastly different relative importance of this correction (cf. Figure 1), making it particularly critical to converge this term for the nonpolar−nonpolar and polar−nonpolar dimers. The largest errors at the $\delta_{(Q)}$/aDZ level amount to 132.0, 119.9, and 71.6% for Ne−Ne, H_2−HF, and H_2O−H_2O (C_{2v}), respectively.

For most of the systems, if the $\delta_{(Q)}$ calculation is feasible up to the aXZ basis, the δ_T contribution can be obtained also in the a(X + 1)Z set. However, the statistical errors in Figure 4 indicate that the improvement of δ_T is not really beneficial unless one improves $\delta_{(Q)}$ at the same time. In fact, the δ_T/aTZ + $\delta_{(Q)}$/aDZ estimates perform only a little bit better than $\delta_{T+(Q)}$/aDZ (a MURE of 34.2% versus 38.6%), and δ_T/aQZ + $\delta_{(Q)}$/aTZ compared to $\delta_{T+(Q)}$/aTZ exhibits the same trend (a MURE of 11.4% versus 15.7% excluding the CH_4−CH_4 complex). Thus, a separate δ_T calculation using a basis set beyond the $\delta_{(Q)}$ capabilities is usually not worthwhile. The largest errors at the $\delta_{T+(Q)}$/aDZ level amount to 162.3, 122.2, and 98.5% for HF−HF, H_2O−H_2O (C_{2v}), and Ne−Ne, respectively, and clearly show that extreme caution is needed if one wishes to include post-CCSD(T) interaction energy contributions using basis sets of this size.

A. Anisotropy of the Post-CCSD(T) Contributions.

Except for the high-symmetry configurations of the H_2O−H_2O and N_2−N_2 complexes, the discussion so far concerned only geometries near the van der Waals minima. While the importance, and slow basis set convergence, of post-CCSD(T) effects at near-minimum geometries has been clearly illustrated, one could hope that these effects exhibit low anisotropy and effectively provide a nearly spherical contribution that has minimal effects on, say, spectral lines. Unfortunately, our benchmark calculations for several different angular configurations of LiH−LiH (Table SIII in the Supporting Information), H_2−CO (Table 8), and Ar−HF (Table 9) (the geometries for all configurations are given in the Supporting Information) indicate that the post-CCSD(T) contributions can have very strong anisotropy. For different orientations presented in Tables 8, 9 and SIII, the largest-basis (nonextrapolated) $\delta_{T+(Q)}$

Table 8. Anisotropy of Various Interaction Energy Components (in cm^{-1}) for the H_2−CO Complex and Two Basis Sets[a]

	(0°,0°,0°)	(0°,90°,0°)	(0°,180°,0°)	(45°,45°,45°)
		aDZ		
δ_T	−0.119	−0.291	−1.736	−0.226
$\delta_{(Q)}$	−0.174	−0.309	−0.794	−0.181
$\delta_{T+(Q)}$	−0.293	−0.600	−2.531	−0.406
CCSD(T)	−48.358	−16.553	−74.655	−20.352
		aTZ		
δ_T	−0.185	−0.214	−1.368	−0.154
$\delta_{(Q)}$	−0.219	−0.373	−1.055	−0.268
$\delta_{T+(Q)}$	−0.403	−0.587	−2.423	−0.421
CCSD(T)	−53.221	−18.475	−86.638	−23.799

[a] The intermolecular distance R is set to R = 8.0 bohr, whereas the intramolecular ones, r_{HH} and r_{CO}, are equal to 1.4487 bohr and 2.1399 bohr, respectively. The three angles are defined in the same way as in ref 68: the Cartesian coordinates for all four configurations are given in the Supporting Information.

Table 9. Interaction Energy Components (in cm^{-1}) for the Ar−HF Complex As Functions of the Angle θ between the Lines Going from the HF Center of Mass to the Ar and H Atoms[a]

θ	0°	90°	180°
		aDZ	
δ_T	−1.279	−0.267	−0.253
$\delta_{(Q)}$	−0.815	0.087	0.167
$\delta_{T+(Q)}$	−2.094	−0.180	−0.086
CCSD(T)	−98.690	−10.148	−43.114
		aTZ	
δ_T	−0.877	−0.233	0.172
$\delta_{(Q)}$	−1.920	−0.409	−0.296
$\delta_{T+(Q)}$	−2.797	−0.642	−0.124
CCSD(T)	−186.560	−53.046	−75.358

[a] The intermolecular distance R is set to R = 6.5 bohr and the intramolecular one r_{HF} is equal to 1.7629 bohr.

contributions constitute 0.2–0.9%, 0.8–3.2%, and 0.2–1.5% of the frozen-core CCSD(T) interaction energy for LiH–LiH, H_2–CO, and Ar–HF, respectively. Moreover, the basis set convergence varies significantly with geometry: for three of the H_2–CO configurations in Table 8, the aDZ basis set recovers 96–104% of the aTZ value for $\delta_{T+(Q)}$; however, for the remaining configuration, this percentage is 73%. The agreement between the two bases for three orientations is actually a consequence of error cancellation between the δ_T and $\delta_{(Q)}$ terms (for which the aDZ results constitute 64–147% and 68–83%, respectively, of the aTZ ones). Such a cancellation cannot be taken for granted and it does not occur for the fourth geometry. An even more striking example of error cancellation is the $\theta = 0°$ orientation of the Ar–HF complex. In this case, when the basis set is changed from aDZ to aTZ, the value of δ_T decreases by 31%, the value of $\delta_{(Q)}$ increases by 136%, whereas the total $\delta_{T+(Q)}$ term increases by 34%. For $\theta = 90°$, such cancellation is not present and the value of $\delta_{T+(Q)}$ for aTZ is over three times larger than for aDZ. For the test complexes and geometries presented in Tables 8, 9, and SIII, there does not appear to be a pattern of change in the anisotropy when the quality of the basis set is increased. Both absolute values of $\delta_{T+(Q)}$ and its relative values with respect to the CCSD(T) interaction energy can increase or decrease for different angular orientations of the interacting subsystems.

The results in Tables 8 and 9, and in Table SIII in the Supporting Information, show that the inclusion of a properly converged post-CCSD(T) interaction energy contribution is even more critical for the anisotropy of the potential energy surface than for the near-minimum interaction energy. The post-CCSD(T) contributions can be especially important for the relative depths of global and local minima or for the heights of energy barriers. For instance, for H_2–CO the difference of the $\delta_{T+(Q)}$ values between the (0°, 0°, 0°) and (0°, 180°, 0°) orientations is equal to 2.0 cm^{-1} while the difference of the CCSD(T) interaction energies for these geometries amounts to 33.4 cm^{-1}. Thus, the inclusion of the $\delta_{T+(Q)}$ interaction energy term changes the relative energy by 6%. Not surprisingly, the inclusion of interaction energy terms up to CCSDT(Q) proved essential for the recovery and assignment of the experimental high-resolution infrared spectrum of *ortho*-H_2–CO.[25,31]

B. MP2 Frozen Natural Orbital Approximation. In view of the highly unfavorable scaling of high-order coupled-cluster methods with the number of virtual orbitals it is desirable to introduce approximations that reduce this number without a significant adverse effect on the interaction energies. Several approaches to restrict the virtual space have been proposed:[63,64] in this work, we utilize the MP2 frozen natural orbital (FNO) approach[65] as implemented in CCSDT and CCSDT(Q) by Rolik and Kállay.[54] In the MP2 FNO method, the natural orbitals are obtained as eigenvectors of the first-order Møller–Plesset density matrix. The corresponding eigenvalues, that is, the natural orbital occupation numbers, are then sorted and the orbitals with sufficiently low occupations can be removed from the virtual space with little error. In the implementation of ref 54, a *cumulative* threshold ε_{FNO} is employed.[66] Specifically, natural orbitals are added to the virtual space, in the order of decreasing occupation numbers, until the cumulative occupation of all included orbitals (occupied and virtual) exceeds ε_{FNO} times the number of electrons. The remaining natural orbitals are removed from further consideration (care is taken to avoid splitting degenerate sets of orbitals). Rolik and Kállay[54] investigated the accuracy of the δ_T and $\delta_{(Q)}$ contributions to molecular energies and heats of formation as a function of ε_{FNO} and recommended a threshold of 0.975 for an optimal combination of accuracy and efficiency. Unfortunately, as we will show below, setting ε_{FNO} = 0.975 is not accurate enough for the small δ_T and $\delta_{(Q)}$ contributions to noncovalent interaction energies.

The convergence of the δ_T and $\delta_{(Q)}$ interaction energy contributions for the C_{2v} geometry of the water dimer as a function of the ε_{FNO} threshold is shown in Table 10. This convergence turns out to be quite slow: a threshold of 0.99 leads to an overestimation of the δ_T term up to six times. The $\delta_{(Q)}$ contribution is less sensitive to the FNO approximation: nevertheless, the error for ε_{FNO} = 0.99 amounts to 32% in the aDZ basis and 11% in aTZ. The results of Table 10 suggest that the minimum acceptable ε_{FNO} threshold for noncovalent interactions is 0.9999 for $\delta_{(Q)}$ (errors up to 16%) and 0.99999 for δ_T (errors up to 11%). Unfortunately, such tight thresholds correspond to a fairly small reduction of the virtual space so that the speedup afforded by the FNO approximation is quite limited. In fact, the C_{2v} water dimer (Table 10) is the only system for which we obtained, with significant computational effort, an FNO result (the $\delta_{(Q)}$/aQZ value) for which the corresponding nonapproximate value was out of reach. The $\delta_{(Q)}$/aQZ contribution for ε_{FNO} = 0.9999 can be expected to be accurate (the accuracy of the FNO $\delta_{(Q)}$ terms for a given threshold increases with the basis set size, cf. Table 10) and the quadruples contribution converges particularly slow for the water dimer (cf. Table 6), so the availability of the aQZ result thanks to the FNO approximation is quite helpful. However, this situation should be viewed as an exception rather than a rule as the FNO approach using reliable thresholds provides only modest performance gains (a similar ε_{FNO} = 0.9999 calculation would be unfeasible for the less symmetric, global-minimum geometry of the water dimer).

Table 10. Interaction Energy Contributions (in cm^{-1}) for the H_2O–H_2O (C_{2v}) Complex Calculated at Different FNO Thresholds ε_{FNO}[a]

ε_{FNO}	Nbf	CCSD(T)	δ_T	$\delta_{(Q)}$	$\delta_{T+(Q)}$
		aDZ			
0.99	50	−979.489	2.524	−0.966	1.558
0.999	64	−1021.655	1.465	−1.542	−0.077
0.9999	74	−1021.808	1.181	−0.611	0.570
0.999 99	78	−1026.659	1.136	−0.738	0.398
1	82	−1026.272	1.137	−0.730	0.407
		aTZ			
0.99	79	−963.346	1.953	−2.006	−0.053
0.999	126	−1078.499	0.999	−2.190	−1.191
0.9999	156	−1101.515	0.479	−2.124	−1.645
0.999 99	171	−1107.233	0.334	−2.249	−1.915
1	184	−1107.160	0.302	−2.264	−1.962
		aQZ			
0.99	99	−962.430	1.926	−2.390	−0.464
0.999	197	−1143.072	1.431	−2.458	−1.027
0.9999	271	−1136.522	0.696	−2.441	−1.745
1	344	−1141.024	0.552		

[a] The FNOs with the largest occupation numbers are retained until their cumulative occupation exceeds ε_{FNO} times the number of electrons; the remaining FNOs are discarded. A threshold of one represents the full calculation without any FNO truncation of basis functions. The quantity "Nbf" represents the number of basis functions after the FNO truncation.

C. Effects of the Frozen Core Approximation. In our calculations so far, only valence electrons were correlated. In contrast, the small-bases studies of Hobza et al.[19−21] correlated all electrons. Therefore, it is worth checking if the conclusions reached on the basis of the frozen-core calculations still hold when all-electron interaction energies are considered. As the importance of the core−core and core−valence correlation varies widely among the atoms present in our test systems, we decided to investigate the all-electron interaction energies for three dimers that represent the best- and worst-case scenarios: Ne−Ne (where the frozen-core approximation is expected to be very accurate), He−LiH, and LiH−LiH (for which the effects of the 1*s* lithium correlation can be significant). The all-electron results, in the same format as in Tables 1−7, are presented in Tables SIII (LiH−LiH) and SIV (He−LiH and Ne−Ne) in the Supporting Information. In addition to the 6-31G*(0.25), 6-31G**-(0.25,0.15), and a*XZ* results, we have listed the interaction energy contributions obtained in the polarized core and valence aug-cc-pCV*XZ*≡aCV*XZ* sequence.[67]

The results in Tables SIII and SIV in the Supporting Information indicate that, as expected, the interaction energy correction due to core−core and core−valence correlation amounts to a small fraction of the post-CCSD(T) correction for Ne−Ne, but completely dominates the latter for He−LiH and LiH−LiH. However, virtually all of this correction is recovered at the CCSD(T) level. In the largest aCV*XZ* basis sets considered, the core−core and core−valence correlation contribution constitutes 0−14% of δ_T and 3−25% of $\delta_{(Q)}$. While the all-electron δ_T and $\delta_{(Q)}$ corrections should formally be computed using the aCV*XZ* bases, the corresponding a*XZ* results turn out to provide very reasonable approximations. Overall, the results in Tables SIII and SIV indicate that the standard practice of treating the (CCSD(T)-level) core correlation and (frozen-core) post-CCSD(T) interaction energy corrections as additive[24,30,37,40] is well justified and that the basis set convergence patterns of the δ_T and $\delta_{(Q)}$ interaction energy components are very similar with and without the frozen core approximation.

IV. SUMMARY

We have studied the basis set convergence of the post-CCSD(T) coupled-cluster interaction energy contributions for 21 weakly bound dimers including the smallest members of the A24 set.[20] By performing CCSDT(Q) calculations in at least the aTZ basis set, and CCSDT calculations in at least aQZ (except for one system), we were able to assess the accuracy of small-basis results. We found that, unfortunately, the 6-31G*(0.25) and 6-31G**(0.25,0.15) bases suggested for post-CCSD(T) corrections by Hobza et al.[19−21] provide a very poor description of the CCSDT- and CCSDT(Q)-level effects, with mean unsigned relative errors for the $\delta_{T+(Q)}$ sum on the order of 80% for 6-31G**(0.25,0.15) and 110% for 6-31G*(0.25) (thus, it is often better to neglect the post-CCSD(T) terms completely than to estimate them using these small basis sets). Upgrading the basis set to aDZ reduces the average error to about 35%.

The overall importance of the post-CCSD(T) interaction energy contributions varies dramatically with the size and polarity of the monomers. In agreement with the findings of refs 19 and 21, and of earlier studies for individual complexes,[22,24] we observe that the full quadruples contribution δ_Q is negligible for all dimers except for N_2−N_2. However, the CCSDT and CCSDT(Q) corrections are generally of similar magnitude: the neglect of $\delta_{(Q)}$ is a viable approximation only for the four-electron dimers. The total $\delta_{T+(Q)}$ effect amounts to about 1−2% of the CCSD(T) interaction energy (less for the polar−polar dimers) and can contribute even more to the interaction energy anisotropy, making it critical to go up to CCSDT(Q) in the calculations of potential energy surfaces for high-resolution spectroscopic applications. On the average, the sum $\delta_{T+(Q)}$ converges a little faster (in relative terms) than the δ_T and $\delta_{(Q)}$ terms separately; however, the error cancellation between δ_T and $\delta_{(Q)}$ is by no means systematic.

Overall, the basis set convergence of the δ_T and $\delta_{(Q)}$ interaction energy contributions is somewhat disappointing. Even at the aTZ basis set level, the obtained corrections seem to be quite far from converging (we estimate the mean accuracy of the $\delta_{T+(Q)}$/aTZ estimate to be about 15%). Obtaining the benchmark $\delta_{T+(Q)}$/CBS value to within a few percent is only feasible for four-electron dimers (for which the convergence of the coupled-cluster expansion is particularly fast so that $\delta_{(Q)}$ is much smaller than δ_T). Thus, as observed in some recent potential energy surface studies,[24−26] the $\delta_{T+(Q)}$ terms, even computed in the aTZ basis or larger, remain one of the largest sources of residual uncertainty in the final potential as long as highly accurate CCSD(T)/CBS limits are obtained using state-of-the-art approaches. Thus, further research into the techniques that make high-order CC calculations more efficient is highly desired. One of such techniques, the MP2 frozen natural orbital approximation, was tested in this work with limited success. While this approximation provided the only way to obtain the $\delta_{(Q)}$/aQZ result for the C_{2v} water dimer, the required FNO thresholds were too tight to afford a significant decrease in the size of the virtual space. As the inclusion of interaction energy contributions through CCSDT(Q) has been integral to the development of top-accuracy interaction potentials in recent years, we are in a place where the δ_T and $\delta_{(Q)}$ calculations are both a necessity and a bottleneck. Thus, further improvements in the accuracy of potential energy surfaces hinge on the design of new accurate approximations, new basis sets specifically optimized for the post-CCSD(T) corrections, or both.

■ ASSOCIATED CONTENT

Ⓢ Supporting Information

Geometries and CCSD(T)/CBS interaction energies for all systems (Table SI), benchmark MP2, δ_{CCSD}, $\delta_{(T)}$, δ_T, $\delta_{(Q)}$, and δ_Q interaction energy contributions for all systems (Table SII), all-electron post-CCSD(T) contributions for selected systems (Tables SIII−SIV), and Cartesian coordinates for all complexes investigated in this work. This material is available free of charge via the Internet at http://pubs.acs.org/.

■ AUTHOR INFORMATION

Corresponding Author

*Email: patkowsk@auburn.edu.

Notes

The authors declare no competing financial interest.

■ ACKNOWLEDGMENTS

We thank Dr. Krzysztof Szalewicz for his inspiration and his help in establishing the collaboration that led to this work. D.G.A.S. and K.P. are supported by the U.S. National Science Foundation CAREER Award No. CHE-1351978 and by the startup funding from Auburn University. H.A.W. and M.S. acknowledge financial support from the National Science Council of Taiwan (NSC 102-2113-M-009-015-MY3) and from the Ministry of Education of Taiwan (MOE-ATU project).

REFERENCES

(1) Čížek, J. *J. Chem. Phys.* **1966**, *45*, 4256−4266.

(2) Paldus, J.; Čížek, J.; Shavitt, I. *Phys. Rev. A* **1972**, *5*, 50−67.

(3) Raghavachari, K.; Trucks, G. W.; Pople, J. A.; Head-Gordon, M. *Chem. Phys. Lett.* **1989**, *157*, 479−483.

(4) Jurečka, P.; Šponer, J.; Černý, J.; Hobza, P. *Phys. Chem. Chem. Phys.* **2006**, *8*, 1985−1993.

(5) Takatani, T.; Hohenstein, E. G.; Malagoli, M.; Marshall, M. S.; Sherrill, C. D. *J. Chem. Phys.* **2010**, *132*, 144104.

(6) Podeszwa, R.; Patkowski, K.; Szalewicz, K. *Phys. Chem. Chem. Phys.* **2010**, *12*, 5974−5979.

(7) Faver, J. C.; Benson, M. L.; He, X.; Roberts, B. P.; Wang, B.; Marshall, M. S.; Kennedy, M. R.; Sherrill, C. D.; Merz, K. M., Jr. *J. Chem. Theory Comput.* **2011**, *7*, 790−797.

(8) Řezáč, J.; Riley, K. E.; Hobza, P. *J. Chem. Theory Comput.* **2011**, *7*, 2427−2438.

(9) Halkier, A.; Helgaker, T.; Jørgensen, P.; Klopper, W.; Koch, H.; Olsen, J.; Wilson, A. K. *Chem. Phys. Lett.* **1998**, *286*, 243−252.

(10) Schwenke, D. W. *J. Chem. Phys.* **2005**, *122*, 014107.

(11) Tao, F.-M.; Pan, Y.-K. *J. Phys. Chem.* **1991**, *95*, 3582−3588.

(12) Hättig, C.; Klopper, W.; Köhn, A.; Tew, D. P. *Chem. Rev.* **2012**, *112*, 4−74.

(13) Kong, L.; Bischoff, F. A.; Valeev, E. F. *Chem. Rev.* **2012**, *112*, 75−107.

(14) Noga, J.; Bartlett, R. J. *J. Chem. Phys.* **1987**, *86*, 7041−7050.

(15) Bomble, Y. J.; Stanton, J. F.; Kállay, M.; Gauss, J. *J. Chem. Phys.* **2005**, *123*, 054101.

(16) Kállay, M.; Gauss, J. *J. Chem. Phys.* **2005**, *123*, 214105.

(17) Oliphant, N.; Adamowicz, L. *J. Chem. Phys.* **1991**, *94*, 1229−1235.

(18) Kucharski, S. A.; Bartlett, R. J. *Theor. Chim. Acta* **1991**, *80*, 387−405.

(19) Řezáč, J.; Šimová, L.; Hobza, P. *J. Chem. Theory Comput.* **2013**, *9*, 364−369.

(20) Řezáč, J.; Hobza, P. *J. Chem. Theory Comput.* **2013**, *9*, 2151−2155.

(21) Šimová, L.; Řezáč, J.; Hobza, P. *J. Chem. Theory Comput.* **2013**, *9*, 3420−3428.

(22) Noga, J.; Kállay, M.; Valiron, P. *Mol. Phys.* **2006**, *104*, 2337−2345.

(23) Jäger, B.; Hellmann, R.; Bich, E.; Vogel, E. *Mol. Phys.* **2009**, *107*, 2181−2188.

(24) Patkowski, K.; Szalewicz, K. *J. Chem. Phys.* **2010**, *133*, 094304.

(25) Jankowski, P.; Surin, L. A.; Potapov, A.; Schlemmer, S.; McKellar, A. R. W.; Szalewicz, K. *J. Chem. Phys.* **2013**, *138*, 084307.

(26) Smith, D. G. A.; Patkowski, K.; Trinh, D.; Balakrishnan, N.; Lee, T.-G.; Forrey, R. C.; Yang, B. H.; Stancil, P. C. *J. Phys. Chem. A* **2014**, DOI: 10.1021/jp412048w.

(27) Patkowski, K.; Cencek, W.; Jeziorska, M.; Jeziorski, B.; Szalewicz, K. *J. Phys. Chem. A* **2007**, *111*, 7611−7623.

(28) Bakr, B. W.; Smith, D. G. A.; Patkowski, K. *J. Chem. Phys.* **2013**, *139*, 144305.

(29) Patkowski, K.; Cencek, W.; Jankowski, P.; Szalewicz, K.; Mehl, J. B.; Garberoglio, G.; Harvey, A. H. *J. Chem. Phys.* **2008**, *129*, 094304.

(30) Hellmann, R.; Bich, E.; Vogel, E. *Mol. Phys.* **2008**, *106*, 133−140.

(31) Jankowski, P.; McKellar, A. R. W.; Szalewicz, K. *Science* **2012**, *336*, 1147−1150.

(32) Slawik, M.; Li, Y.-T.; Patkowski, K.; Jankowski, P.; Witek, H. A. (to be submitted).

(33) Jankowski, P. *J. Chem. Phys.* **2004**, *121*, 1655−1662.

(34) Jankowski, P.; Ziółkowski, M. *Mol. Phys.* **2006**, *104*, 2293−2302.

(35) Jankowski, P. *J. Chem. Phys.* **2008**, *128*, 154311.

(36) Hellmann, R. *Mol. Phys.* **2013**, *111*, 387−401.

(37) Lane, J. R. *J. Chem. Theory Comput.* **2013**, *9*, 316−323.

(38) Przybytek, M.; Patkowski, K.; Jeziorski, B. *Collect. Czech. Chem. Commun.* **2004**, *69*, 141−176.

(39) Pieniazek, P. A.; Arnstein, S. A.; Bradforth, S. E.; Krylov, A. I.; Sherrill, C. D. *J. Chem. Phys.* **2007**, *127*, 164110.

(40) Patkowski, K.; Podeszwa, R.; Szalewicz, K. *J. Phys. Chem. A* **2007**, *111*, 12822−12838.

(41) Šponer, J.; Leszczynski, J.; Hobza, P. *J. Phys. Chem.* **1996**, *100*, 1965−1974.

(42) Hobza, P.; Šponer, J. *Chem. Rev.* **1999**, *99*, 3247−3276.

(43) Dunning, T. H., Jr. *J. Chem. Phys.* **1989**, *90*, 1007−1023.

(44) Kendall, R. A.; Dunning, T. H., Jr.; Harrison, R. J. *J. Chem. Phys.* **1992**, *96*, 6796−6806.

(45) Dunning, T. H., Jr.; Peterson, K. A.; Wilson, A. K. *J. Chem. Phys.* **2001**, *114*, 9244−9253.

(46) Woon, D. E.; Dunning Jr., T. H. To be published.

(47) Schuchardt, K. L.; Didier, B. T.; Elsethagen, T.; Sun, L.; Gurumoorthi, V.; Chase, J.; Li, J.; Windus, T. L. *J. Chem. Inf. Model.* **2007**, *47*, 1045−1052.

(48) Prascher, B. P.; Woon, D. E.; Peterson, K. A.; Dunning, T. H., Jr; Wilson, A. K. *Theor. Chem. Acc.* **2011**, *128*, 69−82.

(49) Kállay, M.; Surján, P. R. *J. Chem. Phys.* **2001**, *115*, 2945−2954.

(50) MRCC, a quantum chemical program suite written by Kállay, M.; Rolik, Z.; Ladjánszki, I.; Szegedy, L.; Ladóczki, B.; Csontos, J.; Kornis, B. (a version from October 2013). See also http://www.mrcc.hu. (accessed June 2, 2014).

(51) Rolik, Z.; Szegedy, L.; Ladjánszki, I.; Ladóczki, B.; Kállay, M. *J. Chem. Phys.* **2013**, *139*, 094105.

(52) Werner, H.-J. et al. *MOLPRO, version 2012.1, a package of ab initio programs, 2012*, see http://www.molpro.net (accessed June 2, 2014).

(53) Stanton, J. et al. CFOUR, a quantum chemical program package, containing the integral packages MOLECULE (Almlöf, J.; Taylor, P.R.), PROPS (Taylor, P.R.), ABACUS (Helgaker, T.; Jensen, H.J. Aa.; Jørgensen, P.; Olsen, J.), and ECP routines by Mitin, A. V.; van Wüllen, C. For the current version, see http://www.cfour.de (accessed June 2, 2014).

(54) Rolik, Z.; Kállay, M. *J. Chem. Phys.* **2011**, *134*, 124111.

(55) McMahon, J. D.; Lane, J. R. *J. Chem. Phys.* **2011**, *135*, 154309.

(56) Patkowski, K. *J. Chem. Phys.* **2012**, *137*, 034103.

(57) Patkowski, K. *J. Chem. Phys.* **2013**, *138*, 154101.

(58) Burns, L. A.; Marshall, M. S.; Sherrill, C. D. *J. Chem. Theory Comput.* **2014**, *10*, 49−57.

(59) Mentel, Ł. M.; Baerends, E. J. *J. Chem. Theory Comput.* **2014**, *10*, 252−267.

(60) Burns, L. A.; Vazquez-Mayagoitia, A.; Sumpter, B. G.; Sherrill, C. D. *J. Chem. Phys.* **2011**, *134*, 084107.

(61) Marshall, M. S.; Burns, L. A.; Sherrill, C. D. *J. Chem. Phys.* **2011**, *135*, 194102.

(62) Rode, M.; Sadlej, J.; Moszyński, R.; Wormer, P. E. S.; van der Avoird, A. *Chem. Phys. Lett.* **1999**, *314*, 326−332.

(63) Adamowicz, L.; Bartlett, R. J. *J. Chem. Phys.* **1987**, *86*, 6314−6324.

(64) Neogrády, P.; Pitoňák, M.; Urban, M. *Mol. Phys.* **2005**, *103*, 2141−2157.

(65) Sosa, C.; Geertsen, J.; Trucks, G. W.; Bartlett, R. J.; Franz, J. A. *Chem. Phys. Lett.* **1989**, *159*, 148−154.

(66) Landau, A.; Khistyaev, K.; Dolgikh, S.; Krylov, A. I. *J. Chem. Phys.* **2010**, *132*, 014109.

(67) Peterson, K. A.; Dunning, T. H., Jr. *J. Chem. Phys.* **2002**, *117*, 10548−10560.

(68) Jankowski, P.; Szalewicz, K. *J. Chem. Phys.* **2005**, *123*, 104301.

Appendix B

Interactions between Methane and Polycyclic Aromatic Hydrocarbons: A High Accuracy Benchmark Study

JCTC Journal of Chemical Theory and Computation
Article
pubs.acs.org/JCTC

Interactions between Methane and Polycyclic Aromatic Hydrocarbons: A High Accuracy Benchmark Study

Daniel G. A. Smith and Konrad Patkowski*

Department of Chemistry and Biochemistry, Auburn University, Auburn, Alabama 36849, United States

Ⓢ *Supporting Information*

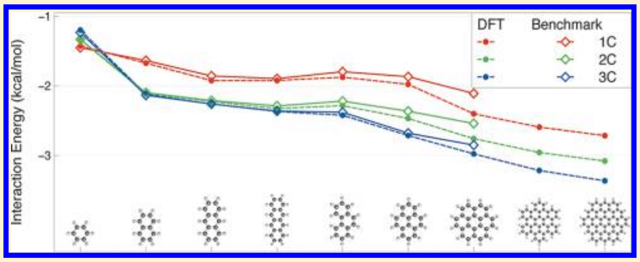

ABSTRACT: Minimum energy structures and interaction energies are obtained for a series of polycyclic aromatic hydrocarbons (PAHs) interacting with a methane molecule. The PAHs include benzene, naphthalene, anthracene, phenanthrene, tetracene, pyrene, and coronene. Interaction energies are calculated using the highest level of theory and basis set available, that is, complete-basis-set extrapolated MP2 plus a conventional or explicitly correlated CCSD(T) correction in moderately sized basis sets. The results show that the singly coordinated minimum configuration observed earlier for benzene−methane is no longer the global minimum one for naphthalene and larger PAHs. Instead, triply coordinated geometries are lower in energy. The global minimum structures for methane interacting with extended systems like graphene sheets and carbon nanotubes are likely to be triply coordinated as well. A variety of novel dispersion-including DFT approaches are compared against the wave-function-based benchmark potential energy curves. The top performer, the B3LYP functional combined with the -D3 dispersion correction, is then employed to calculate interaction energies for methane interacting with hexabenzocoronene and circumcoronene in order to estimate the methane adsorption energy on graphite. The delicate balance between dispersion and exchange in PAH−methane interactions is elucidated using symmetry-adapted perturbation theory with a DFT description of monomers. The present study provides an important benchmark for the design and tuning of more approximate methods for an accurate description of hydrocarbon physisorption on carbon nanostructures.

1. INTRODUCTION

Weak intermolecular interactions, especially those dominated by dispersion, are a challenge for *ab initio* quantum chemistry because of a simultaneous need for a nearly complete one-electron basis set and a high-level treatment of electron correlation.[1] Fulfilling the first of these needs is substantially aided by complete-basis-set (CBS) extrapolations,[2,3] bond functions,[4] and, most recently, the explicitly correlated R12 and F12 approaches.[5,6] As far as the second need is concerned, the "gold standard" of electronic structure theory, the single-reference coupled-cluster method with single, double, and noniterative triple excitations [CCSD(T)], provides weak interaction energies accurate to a few percent (with a notable exception of systems where significant static correlation is present[7]) as long as the basis set is sufficiently large. However, the computational cost of a CCSD(T) calculation scales like N^7 with the system size and becomes prohibitively expensive even for moderately large dimers. Therefore, significant effort is being invested in devising methods that produce accurate weak interaction energies and exhibit a more favorable scaling. While density functional theory (DFT) using standard functionals fails remarkably for dispersion-dominated interaction energies,[8,9] many novel DFT approaches are quite successful at accounting for dispersion.[10−21] At the same time, the typical overestimation of dispersion by second-order Møller−Plesset perturbation theory (MP2) is addressed by various spin-component-scaled and related wave-function-based approaches.[22−26] Hybrid wave-function-DFT methods[27−30] also deliver comparable accuracy. The DFT- and MP2-based approaches scale like N^4 or N^5 and can be applied to interactions of much larger systems than CCSD(T). On the other hand, the accuracy of these methods varies, and extensive benchmarking is necessary to determine which of them are appropriate for studying weak interactions at a desired level of accuracy.

The set of high-quality benchmark interaction energies available today is quite impressive. While most older benchmark sets focused on interaction energies near the respective van der Waals minima,[31−33] it was realized, most notably by Sherrill and collaborators, that the accuracy at the minima is not necessarily retained throughout the entire range of intermolecular distances. Therefore, newer benchmark sets include intermolecular distances both smaller and larger than the minimum separations.[34−37] At the same time, the accuracy of some of the older benchmarks, most notably the S22 set,[33] was considerably improved.[38−41] Extensive studies of the performance of various approximate DFT- and MP2-based approaches have been carried out,[42] and while some methods are clearly better than others, there is no single winner that accurately

Received: October 11, 2012
Published: November 7, 2012

dx.doi.org/10.1021/ct3008809 | *J. Chem. Theory Comput.* 2013, 9, 370−389

reproduces high-accuracy benchmark interaction energies across the entire spectrum of systems. Therefore, any application of approximate DFT or wave function theories to a class of systems of practical interest should be accompanied by a verification that the chosen approach satisfactorily recovers benchmark interaction energies for similar systems. Such a verification is the heart of the present work, and the goal behind it is a better understanding of hydrocarbon physisorption on graphene sheets[43] and carbon nanotubes.[44]

The adsorption of molecules on carbon nanostructures has been the subject of numerous experimental and theoretical studies.[45] The ability of graphene and nanotubes to effectively bind hydrogen makes these structures a viable medium for hydrogen storage,[46] a critical issue on the road toward clean hydrogen-based energy. The adsorption of methane, and of other small hydrocarbons, on carbon nanostructures is another highly active area of research due to its importance for natural gas storage, transport, fuel-cell combustion, and detection.[47,48] It should be noted that physisorption, the process of binding molecules (adsorbates) to surfaces via van der Waals forces,[49] is inherently harder to model computationally[50] than chemisorption (where the adsorbate−surface bonds are covalent). In particular, an accurate treatment of dispersion energy is absolutely crucial. Nevertheless, the majority of existing computational studies of physisorption use either empirical, Lennard-Jones interaction potentials, or standard density functionals like LDA, B3LYP,[51,52] or PBE.[53] While such approaches can yield useful qualitative results,[54−56] their accuracy is inherently limited. Indeed, studies for model systems indicate that the performance of standard density functionals for carbon-nanostructure adsorption is inferior[57] to that of novel functionals like M05-2X.[13] The use of state-of-the-art accurate N^4 and/or N^5 methods, paired with their careful benchmarking against near-CBS CCSD(T) interaction energies, is required to develop more accurate physisorption potentials. For the hydrocarbon physisorption on carbon nanostructures, the natural choice of model systems for benchmarking is polycyclic aromatic hydrocarbons (PAHs) interacting with methane. The PAHs investigated in this work include benzene, naphthalene, anthracene, tetracene, phenanthrene, pyrene, and coronene.

The benzene−methane complex has been extensively studied using accurate *ab initio* methods (in particular, as a member of the S22[33,39,40] and NBC10[34] test sets). However, CCSD(T)-level interaction energies for complexes of methane with larger PAHs are virtually limited to a single study by Tsuzuki et al.[58] In this reference, lowest-energy structures of the benzene−methane, naphthalene−methane, and pyrene−methane complexes were determined using MP2 calculations in bases up to cc-pVQZ (nonaugmented correlation-consistent quadruple-ζ[59]) plus a CCSD(T) correction in a very small 6-31G* basis. Tsuzuki et al.[58] found that the singly coordinated (1C) structure (with only one of the methane hydrogen atoms closer to the PAH plane than the methane carbon atom) of the benzene−methane global minimum ceases to be the lowest-energy structure for larger PAHs in favor of the doubly coordinated (2C) and triply coordinated (3C) configurations (for which two and three methane hydrogens, respectively, are closer to the PAH plane than the methane carbon). On the basis of the observations of ref 58, it is likely that the benzene−methane complex is an exception rather than the rule, and one needs to go to larger PAHs to even qualitatively recover the adsorption characteristics of extended carbon nanostructures. At the same time, the results of ref 58 are clearly not converged with respect to the basis set, and their accuracy warrants further investigation.

In this work, accurate *ab initio* interaction energies are obtained for the lowest-energy structures of PAH−methane dimers (one lowest-energy structure for each coordination: 1C, 2C, and 3C). We will follow the standard technique employed to generate benchmark interaction energy databases[33] and compute interaction energies as sums of the CBS-extrapolated MP2 contribution and a CCSD(T) correction. The interaction energies obtained in this way for one-dimensional cuts through the potential energy surfaces (passing through the lowest-energy 1C, 2C, and 3C configurations) are then used to gauge the accuracy of a number of modern dispersion-including DFT approaches. Additionally, the relative importance of different interaction energy contributions (electrostatics, induction, dispersion, and exchange) is studied using symmetry-adapted perturbation theory with a DFT description of monomers [SAPT(DFT)].[27,28] The observed trends in the binding energies for different coordinations allow for improved predictions of the adsorption energetics of methane on extended carbon nanostructures. Our approach is somewhat similar in spirit to the hydrogen adsorption study of ref 60 and the water adsorption study of ref 61, where accurate benchmark interaction energies for medium-sized models were used to extrapolate to the case of an infinite graphene sheet. However, our study involves a larger variety of wave-function- and DFT-based approaches all the way through CCSD(T) while refs 60 and 61 employed more approximate DFT/CC and SAPT(DFT) methods, respectively. It should be noted that an extension of our wave function calculations to still larger PAHs, apart from being computationally unfeasible at present, would encounter a serious problem as the increasingly polyradical character of large PAHs[62] inevitably breaks down the single-reference CCSD(T) treatment at some point. Fortunately, such a breakdown does not yet occur for systems studied here, as indicated by reasonably low values of the T1 and D1 coupled-cluster diagnostics.[63]

The structure of the rest of this paper is as follows. In Section 2, the approach used to obtain benchmark interaction energies is specified together with the approximate *ab initio* methods employed and the relevant computational details. The numerical results are presented and discussed in Section 3. Finally, Section 4 presents conclusions.

2. METHODOLOGY AND COMPUTATIONAL DETAILS

The Molpro code[64] was used to obtain all the MP2 and CCSD(T) interaction energies. The MP2 computations utilized density fitting (DF)[65] and employed standard orbital and auxiliary bases aug-cc-pV*X*Z[59,66] and aug-cc-pV*X*Z/MP2FIT,[67,68] respectively. The DF-HF interaction energy and the correlation part of the DF-MP2 interaction energy exhibit mean unsigned errors (MUE; averaged over all benzene−methane and naphthalene−methane complexes at the aug-cc-pVTZ level) of 0.005 and 0.001 kcal/mol, respectively, with respect to the non-density-fitted results. For the points where the comparison is possible at the aug-cc-pVQZ level, the DF-HF error further decreases to 0.001 kcal/mol, and the DF-MP2 error is reduced below convergence thresholds. It is worth noting that the sign and magnitude of the errors remain practically constant across the entire potential curve. As the computational cost of DF-MP2 is a small fraction of that of conventional MP2, only DF-MP2 calculations are feasible in

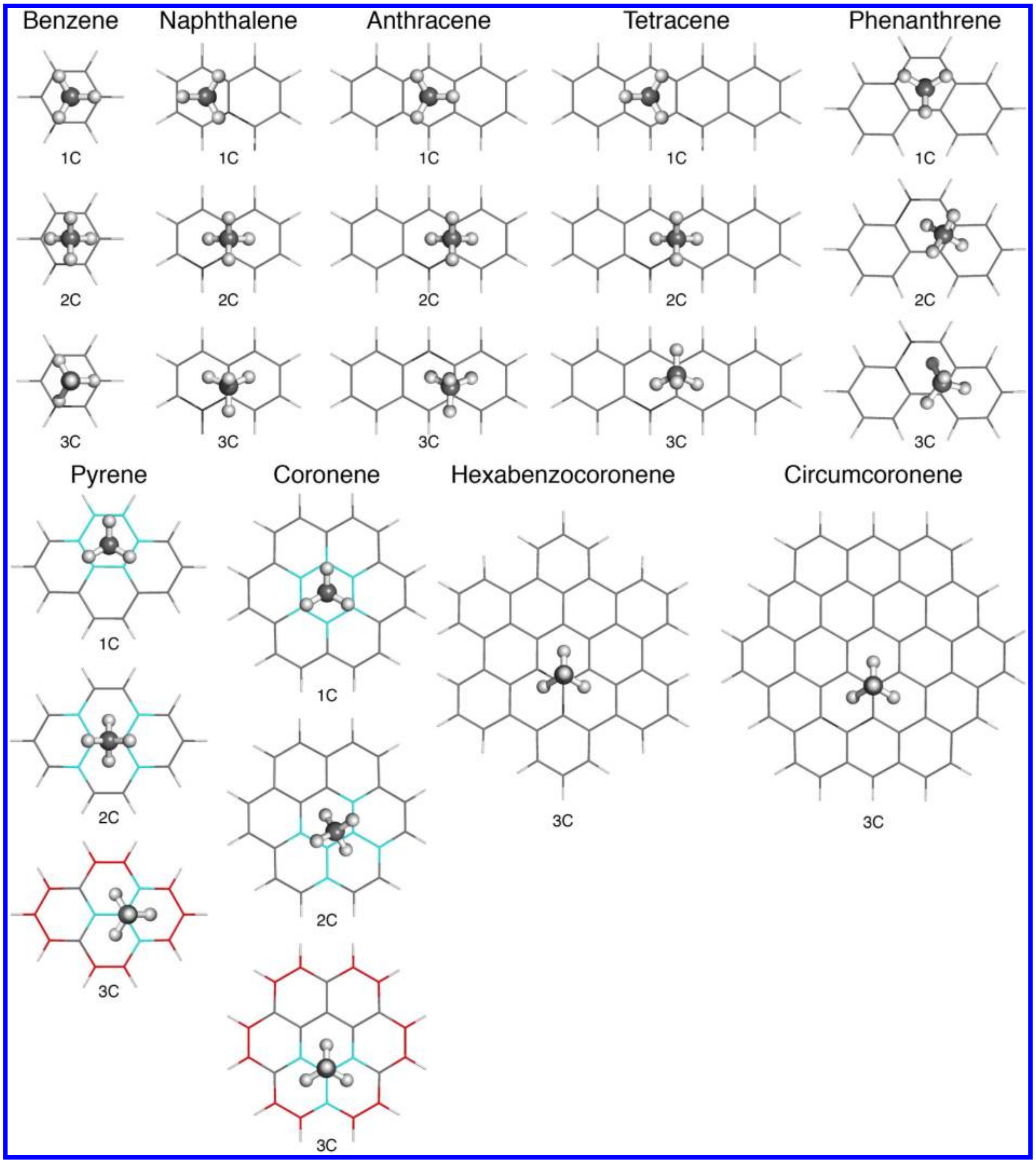

Figure 1. The optimized 1C, 2C, and 3C structures for all dimers considered in the present work. The colors on the pyrene and coronene structures mark carbon atoms that are assigned differently augmented basis sets within the core-DZ and local-DZ approaches—see section 3.1 for details.

quadruple- and quintuple-zeta bases. The "DF-" qualifier will be dropped from now on. The CCSD(T) calculations were performed in the conventional, non-density-fitted way and utilized the aug-cc-pV*X*Z bases. For basis sets involving midbond functions, the additional functions were located halfway between the carbon atom of the methane molecule and the plane of the PAH. These functions were chosen as the hydrogenic set from the same aug-cc-pV*X*Z orbital basis as the atom-centered functions. Unless otherwise stated, all calculations employed the counterpoise (CP) correction for basis set superposition error.[69,70] The 1s carbon electrons were not correlated.

2.1. Geometry Optimizations. To obtain the lowest-energy configurations for each coordination, a three-dimensional scan of the potential energy surface (PES) for a given orientation of methane was first completed at the MP2/aug-cc-pVDZ level, and the most favorable location of methane was narrowed down to 0.01 Å. Full counterpoise-corrected six-dimensional geometry optimizations (that is, only the intramolecular degrees of freedom were frozen) were then run at the MP2/aug-cc-pVTZ level to find the final geometries. The lowest-energy configurations for all three coordinations represent some local minima on the full six-dimensional PES except for 1C phenanthrene−methane and 1C tetracene−methane. The most relevant one-dimensional cuts through the

PES, along the direction z perpendicular to the PAH plane, are then examined. The values of z given throughout the rest of the text are the distances between the methane carbon and the PAH plane. The lowest-energy geometries for each dimer and each coordination are displayed in Figure 1.

2.2. Benchmark Energies from Wave Function Methods.

Following the standard practice in the field,[33] the benchmark interaction energy is calculated as

$$E_{\text{int}}^{\text{benchmark}} = E_{\text{int}}^{\text{MP2}}(\text{aug-cc-pV}(X-1)\text{Z}, \text{aug-cc-pV}X\text{Z}) + \Delta E_{\text{int}}^{\text{CCSD(T)}}(\text{aug-cc-pV}(X'-1)\text{Z}, \text{aug-cc-pV}X'\text{Z}) \qquad (1)$$

where $E_{\text{int}}^{\text{X}} = E_{\text{AB}}^{\text{X}} - E_{\text{A}}^{\text{X}} - E_{\text{B}}^{\text{X}}$ is the supermolecular interaction energy at a given level of theory, $\Delta E_{\text{int}}^{\text{CCSD(T)}} = E_{\text{int}}^{\text{CCSD(T)}} - E_{\text{int}}^{\text{MP2}}$ is the CCSD(T) contribution missing at the MP2 level, and the notation (basis1,basis2) means that the bases "basis1" and "basis2" have been employed in the standard X^{-3} extrapolation for the correlation part of the interaction energy.[2] The SCF part of the interaction energy was taken from the calculation using the larger of the two bases and not extrapolated. We will employ the short-hand notation MP2/(X − 1,X) and ΔCCSD(T)/(X − 1,X) for $E_{\text{int}}^{\text{MP2}}$ (aug-cc-pV(X − 1)Z,aug-cc-pVXZ) and $\Delta E_{\text{int}}^{\text{CCSD(T)}}$ (aug-cc-pV(X − 1)Z,aug-cc-pVXZ), respectively. Moreover, ΔCCSD(T)/aXZ will denote a correction that is computed in the aug-cc-pVXZ≡aXZ basis set and not extrapolated.

To investigate the basis set convergence of the ΔCCSD(T) contribution, explicitly correlated CCSD(T)-F12 calculations were performed for benzene−methane and naphthalene−methane using the MOLPRO[64] code. The CCSD(T)-F12a and CCSD(T)-F12b approximations[71,72] employ the default explicitly correlated *Ansätze*, geminal parameters, and auxiliary bases. Because the triples contributions to CCSD(T)-F12a and CCSD(T)-F12b do not include explicit correlation (an explicitly correlated (T) correction has been derived only recently[73] and exhibits a steeper computational scaling), we tested the popular estimate of the missing F12 contributions to $\Delta E^{(\text{T})} = E^{\text{CCSD(T)}} - E^{\text{CCSD}}$ via scaling:

$$\Delta E^{(\text{T})-\text{F12}} \approx \Delta E^{(\text{T})} \cdot \frac{E_{\text{corr}}^{\text{MP2}-\text{F12}}}{E_{\text{corr}}^{\text{MP2}}} \qquad (2)$$

where the subscript "corr" denotes the correlation energy at a given level of theory. To ensure size consistency, the scaling factor determined for the dimer was also used in the counterpoise-corrected calculations for monomers.[38] The CCSD(T)-F12 approach in its various approximate variants provides greatly improved weak interaction energies in double- and triple-ζ basis sets compared to conventional CCSD(T)[38,74,75] (however, the improvement is somewhat diminished in larger basis sets[76,77]). For the popular S22 database[33] that includes the benzene−methane complex, the MUE of the scaled-triples CCSD(T)-F12b/aDZ method amounts to 0.10 kcal/mol, about a 4-fold improvement over conventional CCSD(T).[75,78]

2.3. DFT Calculations.

Out of the many novel variants of DFT proposed to overcome the failure to recover dispersion, the two main groups are the DFT+D approaches (where a more or less empirical dispersion correction is added on top of a standard density-functional calculation) and the functionals specifically optimized for benchmark weak interaction energies. In this work, we tested a few representative members of each group. For DFT+D, we employed the widely popular B3LYP[51,52] and PBE[53] functionals as well as Grimme's reparameterization[12] of Becke's B97 functional.[79] These three functionals were augmented by Grimme's empirical dispersion terms in the -D2[12] and -D3[19] variants. The -D2 and -D3 corrections were calculated using Grimme's DFT+D program V2.1 Rev 6.

The DFT+D interaction energies were calculated using MOLPRO 2010.1[64] locally modified to include Grimme's reparameterization of B97. The requested energy convergence threshold was 10^{-7} hartree, and the corresponding autogenerated MOLPRO grids were used. The calculations employed density fitting with the standard cc-pVXZ/JKFIT auxiliary basis sets.[80] It should be noted that the version of B3LYP used was equivalent to the B3LYP card in Gaussian[81] so that the correlation functional contained a VWN3 contribution, not VWN5.[82] As the CP correction is by no means guaranteed to improve DFT results even for dispersion-bound systems, all DFT variants were tested both with and without it.

The second group, the interaction-optimized functionals, included M05-2X,[13] M06-2X,[16] and ωB97X-D.[15] All interaction energies for these functionals were calculated by Gaussian 09[81] using the UltraFine grid that corresponds to a pruned set of 99 radial shells and 590 angular points per atom. While the size of the grid is fairly large, the M05-2X and M06-2X meta-GGA functionals still exhibit small "wiggles" in the interaction potential, especially at medium distances. This effect, which has been noted before for functionals of this kind,[83] could be avoided at still larger grid sizes; however, this would not change any of our conclusions regarding the selection of the best functional(s).

2.4. SAPT(DFT) Analysis.

The density-fitted SAPT(DFT) approach[27] (also termed DFT-SAPT[28]) was used to examine the importance of different contributions to the interaction energy. The monomer DFT calculations employed the PBE0 functional[53,84] and were performed using the DALTON code.[85] The developers' version of the SAPT2008 code[86] was used for the subsequent computation of SAPT(DFT) corrections. The Fermi−Amaldi−Tozer−Handy asymptotic correction[87] was employed in all SAPT(DFT) computations, with the monomer ionization potentials taken from the NIST Webbook.[88] The coupled Kohn−Sham (CKS) values of the exchange-induction and exchange-dispersion corrections were computed exactly rather than estimated by scaling the uncoupled results. These exchange corrections were included in the SAPT(DFT) estimates of induction and dispersion energy, respectively, as in previous work.[18] This is especially important for the induction correction which is known to exhibit significant quenching by its exchange-induction counterpart.[89,90]

2.5. Statistical Analysis of Approximate Approaches.

At the time when benchmark databases of weak interaction energies contained only near-minimum geometries, the natural measures of the accuracy of a given approximate approach were the mean unsigned error (MUE) and mean unsigned relative error (MURE).[91] For benchmarks that encompass different regions of the PES, neither quantity is, however, particularly relevant. As the energies for different intermolecular separations are widely different, the MUE is strongly influenced by the relative abundance of points from different regions (repulsive, near-minimum, and asymptotic) in the test set. Therefore, the MUE values presented here will refer to the minimum intermolecular separations only and will not include any data for other separations (we will use the name "minima MUE").

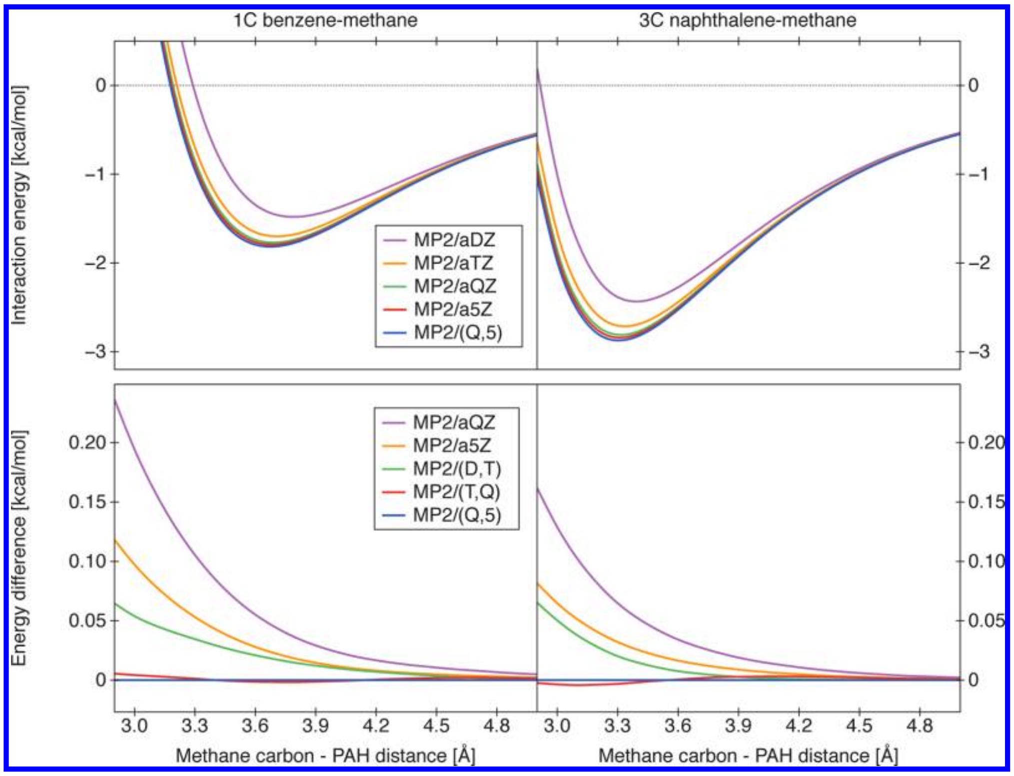

Figure 2. CP-corrected MP2/FC interaction energies (in kcal/mol) for the 1C benzene−methane (left panels) and 3C naphthalene−methane (right panels) complexes as functions of the methane carbon−PAH plane distance *z* (in Ångstroms). The upper panels display total interaction energies, while the lower panels show interaction energy differences with respect to the highest-level MP2/(Q,5) results.

Table 1. The MP2 and ΔCCSD(T) Contributions to the Benzene−Methane Interaction Energy at the Global-Minimum 1C Configuration with the Methane Carbon−PAH Plane Distance of 3.76 Å[a]

	without midbond				with midbond			
method	D	T	Q	5	D	T	Q	5
MP2	−1.478	−1.691	−1.754	−1.774	−1.551	−1.724	−1.765	−1.780
ext.		−1.777	−1.795	−1.793		−1.794	−1.795	−1.794
MP2-F12	−1.745	−1.785	−1.792	−1.794	−1.760	−1.789	−1.793	−1.794
ext.		−1.802	−1.795	−1.795		−1.803	−1.795	−1.795
ΔCCSD(T)	0.326	0.339	0.349		0.322	0.340	0.352	
ext.		0.345	0.356			0.348	0.360	
ΔCCSD(T)-F12a	0.358	0.358	0.359		0.352	0.356	0.360	
ext.		0.358	0.360			0.358	0.362	
ΔCCSD(T)-F12b	0.343	0.354	0.358		0.330	0.350	0.357	
ext.		0.359	0.361			0.358	0.362	
CCSD(T)/(*X*−1,*X*)		−1.438	−1.440			−1.448	−1.435	
MP2/(Q,5)+ΔCCSD(T)/a*XZ*	−1.468	−1.455	−1.445		−1.472	−1.454	−1.442	
MP2/(Q,5)+ΔCCSD(T)/(*X*−1,*X*)		−1.449	−1.437			−1.446	−1.433	
CCSD(T)-F12a/(*X*−1,*X*)		−1.449	−1.435			−1.447	−1.434	
MP2-F12/(Q,5)+ΔCCSD(T)-F12a/a*XZ*	−1.436	−1.436	−1.434		−1.441	−1.437	−1.434	
MP2-F12/(Q,5)+ΔCCSD(T)-F12a/(*X*−1,*X*)		−1.436	−1.433			−1.436	−1.432	
CCSD(T)-F12b/(*X*−1,*X*)		−1.448	−1.434			−1.447	−1.434	
MP2-F12/(Q,5)+ΔCCSD(T)-F12b/a*XZ*	−1.450	−1.439	−1.435		−1.463	−1.444	−1.437	
MP2-F12/(Q,5)+ΔCCSD(T)-F12b/(*X*−1,*X*)		−1.435	−1.432			−1.436	−1.431	

[a] Conventional and explicitly correlated results in a*XZ* bases with and without midbond functions (see text for the details of bond functions) are shown as functions of *X*. The rows marked "ext." display the CBS-extrapolated results where the values in the "*X*" column were obtained using the (*X*−1,*X*) extrapolation. The bottom part of the table contains different estimates of the total CCSD(T)/CBS interaction energy. The (T) triples correction was not scaled in CCSD(T)-F12a but scaled in CCSD(T)-F12b. The energy unit is 1 kcal/mol.

The MURE is, in turn, often dominated by a single data point close to where the interaction energy crosses zero. To avoid this artifactual domination, several modified quantities have been proposed including an energy-dependent weighted average of the relative errors[36] and the *median* unsigned relative error.[92] We will present the latter quantity, averaged over all data points at all intermolecular separations, and denote it as MeURE to stress the difference with respect to the conventional MURE. Additionally, in order to assess the accuracy of the minimum geometries (across a given one-dimensional cut) predicted by different methods, we will use the "minima z difference", the mean absolute deviation of the lowest-energy intermolecular distance z predicted by a given approach from the benchmark value.

3. NUMERICAL RESULTS AND DISCUSSION

3.1. Benchmark Interaction Energies. In this section, we describe how the benchmark wave-function-based PAH−methane interaction energies were obtained using large-basis MP2 and CCSD(T) calculations. The quality of different approximations to the CCSD(T) CBS limit will first be assessed based on the results for the two smallest dimers, benzene−methane and naphthalene−methane. The observations made for these two systems will allow us to select the algorithms to compute benchmark CCSD(T)/CBS interaction energies for larger systems and to estimate their accuracy.

The MP2 interaction energies as functions of the methane carbon−PAH plane distance z are displayed in Figure 2 for 1C benzene−methane (left panels) and 3C naphthalene−methane (right panels). The upper panels in Figure 2 show absolute interaction energies, while the lower panels display differences between various calculated and extrapolated results. The results presented in Figure 2 show that the MP2 interaction energies exhibit smooth convergence with the basis set cardinal number X. This convergence is consistent with the X^{-3} dependence of the correlation energy. As a result, CBS extrapolation improves the results substantially. The smallest-basis extrapolated values, MP2/(D,T), are consistently more accurate than the largest-basis nonextrapolated ones, MP2/a5Z, and the MP2/(T,Q) results are virtually identical to MP2/(Q,5). Thus, basis sets as small as aTZ can be used in the MP2 component as long as the CBS extrapolation is performed.

It is obviously not possible to achieve the same level of basis set saturation in the CCSD(T) approach. Therefore, to understand the effect of basis set size, we first focused on the 1C global minimum of the benzene−methane dimer and obtained an extended set of CCSD(T) interaction energies including results in basis sets up to aQZ, results in bases containing midbond functions, and approximate CCSD(T)-F12 energies. The MP2 and ΔCCSD(T) interaction energy contributions obtained in this way have been gathered in Table 1. The same table contains estimates of the total interaction energy obtained by a straightforward CBS extrapolation of the CCSD(T) results or an augmentation of the MP2/CBS value with the ΔCCSD(T) correction that is either computed or CBS-extrapolated. The main purpose of Table 1 is to assess the accuracy to which the CBS limit can be determined when the system size limits the CCSD(T) basis set choice to aTZ (as is the case for naphthalene−methane) or aDZ (for all PAHs larger than naphthalene). We tested the CCSD(T)-F12 approach with and without the scaling of triples, eq 2, and found that the scaling is beneficial for CCSD(T)-F12b but harmful for CCSD(T)-F12a (the latter observation indicates that the CCSD(T)-F12a approach, formally more approximate than CCSD(T)-F12b,[71] strongly benefits from a cancellation of errors between the CCSD part and the triples part[77]). Therefore, only the unscaled-triples CCSD(T)-F12a results and scaled-triples CCSD(T)-F12b results are listed in Table 1. The interaction energies from all four CCSD(T)-F12 variants can be found in Table SI in the Supporting Information.

The nonextrapolated MP2 and MP2-F12 results in Table 1 all converge smoothly to the CBS limit and demonstrate that the addition of F12 helps more than the addition of midbond functions. Nevertheless, the MP2-F12 results with bond functions are the best out of the four variants. The best non-F12 interaction energy, the a5Z+midbond result, is surpassed in accuracy by MP2-F12 at the aTZ level without midbond functions. Since the interaction energies increase smoothly with the basis set size for all sequences, extrapolation greatly improves the results. All (T,Q) and (Q,5) extrapolated values agree to within 0.002 kcal/mol, and we can establish the value −1.794 ± 0.001 kcal/mol as the benchmark MP2 interaction energy. Although the F12 approach greatly improves the computed MP2 values, Table 1 shows that the non-F12 results become just as accurate upon extrapolation. As all of the MP2 benchmarks for larger systems will be obtained from extrapolations at the (T,Q) or (Q,5) levels, no explicitly correlated treatment of the MP2 contribution will be necessary.

The ΔCCSD(T) corrections shown in Table 1 demonstrate a moderately fast convergence with the basis set size. Extrapolation does assist in the convergence of ΔCCSD(T); however, the results extrapolated from different sequences vary somewhat. The CCSD(T)-F12 approaches, especially CCSD(T)-F12a, exhibit a faster convergence than conventional CCSD(T). The convergence of ΔCCSD(T)-F12 is smooth for all variants, and extrapolation works very well, with all extrapolated values within 0.004 kcal/mol of each other. The results in Table 1 indicate a benchmark ΔCCSD(T) value of 0.361 ± 0.001 kcal/mol (encompassing all (T,Q)-extrapolated results except for the least accurate one, the conventional CCSD(T) value without midbond functions), which corresponds to the total CCSD(T) interaction energy of −1.433 ± 0.002 kcal/mol.

It is not possible to perform CCSD(T)/aQZ calculations for systems larger than benzene−methane. If the CCSD(T)/aTZ calculations are feasible (as is the case for the naphthalene−methane complex), there exist four sensible ways of estimating the benchmark CCSD(T)/CBS limit from either conventional or explicitly correlated calculations: CCSD(T)/(D,T), MP2/(Q,5)+ΔCCSD(T)/(D,T), MP2/(Q,5)+ΔCCSD(T)/aTZ, and MP2/(Q,5)+ΔCCSD(T)/aDZ. As shown in Table 1, for benzene−methane, these four variants lead to absolute errors of 0.005−0.035 kcal/mol compared to the benchmark interaction energy established using (T,Q) extrapolations of the ΔCCSD(T) term. The addition of midbond functions does not lead to an overall error reduction, and such functions will not be used for subsequent dimers. On the other hand, the explicitly correlated approach clearly improves the basis set convergence, and the F12a- and F12b-based results become virtually identical upon extrapolation. As the accuracy of the (unscaled-triples) F12a approach is probably quite accidental, we will focus on the F12b variant. Out of the four CCSD(T)-F12b-based estimates, the most accurate MP2-F12/(Q,5)+ΔCCSD(T)-F12b/(D,T) approach, with an error of just −0.002 kcal/mol, is also preferred on theoretical grounds as it involves the largest basis sets at each level of theory. As

Table 2. The MP2 and ΔCCSD(T) Contributions to the Naphthalene−Methane Interaction Energy at the Minimum Configurations for Each of the Three Coordinations[a]

	1C configuration				2C configuration				3C configuration			
method	D	T	Q	5	D	T	Q	5	D	T	Q	5
MP2	−1.820	−2.022	−2.080	−2.098	−2.372	−2.619	−2.696	−2.721	−2.433	−2.685	−2.765	−2.791
ext.		−2.102	−2.118	−2.117		−2.730	−2.747	−2.746		−2.801	−2.817	−2.816
ΔCCSD(T)	0.462	0.476			0.624	0.642			0.657	0.677		
ext.		0.483				0.650				0.683		
CCSD(T)/(X−1,X)		−1.624				−2.088				−2.126		
MP2/(Q,5)+ΔCCSD(T)/aXZ	−1.655	−1.640			−2.120	−2.102			−2.159	−2.140		
MP2/(Q,5)+ΔCCSD(T)/(X−1,X)		−1.634				−2.095				−2.132		
MP2/(Q,5)+ΔCCSD(T)-F12a/aXZ	−1.622	−1.621			−2.075	−2.078			−2.113	−2.114		
MP2/(Q,5)+ΔCCSD(T)-F12a/(X−1,X)		−1.621				−2.079				−2.115		
MP2/(Q,5)+ΔCCSD(T)-F12b/aXZ	−1.650	−1.631			−2.109	−2.090			−2.147	−2.127		
MP2/(Q,5)+ΔCCSD(T)-F12b/(X−1,X)		−1.623				−2.082				−2.119		

[a] The methane carbon−PAH plane distances are equal to 3.73, 3.49, and 3.41 Å for the 1C, 2C, and 3C geometries, respectively. Conventional MP2 and ΔCCSD(T) results in the aXZ bases are shown as functions of X. The rows marked "ext." display the CBS-extrapolated results where the values in the "X" column were obtained using the (X−1,X) extrapolation. The different estimates of the total CCSD(T)/CBS interaction energy are also given for each configuration including the values that utilize the CCSD(T)-F12a (unscaled triples) and CCSD(T)-F12b (scaled triples) calculations. The energy unit is 1 kcal/mol.

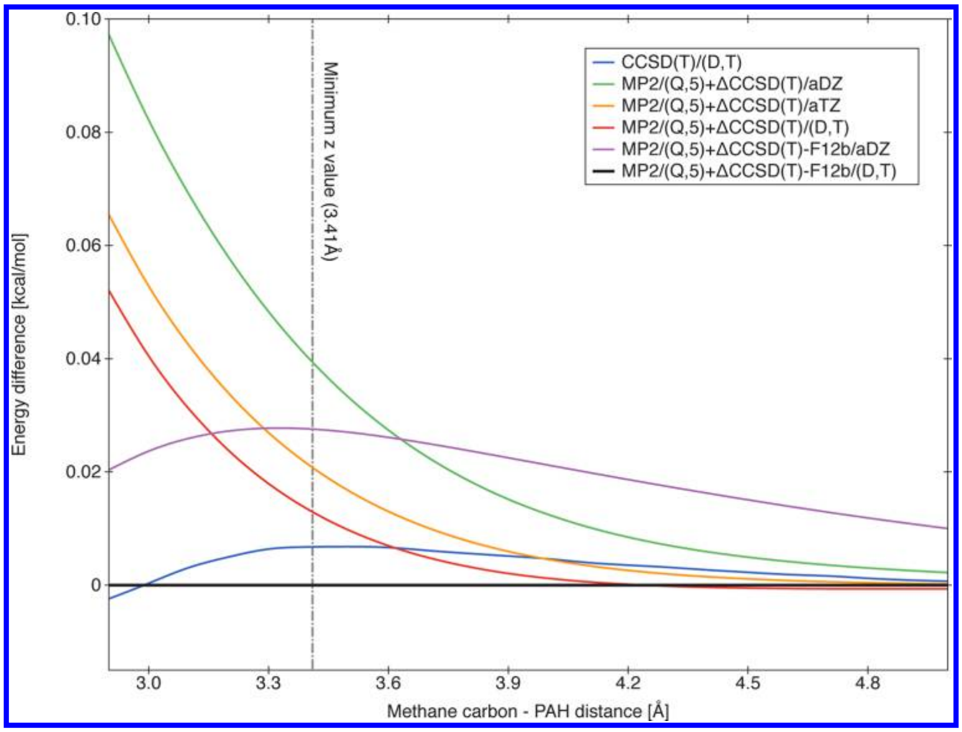

Figure 3. Differences between the benchmark MP2/(Q,5)+ΔCCSD(T)-F12b/(D,T) interaction energy and other CCSD(T)/CBS estimates for the 3C naphthalene−methane complex. The triples term in CCSD(T)-F12b was scaled according to eq 2.

discussed above, the conventional MP2/(Q,5) interaction energy is also virtually converged, and the MP2/(Q,5)+ΔCCSD(T)-F12b/(D,T) approach should be just as accurate but less computationally demanding. We will use the latter theory level to establish the benchmark benzene−methane potential energy curves, as the CCSD(T)/aQZ calculations for more than a few points would be too time-consuming. Overall, the restriction of coupled-cluster calculations to the aTZ basis introduces an error of up to 0.003 kcal/mol (CCSD(T)-F12) or 0.016 kcal/mol (conventional CCSD(T)) in the CCSD(T)/CBS estimate. A further restriction to aDZ increases this error to about 0.02 kcal/mol for CCSD(T)-F12 or 0.04 kcal/mol for conventional CCSD(T). Even this last error, amounting to less than 3% of the interaction energy, is remarkably low, and the results in Table 1 provide strong evidence that our benchmark interaction energies for all systems are highly accurate.

Table 3. The MP2 and ΔCCSD(T) Contributions to Pyrene−Methane and Coronene−Methane Interaction Energies (in kcal/mol) Computed Using Different Partially Augmented Basis Sets Defined in the Text[a]

	pyrene−methane				coronene−methane			
basis	size	1C	2C	3C	size	1C	2C	3C
				MP2				
cc-pVDZ	308	−1.157	−1.484	−1.630	430	−1.493	−1.746	−1.897
local-DZ	369−387	−2.166	−2.741	−3.046	491−509	−2.603	−3.069	−3.362
jun-cc-pVDZ	376	−1.613	−2.073	−2.331	530	−2.057	−2.428	−2.693
core-DZ	427	−2.171	−2.774	−3.141	611	−2.673	−3.133	−3.521
heavy-DZ	461	−2.128	−2.836	−3.028	655	−2.595	−3.051	−3.381
heavy′-DZ	477	−2.221	−2.688	−3.218	671	−2.687	−3.186	−3.559
aug-cc-pVDZ	517	−2.227	−2.853	−3.229	719	−2.691	−3.192	−3.565
CBS		−2.519	−3.198	−3.639		−2.997	−3.543	−3.964
				ΔCCSD(T)				
cc-pVDZ	308	0.581	0.718	0.815	430	0.767	0.868	0.953
local-DZ	369−387	0.656	0.835	0.957	491−509	0.881	1.005	1.115
jun-cc-pVDZ	376	0.614	0.771	0.886	530	0.818	0.948	1.037
core-DZ	427	0.659	0.838	0.963	611	0.894	1.003	1.130
heavy-DZ	461	0.675	0.851	0.974	655			
heavy′-DZ	477	0.660	0.838	0.963	671			
aug-cc-pVDZ	517	0.658	0.836	0.962	719			

[a] A blank space signifies that the CCSD expansion failed to converge due to linear dependencies in the basis set. The MP2/CBS values listed for comparison were obtained from the (Q,5) extrapolation for pyrene−methane and the (T,Q) one for coronene−methane. The size of the local-DZ basis set is slightly different for different coordinations. Thus, a range of values is listed.

The MP2 and ΔCCSD(T) contributions to benchmark naphthalene−methane interaction energies for the deepest minima corresponding to each of the three coordinations (the 3C minimum is the global one) are shown in Table 2 along with the different estimates of the CCSD(T)/CBS limit. As expected, the MP2 interaction energy grows monotonically with basis set size, and all (T,Q) and (Q,5) extrapolations agree to within 0.001 kcal/mol of each other. The conventional ΔCCSD(T) term also exhibits smooth convergence, but the aDZ and aTZ bases are insufficient to narrow this term down to better than 0.01−0.02 kcal/mol. Consequently, the highest-level conventional estimates of the CBS limit, the MP2/(Q,5)+ΔCCSD(T)/(D,T) values, are overestimated by 0.011−0.013 kcal/mol compared to the MP2/(Q,5)+ΔCCSD(T)-F12b/(D,T) result (note how the discrepancies between methods are consistent across all structures). The latter approach, chosen as a benchmark for the benzene−methane potential energy curves based on Table 1, will also be employed to generate benchmark curves for naphthalene−methane. A fair estimate of the accuracy of the benchmark is the difference between the MP2/(Q,5)+ΔCCSD(T)-F12a/(D,T) and MP2/(Q,5)+ΔCCSD(T)-F12b/(D,T) values, which amounts to 0.002−0.004 kcal/mol for the three coordinations. The observed accuracy of the conventional MP2/(Q,5)+ΔCCSD(T)/(D,T) estimates is similar to that found for the benzene−methane dimer. The same is also true for the aDZ-based estimates MP2/(Q,5)+ΔCCSD(T)/aDZ (errors of 0.03−0.04 kcal/mol) and MP2/(Q,5)+ΔCCSD(T)-F12b/aDZ (errors slightly below 0.03 kcal/mol). Thus, the satisfactory accuracy of even the simplest MP2/(Q,5)+ΔCCSD(T)/aDZ estimate is likely transferable to dimers involving larger PAHs. Moreover, unlike the MP2/(Q,5)+ΔCCSD(T)/(D,T) case where the improvement brought about by the F12b approach is enormous, the advantage of MP2/(Q,5)+ΔCCSD(T)-F12b/aDZ over MP2/(Q,5)+ΔCCSD(T)/aDZ is quite modest and does not justify the additional computational effort. Therefore, all benchmarks for anthracene−methane and larger complexes will employ the conventional MP2/(Q,5)+ΔCCSD(T)/aDZ level.

Figure 3 demonstrates the differences between the benchmark MP2/(Q,5)+ΔCCSD(T)-F12b/(D,T) value and various other CCSD(T)/CBS estimates for the 3C naphthalene−methane complex over the relevant range of z distances. At a minimum separation of 3.41 Å, all six extrapolation schemes agree to within 0.04 kcal/mol. Out of the four non-F12 schemes, the CCSD(T)/(D,T) extrapolation performs best at the minimum and at shorter distances. This is quite surprising as, without extrapolation, the CCSD(T)/aTZ curve differs from the benchmark by 0.1−0.3 kcal/mol in this z range, much more than any of the MP2/(Q,5)+ΔCCSD(T) variants. Therefore, the performance of CCSD(T)/(D,T) likely benefits from a fortunate cancellation of errors. The conventional MP2/(Q,5)+ΔCCSD(T) estimates start deviating from the benchmark in the repulsive region, which indicates that the short-range dynamical correlation (interelectronic cusp[5]) effects, which are poorly reproduced by conventional Gaussian basis sets, become increasingly important. For large z, the CCSD(T)/(D,T) approach is nearly as accurate as MP2/(Q,5)+ΔCCSD(T)/(D,T) and MP2/(Q,5)+ΔCCSD(T)/aTZ and clearly more accurate than MP2/(Q,5)+ΔCCSD(T)/aDZ. If only the aDZ basis set is available for the ΔCCSD(T) correction, the MP2/(Q,5)+ΔCCSD(T)-F12b/aDZ approach is superior to MP2/(Q,5)+ΔCCSD(T)/aDZ in the repulsive region but inferior at large z, where the latter, simpler alternative becomes increasingly accurate.

The CCSD(T)/aDZ interaction energies can only be obtained for systems up to the size of pyrene−methane. While recent algorithmic improvements and scalable parallel implementations have significantly extended the range of systems for which CCSD(T) calculations are possible,[93−95] the presence of diffuse basis functions on multiple centers inevitably leads to near linear dependencies in the basis set. It is these dependencies and the associated CCSD convergence problems, not the CPU time and/or resource limitations, that prevented us from calculating the coronene−methane CCSD(T) interaction energies in the full aDZ basis set. To overcome the linear dependency issues, at least some of the offending basis functions have to be removed. A selective removal of diffuse functions has been proposed before[33,96,97] as a way to decrease the number of basis functions without affecting the results significantly—see ref 98 for a systematic study. One of the most popular approaches is the removal of all diffuse functions on hydrogen and helium atoms while keeping all diffuse functions on heavier atoms. The a*XZ* basis sets trimmed in this way have been called aug′-cc-pV*XZ*,[96] heavy-aug-cc-pV*XZ* (heavy-*XZ*),[99] and jul-cc-pV*XZ*, the first member of the "calendar" basis set family.[100] For the purpose of coronene−methane CCSD(T) calculations, we introduce three additional augmentation schemes that successively eliminate basis functions that will likely have little impact on the interaction energy, that is, the diffuse functions located furthest from the region between the interacting molecules. First, as the diffuse functions on methane hydrogens likely play a much more important role than the diffuse functions on coronene hydrogens, we form the heavy′-aug-cc-pVDZ (heavy′-DZ) basis where only diffuse functions from the PAH hydrogens are removed from the full aDZ set. Further basis functions that likely play a small role in the overall interaction energy are the highest-angular-momentum (*d*) diffuse functions on the outermost carbons: their removal from heavy′-DZ leads to a set that will be denoted as core-aug-cc-pVDZ (core-DZ). Finally, an approach where only the methane atoms and the innermost PAH carbon atoms (those within 2.1 Å of the methane carbon's projection onto the PAH plane) retain diffuse functions is labeled as local-aug-cc-pVDZ (local-DZ). Note that all diffuse functions on methane are present in heavy′-DZ, core-DZ, and local-DZ. Pictorial representations of the different augmentation schemes in the pyrene−methane and coronene−methane complexes are displayed in Figure 1. The red colored carbon atoms have the highest angular momentum diffuse functions removed in the core-DZ basis set (the red colored set is the same for all coordinations and has been marked on the 3C structures only). The cyan colored carbon atoms are those that have diffuse functions in the local-DZ basis.

A comparison of the MP2 interaction energies and ΔCCSD(T) corrections computed using different augmentation schemes of the cc-pVDZ basis is shown in Table 3. This table contains results for pyrene−methane (for which we can compute CCSD(T) in all basis sets including full aDZ) and coronene−methane (for which we were not able to converge the CCSD iterations for the most diffuse bases). The results computed using the jun-cc-pVDZ set,[100] obtained from the jul-cc-pVDZ≡heavy-DZ one via a removal of all diffuse *d* functions on carbon atoms, are listed in Table 3 as well.

The pyrene−methane results in Table 3 demonstrate that diffuse functions are quite important for both the MP2 interaction energy and the ΔCCSD(T) correction and should, whenever possible, be included at the aDZ level in order to obtain accurate results. The key question is which diffuse functions play the least important role in the ΔCCSD(T)/aDZ correction. First, in order to examine the importance of diffuse functions on hydrogens, the heavy′-DZ and heavy-DZ basis sets are compared to the full aDZ. The resulting MUE on the three pyrene−methane complexes are 0.002 and 0.014 kcal/mol, respectively. We note that while the removal of diffuse functions from the methane hydrogens has a fairly small impact on the ΔCCSD(T) correction, these functions do not appear to aggravate the linear dependency issues and can be safely included in any augmentation scheme. On the other hand, the diffuse functions on the PAH hydrogens have a very small contribution to the ΔCCSD(T) correction. Therefore, these basis functions are removed in the subsequent augmentation schemes.

The further reduction of diffuse basis functions leading to the core-DZ and local-DZ sets has little impact on the MP2 interaction energy and the ΔCCSD(T) term. For the latter, the pyrene−methane MUE (with respect to the full aDZ set) amount to 0.001 and 0.003 kcal/mol for core-DZ and local-DZ, respectively. It is of interest that both basis sets capture the aDZ interaction energies better than the heavy-DZ basis despite being smaller and causing fewer CCSD convergence problems. In fact, we were able to compute the coronene−methane CCSD(T) interaction energies in both core-DZ and local-DZ but not in heavy-DZ. The results in Table 3 demonstrate that, for the two dimers presented, the differences between the ΔCCSD(T) terms in two basis sets are roughly an order of magnitude smaller than the differences in the MP2 interaction energy. Moreover, the relative accuracies provided by different augmentation schemes are fairly constant across different coordinations.

The pyrene−methane results in Table 3 suggest that the coronene−methane ΔCCSD(T) corrections computed in the core-DZ and local-DZ bases should be within 0.01 kcal/mol from the full aDZ result. Interestingly, the differences between core-DZ and local-DZ for coronene−methane are larger than for pyrene−methane and (slightly) exceed 0.01 kcal/mol for two of the three coordinations. On the basis of the observed CCSD convergence patterns (we could not converge the core-DZ result as tightly as the other ones) and on the behavior of the results as a function of *z* (not shown), we believe that the primary reason for the larger differences is residual convergence problems affecting the core-DZ result. Nevertheless, the observed level of agreement between core-DZ and local-DZ provides, together with the pyrene−methane results, a strong justification for using the local-DZ basis for our benchmark coronene−methane CCSD(T) calculations and suggests that the additional errors incurred in this way do not exceed 0.01 kcal/mol. Therefore, the benchmark coronene−methane interaction energies will be obtained at the MP2/(T,Q)+ΔCCSD(T)/local-DZ level. Finally, it is worth noting that the importance of particular diffuse functions depends on the proximity of their centers to the interaction region much more strongly than on the type of the atom. Indeed, the lack of diffuse functions on distant PAH carbon atoms in the local-DZ basis set turns out to be a less severe approximation than the lack of diffuse functions on methane hydrogens in the jun-cc-pVDZ and jul-cc-pVDZ≡heavy-DZ bases. Thus, the "calendar" basis sets are not a particularly good choice of partial augmentation for our systems as the CCSD(T) approach does not converge in jul-cc-pVDZ and leads to fairly inaccurate results in jun-cc-pVDZ.

The accuracy of the benchmark results obtained in this section depends both on the accuracy to which the CCSD(T)/CBS limit was determined and on the magnitude of the effects neglected in the rigid-monomer, frozen-core CCSD(T) approach. As expected, the correction for the core−core and core−valence correlation is very small—it amounts to 0.004 kcal/mol for the 1C benzene−methane minimum geometry at the CCSD(T)/aug-cc-pCVTZ level of theory. The monomer

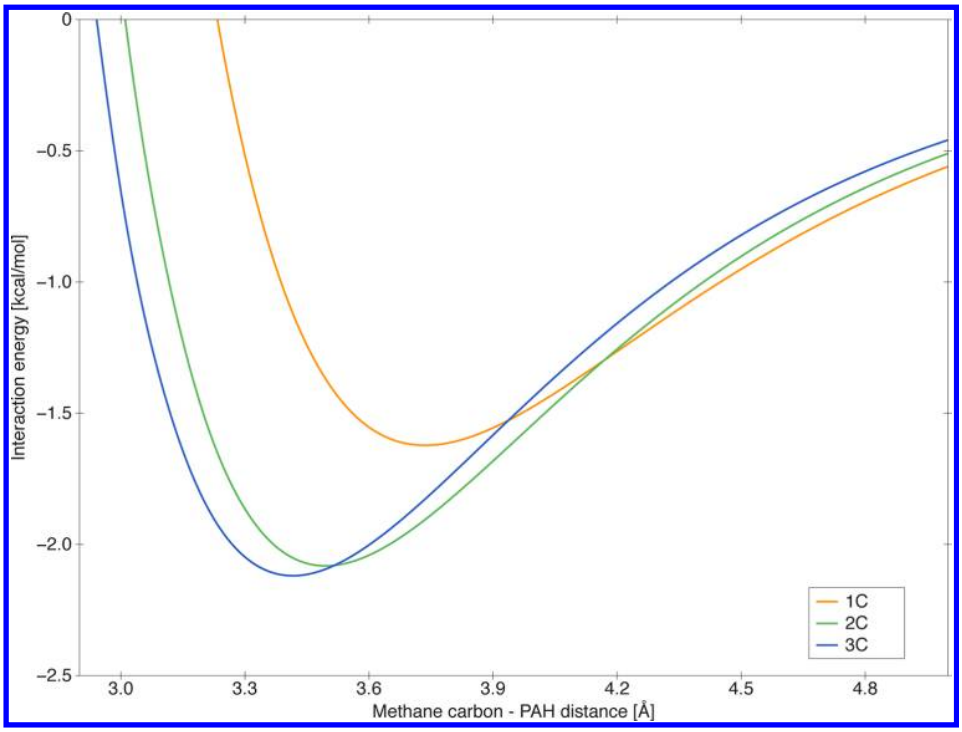

Figure 4. MP2/(Q,5)+ΔCCSD(T)-F12b/(D,T) benchmark interaction potentials for the three coordinations of the naphthalene−methane complex.

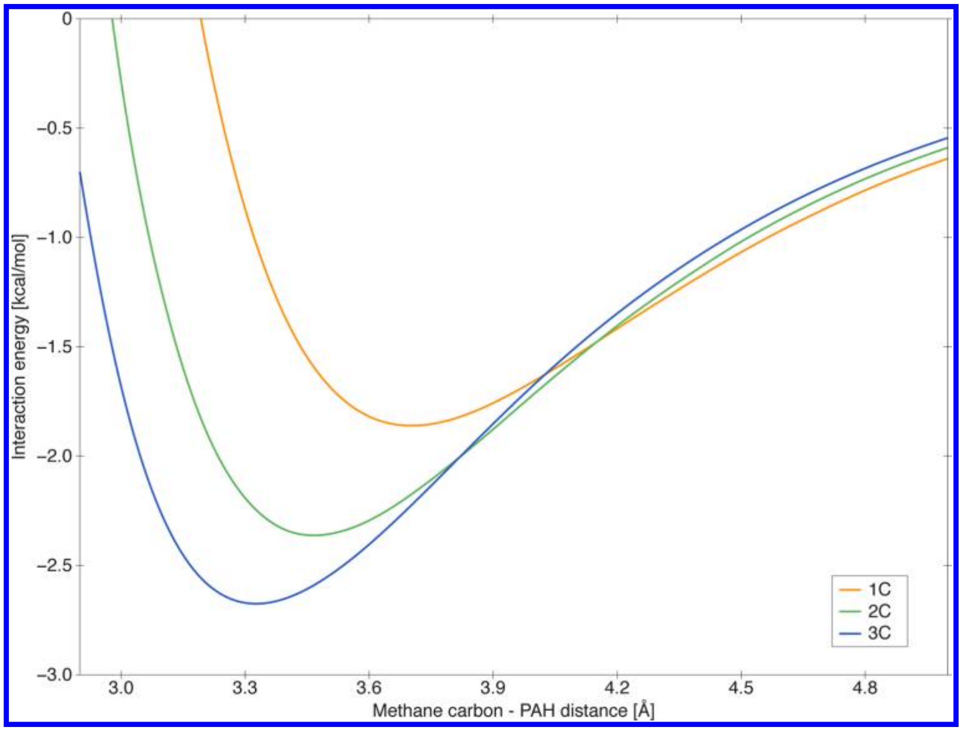

Figure 5. MP2/(Q,5)+ΔCCSD(T)/aDZ benchmark interaction potentials for the three coordinations of the pyrene−methane complex.

flexibility effects can be estimated by comparing the van der Waals well depth obtained with the monomers frozen at their monomer-optimized geometries (as is the case throughout this work) to the well depth computed by minimization of the CP-corrected interaction energy between fully flexible monomers. In the latter case, the specific quantity that needs to be minimized is

$$E_{\text{int}}^{\text{flexible}} = [E^{\text{AB}}(\text{AB}) - E^{\text{AB}}(\text{A}) - E^{\text{AB}}(\text{B})] + [E^{\text{A}}(\text{A}) - E_0^{\text{A}}(\text{A})] + [E^{\text{B}}(\text{B}) - E_0^{\text{B}}(\text{B})] \quad (3)$$

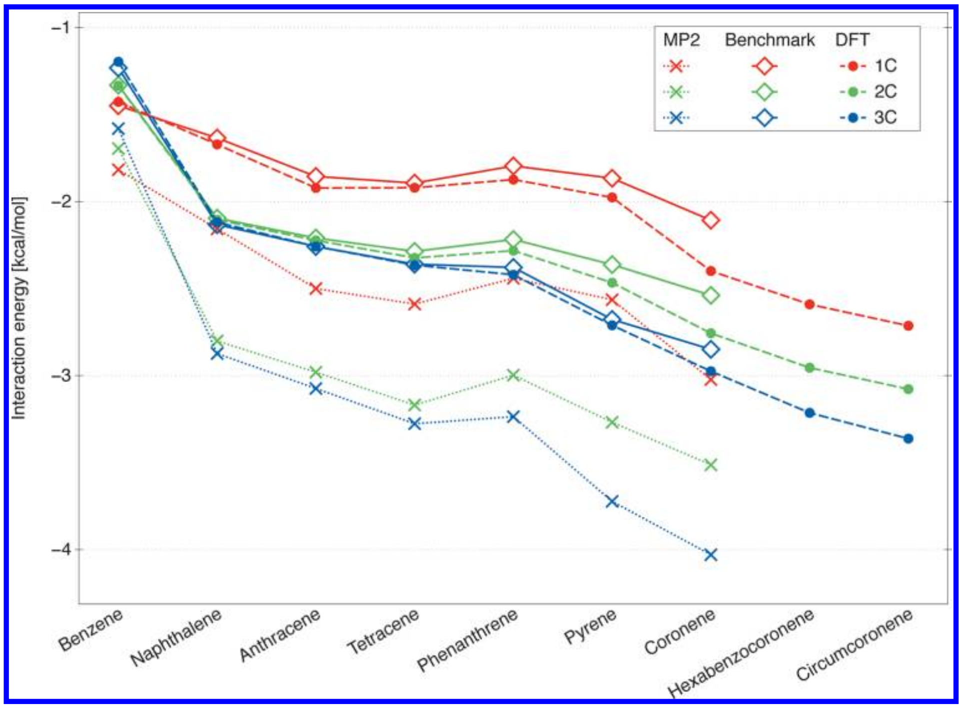

Figure 6. Comparison of the interaction energies calculated by different approaches for the 1C, 2C, and 3C minimum structures (obtained as described in the text) of all PAH−methane dimers considered here. The DFT results are computed at the B3LYP-D3/aDZ level. The MP2 ones are taken from the (Q,5) extrapolation [(T,Q) for coronene], and the "Benchmark" values are calculated at the MP2+ΔCCSD(T) level as described in the text.

where the superscripts denote the basis set (dimer-centered or monomer-centered), the symbols in parentheses denote the subsystems, and the subscript 0 signifies the nonrelaxed optimized geometry of the monomer. For the 1C benzene−methane complex, the flexible well depth obtained by minimizing eq 3 (with the benzene monomer constrained to the D_{6h} symmetry and the dimer to C_{3v} symmetry) at the MP2 level of theory is larger by only 0.005 kcal/mol (aDZ) and 0.001 kcal/mol (aTZ) than the conventional rigid well depth. Moreover, the changes in the bond lengths do not exceed 0.004 Å. To justify the symmetry restriction, we performed a completely unrestricted MP2/aTZ dimer optimization, which lowered the interaction energy further by 0.001 kcal/mol. We conclude that the monomer flexibility effects on the benchmark energies obtained herein do not exceed 0.005 kcal/mol at the minimum.

It is harder to estimate the benchmark uncertainty due to the neglect of coupled-cluster excitations beyond CCSD(T). Such an estimate (although in a very small 6-31G*(0.25) basis set) was obtained for several structures of the benzene dimer by Pitoňák et al.[101] via an approximate account of the quadruple excitations at the CCSD(TQ$_f$) level.[102] The interaction energy contributions beyond CCSD(T) ranged between 0.021 and 0.043 kcal/mol.[101] As the van der Waals well depth for the benzene dimer is about twice as large as for benzene−methane,[33,39,40] the beyond-CCSD(T) effects on the latter quantity are not likely to exceed 0.03 kcal/mol. To verify this, we computed the full CCSDT/6-31G* interaction energy at the 1C benzene−methane minimum using the CFOUR program.[103] The triples effects beyond CCSD(T) decrease the interaction energy by 0.014 kcal/mol. It should be stressed that the 6-31G* basis set, the largest one feasible at this level, is far from adequate—the CCSD(T) interaction energy in this basis is just −0.02 kcal/mol. Nevertheless, the beyond-CCSD(T) effects provide one of the largest contributions to the overall uncertainty of our CCSD(T)/CBS benchmark but should not exceed a few hundredths of a kilocalorie per mole.

Figures 4 and 5 display one-dimensional cuts through the interaction potentials for all three coordinations of the naphthalene−methane and pyrene−methane complexes, respectively. These figures show that the benzene−methane dimer with its 1C global minimum[34,58] is nothing but a special case as the 1C coordination is actually the least binding one for all other PAHs. Moreover, Figures 4 and 5, the analogous graphs for other dimers given in the Supporting Information (Figures S1−S4), and Figure 6, which collects the lowest interaction energies for all systems and all coordinations, illustrate the different character of binding in linear and nonlinear acenes. While the global minima are triply coordinated in all cases, for linear PAHs, the 2C coordination exhibits a local minimum that is only slightly shallower than the 3C one, cf. Figure 6. The nonlinear PAHs clearly favor the 3C configuration—the 2C lowest-energy structures are significantly less binding.

3.2. DFT Calculations.

In this section, we examine how well different DFT functionals capture the benchmark interaction energies. At first, we will restrict ourselves to the complexes with the most accurate MP2/(Q,5)+ΔCCSD(T)-F12b/(D,T) benchmark potentials: benzene−methane and naphthalene−methane. On the basis of the performance of different DFT approaches on six one-dimensional potential cuts (the interaction energy as a function of z for 1C, 2C, and 3C orientations of benzene−methane and naphthalene−methane) evaluated using the quantities described in section 2.5, we will determine the best DFT functionals to use for PAH−methane complexes. Subsequently, the best functionals will be compared

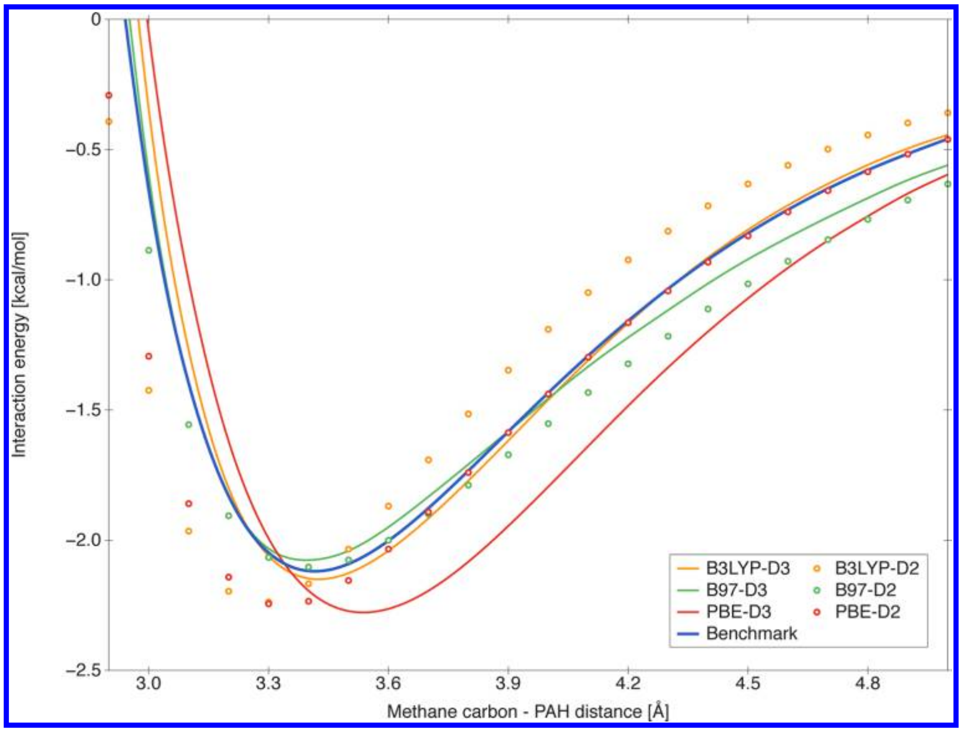

Figure 7. CP-corrected DFT+D/aTZ interaction potentials for the 3C naphthalene−methane complex as compared to the MP2/(Q,5)+ΔCCSD(T)-F12b/(D,T) benchmark.

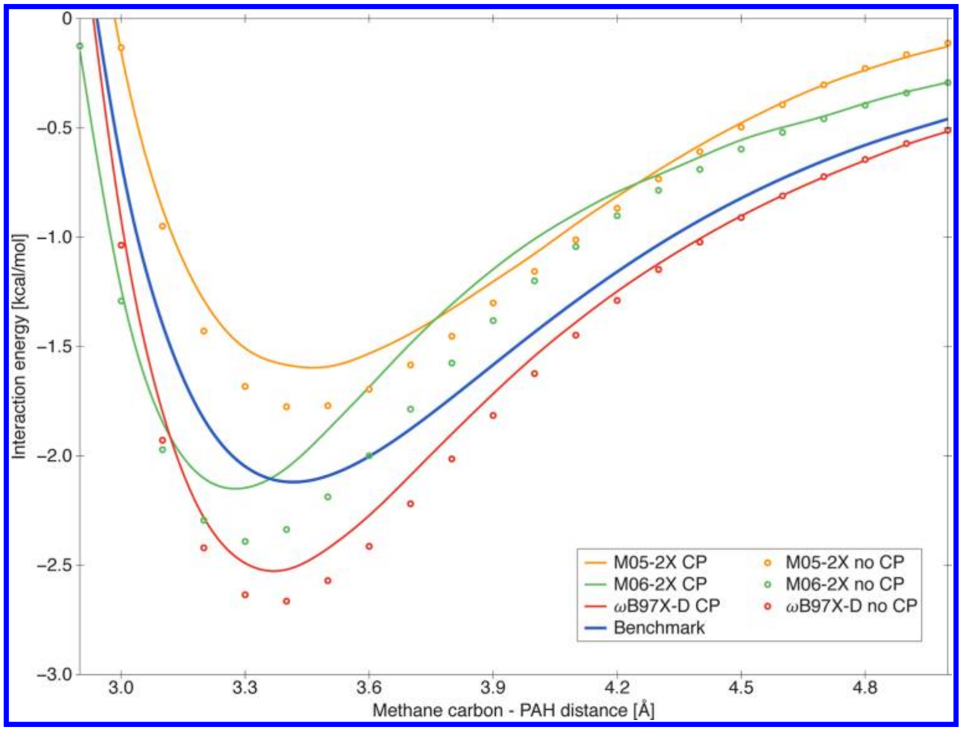

Figure 8. M05-2X, M06-2X, and ωB97X-D interaction potentials computed in the aTZ basis set (with and without the CP correction) for the 3C naphthalene−methane complex as compared to the MP2/(Q,5)+ΔCCSD(T)-F12b/(D,T) benchmark.

against the wave function-based benchmarks for the entire set of complexes to verify whether the good performance on smaller dimers is carried on to larger systems. In the last part, we will employ the best selected DFT variant to larger dimers where no reliable CCSD(T)-level benchmarks can be obtained—the hexabenzocoronene−methane and circumcoronene−methane systems. It should be noted that our DFT results for benzene−methane and naphthalene−methane were calculated using Gaussian[81] without density fitting, while the results for the remaining complexes were obtained with density

Table 4. Minimum Interaction Energies E_{int} and Optimal Methane Carbon−PAH Plane Distances z_{min} Obtained Using Different Density Functionals and aDZ and aTZ Basis Sets for the 1C, 2C, and 3C Structures of Naphthalene−Methane[a]

		1C configuration		2C configuration		3C configuration	
method	basis	z_{min}	E_{int}	z_{min}	E_{int}	z_{min}	E_{int}
benchmark		3.73	−1.623	3.49	−2.082	3.41	−2.119
CP-corrected							
B3LYP-D2	aDZ	3.60	−1.732	3.34	−2.219	3.27	−2.229
	aTZ	3.59	−1.796	3.34	−2.240	3.28	−2.241
B3LYP-D3	aDZ	3.73	−1.672	3.48	−2.102	3.41	−2.118
	aTZ	3.72	−1.722	3.48	−2.133	3.42	−2.150
B97-D2	aDZ	3.68	−1.710	3.44	−2.103	3.37	−2.127
	aTZ	3.66	−1.754	3.46	−2.091	3.40	−2.103
B97-D3	aDZ	3.72	−1.685	3.44	−2.106	3.37	−2.101
	aTZ	3.70	−1.726	3.46	−2.094	3.39	−2.077
PBE-D2	aDZ	3.63	−1.811	3.39	−2.274	3.32	−2.296
	aTZ	3.62	−1.852	3.40	−2.251	3.34	−2.251
PBE-D3	aDZ	3.81	−1.776	3.60	−2.231	3.52	−2.286
	aTZ	3.81	−1.805	3.61	−2.230	3.54	−2.278
M05-2X	aDZ	3.80	−1.129	3.55	−1.700	3.44	−1.782
	aTZ	3.80	−1.072	3.54	−1.560	3.47	−1.596
M06-2X	aDZ	3.65	−1.359	3.40	−2.205	3.31	−2.392
	aTZ	3.67	−1.273	3.38	−2.009	3.27	−2.149
ωB97X-D	aDZ	3.69	−1.888	3.45	−2.574	3.37	−2.671
	aTZ	3.70	−1.872	3.44	−2.476	3.37	−2.527
CP-uncorrected							
B3LYP-D2	aDZ	3.55	−2.301	3.29	−2.931	3.22	−2.976
	aTZ	3.58	−1.910	3.34	−2.348	3.27	−2.361
B3LYP-D3	aDZ	3.68	−2.172	3.43	−2.729	3.37	−2.791
	aTZ	3.71	−1.826	3.48	−2.229	3.42	−2.261
B97-D2	aDZ	3.60	−2.278	3.37	−2.775	3.32	−2.824
	aTZ	3.65	−1.861	3.45	−2.188	3.38	−2.216
B97-D3	aDZ	3.66	−2.229	3.39	−2.768	3.33	−2.794
	aTZ	3.69	−1.829	3.45	−2.191	3.38	−2.189
PBE-D2	aDZ	3.57	−2.395	3.33	−2.970	3.26	−3.017
	aTZ	3.61	−1.958	3.39	−2.348	3.33	−2.366
PBE-D3	aDZ	3.74	−2.271	3.52	−2.803	3.46	−2.911
	aTZ	3.79	−1.898	3.60	−2.309	3.53	−2.375
M05-2X	aDZ	3.70	−1.755	3.44	−2.438	3.37	−2.582
	aTZ	3.79	−1.216	3.54	−1.694	3.45	−1.754
M06-2X	aDZ	3.58	−2.031	3.35	−2.988	3.26	−3.211
	aTZ	3.65	−1.445	3.37	−2.177	3.26	−2.335
ωB97X-D	aDZ	3.65	−2.419	3.41	−3.201	3.33	−3.336
	aTZ	3.69	−2.001	3.44	−2.596	3.36	−2.666

[a] The energy unit is 1 kcal/mol, and the distance unit is 1 Å.

fitting using the MOLPRO[64] code. A direct comparison of interaction energies between the two codes is difficult due to the different numerical grids employed. For benzene−methane and naphthalene−methane, a comparison of all DFT+D interaction energies between MOLPRO and Gaussian resulted in a MUE of 0.003 kcal/mol and a MeURE of 0.7%, well within acceptable precision.

Figures 7 and 8 show DFT+D and interaction-optimized density functional results, respectively, for the 3C naphthalene−methane complex. In addition, Table 4 collects the locations and depths of the naphthalene−methane minima for all three coordinations, with and without the CP correction, computed using all the DFT approaches tested. While the CP correction does not guarantee increased accuracy, especially in the DFT case, for all DFT+D methods this correction improved the agreement with the benchmark interaction potential, cf. Table 4. Therefore, only CP-corrected values are shown in Figure 7. It should be noted that the -D3 term can employ either the original damping function[19] that goes to zero at short interatomic distances or the Becke−Johnson damping whose short-range limit is a finite nonzero value.[104,105] Additionally, an inclusion of a three-body dispersion term has been suggested for large systems.[19] The resulting four variants of the -D3 correction are compared in Figure S5 in the Supporting Information for the benzene−methane and naphthalene−methane dimers. Neither the Becke−Johnson damping nor the three-body correction improve the results for the most accurate B3LYP-D3 and B97-D3 functionals. Therefore, the original -D3 variant is employed in Table 4, Figure 7, and throughout the rest of this work.

The results in Figures 7 and 8 and Table 4 show that the DFT+D methods generally capture the benchmark interaction

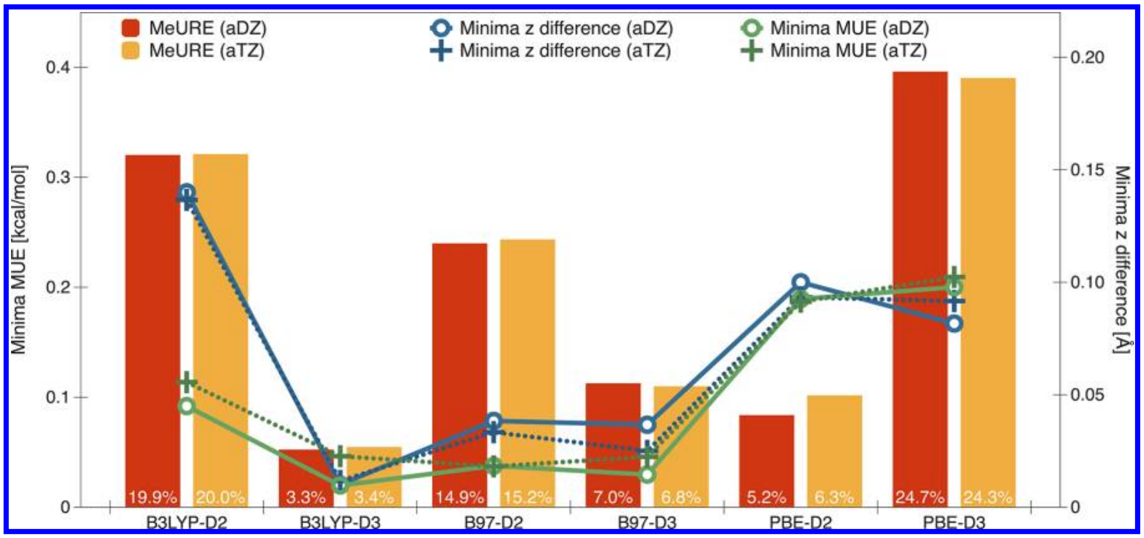

Figure 9. The values of the minima z differences, minima MUE, and MeURE, averaged over all six coordinations of the benzene−methane and naphthalene−methane complexes, for different CP-corrected DFT+D methods.

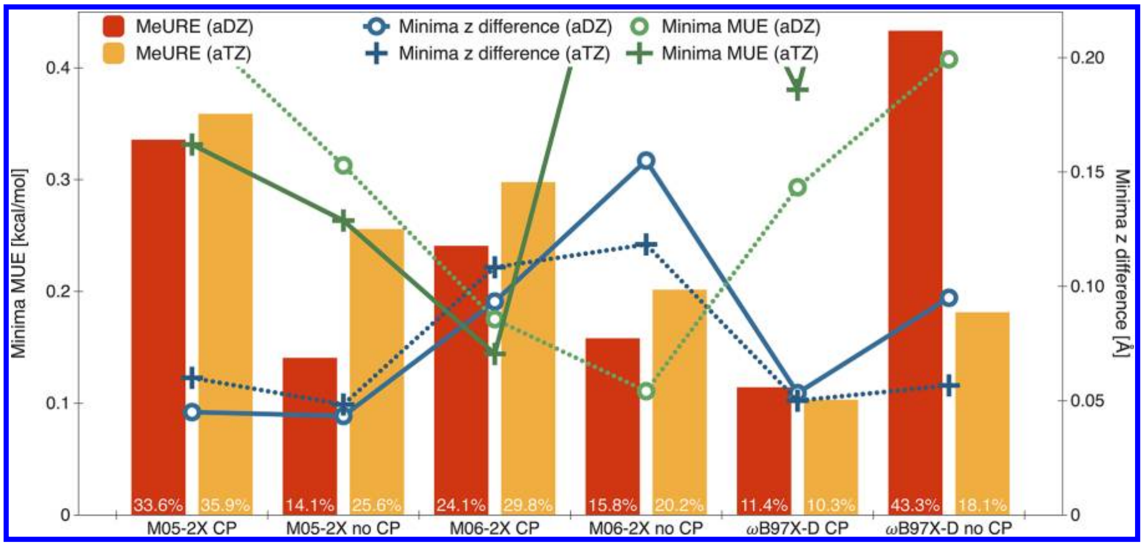

Figure 10. The values of the minima z differences, minima MUE, and MeURE, averaged over all six coordinations of the benzene−methane and naphthalene−methane complexes, for different interaction-optimized functionals (with and without the CP correction).

energy curve better than the interaction-optimized functionals. To quantify the performance of different DFT variants, the minima MUE, MeURE, and the mean minima z differences were computed for the six one-dimensional cuts for the benzene−methane and naphthalene−methane dimers. The pertinent results are shown in Figures 9 and 10 for DFT+D and interaction-optimized functionals, respectively. These figures show that the B3LYP-D3/aDZ approach offers the best performance in terms of all three statistical quantities, and the B3LYP-D3/aTZ, B97-D3/aDZ, and B97-D3/aTZ methods are not much worse. No interaction-optimized functional comes close to the accuracy of the best DFT+D variants for the PAH−methane dimers.

To assess the accuracy of different DFT+D methods for the anisotropy of the interaction energy, a one-dimensional angular cut through the benzene−methane potential energy surface was obtained by rotating the methane molecule around the carbon atom in such a way that the cut passes through all three coordinations of the system. To compare the anisotropy, the 1C structure was taken as the reference point, and energy differences with respect to this reference were compared against the benchmark. The three best DFT+D functionals in terms of MURE are B3LYP-D3/aDZ (0.5%), B97-D2/aTZ (0.5%), and B97-D3/aTZ (0.7%). The complete set of benchmark and DFT+D results for this angular cut is displayed in Figures S6−S7 in the Supporting Information.

Figure 11 demonstrates that the high accuracy of several DFT+D methods is retained for pyrene−methane (and, in fact, for all dimers up to this size). In order to identify the best DFT variant overall, Table 5 shows the three statistical quantities discussed above broken down into different coordinations for the three top performers. Note that, unlike in Figures 9 and 10, the averaging in Table 5 has been carried out over all the systems for which benchmark CCSD(T)-level potential energy curves are available, that is, benzene−methane through pyrene−methane. Table 5 demonstrates that B3LYP-D3/aDZ exhibits the best performance in nearly every category. On the basis of all the statistics presented above, we select the B3LYP-

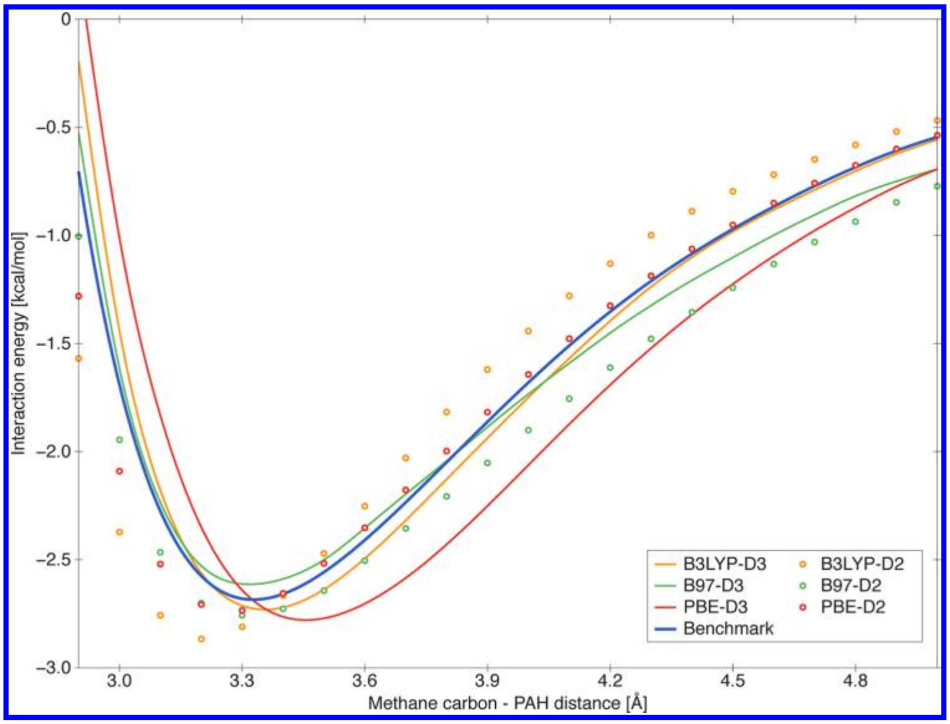

Figure 11. DFT+D/aTZ interaction potentials for the 3C pyrene−methane complex as compared to the MP2/(Q,5)+ΔCCSD(T)/aDZ benchmark.

Table 5. The Three Best DFT+D Functionals in Terms of MeURE Broken down into Different Coordinations of the Complexes[a]

	B3LYP-D3		B97-D3		PBE-D2	
	aDZ	aTZ	aDZ	aTZ	aDZ	aTZ
			minima z difference			
all	0.01	0.01	0.03	0.02	0.09	0.09
1C	0.01	0.01	0.02	0.03	0.09	0.10
2C	0.02	0.01	0.04	0.03	0.10	0.09
3C	0.01	0.01	0.03	0.01	0.09	0.07
			minima MUE			
all	0.039	0.072	0.041	0.060	0.151	0.140
1C	0.058	0.107	0.062	0.103	0.158	0.201
2C	0.041	0.070	0.035	0.031	0.157	0.133
3C	0.018	0.038	0.024	0.047	0.137	0.087
			MeURE			
all	2.52%	3.14%	7.01%	6.76%	3.86%	4.13%
1C	3.11%	3.93%	7.06%	6.98%	4.45%	6.20%
2C	2.73%	2.98%	7.20%	6.31%	4.01%	3.86%
3C	1.84%	2.35%	5.74%	7.21%	3.47%	3.04%

[a] The purpose of this breakdown is to illustrate that the lowest-energy structure of the complex is recovered better than the overall statistics suggest. The statistical averaging has been performed over all dimers from benzene−methane through pyrene−methane. The units are 1 Å for the minima z difference and 1 kcal/mol for the minima MUE.

D3/aDZ approach as the method of choice for larger systems, as coronene−methane is the last dimer for which CCSD(T) in any acceptable basis is feasible. It is also of interest that the DFT+D approach slightly overbinds the 1C and 2C structures, which lead to somewhat larger errors compared to the 3C configuration.

The 1C, 2C, and 3C minimum energies for the CCSD(T)/CBS benchmark, MP2/CBS, and the B3LYP-D3/aDZ functional for all dimers studied in this work are collected in Figure 6. The qualitative differences between the minima pattern for linear acenes and nonlinear PAHs are easily discernible at all levels of theory. Figure 6 demonstrates how the B3LYP-D3/aDZ approach performs remarkably well for all systems through pyrene−methane (in the worst case, the 1C pyrene−methane complex, the error is 0.110 kcal/mol or 6.2%) but overbinds the three coronene−methane minima by 0.126−0.292 kcal/mol or 4.2−13.9%. The accuracy of the B3LYP-D3/aDZ approach for coronene−methane is still quite good—for comparison, the MP2/CBS method overbinds the PAH−methane complexes by 30% and more. However, the increase in errors with respect to smaller complexes can be only partially explained by the increased uncertainty of the benchmark itself (due to the use of a reduced local-DZ basis for ΔCCSD(T) and the larger overall interaction energy) which is not expected to exceed 0.1 kcal/mol even for this system. It should be noted that B3LYP-D3/aDZ tends to overestimate the minimum energies more for the 1C and 2C configurations than for the 3C coordination. The second and third best performer overall, the B97-D3 and PBE-D2 functionals, are actually slightly more accurate than B3LYP-D3 for coronene−methane, cf. Table SVII in the Supporting Information. However, both functionals slightly underestimate the minimum intermolecular distances, while B3LYP-D3 is spot on in that respect.

To estimate the adsorption energy of methane on graphene and graphite, larger complexes are needed as there still is a large gap in interaction energy between pyrene−methane and coronene−methane. For systems larger than coronene−methane, the CCSD(T) calculations cannot be performed in a large enough basis set, and MP2 is deemed to overestimate the interaction energy considerably. Therefore, we resorted to the top DFT performer from our tests on smaller complexes, the B3LYP-D3 approach, to study the two largest complexes, hexabenzocoronene−methane and circumcoronene−methane (Figure 1). To find the minima for these systems, starting intermolecular geometries were taken from the coronene−methane dimer, and then the B3LYP-D3/aDZ interaction energies were minimized in a three-dimensional search that disregarded methane rotation. The global-minimum interaction energies for the hexabenzocoronene−methane and circumcoronene−methane complexes are −3.214 and −3.362 kcal/mol, respectively. The latter result should be reasonably close to the graphene−methane interaction energy as the interactions with distant carbon atoms are not likely to change the interaction energy appreciably. Indeed, the addition of one and two additional rings of benzene rings around circumcoronene changes the -D3 empirical dispersion term by −0.087 and −0.118 kcal/mol, respectively, compared to circumcoronene−methane. At this range of distances, dispersion should constitute nearly 100% of interaction energy. Thus, our calculations predict that the minimum graphene−methane interaction energy is about −3.48 kcal/mol.

A direct comparison of the theoretical result to the experimental well depth of methane adsorbed on the (0001) surface of graphite[106] requires taking into account the interactions with the subsurface graphene sheets. To estimate the effect of the subsequent layers in graphite, a simple additive model is assumed where the contribution of each additional layer is estimated using the circumcoronene−methane model and the B3LYP-D3/aDZ approach. The distance between graphene layers in graphite is taken as 3.34 Å, and each layer is shifted by 1.43 Å with respect to the previous one to form an alternate ABAB... structure.[107] Starting with the methane−circumcoronene 3C global minimum geometry, in the models for subsequent layers the circumcoronene molecule is shifted in a way corresponding to the relative position of layers in graphite. The resulting B3LYP-D3 calculations give the adsorption energy contributions from the second, third, fourth, and fifth graphene layers equal to 0.200, 0.023, 0.006, and less than 0.001 kcal/mol, respectively. Thus, taking into account the first four layers, our final estimate of the methane adsorption energy on the (0001) graphite surface amounts to 3.71 kcal/mol. This value is somewhat larger than the experimental result of 2.99 ± 0.24 kcal/mol[106] and the DFT/CC result of 3.23 kcal/mol.[108] We will discuss this discrepancy in more detail in section 3.4.

3.3. SAPT(DFT) Calculations. To provide a better insight into the nature of the PAH−methane bonding and the effects determining the energetic ordering of different coordinations, we performed SAPT(DFT) calculations for several dimers along the same one-dimensional cuts through the potential energy surface as for the benchmark and DFT calculations. The total SAPT(DFT) interaction energies for the 2C and 3C configurations of naphthalene−methane are compared to the benchmark curves in Figure 12. An analogous figure for pyrene−methane is given in the Supporting Information. Figure 12 shows that the absolute accuracy of SAPT(DFT) is not very impressive—the depth of the global minimum is underestimated by 0.27 kcal/mol at the aTZ level. However, a substantial part of this discrepancy can be attributed to the basis set incompleteness effects as indicated by the SAPT(DFT)/aTZ minima being about 0.2 kcal/mol deeper than the SAPT(DFT)/aDZ ones. While SAPT(DFT) is not as accurate overall as the best DFT+D approaches for this system, Figure 12 demonstrates that it recovers the energy difference between the 2C and 3C configurations very well. Therefore, we can expect the SAPT(DFT) energy decomposition to provide reliable insight into the physical origin of interaction energy differences between differently coordinated PAH−methane structures.

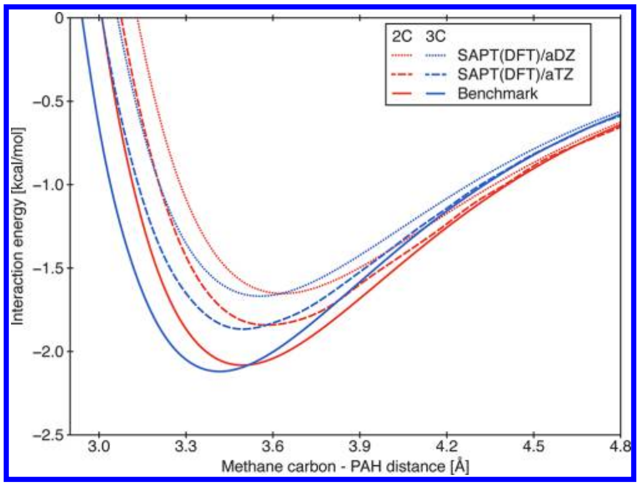

Figure 12. Total SAPT(DFT) interaction energies for the 2C and 3C naphthalene−methane configurations plotted against the benchmark data as functions of the intermolecular coordinate z.

Table 6 shows the SAPT(DFT)/aDZ electrostatics, induction, dispersion, and first-order exchange contributions for the 2C and 3C minima of the naphthalene−methane and pyrene−methane dimers. It is clearly seen that both complexes, while primarily bound by dispersion, also contain a significant amount of attractive electrostatic interaction. While the latter interaction is nearly negligible in the asymptotic region (with the leading contribution coming from the quadrupole−octupole interaction), the charge overlap effects make it substantial in the region of the van der Waals minima. For the naphthalene−methane complex, the electrostatics and first-order exchange effects actually slightly favor the 2C configuration, but the 3C one exhibits more dispersion. As a result of a cancellation of these differences, the 2C and 3C minima are nearly isoenergetic just like we found for all other theory levels, cf. Figure 6. When the PAH is not a linear acene, such as in the pyrene−methane case, Figure 6 shows that the 3C minimum is significantly deeper than the 2C one. As the SAPT(DFT) contributions presented in Table 6 indicate, the 3C configuration exhibits stronger dispersion (and also somewhat stronger electrostatics) that more than makes up for the somewhat larger exchange repulsion compared to the 2C geometry. It is also worth noting that the differences between the SAPT(DFT) contributions for naphthalene−methane and pyrene−methane are much larger for the 3C geometry than for the 2C one. This behavior can be explained by the fact that an "extension" of naphthalene to pyrene for the 2C configuration involves adding atoms that are relatively far from the methane molecule and contribute little to the interaction energy, especially to the short-range first-order exchange part (cf. Figure 1). Conversely, a similar "extension" leading to 3C pyrene−methane involves creating a new aromatic ring directly below one of the methane hydrogens. This increases both the exchange repulsion and the attraction due to electrostatics and dispersion. The latter effect prevails and the 3C structure exhibits a significantly stronger bonding in the pyrene−methane complex than in the naphthalene−methane one.

3.4. Comparison to Other Work. The intermolecular separations z_{min} and interaction energies E_{int} at the global

Table 6. Minimum Intermolecular Distances z_{min}, Interaction Energy Contributions, and Total Interaction Energies E_{int} Predicted by SAPT(DFT)/aDZ for the 2C and 3C Coordinations of Naphthalene−Methane and Pyrene−Methane As Compared to Benchmark[a]

	SAPT(DFT)						benchmark	
system	z_{min}	electrostatics	induction	dispersion	exchange	E_{int}	z_{min}	E_{int}
naphthalene−methane 2C	3.63	−0.834	−0.064	−2.914	2.160	−1.653	3.49	−2.082
naphthalene−methane 3C	3.55	−0.795	−0.060	−3.052	2.239	−1.668	3.41	−2.119
pyrene−methane 2C	3.61	−0.802	−0.051	−3.262	2.248	−1.867	3.47	−2.362
pyrene−methane 3C	3.47	−0.950	−0.049	−3.694	2.590	−2.103	3.33	−2.678

[a] The energy unit is 1 kcal/mol, and the distance unit is 1 Å.

Table 7. Global Minimum Methane Carbon−PAH Plane Separations z_{min} (in Å) and Interaction Energies E_{int} (in kcal/mol) for All Complexes Investigated in the Present Work Compared to Previous Theoretical and Experimental Studies[a]

			this work		other works	
system		theory level	z_{min}	E_{int}	z_{min}	E_{int}
benzene−methane	1C	MP2-F12/(Q,5)+ΔCCSD(T)-F12b/(T,Q)	3.76	−1.433	3.72 [33]	−1.50 [33],[e] −1.448 [39, 41][f] −1.438 [75][g]
naphthalene−methane	3C	MP2/(Q,5)+ΔCCSD(T)-F12b/(D,T)	3.41	−2.119	3.6 [58]	−1.92 [58][h]
antracene-methane	3C	MP2/(Q,5)+ΔCCSD(T)/aDZ	3.40	−2.258		
tetracene-methane	3C	MP2/(Q,5)+ΔCCSD(T)/aDZ	3.40	−2.359		
phenanthrene-methane	3C	MP2/(Q,5)+ΔCCSD(T)/aDZ	3.38	−2.378		
pyrene−methane	3C	MP2/(Q,5)+ΔCCSD(T)/aDZ	3.33	−2.678	3.4 [58], 3.36 [110]	−2.50 [58],[h] −2.91 [110][i]
coronene−methane	3C	MP2/(T,Q)+ΔCCSD(T)/local-DZ	3.32	−2.849	3.31 [108], 3.37 [110]	−2.799 [108],[j] −3.32 [110][i]
hexabenzocoronene−methane	3C	B3LYP-D3/aDZ	3.32	−3.214		
circumcoronene−methane	3C	B3LYP-D3/aDZ	3.32	−3.362		
graphene-methane	3C	est. B3LYP-D3/aDZ	3.32[b]	3.48[c]	3.31 [108], 3.28 [109]	3.23 [108],[k] 3.92 [109][l]
graphite-methane	3C	est. B3LYP-D3/aDZ	3.32[b]	3.71[d]	3.03−3.45 [106]	2.99 ± 0.24 [106][m]

[a] Different estimates of the adsorption energy of methane on graphene and (0001) graphite are also given. The reference numbers for literature values are given in square brackets. [b] Taken from the circumcoronene−methane calculation. [c] The circumcoronene−methane result plus the -D3 correction for interaction with distant carbon atoms. [d] The graphene−methane result plus a B3LYP-D3/aDZ estimate of the contribution from subsurface graphene layers. [e] Original S22 database: MP2/cc-pVTZ optimized geometry, MP2/(cc-pVQZ,cc-pV5Z)+ΔCCSD(T)/(reduced cc-pVTZ) energy. [f] Revised S22 database: MP2/(Q,5)+ΔCCSD(T)/(aTZ+midbond) energy at the geometry from ref 33. [g] CCSD(T)/(heavy-TZ,heavy-QZ). [h] MP2(cc-pVDZ,cc-pVTZ)+ΔCCSD(T)/6-31G* energy at the MP2/6-31G*(0.25) optimized geometry. [i] BLYP-D3/aTZ. [j] DFT/CC using the PBE functional and the aQZ basis. [k] Periodic DFT/CC using the PBE functional and a plane-wave basis. [l] MP2/aTZ. [m] Experiment.

minima for all dimers considered in this work, including the estimates of the adsorption energy of methane on graphene and graphite, are collected in Table 7 and compared to the most accurate literature results. It should be noted that, in a few cases, different minimum structures were found in the previous studies. Specifically, Tsuzuki et al. found,[58] through an MP2/6-31G*(0.25) geometry optimization, a naphthalene−methane minimum structure that is an intermediate between the 2C and 3C ones (closer to the 2C configuration). The ordering of the minima found by Thierfelder et al.[109] for graphene−methane (using MP2 for a finite cluster and periodic DFT for an infinite sheet) varies with the method and density functional employed. Finally, Qiu et al.[110] considered nine different structures of coronene−methane, but neither of them corresponds to the global minimum located in this work. The lowest-energy structure of ref 110, a 3C configuration but with the methane carbon placed over the center of the inner coronene ring, exhibits an interaction energy (minimized with respect to the z distance) of −2.686 kcal/mol at the MP2(T,Q)+ΔCCSD(T)/local-DZ level, 0.162 kcal/mol above the global minimum.

The first system in Table 7, the benzene−methane complex, has been the subject of numerous high-level *ab initio* studies.[33,34,38−40,75,111] The present work is the only one where the CCSD(T) interaction energy was computed in a fully augmented quadruple-ζ basis set (although Marchetti and Werner[75] used heavy-QZ) so that our result is theoretically the most accurate. However, the most accurate previous results were already well converged, so the improvement is very modest. On the contrary, the only CCSD(T) interaction energies available for larger PAH−methane dimers, the results of Tsuzuki et al.[58] for naphthalene−methane and pyrene−methane, are underestimated by about 0.2 kcal/mol. Obviously, the small 6-31G* basis used to compute ΔCCSD(T) in ref 58 is far from complete.

The BLYP-D3 pyrene−methane and coronene−methane interaction energies from ref 110 are overestimated by 0.23 and 0.47 kcal/mol, respectively, relative to our benchmarks. Clearly, the performance of BLYP-D3 is not competitive with that of the best DFT+D variants tested in this work, most notably B3LYP-D3 (cf. the minima MUE values in Table 5). On the other hand, the excellent agreement (to 0.05 kcal/mol) of our coronene−methane result with the DFT/CC one of Rubeš et al.[108] provides a strong validation of the assumption that the differences between CCSD(T) and DFT, computed for small dimers, are transferable to larger PAH−methane complexes (note the agreement between the minimum geometries too). This underlying assumption of the DFT/CC approach is also employed by us to justify the selection of an optimal DFT+D variant for large systems via a comparison to benchmark small-system CCSD(T) interaction energies.

As far as the methane adsorption energy on infinite carbon structures is concerned, the review work of Vidali et al.[106]

recommended, based on a number of experimental studies, the value of 2.99 ± 0.24 kcal/mol as the zero-coverage adsorption well depth of methane on the (0001) surface of graphite and 3.24 ± 0.21 Å as the distance between the methane carbon and the surface. While all computational studies give adsorption distances within the broad experimental range, the same is not true for the adsorption energy. The periodic DFT/CC result of Rubeš et al.[108] is at the upper end of the experimental range while our estimate, although certainly more accurate than the MP2 one of ref 109, is 0.48 kcal/mol above the higher experimental limit. The reason for this discrepancy is that the B3LYP-D3/aDZ approach employed by us somewhat overestimates the global-minimum interaction energies (cf. Figure 6). The extent of this overestimation has been observed to increase between pyrene−methane and coronene−methane (from 0.033 to 0.126 kcal/mol), and it is likely that this trend continues to circumcoronene−methane. In that case, the B97-D3/aDZ approach, which overestimates the coronene−methane global-minimum interaction energy by only 0.053 kcal/mol, might accidentally be a better choice for extended systems even though it is inferior to B3LYP-D3 for the description of the entire potential energy curve (as indicated by the larger MeURE values in Figure 9 and Table 5). The B97-D3/aDZ circumcoronene−methane interaction energy amounts to −3.217 kcal/mol for the z distance of 3.32 Å. If this result is augmented with the corrections for the more distant carbon atoms in the first graphene sheet and the subsurface graphene layers, the resulting B97-D3/aDZ estimate of the methane adsorption energy on graphite amounts to 3.58 kcal/mol, less than for B3LYP-D3/aDZ but still outside the experimental range. Finally, let us note that if the graphene−methane result of Rubeš et al.[108] is augmented by our estimate of the contributions from subsurface graphene layers (neglected in ref 108), the resulting adsorption energy of 3.46 kcal/mol is also above the upper experimental limit. Thus, it is possible that the experimental value is somewhat underestimated and the deviation of our B3LYP-D3/aDZ result from the true adsorption energy is no more than 0.2 kcal/mol.

4. SUMMARY

High-accuracy benchmark interaction energies were obtained for weakly interacting complexes of aromatic hydrocarbons (benzene, naphthalene, anthracene, phenanthrene, tetracene, pyrene, and coronene) with methane. The energies were computed by the supermolecular MP2 approach extrapolated to the complete basis set limit plus a CCSD(T) correction calculated in a moderate basis set (up to aQZ for benzene−methane, aTZ for naphthalene−methane, aDZ for anthracene−methane through pyrene−methane, and local-DZ for coronene−methane). The calculations for benzene−methane and naphthalene−methane utilized the explicitly correlated CCSD(T)-F12a/b approach while all other systems were treated using conventional CCSD(T). An extensive basis set convergence analysis indicates that our benchmark interaction energies are accurate to a few hundredths of a kilocalorie per mole.

Our CCSD(T) results indicate that the very well studied benzene−methane complex is not at all representative of the interactions between methane and larger PAHs. The benzene−methane global minimum is singly coordinated (1C); that is, only one methane hydrogen points toward the benzene plane. For all other complexes (that have not been studied at the CCSD(T) level before except for the very small-basis work of Tsuzuki et al.[58]), the 1C structure is significantly less bound than the 2C and 3C ones. The global minimum for naphthalene−methane and all larger complexes is triply coordinated; however, the linear and nonlinear PAHs lead to a qualitatively different behavior. In the nonlinear case, the 3C structure is highly favored over all others as, except for the phenanthrene complex, all three hydrogens can be placed on top of different aromatic rings. Such a placement is not possible for linear acenes: as a result, the 2C and 3C minima are nearly isoenergetic in this case. The binding patterns between methane and PAHs can be understood in terms of a competition between dispersion, exchange repulsion, and electrostatics as illustrated by the SAPT(DFT) decomposition of the interaction energy performed for selected dimers.

The CCSD(T)-level benchmarks developed here were used to investigate the accuracy of several novel DFT approaches for the PAH−methane interaction energies. The comparisons included one-dimensional cuts through the PAH−methane potential energy surfaces passing through the deepest minima in each of the three coordinations. Thus, the optimal DFT variant needs to provide a uniformly high accuracy for all intermolecular distances, not just around the van der Waals minima. The tested approaches included DFT+D (with the B3LYP, PBE, and Grimme's reparameterization of B97[12] as the density functionals and Grimme's -D2[12] and -D3[19] empirical corrections for dispersion) and functionals specifically optimized for weak intermolecular interactions (M05-2X, M06-2X, and ωB97X-D). While the latter group of functionals somewhat underperformed for the complexes studied here, the DFT+D approach, employing the aDZ and aTZ basis sets and including the counterpoise correction, reproduced the benchmark results very well. The accuracy of the CP-corrected B3LYP-D3/aDZ method was particularly remarkable and consistent across different dimers (benzene−methane through pyrene−methane), coordinations, and distances, with an overall mean unsigned error at the minima equal to 0.039 kcal/mol and a median unsigned relative error for all points amounting to 2.52%. The B3LYP-D3 functional performed similarly well in the aTZ basis set, and the B97-D3 approach came a close second. The accuracy of the B3LYP-D3/aDZ method somewhat deteriorated for the coronene−methane complex, but the global minimum was still reproduced to within 0.13 kcal/mol.

The excellent reproduction of benchmark results with the B3LYP-D3 approach suggests that it should be the method of choice for studying interactions of methane with larger PAHs as well as with extended structures such as graphene sheets and carbon nanotubes. We performed the first step in this direction and computed B3LYP-D3/aDZ interaction energies for the three coordinations of hexabenzocoronene−methane and circumcoronene−methane. Compared to the coronene−methane dimer, the presence of an additional outer ring of benzene rings increases the binding by about 0.5 kcal/mol. As the main binding force is provided by dispersion, an extension of the PAH beyond circumcoronene results in a small change in the interaction energy and can be modeled by the empirical dispersion term alone. The inclusion of the effect of this extension and of the contribution from the subsequent layers leads to estimated methane adsorption energies on graphite equal to 3.71 (B3LYP-D3) and 3.58 (B97-D3) kcal/mol, close to the experimental value but above its upper limit. A similar estimate of the adsorption energy of methane on the inner and outer surfaces of a carbon nanotube needs to take into account, in addition to all other effects, the nanotube curvature. Further work in this direction is in progress in our group.

■ ASSOCIATED CONTENT

Ⓢ Supporting Information

Additional CCSD(T)-F12 results for benzene−methane (Table SI), potential minima for all systems and density functionals (Tables SII−SVII), benchmark interaction potentials for all systems (Figures S1−S4), comparison of different -D3 variants (Figure S5), anisotropy of the benzene−methane potential (Figures S6−S7), and SAPT(DFT) curves for pyrene−methane (Figure S8). This information is available free of charge via the Internet at http://pubs.acs.org/.

■ AUTHOR INFORMATION

Corresponding Author

*E-mail: patkowsk@auburn.edu.

Notes

The authors declare no competing financial interest.

■ ACKNOWLEDGMENTS

This research was supported by the Donors of the American Chemical Society Petroleum Research Fund and by the startup funding from Auburn University. Some of the calculations were performed at the Alabama Supercomputer Center.

■ REFERENCES

(1) Chałasiński, G.; Szczęśniak, M. M. *Chem. Rev.* **2000**, *100*, 4227−4252.

(2) Halkier, A.; Helgaker, T.; Jørgensen, P.; Klopper, W.; Koch, H.; Olsen, J.; Wilson, A. K. *Chem. Phys. Lett.* **1998**, *286*, 243−252.

(3) Schwenke, D. W. *J. Chem. Phys.* **2005**, *122*, 014107.

(4) Tao, F.-M.; Pan, Y.-K. *J. Chem. Phys.* **1991**, *95*, 3582−3588.

(5) Hättig, C.; Klopper, W.; Köhn, A.; Tew, D. P. *Chem. Rev.* **2012**, *112*, 4−74.

(6) Kong, L.; Bischoff, F. A.; Valeev, E. F. *Chem. Rev.* **2012**, *112*, 75−107.

(7) Patkowski, K.; Podeszwa, R.; Szalewicz, K. *J. Phys. Chem. A* **2007**, *111*, 12822−12838.

(8) Peréz-Jordá, J. M.; Becke, A. D. *Chem. Phys. Lett.* **1995**, *233*, 134−137.

(9) Wu, X.; Vargas, M. C.; Nayak, S.; Lotrich, V. F.; Scoles, G. *J. Chem. Phys.* **2001**, *115*, 8748−8757.

(10) Wu, Q.; Yang, W. *J. Chem. Phys.* **2002**, *116*, 515−524.

(11) Dion, M.; Rydberg, H.; Schröder, E.; Langreth, D. C.; Lundqvist, B. I. *Phys. Rev. Lett.* **2004**, *92*, 246401.

(12) Grimme, S. *J. Comput. Chem.* **2006**, *27*, 1787−1799.

(13) Zhao, Y.; Schultz, N. E.; Truhlar, D. G. *J. Chem. Theory Comput.* **2006**, *2*, 364−382.

(14) Becke, A. D.; Johnson, E. R. *J. Chem. Phys.* **2007**, *127*, 124108.

(15) Chai, J.-D.; Head-Gordon, M. *Phys. Chem. Chem. Phys.* **2008**, *10*, 6615−6620.

(16) Zhao, Y.; Truhlar, D. G. *Theor. Chem. Acc.* **2008**, *120*, 215−241.

(17) Tkatchenko, A.; Scheffler, M. *Phys. Rev. Lett.* **2009**, *102*, 073005.

(18) Pernal, K.; Podeszwa, R.; Patkowski, K.; Szalewicz, K. *Phys. Rev. Lett.* **2009**, *103*, 263201.

(19) Grimme, S.; Antony, J.; Ehrlich, S.; Krieg, H. *J. Chem. Phys.* **2010**, *132*, 154104.

(20) Steinmann, S. N.; Corminboeuf, C. *J. Chem. Theory Comput.* **2010**, *6*, 1990−2001.

(21) Vydrov, O. A.; Van Voorhis, T. *J. Chem. Phys.* **2010**, *133*, 244103.

(22) Grimme, S. *J. Chem. Phys.* **2003**, *118*, 9095−9102.

(23) Hill, J. G.; Platts, J. A. *J. Chem. Theory Comput.* **2007**, *3*, 80−85.

(24) DiStasio, R. A., Jr.; Head-Gordon, M. *Mol. Phys.* **2007**, *105*, 1073−1083.

(25) Takatani, T.; Hohenstein, E. G.; Sherrill, C. D. *J. Chem. Phys.* **2008**, *128*, 124111.

(26) Pitoňák, M.; Neogrady, P.; Černý, J.; Grimme, S.; Hobza, P. *ChemPhysChem* **2009**, *10*, 282−289.

(27) Misquitta, A. J.; Podeszwa, R.; Jeziorski, B.; Szalewicz, K. *J. Chem. Phys.* **2005**, *123*, 214103.

(28) Hesselmann, A.; Jansen, G.; Schütz, M. *J. Chem. Phys.* **2005**, *122*, 014103.

(29) Hesselmann, A. *J. Chem. Phys.* **2008**, *128*, 144112.

(30) Bludský, O.; Rubeš, M.; Soldán, P.; Nachtigall, P. *J. Chem. Phys.* **2008**, *128*, 114102.

(31) Zhao, Y.; Truhlar, D. G. *J. Chem. Theory Comput.* **2005**, *1*, 415−432.

(32) Zhao, Y.; Truhlar, D. G. *J. Phys. Chem. A* **2005**, *109*, 5656−5667.

(33) Jurečka, P.; Šponer, J.; Černý, J.; Hobza, P. *Phys. Chem. Chem. Phys.* **2006**, *8*, 1985−1993.

(34) Sherrill, C. D.; Takatani, T.; Hohenstein, E. G. *J. Phys. Chem. A* **2009**, *113*, 10146−10159.

(35) Gráfová, L.; Pitoňák, M.; Řezáč, J.; Hobza, P. *J. Chem. Theory Comput.* **2010**, *6*, 2365−2376.

(36) Thanthiriwatte, K. S.; Hohenstein, E. G.; Burns, L. A.; Sherrill, C. D. *J. Chem. Theory Comput.* **2011**, *7*, 88−96.

(37) Řezáč, J.; Riley, K. E.; Hobza, P. *J. Chem. Theory Comput.* **2011**, *7*, 2427−2438.

(38) Marchetti, O.; Werner, H. *Phys. Chem. Chem. Phys.* **2008**, *10*, 3400−3409.

(39) Podeszwa, R.; Patkowski, K.; Szalewicz, K. *Phys. Chem. Chem. Phys.* **2010**, *12*, 5974−5979.

(40) Takatani, T.; Hohenstein, E. G.; Malagoli, M.; Marshall, M. S.; Sherrill, C. D. *J. Chem. Phys.* **2010**, *132*, 144104.

(41) Marshall, M. S.; Burns, L. A.; Sherrill, C. D. *J. Chem. Phys.* **2011**, *135*, 194102.

(42) Burns, L. A.; Vazquez-Mayagoitia, A.; Sumpter, B. G.; Sherrill, C. D. *J. Chem. Phys.* **2011**, *134*, 084107.

(43) Novoselov, K. S.; Geim, A. K.; Morozov, S. V.; Jiang, D.; Zhang, Y.; Dubonos, S. V.; Grigorieva, I. V.; Firsov, A. A. *Science* **2004**, *306*, 666−669.

(44) Iijima, S. *Nature* **1991**, *354*, 56−58.

(45) Britz, D. A.; Khlobystov, A. N. *Chem. Soc. Rev.* **2006**, *35*, 637−659.

(46) Dillon, A. C.; Jones, K. M.; Bekkedahl, T. A.; Kiang, C. H.; Bethune, D. S.; Heben, M. J. *Nature* **1997**, *386*, 377−379.

(47) Kong, J.; Franklin, N. R.; Zhou, C. W.; Chapline, M. G.; Peng, S.; Cho, K. J.; Dai, H. J. *Science* **2000**, *287*, 622−625.

(48) Duren, T.; Sarkisov, L.; Yaghi, O. M.; Snurr, R. Q. *Langmuir* **2004**, *20*, 2683−2689.

(49) Bruch, L. W.; Diehl, R. D.; Venables, J. A. *Rev. Mod. Phys.* **2007**, *79*, 1381−1454.

(50) Murdachaew, G.; de Gironcoli, S.; Scoles, G. *J. Phys. Chem. A* **2008**, *112*, 9993−10005.

(51) Becke, A. D. *J. Chem. Phys.* **1993**, *98*, 5648−5652.

(52) Stephens, P. J.; Devlin, F. J.; Chabalowski, C. F.; Frisch, M. J. *J. Phys. Chem.* **1994**, *98*, 11623−11627.

(53) Perdew, J. P.; Burke, K.; Ernzerhof, M. *Phys. Rev. Lett.* **1996**, *77*, 3865−3868.

(54) Yang, S.; Ouyang, L.; Phillips, J. M.; Ching, W. Y. *Phys. Rev. B* **2006**, *73*, 165407.

(55) Albesa, A. G.; Fertitta, E. A.; Vicente, J. L. *Langmuir* **2010**, *26*, 786−795.

(56) Liu, Y. Y.; Wilcox, J. *Environ. Sci. Technol.* **2011**, *45*, 809−814.

(57) Wong, B. M. *J. Comput. Chem.* **2009**, *30*, 51−56.

(58) Tsuzuki, S.; Honda, K.; Fujii, A.; Uchimaru, T.; Mikami, M. *Phys. Chem. Chem. Phys.* **2008**, *10*, 2860−2865.

(59) Dunning, T. H., Jr. *J. Chem. Phys.* **1989**, *90*, 1007−1023.

(60) Špirko, V.; Rubeš, M.; Bludský, O. *J. Chem. Phys.* **2010**, *132*, 194708.

(61) Jenness, G. R.; Karalti, O.; Jordan, K. D. *Phys. Chem. Chem. Phys.* **2010**, *12*, 6375−6381.

(62) Hachmann, J.; Dorando, J. J.; Avilés, M.; Chan, G. K.-L. *J. Chem. Phys.* **2007**, *127*, 134309.

(63) Janssen, C. L.; Nielsen, I. M. B. *Chem. Phys. Lett.* **1998**, *290*, 423−430.

(64) Werner, H. J.; Knowles, P. J.; Knizia, G.; Manby, F. R.; Schütz, M.; Celani, P.; Korona, T.; Lindh, R.; Mitrushenkov, A.; Rauhut, G.; Shamasundar, K. R.; Adler, T. B.; Amos, R. D.; Bernhardsson, A.; Berning, A.; Cooper, D. L.; Deegan, M. J. O.; Dobbyn, A. J.; Eckert, F.; Goll, E.; Hampel, C.; Hesselmann, A.; Hetzer, G.; Hrenar, T.; Jansen, G.; Köppl, C.; Liu, Y.; Lloyd, A. W.; Mata, R. A.; May, A. J.; McNicholas, S. J.; Meyer, W.; Mura, M. E.; Nicklass, A.; O'Neill, D. P.; Palmieri, P.; Pflüger, K.; Pitzer, R.; Reiher, M.; Shiozaki, T.; Stoll, H.; Stone, A. J.; Tarroni, R.; Thorsteinsson, T.; Wang, M.; Wolf, A. *MOLPRO*, version 2010.1; Cardiff University: Cardiff, U. K.; Universität Stuttgart: Stuttgart, Germany, 2010. See http://www.molpro.net (accessed Nov 6, 2012).

(65) Werner, H.-J.; Manby, F. R.; Knowles, P. J. *J. Chem. Phys.* **2003**, *118*, 8149−8160.

(66) Kendall, R. A.; Dunning, T. H., Jr.; Harrison, R. J. *J. Chem. Phys.* **1992**, *96*, 6796−6806.

(67) Weigend, F.; Köhn, A.; Hättig, C. *J. Chem. Phys.* **2002**, *116*, 3175−3183.

(68) Hättig, C. *Phys. Chem. Chem. Phys.* **2005**, *7*, 59−66.

(69) Boys, S. F.; Bernardi, F. *Mol. Phys.* **1970**, *19*, 553−566.

(70) van Duijneveldt, F. B.; van Duijneveldt-van de Rijdt, J. G. C. M.; van Lenthe, J. H. *Chem. Rev.* **1994**, *94*, 1873−1885.

(71) Adler, T. B.; Knizia, G.; Werner, H.-J. *J. Chem. Phys.* **2007**, *127*, 221106.

(72) Knizia, G.; Adler, T. B.; Werner, H.-J. *J. Chem. Phys.* **2009**, *130*, 054104.

(73) Köhn, A. *J. Chem. Phys.* **2009**, *130*, 131101.

(74) Tew, D. P.; Klopper, W.; Hättig, C. *Chem. Phys. Lett.* **2008**, *452*, 326−332.

(75) Marchetti, O.; Werner, H.-J. *J. Phys. Chem. A* **2009**, *113*, 11580−11585.

(76) McMahon, J. D.; Lane, J. R. *J. Chem. Phys.* **2011**, *135*, 154309.

(77) Patkowski, K. *J. Chem. Phys.* **2012**, *137*, 034103.

(78) Marshall, M. S.; Sherrill, C. D. *J. Chem. Theory Comput.* **2011**, *7*, 3978−3982.

(79) Becke, A. D. *J. Chem. Phys.* **1997**, *107*, 8554−8560.

(80) Weigend, F. *Phys. Chem. Chem. Phys.* **2002**, *4*, 4285−4291.

(81) Frisch, M. J.; Trucks, G. W.; Schlegel, H. B.; Scuseria, G. E.; Robb, M. A.; Cheeseman, J. R.; Scalmani, G.; Barone, V.; Mennucci, B.; Petersson, G. A.; Nakatsuji, H.; Caricato, M.; Li, X.; Hratchian, H. P.; Izmaylov, A. F.; Bloino, J.; Zheng, G.; Sonnenberg, J. L.; Hada, M.; Ehara, M.; Toyota, K.; Fukuda, R.; Hasegawa, J.; Ishida, M.; Nakajima, T.; Honda, Y.; Kitao, O.; Nakai, H.; Vreven, T.; Montgomery, J. A., Jr.; Peralta, J. E.; Ogliaro, F.; Bearpark, M.; Heyd, J. J.; Brothers, E.; Kudin, K. N.; Staroverov, V. N.; Kobayashi, R.; Normand, J.; Raghavachari, K.; Rendell, A.; Burant, J. C.; Iyengar, S. S.; Tomasi, J.; Cossi, M.; Rega, N.; Millam, J. M.; Klene, M.; Knox, J. E.; Cross, J. B.; Bakken, V.; Adamo, C.; Jaramillo, J.; Gomperts, R.; Stratmann, R. E.; Yazyev, O.; Austin, A. J.; Cammi, R.; Pomelli, C.; Ochterski, J. W.; Martin, R. L.; Morokuma, K.; Zakrzewski, V. G.; Voth, G. A.; Salvador, P.; Dannenberg, J. J.; Dapprich, S.; Daniels, A. D.; Farkas, O.; Foresman, J. B.; Ortiz, J. V.; Cioslowski, J.; Fox, D. J. *Gaussian 09*, revision A.1. Gaussian Inc.: Wallingford, CT, 2009.

(82) Vosko, S. H.; Wilk, L.; Nusair, M. *Can. J. Phys.* **1980**, *58*, 1200.

(83) Johnson, E. R.; Becke, A. D.; Sherrill, C. D.; DiLabio, G. A. *J. Chem. Phys.* **2009**, *131*, 034111.

(84) Adamo, C.; Barone, V. *J. Chem. Phys.* **1999**, *110*, 6158−6170.

(85) DALTON, a molecular electronic structure program, release 2.0 (2005). See http://daltonprogram.org (accessed Nov 6, 2012).

(86) Bukowski, R.; Cencek, W.; Jankowski, P.; Jeziorska, M.; Jeziorski, B.; Kucharski, S. A.; Lotrich, V. F.; Misquitta, A. J.; Moszyński, R.; Patkowski, K.; Podeszwa, R.; Rybak, S.; Szalewicz, K.; Williams, H. L.; Wheatley, R. J.; Wormer, P. E. S.; Żuchowski, P. S. *SAPT2008*; University of Delaware: Newark, DE; University of Warsaw: Warsaw, Poland (http://www.physics.udel.edu/∼szalewic/SAPT/SAPT.html, accessed Nov 6, 2012).

(87) Tozer, D. J.; Handy, N. C. *J. Chem. Phys.* **1998**, *109*, 10180−10189.

(88) Lias, S. G. *Ionization Energy Evaluation, in NIST Chemistry WebBook, NIST Standard Reference Database Number 69*; Linstrom, P. J., Mallard, W. G., Eds.; National Institute of Standards and Technology: Gaithersburg MD. http://webbook.nist.gov (accessed Nov 6, 2012).

(89) Patkowski, K.; Szalewicz, K.; Jeziorski, B. *J. Chem. Phys.* **2006**, *125*, 154107.

(90) Patkowski, K.; Szalewicz, K.; Jeziorski, B. *Theor. Chem. Acc.* **2010**, *127*, 211−221.

(91) Zhao, Y.; Truhlar, D. G. *J. Phys. Chem. A* **2006**, *110*, 5121−5129.

(92) Podeszwa, R.; Szalewicz, K. *J. Chem. Phys.* **2012**, *136*, 161102.

(93) Yoo, S.; Aprà, E.; Zeng, X. C.; Xantheas, S. S. *J. Phys. Chem. Lett.* **2010**, *1*, 3122−3127.

(94) Ziółkowski, M.; Jansík, B.; Kjærgaard, T.; Jørgensen, P. *J. Chem. Phys.* **2010**, *133*, 014107.

(95) Janowski, T.; Pulay, P.; Karunarathna, A. A. S.; Sygula, A.; Saebø, S. *Chem. Phys. Lett.* **2011**, *512*, 155−160.

(96) Sullivan, M. B.; Iron, M. A.; Redfern, P. C.; Martin, J. M. L.; Curtiss, L. A.; Radom, L. *J. Phys. Chem. A* **2003**, *107*, 5617−5630.

(97) Sinnokrot, M. O.; Sherrill, C. D. *J. Phys. Chem. A* **2004**, *108*, 10200−10207.

(98) Papajak, E.; Zheng, J.; Xu, X.; Leverentz, H. R.; Truhlar, D. G. *J. Chem. Theory Comput.* **2011**, *7*, 3027−3034.

(99) ElSohly, A.; Tschumper, S. *Int. J. Quantum Chem.* **2009**, *109*, 91−96.

(100) Papajak, E.; Leverentz, H. R.; Zheng, J.; Truhlar, D. G. *J. Chem. Theory Comput.* **2009**, *5*, 1197−1202.

(101) Pitoňák, M.; Neogrády, P.; Řezáč, J.; Jurečka, P.; Urban, M.; Hobza, P. *J. Chem. Theory Comput.* **2008**, *4*, 1829−1834.

(102) Kucharski, S. A.; Bartlett, R. J. *J. Chem. Phys.* **1998**, *108*, 9221−9226.

(103) Stanton, J.; Gauss, J.; Harding, M.; Szalay, P.; Auer, A.; Bartlett, R.; Benedikt, U.; Berger, C.; Bernholdt, D.; Bomble, Y.; Christiansen, O.; Heckert, M.; Heun, O.; Huber, C.; Jagau, T.-C. et al. *CFOUR*, a quantum chemical program package, containing the integral packages MOLECULE (Almlöf, J.; Taylor, P. R.), PROPS (Taylor, P. R.), ABACUS (Helgaker, T.; Jensen, H. J. Aa.; Jørgensen, P.; Olsen, J.), and ECP routines (Mitin, A. V.; van Wüllen, C.). For the current version, see http://www.cfour.de (accessed Nov 6, 2012).

(104) Johnson, E. R.; Becke, A. D. *J. Chem. Phys.* **2005**, *123*, 024101.

(105) Grimme, S.; Ehrlich, S.; Goerigk, L. *J. Comput. Chem.* **2011**, *32*, 1456−1465.

(106) Vidali, G.; Ihm, G.; Kim, H. Y.; Cole, M. W. *Surf. Sci. Rep.* **1991**, *12*, 135−181.

(107) Podeszwa, R. *J. Chem. Phys.* **2010**, *132*, 044704.

(108) Rubeš, M.; Kysilka, J.; Nachtigall, P.; Bludský, O. *Phys. Chem. Chem. Phys.* **2010**, *12*, 6438−6444.

(109) Thierfelder, C.; Witte, M.; Blankenburg, S.; Rauls, E.; Schmidt, W. G. *Surf. Sci.* **2011**, *605*, 746−749.

(110) Qiu, N.-X.; Xue, Y.; Guo, Y.; Sun, W.-J.; Chu, W. *Comp. Theor. Chem.* **2012**, *992*, 37−47.

(111) Ringer, A. L.; Figgs, M. S.; Sinnokrot, M. O.; Sherrill, C. D. *J. Phys. Chem. A* **2006**, *110*, 10822−10828.

Appendix C

Toward an Accurate Description of Methane Physisorption on Carbon Nanotubes

THE JOURNAL OF PHYSICAL CHEMISTRY C
Article
pubs.acs.org/JPCC

Toward an Accurate Description of Methane Physisorption on Carbon Nanotubes

Daniel G. A. Smith and Konrad Patkowski*

Department of Chemistry and Biochemistry, Auburn University, Auburn, Alabama 36849

Supporting Information

ABSTRACT: We present a high-level ab initio investigation of the effects of model size and curvature on the exterior and interior binding energy of methane on single-walled carbon nanotubes. The interaction energies of methane with curved coronene were computed using complete basis set MP2 with a CCSD(T) correction. A variety of novel dispersion-including density functional approaches were then compared to the benchmark data. The top-performing functionals were used to calculate binding energies between methane and larger nanotube fragments all the way through infinite nanotubes. The methane binding energy of a narrow (9,0) carbon nanotube, compared to a flat graphene surface, is decreased by 32% on the exterior but increased by 185% on the interior.

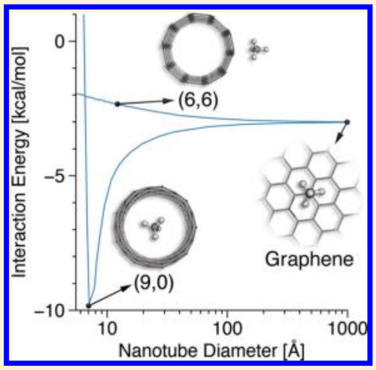

I. INTRODUCTION

Noncovalent interactions between carbon nanostructures and small molecules have been the subject of numerous experimental and theoretical studies.[1−11] The physisorption of methane on carbon nanotubes has been of particular interest due to the proposed applications of nanotubes for methane storage,[12,13] as molecular sieves to separate CO_2 from flue gases,[14−16] and as catalysts for important processes such as C−H bond activation in organic synthesis.[17,18] However, the majority of existing theoretical studies for nanotube complexes have used either empirical, Lennard-Jones-type potentials or standard density functionals such as LDA. While such studies can lead to important qualitative findings, their quantitative accuracy leaves significant room for improvement.

As the adsorbate−surface binding is dominated by dispersion, standard density functionals like B3LYP[19,20] or PBE[21] are unable to provide accurate interaction energies. In the past decade, numerous density functional theory (DFT) methods that incorporate dispersion have been introduced and benchmarked on a wide variety of systems.[22−30] While some of the novel methods exhibit average errors at the van der Waals minima as low as 0.2 kcal/mol (0.8 kJ/mol),[29] a systematic behavior of errors across different intermolecular distances cannot be guaranteed. Moreover, the accuracy of a given DFT approach may vary dramatically between different systems.

More accurate interaction energies can be obtained using wave function methods for models involving small fragments of a graphene sheet such as polycyclic aromatic hydrocarbons (PAHs) or curved PAHs as fragments of nanotubes. The current gold standard in electronic structure theory, the coupled-cluster approach with singles, doubles, and perturbative triples (CCSD(T)), provides interaction energies accurate to about 1−2%[31] at the complete basis set (CBS) limit. However, CCSD(T) calculations in bases large enough for direct CBS extrapolation are only feasible for PAHs up to naphthalene (11 carbon atoms). We have previously shown[32] that the composite MP2/CBS+ΔCCSD(T) method provides an excellent approximation to CCSD(T)/CBS for PAH−methane complexes even when the $\Delta\text{CCSD(T)} = E_{\text{CCSD(T)}} - E_{\text{MP2}}$ correction is limited to the aug-cc-pVDZ basis set. At this basis set level, PAHs up to coronene (24 carbon atoms) are feasible. Second-order Møller−Plesset perturbation theory (MP2) calculations are feasible for model dimers involving at least circumcoronene (54 carbon atoms); however, MP2 typically overbinds dispersion-bound systems by 20−40%.[32,33] Several approaches to correct this overbinding by proper scaling of the parallel- and antiparallel-spin contributions have been proposed;[34−36] however, none of them consistently deliver accuracy comparable to CCSD(T). Among the approaches that exhibit the (MP2-like) N^5 scaling with the system size, the most accurate interaction energies are likely provided by those where the dispersion energy is computed using frequency-dependent polarizabilities from time-dependent DFT, such as DFT-SAPT[37,38] and MP2C.[39] Indeed, these methods have been successfully employed to compute accurate PAH−water,[40−42] PAH−CO_2,[43] and PAH−rare gas[44] interaction energies. However, our recent study of the PAH−methane complexes[32] indicates that the DFT−SAPT approach, while likely quite accurate at the CBS limit, exhibits relatively slow basis set convergence. Thus, we prefer not to rely on any level of theory below CCSD(T) as a trustworthy source of benchmark PAH−methane interaction energies.

Received: November 3, 2013
Revised: December 6, 2013
Published: December 12, 2013

dx.doi.org/10.1021/jp410826p | *J. Phys. Chem. C* 2014, 118, 544−550

A variety of different dispersion-corrected DFT functionals were tested in ref 32. It was shown that the DFT plus atom-pairwise dispersion correction (DFT+D) methods[45] replicated the CCSD(T) benchmarks significantly better than the interaction-optimized functionals such as M05-2X,[46] M06-2X,[24] and ωB97X-D.[25] The most accurate DFT+D method for the PAH−methane complexes was the B3LYP functional combined with Grimme's -D3 dispersion correction[27] in the aug-cc-pVDZ basis set, with a median unsigned relative error of 3.3% and a mean unsigned error (MUE) at the minima of 0.04 kcal/mol compared to the CCSD(T)-level benchmark.

In this work, we extend the investigation of ref 32 to complexes of methane with nanotube fragments of different curvature. As there is no guarantee that the impressive accuracy of B3LYP-D3/aDZ interaction energies is retained for curved hydrocarbons, we extend the benchmark CCSD(T)-level calculations to complexes containing a curved coronene molecule. The top performing DFT variants are used to investigate the dependence of interaction energy on the nanotube diameter, adsorption site (interior/exterior), intermolecular distance, and the coordination of the methane molecule. Perhaps most importantly, we determine the minimum sizes of the curved PAH models that provide converged values of the nanotube binding energies. While for the PAH−water interaction even the smallest, benzene−water model was found to be reasonably accurate;[40,41,47] for nonpolar adsorbates much larger fragments are required,[32,47,48] and it is likely that still larger curved PAHs may be needed to describe interior adsorption where a large number of surface atoms are in close proximity to the adsorbate molecule. Finally, we test the validity of finite PAH models by performing plane-wave DFT calculations for complexes of methane with infinite nanotubes.

The structure of the rest of this paper is as follows. In section II we describe the ab initio methodology employed to compute interaction energies and give the pertinent computational details. We present and analyze our numerical results in section III. Finally, section IV contains conclusions.

II. METHODS

We consider two classes of model complexes in which the nanotube is represented by coronene-shaped (C_n) and toroidal (T_n) fragments, as illustrated in Figure 1. Specifically, the C_n fragment is obtained by a successive addition of n layers of peri-fused benzene rings around a central benzene ring (so that C_1 denotes curved coronene, C_2 is curved circumcoronene, and so on). The T_n model denotes a full toroidal fragment, that is, a nanotube of finite length. The number of benzene rings along the nanotube axis is the same for the C_n and T_n models.

To construct the model geometries, larger nanotube pieces were first generated using the TUBEGEN program.[49] The desired fragment was then cut from the TUBEGEN output so that its curvature corresponds to a particular zigzag (k,0) or armchair (k,k) nanotube.[1] When the width of the C_n fragment is larger than the circumference of the nanotube, the fragment is wrapped around and may actually contain a T_m fragment, $m < n$, as a subset (see Figures S2−S3 in the Supporting Information for examples). The cleaved carbon−carbon bonds in all fragments were capped with hydrogen atoms.

The MOLPRO code[50] was used to obtain all MP2, CCSD(T), and DFT interaction energies. We employed the Dunning bases aug-cc-pVXZ≡aXZ[51,52] as well as the Turbomole def2 series of basis sets.[53] As observed in ref 32, calculations of the ΔCCSD(T) correction in the full aDZ basis for the methane−coronene complex are not possible due to near linear dependencies in the basis set. Truncation of the aDZ basis to jun-cc-pVDZ[54] did remove the linear dependencies; however, the accuracy of the resulting ΔCCSD(T) correction was not satisfactory. A much better result was obtained using a different truncation scheme where only the methane atoms and the six coronene carbon atoms closest to the methane carbon (seven closest carbon atoms if the sixth and seventh one are symmetry equivalent) had diffuse functions in the basis set. The resulting set will be denoted as local-aDZ (laDZ).[32] The notation MP2/(basis1,basis2) means that the bases "basis1" and "basis2" have been employed in the standard X^{-3} extrapolation of the correlation part of the MP2 interaction energy.[55]

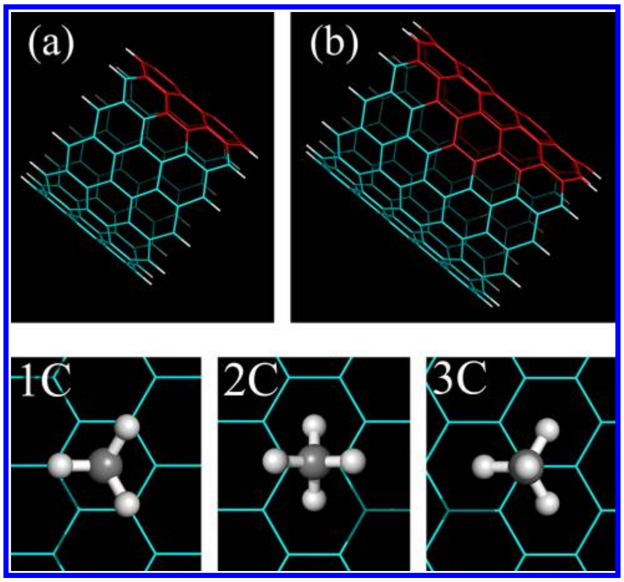

Figure 1. Upper panel: example fragments cut out from a (12,0) nanotube. (a) The T_1 fragment in teal with the C_1 fragment in red. (b) The T_2 fragment in teal with the C_2 fragment in red. Analogous models cut out from an armchair nanotube can be found in Figure S1 of the Supporting Information. Lower panel: the three possible coordinations of methane in their respective idealized graphene minima.

The DFT functionals employed were B3LYP,[19,20] PBE,[21] and Grimme's reparameterization[22] of Becke's B97 functional.[56] These functionals were augmented by Grimme's atom-pairwise dispersion terms in the -D2[22] and -D3[27] variants. The -D2 correction and the four variants of the -D3 correction (with either Chai−Head-Gordon[25] or Becke−Johnson (BJ) damping[57] and with or without the three-body term -$E^{(3)}$) were calculated using Grimme's DFT+D program V3 Rev. 0. All calculations employed the counterpoise correction for basis set superposition error.[58,59] The MP2 and DFT calculations employed density fitting.[60,61] The distance z from the methane carbon to the nanotube surface is defined relative to the closest point on the cylinder on which all nanotube carbons are located.

The plane-wave periodic DFT calculations for complexes of methane with finite and infinite nanotubes were performed with the VASP code.[62−64] The box size for VASP calculations was the nanotube diameter +10 Å for dimensions perpendicular to the nanotube axis. For the axis parallel to the nanotube, the unit cell length was the fragment length plus 10 Å for finite

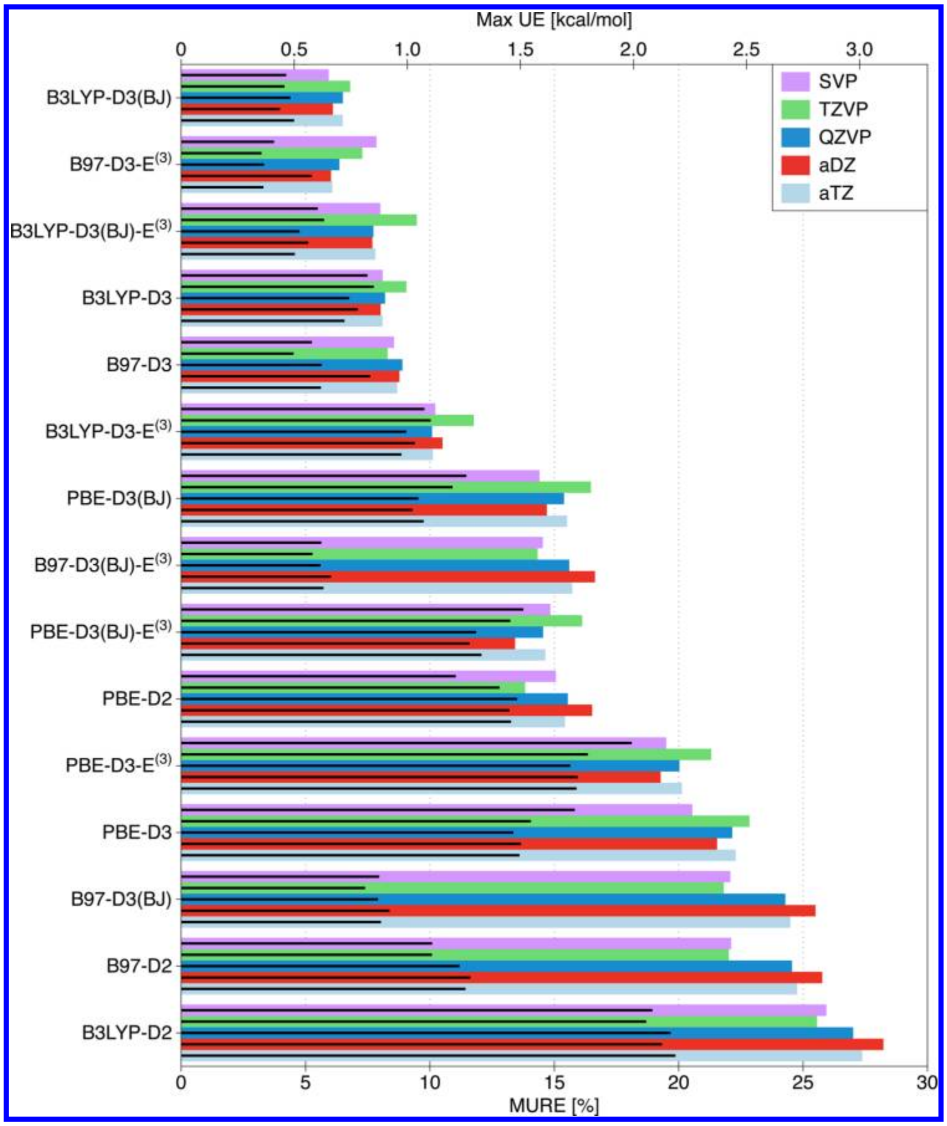

Figure 2. Max UE (black lines) and MURE (bars) statistics of the best-performing DFT+D methods compared to the benchmark CCSD(T)-level results for the 108 C_1 model geometries. The methods are sorted by the MURE in the SVP basis set.

models and the length of a T_3 segment (14.8 Å for armchair and 12.8 Å for zigzag) for the infinite nanotube calculations. The plane-wave energy cutoff was 400 eV.

III. RESULTS AND DISCUSSION

A. Curved Coronene. The five models chosen for the CCSD(T)-level benchmarks were the C_1 (coronene-sized) fragments of the (5,5), (7,0), (9,0), (12,0), and (5000,0) nanotubes. The last fragment was used to represent graphene: it deviates from a flat plane by just 0.003 Å at the C_1 size and 0.012 Å at the C_4 size. We have followed the nomenclature of singly, doubly, and triply coordinated (1C, 2C, and 3C) configurations,[32] where nC involves n methane hydrogens closer to the nanotube surface than the methane carbon. To obtain the exterior and interior minima for each coordination, the methane molecule was initially placed in an idealized minimum for a flat graphene sheet, as shown in Figure 1. The complex geometries were then optimized (with the monomer geometries frozen) using the B3LYP-D3/aDZ method which previously showed excellent agreement with wave function-based approaches for the methane−PAH complexes.[32] For curved nanotube fragments all geometry optimizations, except those of the zigzag 3C structures, resulted in the methane carbon directly over the center of the coronene molecule. The methane in the exterior zigzag 3C models remained near its location in the idealized graphene structure, as shown in Figure S4 of the Supporting Information. The minimum geometries for the flat (5000,0) fragment were similar to the idealized graphene minima, Figure 1.

The 27 minima obtained in this way (interior and exterior sites for curved coronene and one minimum for flat coronene at each coordination) were then investigated at the MP2/(aTZ,aQZ)+ΔCCSD(T)/laDZ level at the minimum z distance and at 0.9, 1.2, and 1.4 times the minimum z distance, giving a total of 108 CCSD(T) results against which different DFT methods can be benchmarked. The DFT methods tested were the best performers from our work on methane−PAH complexes:[32] B97, PBE, and B3LYP with the def2 SVP, TZVP, QZVP and Dunning DZ, aDZ, TZ, aTZ basis sets combined with all possible variants of Grimme's dispersion correction:

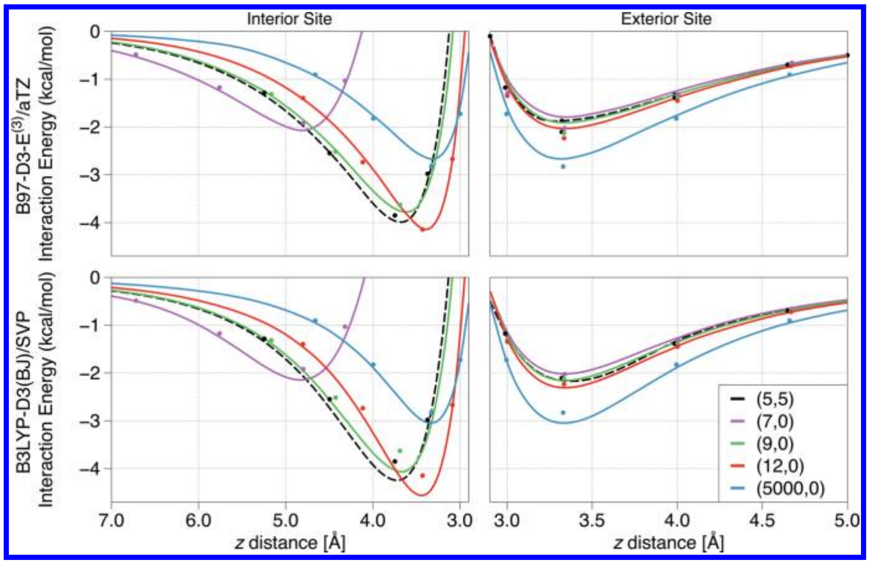

Figure 3. Interior and exterior methane-curved coronene (C_1) potential energy curves in the 3C configuration. The points represent MP2/(aTZ,aQZ)+ΔCCSD(T)/laDZ calculations while the solid lines display the best DFT variants for the interior and exterior sites, B97-D3-E$^{(3)}$/aTZ (upper panels) and B3LYP-D3(BJ)/SVP (lower panels), respectively.

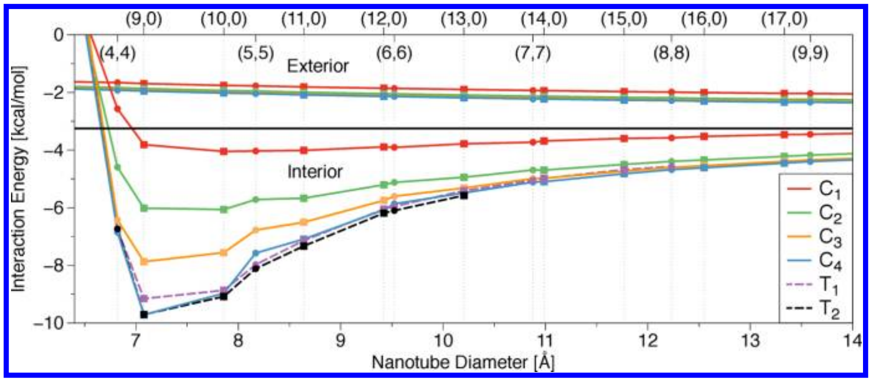

Figure 4. Methane−nanotube fragment interaction energies in the 3C configuration, computed using B97-D3-E$^{(3)}$/SVP for interior sites and B97-D3/SVP for exterior sites, as functions of the nanotube diameter. Zigzag and armchair nanotubes are represented by squares and circles, respectively. The black line is the 3C value for flat graphene calculated at the B97-D3/SVP level using the C_4 model.

-D2,[22] -D3,[27] -D3(BJ),[57] -D3-E$^{(3)}$, and -D3(BJ)-E$^{(3)}$, giving a total of 105 different combinations of functionals, basis sets, and dispersion corrections.

The accuracy of different DFT variants with respect to the CCSD(T)-level benchmarks is displayed in Figure 2 using two statistical measures: the mean unsigned relative error (MURE) and the maximum unsigned error (Max UE). The MURE, Max UE, and MUE values for all 105 variants are given in Figures S5−S7 in the Supporting Information. Figure 2 shows that the DFT+D performance is strongly dependent on the selection of a functional but only weakly dependent on the basis set. As far as the dispersion term is concerned, -D3 is significantly more accurate than -D2 for the B97 and B3LYP functionals: only for PBE the performance of -D2 and -D3 is similar. Among different -D3 variants, the inclusion or omission of the three-body term has little effect. However, the choice of the damping term is quite significant, with the BJ damping performing better than the original "zero-damping" for B3LYP and PBE and worse for B97. The wide range of accuracy displayed in Figure 2 emphasizes that while the best DFT+D variants can lead to excellent agreement with high level ab initio benchmarks, the selection of the functional and the dispersion correction are of utmost importance.

The best functional overall is B97-D3-E$^{(3)}$/aTZ with a MURE of 5.7% and Max UE of 0.36 kcal/mol. Considering the exterior and interior sites separately (and excluding the (5000,0) data), the best functionals for interior and exterior structures are B97-D3-E$^{(3)}$/aTZ (MURE 4.3%) and B3LYP-D3(BJ)/SVP (MURE 3.4%), respectively. The previously recommended B3LYP-D3/aDZ functional[32] has a MURE of 4.0% and 12.1% for the exterior and interior geometries, respectively.

The benchmark CCSD(T) results and methane-curved coronene potential energy curves from the two best DFT functionals are shown in Figure 3, demonstrating the good performance of the top DFT+D variants across the entire van der Waals well. As predicted by a simple consideration of the number of nanotube atoms in the vicinity of methane, and as well established by both theory and experiment for different adsorbate molecules,[65−68] when the nanotube becomes smaller, the exterior binding energies decrease while the interior binding energies increase. The 3C binding energy for the flat (5000,0) fragment is reduced by as much as 28% outside the smallest nanotube investigated at the CCSD(T) level, (7,0). The analogous interior 3C binding energy is increased by 28% and 47% for the (9,0) and (12,0) nanotubes, respectively. It is worth noting that the minimum *z* distances for all interior coordinations of the (7,0) nanotube are larger than its radius (2.76 Å) indicating that the methane molecule is unlikely to fit inside this particular nanotube.

B. Nanotube Fragments. To examine the effect of model size on the binding energy, the best nonhybrid DFT+D scheme utilizing the smallest basis set (SVP) was picked for the interior and exterior geometries. Calculations at this level are feasible for models up to C_4 and T_2, and, as shown in Figure 2, the SVP basis set delivers accuracy comparable to that of larger bases. The best variant for the interior case is B97-D3-$E^{(3)}$/SVP (MURE 5.4%) and for the exterior case is B97-D3/SVP (MURE 6.7%). The *z* distance for the 3C idealized graphene minima (Figure 1) was optimized for both the interior and exterior sites for all nanotubes between 5 and 14 Å in diameter and all fragments C_1−C_4 as well as all T_1−T_2 fragments less than 200 atoms in size (corresponding to nanotube diameters less than 12.5 and 10.5 Å for T_1 and T_2, respectively). The resulting interaction energies for different fragments are displayed in Figure 4. As clearly seen in this figure, the exterior binding energies converge rapidly with the fragment size. Taking the C_4 fragment as a benchmark, the C_1, C_2, and C_3 models capture 87%, 97%, and 99% of the exterior binding energy while requiring roughly 2%, 10%, and 30% of calculation time, respectively. With the C_2 fragment capturing the majority of the exterior binding energy, it is preferable to use the more expensive, hybrid B3LYP-D3(BJ)/SVP functional which can be expected to perform extremely well in this context, as its MURE on the 48 exterior C_1 structures is just 3.4%.

The interior binding energy is much more variable with respect to the fragment size, at least for nanotubes with a diameter smaller than 20 Å (for larger nanotubes the convergence with respect to fragment size is nearly identical to that for the exterior site). This is understandable as the methane−nanotube binding is primarily a dispersion effect, and, due to the curvature of the nanotube, interior sites have more carbon atoms in close proximity to methane than exterior sites. For the (9,0) nanotube, which exhibits the strongest interior binding, the C_1 fragment captures only 37% of the interaction energy compared to the most complete T_2 calculation. The best possible energy results from using the T_2 model for nanotubes smaller than 10.6 Å in diameter and the C_4 model for larger nanotubes where a T_2 calculation is not feasible.

Our best binding energy estimates for all three coordinations and both interior and exterior sites are shown in Figure 5. In this figure, the minima for all coordinations were optimized using the best theory level and fragment size feasible. For the exterior sites, the B3LYP-D3(BJ)/SVP approach was used for the C_2 fragment. In particular, for the 2C exterior configuration, there are two separate minima, with the methane carbon above the central ring being the lowest-energy structure for nanotubes less than 20 Å in diameter and the methane carbon above a carbon−carbon bond corresponding to lower energy for nanotubes greater than 20 Å in diameter. For the 3C exterior configuration neither the idealized graphene structure nor the geometry with the methane carbon over the midpoint of the central benzene ring is the global minimum. Instead, a structure halfway between these two appears to be the minimum for small nanotubes, slowly shifting toward the idealized graphene minimum as the nanotube increases in size. The shifting minima locations are illustrated in the Supporting Information, Figures S8−S11. For the interior sites, only the *z* distance was optimized as our B97-D3-$E^{(3)}$/SVP tests for the C_2, T_1, and T_2 fragments showed no improvement over the idealized graphene minima.

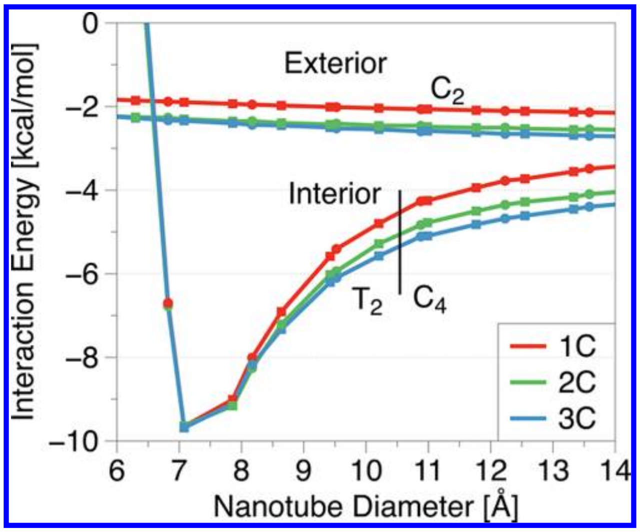

Figure 5. Our best interaction energy estimates for a methane molecule physisorbed onto different carbon nanotubes at the lowest-energy 1C, 2C, and 3C configurations. The exterior results are B3LYP-D3(BJ)/SVP using the C_2 model, and the interior results are B97-D3-$E^{(3)}$/SVP with the T_2 and C_4 fragments. Zigzag and armchair nanotubes are represented by squares and circles, respectively.

The results in Figure 5 illustrate that for large nanotubes the interior and exterior adsorption energies follow the same pattern as for flat graphene and its finite fragments;[32] that is, the 3C structure is the most favorable followed by the 2C one. However, for smaller nanotubes, for which the inside adsorption is particularly favorable, the energy differences between the 1C, 2C, and 3C structures nearly vanish. This behavior is understandable as a methane molecule inside a narrow nanotube is differently coordinated with respect to different hexagonal faces at a similar distance from it. Another interesting observation from Figure 5 is that there is virtually no difference in the adsorption characteristics of zigzag and armchair nanotubes: the nanotube diameter appears to be the dominating factor that determines the binding energies.

C. Infinite Nanotubes. To ensure that the finite models provide a reasonable description of the physisorption onto extended nanotubes, plane-wave periodic DFT calculations for the complexes of methane with the T_2 and T_3 fragments as well as with infinite nanotubes were performed with the VASP code.[62−64] Comparing the T_2 and T_3 fragments to the infinite nanotube calculations, we obtain an average difference of 1.3% and 0.5%, respectively, for all interior and exterior coordinations of zigzag and armchair nanotubes between 6 and 14 Å in diameter. Representative results are shown in Table 1 which also contains the Gaussian-basis T_2 results (computed with MOLPRO) which agree reasonably well with the VASP values confirming that both approaches are sufficiently converged with respect to the basis set.

Table 1 demonstrates that, at least for the PBE-D3 functional, the fragments studied here accurately represent the adsorption on infinite nanotubes. We acknowledge that the

Table 1. Interior and Exterior Methane Binding Energies (in kcal/mol) in the 3C Configuration for Several Nanotubes, Computed Using PBE-D3(BJ)/SVP (with MOLPRO) and Plane-Wave PBE-D3(BJ) (with VASP)

			MOLPRO	VASP		
nanotube	diameter (Å)	site	T_2	T_2	T_3	infinite
(10, 0)	7.8	exterior	−2.176	−2.245	−2.285	−2.297
		interior	−9.454	−9.352	−9.511	−9.540
(6, 6)	8.2	exterior	−2.201	−2.270	−2.296	−2.313
		interior	−8.730	−8.693	−8.751	−8.810
(7, 7)	9.6	exterior	−2.282	−2.351	−2.368	−2.389
		interior	−6.459	−6.387	−6.440	−6.474
(13, 0)	10.2	exterior	−2.320	−2.393	−2.411	−2.425
		interior	−5.782	−5.755	−5.827	−5.862

pairwise-additive dispersion approach employed in this work cannot model the long-range polarizability in infinite metallic nanotubes that could change the dispersion energy considerably.[69,70] However, a recent experimental study comparing the adsorption energies of noble gases and *n*-heptane on metallic and nonmetallic single-walled carbon nanotubes[71,72] suggests that the long-range polarizability effects on the binding energy are negligible for nonpolar adsorbates.

IV. CONCLUSIONS

We have demonstrated that several DFT+D variants reproduce CCSD(T)-level interaction energies between methane and curved coronene to a few percent. Extensive calculations using the best DFT+D variants have illuminated the effects of nanotube curvature and fragment size on the methane binding energy. The results indicate that, for the exterior binding, the C_2 (54 carbon atoms) nanotube fragment captures virtually all of the interaction energy; for the interior sites, fragments as large as C_4 (150 carbon atoms) or T_2 (up to 168 carbon atoms) are required. In addition, we have demonstrated through the use of plane-wave DFT that the finite nanotube models considered here work just as well as the infinite ones. For a (9,0) nanotube, the increased curvature reduces the exterior binding energy by 32% and increases the interior binding energy by up to 185%, to −9.76 kcal/mol.

Our conclusions regarding the strong enhancement of the interior adsorption energy, and the less pronounced but significant reduction of the exterior adsorption energy, with increasing nanotube curvature are neither new nor surprising. The same tendencies have already been observed by both experiment[67] and lower-level ab initio calculations.[66] However, this work as well as ref 32 illustrates that the accuracy of DFT- or MP2-based adsorption potentials can be quite poor unless a careful selection of the DFT approach and of the dispersion expression is performed through comparisons with high-level methods such as CCSD(T) for relevant benchmark systems. Thus, it is gratifying that our work, one of the first to study small molecule nanotube adsorption at such a high level of theory (the effect of curvature on the $\pi-\pi$ stacking interactions of coronene and corannulene has been thoroughly investigated[73] including comparisons to benchmark energies of QCISD(T)/aug-cc-pVTZ quality[74]), confirms the trends observed using more approximate approaches. At the same time, while we have been able to select DFT+D variants that accurately reproduce benchmark data for all curvatures and intermolecular separations considered, the fairly strong dependence of the DFT+D performance on the particular variant of the dispersion correction (-D2, -D3, -D3(BJ), -D3-$E^{(3)}$, or -D3(BJ)-$E^{(3)}$) suggests some caution. Clearly, the binding energies are strongly dependent on the "intermediate-range" interaction, where the dispersion energy cannot be described by either pure semilocal DFT (as in short-range) or the undamped asymptotic expansion (as in long-range). In this range, the single damping function employed in -D2 or -D3 might have a hard time accounting for both the physical charge-overlap effects on dispersion energy[75] and the switching off of dispersion at distances where the density functional itself is able to account for it. Therefore, the dispersion corrections proposed by Steinmann et al.,[76−78] accounting for the two phenomena using two separate damping functions, might be the preferred choice in future studies on similar systems in case standard DFT+D fails to provide consistent accuracy across different intermolecular separations. In any case, a comparison against high-level wave function-based benchmarks is essential to validate the accuracy of the selected DFT approach.

■ ASSOCIATED CONTENT

Ⓢ Supporting Information

Cartesian coordinates and figures as described in text. This material is available free of charge via the Internet at http://pubs.acs.org.

■ AUTHOR INFORMATION

Corresponding Author

*E-mail: patkowsk@auburn.edu.

Notes

The authors declare no competing financial interest.

■ ACKNOWLEDGMENTS

This research was supported by the Donors of the American Chemical Society Petroleum Research Fund and by the startup funding from Auburn University. Some of the calculations were performed at the Alabama Supercomputer Center. We thank Dr. Lynn Mandeltort for reading and commenting on the manuscript.

■ REFERENCES

(1) Britz, D. A.; Khlobystov, A. N. *Chem. Soc. Rev.* **2006**, *35*, 637−659.

(2) Kong, J.; Franklin, N. R.; Zhou, C. W.; Chapline, M. G.; Peng, S.; Cho, K. J.; Dai, H. J. *Science* **2000**, *287*, 622−625.

(3) Yang, S.; Ouyang, L.; Phillips, J. M.; Ching, W. Y. *Phys. Rev. B* **2006**, *73*, 165407.

(4) Huang, L.; Zhang, L.; Shao, Q.; Lu, L.; Lu, X.; Jiang, S.; Shen, W. *J. Phys. Chem. C* **2007**, *111*, 11912−11920.

(5) Kauffman, D. R.; Star, A. *Angew. Chem., Int. Ed.* **2008**, *47*, 6550−6570.

(6) Albesa, A. G.; Fertitta, E. A.; Vicente, J. L. *Langmuir* **2010**, *26*, 786−795.

(7) Rubeš, M.; Kysilka, J.; Nachtigall, P.; Bludský, O. *Phys. Chem. Chem. Phys.* **2010**, *12*, 6438−6444.

(8) Voloshina, E.; Usvyat, D.; Schütz, M.; Dedkov, Y.; Paulus, B. *Phys. Chem. Chem. Phys.* **2011**, *13*, 12041−12047.

(9) Liu, Y. Y.; Wilcox, J. *Environ. Sci. Technol.* **2011**, *45*, 809−814.

(10) Zöttl, S.; Kaiser, A.; Bartl, P.; Leidlmair, C.; Mauracher, A.; Probst, M.; Denifl, S.; Echt, O.; Scheier, P. *J. Phys. Chem. Lett.* **2012**, *3*, 2598−2603.

(11) Lazar, P.; Karlický, F.; Jurečka, P.; Kocman, M.; Otyepková, E.; Šafářová, K.; Otyepka, M. *J. Am. Chem. Soc.* **2013**, *135*, 6372−6377.

(12) Cao, D.; Zhang, X.; Chen, J.; Wang, W.; Yun, J. *J. Phys. Chem. B* **2003**, *107*, 13286−13292.

(13) Duren, T.; Sarkisov, L.; Yaghi, O. M.; Snurr, R. Q. *Langmuir* **2004**, *20*, 2683−2689.

(14) Bucior, B. J.; Chen, D.-L.; Liu, J.; Johnson, J. K. *J. Phys. Chem. C* **2012**, *116*, 25904−25910.

(15) Liu, H.; Cooper, V. R.; Dai, S.; Jiang, D. *J. Phys. Chem. Lett.* **2012**, *3*, 3343−3347.

(16) Kowalczyk, P. *Phys. Chem. Chem. Phys.* **2012**, *14*, 2784−2790.

(17) Hu, X.; Zhou, Z.; Lin, Q.; Wu, Y.; Zhang, Z. *Chem. Phys. Lett.* **2011**, *503*, 287−291.

(18) Su, D. S.; Perathoner, S.; Centi, G. *Chem. Rev.* **2013**, *113*, 5782−5816.

(19) Becke, A. D. *J. Chem. Phys.* **1993**, *98*, 5648−5652.

(20) Stephens, P. J.; Devlin, F. J.; Chabalowski, C. F.; Frisch, M. J. *J. Phys. Chem.* **1994**, *98*, 11623−11627.

(21) Perdew, J. P.; Burke, K.; Ernzerhof, M. *Phys. Rev. Lett.* **1996**, *77*, 3865−3868.

(22) Grimme, S. *J. Comput. Chem.* **2006**, *27*, 1787−1799.

(23) Becke, A. D.; Johnson, E. R. *J. Chem. Phys.* **2007**, *127*, 124108.

(24) Zhao, Y.; Truhlar, D. G. *Theor. Chem. Acc.* **2008**, *120*, 215−241.

(25) Chai, J.-D.; Head-Gordon, M. *Phys. Chem. Chem. Phys.* **2008**, *10*, 6615−6620.

(26) Tkatchenko, A.; Scheffler, M. *Phys. Rev. Lett.* **2009**, *102*, 073005.

(27) Grimme, S.; Antony, J.; Ehrlich, S.; Krieg, H. *J. Chem. Phys.* **2010**, *132*, 154104.

(28) Vydrov, O. A.; Van Voorhis, T. *J. Chem. Phys.* **2010**, *133*, 244103.

(29) Burns, L. A.; Vazquez-Mayagoitia, A.; Sumpter, B. G.; Sherrill, C. D. *J. Chem. Phys.* **2011**, *134*, 084107.

(30) Risthaus, T.; Grimme, S. *J. Chem. Theory Comput.* **2013**, *9*, 1580−1591.

(31) Řezáč, J.; Hobza, P. *J. Chem. Theory Comput.* **2013**, *9*, 2151−2155.

(32) Smith, D. G. A.; Patkowski, K. *J. Chem. Theory Comput.* **2013**, *9*, 370−389.

(33) Riley, K. E.; Pitoňák, M.; Jurečka, P.; Hobza, P. *Chem. Rev.* **2010**, *110*, 5023−5063.

(34) Grimme, S. *J. Chem. Phys.* **2003**, *118*, 9095−9102.

(35) Hill, J. G.; Platts, J. A. *J. Chem. Theory Comput.* **2007**, *3*, 80−85.

(36) DiStasio, R. A., Jr.; Head-Gordon, M. *Mol. Phys.* **2007**, *105*, 1073−1083.

(37) Hesselmann, A.; Jansen, G.; Schütz, M. *J. Chem. Phys.* **2005**, *122*, 014103.

(38) Misquitta, A. J.; Podeszwa, R.; Jeziorski, B.; Szalewicz, K. *J. Chem. Phys.* **2005**, *123*, 214103.

(39) Hesselmann, A. *J. Chem. Phys.* **2008**, *128*, 144112.

(40) Jenness, G. R.; Jordan, K. D. *J. Phys. Chem. C* **2009**, *113*, 10242−10248.

(41) Jenness, G. R.; Karalti, O.; Jordan, K. D. *Phys. Chem. Chem. Phys.* **2010**, *12*, 6375−6381.

(42) Jenness, G. R.; Karalti, O.; Al-Saidi, W. A.; Jordan, K. D. *J. Phys. Chem. A* **2011**, *115*, 5955−5964.

(43) Quiñonero, D.; Frontera, A.; Deyà, P. M. *J. Phys. Chem. C* **2012**, *116*, 21083−21092.

(44) Bartolomei, M.; Carmona-Novillo, E.; Hernández, M. I.; Campos-Martínez, J.; Pirani, F. *J. Phys. Chem. C* **2013**, *117*, 10512−10522.

(45) Grimme, S. *WIREs Comput. Mol. Sci.* **2011**, *1*, 211−228.

(46) Zhao, Y.; Schultz, N. E.; Truhlar, D. G. *J. Chem. Theory Comput.* **2006**, *2*, 364−382.

(47) Kysilka, J.; Rubeš, M.; Grajciar, L.; Nachtigall, P.; Bludský, O. *J. Phys. Chem. A* **2011**, *115*, 11387−11393.

(48) Tsuzuki, S.; Honda, K.; Fujii, A.; Uchimaru, T.; Mikami, M. *Phys. Chem. Chem. Phys.* **2008**, *10*, 2860−2865.

(49) Frey, J. T.; Doren, D. J. *TubeGen 3.4* (web-interface, http://turin.nss.udel.edu/research/tubegenonline.html), University of Delaware, Newark, DE, 2011.

(50) Werner, H.-J. et al. *MOLPRO, version 2010.1, a package of ab initio programs*, 2010; see http://www.molpro.net.

(51) Dunning, T. H., Jr. *J. Chem. Phys.* **1989**, *90*, 1007−1023.

(52) Kendall, R. A.; Dunning, T. H., Jr.; Harrison, R. J. *J. Chem. Phys.* **1992**, *96*, 6796−6806.

(53) Weigend, F.; Ahlrichs, R. *Phys. Chem. Chem. Phys.* **2005**, *7*, 3297−3305.

(54) Papajak, E.; Leverentz, H. R.; Zheng, J.; Truhlar, D. G. *J. Chem. Theory Comput.* **2009**, *5*, 1197−1202.

(55) Halkier, A.; Helgaker, T.; Jørgensen, P.; Klopper, W.; Koch, H.; Olsen, J.; Wilson, A. K. *Chem. Phys. Lett.* **1998**, *286*, 243−252.

(56) Becke, A. D. *J. Chem. Phys.* **1997**, *107*, 8554−8560.

(57) Grimme, S.; Ehrlich, S.; Goerigk, L. *J. Comput. Chem.* **2011**, *32*, 1456−1465.

(58) Boys, S. F.; Bernardi, F. *Mol. Phys.* **1970**, *19*, 553−566.

(59) van Duijneveldt, F. B.; van Duijneveldt-van de Rijdt, J. G. C. M.; van Lenthe, J. H. *Chem. Rev.* **1994**, *94*, 1873−1885.

(60) Polly, R.; Werner, H.-J.; Manby, F. R.; Knowles, P. J. *Mol. Phys.* **2004**, *102*, 2311−2321.

(61) Werner, H.-J.; Manby, F. R.; Knowles, P. J. *J. Chem. Phys.* **2003**, *118*, 8149−8160.

(62) Kresse, G.; Hafner, J. *Phys. Rev. B* **1993**, *47*, 558−561.

(63) Kresse, G.; Furthmüller, J. *Phys. Rev. B* **1996**, *54*, 11169−11186.

(64) Kresse, G.; Furthmüller, J. *Comput. Mater. Sci.* **1996**, *6*, 15−50.

(65) Kondratyuk, P.; Yates, J. T., Jr. *Acc. Chem. Res.* **2007**, *40*, 995−1004.

(66) Chandrakumar, K. R. S.; Srinivasu, K.; Ghosh, S. K. *J. Phys. Chem. C* **2008**, *112*, 15670−15679.

(67) Gotovac, S.; Honda, H.; Hattori, Y.; Takahashi, K.; Kanoh, H.; Kaneko, K. *Nano Lett.* **2007**, *7*, 583−587.

(68) Kostov, M. K.; Cheng, H.; Cooper, A. C.; Pez, G. P. *Phys. Rev. Lett.* **2002**, *89*, 146105.

(69) Misquitta, A. J.; Spencer, J.; Stone, A. J.; Alavi, A. *Phys. Rev. B* **2010**, *82*, 075312.

(70) Dobson, J. F. *Surf. Sci.* **2011**, *605*, 1621−1632.

(71) Chen, D.-L.; Mandeltort, L.; Saidi, W. A.; Yates, J. T., Jr.; Cole, M. W.; Johnson, J. K. *Phys. Rev. Lett.* **2013**, *110*, 135503.

(72) Mandeltort, L.; Chen, D.-L.; Saidi, W. A.; Johnson, J. K.; Cole, M. W.; Yates, J. T., Jr. *J. Am. Chem. Soc.* **2013**, *135*, 7768−7776.

(73) Kennedy, M. R.; Burns, L. A.; Sherrill, C. D. *J. Phys. Chem. A* **2012**, *116*, 11920−11926.

(74) Janowski, T.; Pulay, P.; Karunarathna, A. A. S.; Sygula, A.; Saebø, S. *Chem. Phys. Lett.* **2011**, *512*, 155−160.

(75) Jeziorski, B.; Moszyński, R.; Szalewicz, K. *Chem. Rev.* **1994**, *94*, 1887−1930.

(76) Steinmann, S. N.; Csonka, G.; Corminboeuf, C. *J. Chem. Theory Comput.* **2009**, *5*, 2950−2958.

(77) Steinmann, S. N.; Corminboeuf, C. *J. Chem. Theory Comput.* **2010**, *6*, 1990−2001.

(78) Steinmann, S. N.; Corminboeuf, C. *J. Chem. Theory Comput.* **2011**, *7*, 3567−3577.

Appendix D

Benchmarking the CO_2 Adsorption Energy on Carbon Nanotubes

THE JOURNAL OF
PHYSICAL CHEMISTRY C

Article

pubs.acs.org/JPCC

Benchmarking the CO_2 Adsorption Energy on Carbon Nanotubes

Daniel G. A. Smith and Konrad Patkowski*

Department of Chemistry and Biochemistry, Auburn University, Auburn, Alabama 36849, United States

Ⓢ *Supporting Information*

ABSTRACT: We present benchmark interaction energy calculations of carbon dioxide physisorbed onto flat and curved polycyclic aromatic hydrocarbons as models of carbon nanotubes. The accuracy of the complete-basis-set second-order Møller−Plesset perturbation theory combined with a CCSD(T) coupled-cluster correction in a moderate basis set is first assessed for a series of CO_2−(benzene, naphthalene, and pyrene) complexes to establish the basis set requirements. The same composite approach is then used to compute accurate interaction energies for 195 CO_2−curved coronene geometries representing different intermolecular distances, orientations, and nanotube diameters. The CO_2−curved coronene benchmark data set is then used to assess the performance of a wide variety of dispersion-including DFT functionals. Among them, only the nonlocal VV10 and double-hybrid B2PLYP-D3(BJ) functionals exhibit relative errors below 10%. Interestingly, all DFT variants deviate strongly from the benchmark at short-range because of overdamping. We show that these short-range deficiencies can be corrected by refitting the damping parameters of Grimme's -D3 dispersion approach on the newly constructed data set and that the refitted parameters are also suitable for the complexes of CO_2 with larger polycyclic aromatic hydrocarbons but not for the smaller CO_2−benzene and CO_2−naphthalene systems.

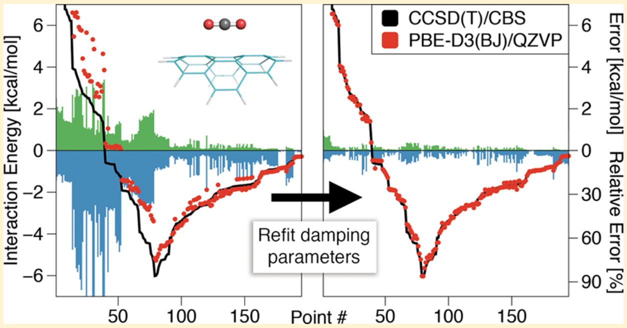

■ INTRODUCTION

Carbon dioxide adsorption onto carbon nanostructures has been the subject of a tremendous amount of experimental and theoretical research. This research is primarily focused on CO_2 sequestration from the atmosphere[1−6] and from flue gases.[7,8] In addition, small-molecule adsorption onto carbon nanostructures has generated intense interest in the development of molecular sensors,[9,10] in the noncovalent functionalization of carbon nanostructures,[11,12] and as a way to mediate reactions.[13]

Computing the interaction potential between small adsorbates and extended carbon nanostructures can be viewed as taking the limit of the interaction energy with a finite nanostructure fragment as its size approaches infinity. In practice, as shown in our recent methane−carbon nanotube adsorption study,[14] this can require a carbon nanostructure fragment of several hundred atoms. At present, the only method that has demonstrated consistent accuracy for noncovalent interactions (NCI) is the current "gold standard" in electronic structure theory, the coupled-cluster approach with singles, doubles, and perturbative triples (CCSD(T)).[15] Although this method can describe NCI to within 1−2%[16,17] at the complete basis set (CBS) limit, it is by no means trivial to compute accurately because of the steep N^7 scaling of the method. Even with the inclusion of novel explicitly correlated CCSD(T) variants, direct extrapolations to the CCSD(T)/CBS limit are restricted to polycyclic aromatic hydrocarbons (PAHs) the size of pyrene (16 carbon atoms). For composite MP2/CBS+ΔCCSD(T) methods, because the bases as small as DZ ≡ cc-pVDZ are not sufficient for the $\Delta\text{CCSD(T)} = E^{\text{CCSD(T)}} - E^{\text{MP2}}$ term, the limit is the complex involving coronene (24 carbon atoms). Such a methane−curved coronene model cut out of a (9,0) nanotube captures 85% of the interaction energy for the exterior minimum structure and just 31% of the interaction energy for the interior minimum structure compared to an infinite nanotube.[14] Larger nanotube fragments could also be treated with approximate low-scaling coupled-cluster methods, making use of the local character of the electron−electron interactions.[18−20] Such methods have recently been applied to nanotube physisorption and weakly interacting systems with considerable success.[21,22] Because we strive to have the uncertainty of the benchmark as low as possible in order to have the resolution necessary to compare different approximate methods, we will not pursue these approaches here.

Because CCSD(T) cannot be used to directly obtain the interaction energy between CO_2 and a carbon nanotube, more approximate methods must be used. Since dispersion is the primary attractive force for these systems, standard density functional theory (DFT) methods are inaccurate. In the past decade, a large number of dispersion-including DFT variants have been proposed, including the atom-pairwise dispersion corrections of Grimme et al.,[23,24] the atom-in-a-molecule dispersion expansion resulting from the Hirshfeld partitioning

Received: December 27, 2014
Revised: February 6, 2015
Accepted: February 9, 2015
Published: February 9, 2015

DOI: 10.1021/jp512926n
J. Phys. Chem. C 2015, 119, 4934−4948

of electron density,[25] the exchange-hole dipole moment (XDM) approach by Becke and Johnson[26] and its dDsC modification by Steinmann and Corminboeuf,[27] functionals specifically optimized for noncovalent interaction energies[28−30] or their dispersionless part,[31] explicitly nonlocal van der Waals correlation functionals,[32,33] and double hybrid DFT functionals,[34,35] which include a portion of the MP2 correlation energy. The overall accuracy for these novel functionals is quite impressive, with average errors at the van der Waals minimum geometries down to about 0.2 kcal/mol (0.8 kJ/mol) in some cases;[36] however, these methods can have large outliers and do not always exhibit systematic accuracy across a range of distances.[14,36,37] A DFT accuracy that strongly varies with distance presents a significant problem when calculating interaction energy derivatives (adhesion forces).[38] Our previous study of methane−carbon nanotube complexes demonstrated that the DFT+D methods performed quite well overall with mean unsigned relative errors (MURE) across the entire potential energy surface (PES) between 5 and 28%. Although the general DFT+D accuracy for methane−carbon nanotube complexes is quite remarkable, careful benchmarking still must be undertaken to reproduce CCSD(T)-quality results for NCIs.

The CO_2−benzene complex has been extensively studied for a number of orientations and distances;[39−42] recently, the performance of novel dispersion-including functionals for this system has been elucidated by Head-Gordon and co-workers.[43] On the other hand, previous theoretical studies for complexes of CO_2 with larger PAHs have primarily focused on the minimum geometry using a variety of DFT methods such as LDA,[44] B97-D2,[45] B971-DCP,[46] and M05-2X.[47] Wave-function-based studies of such systems are so far limited to the CO_2−ovalene complex at the MP2/6-31G level of theory.[48] As such, a systematic benchmarking of successively larger CO_2−PAH complexes with high-level wave-function methods is needed to identify the most appropriate DFT variants.

In this article, we extend the procedure from our previous works[14,49] to the interaction between CO_2 and carbon nanotubes. The basis set convergence of the composite MP2/CBS+ΔCCSD(T) method will be investigated using a series of smaller PAHs ranging from benzene to coronene and both conventional and explicitly correlated methods. The best-feasible composite approach will then be employed for a set of CO_2−coronene structures at various curvatures, distances, and orientations. The benchmark set will be compared against a variety of dispersion including DFT approaches. The best DFT variant will then be used to compute the effects of orientation, fragment size, curvature, and interior/exterior location on the CO_2 adsorption energy on larger nanotube fragments.

The structure of the rest of this paper is as follows. In section II, we describe the ab initio methodology employed to compute interaction energies and give the pertinent computational details. We present and analyze our numerical results in section III. Finally, section IV contains conclusions.

■ METHODS

The MOLPRO code[50] was used to obtain all MP2, SCS-MP2,[51] CCSD(T), and CCSD(T)-F12[52,53] interaction energies. The CCSD(T)-F12a and CCSD(T)-F12b computations employ the default MOLPRO explicitly correlated *Ansätze*, geminal correlation factors, and fitting basis sets.[52,53] When the (T) contribution in CCSD(T)-F12 is scaled, it will be denoted (T**), specifically:

$$\Delta E^{(T^{**})} = \Delta E^{(T)} \frac{E_{\mathrm{corr}}^{\mathrm{MP2-F12}}}{E_{\mathrm{corr}}^{\mathrm{MP2}}} \tag{1}$$

where $\Delta E^{(T)} = E^{\mathrm{CCSD}(T)-\mathrm{F12}} - E^{\mathrm{CCSD-F12}}$ and $E_{\mathrm{corr}}^{\mathrm{MP2-F12}}$ is the MP2−F12 correlation energy from the 3C(FIX) *Ansatz*; the scaling factor determined for the dimer was also used in the counterpoise-corrected computations for monomers to ensure size consistency.[54,55]

The Dunning bases aug-cc-pV*XZ* ≡ a*XZ*[56,57] as well as the Turbomole def2 series of basis sets[58] were employed. A partial augmentation scheme, where only the six carbon atoms on the PAH/nanotube fragment that are closest to the CO_2 carbon (occasionally seven or eight carbon atoms if required by symmetry considerations) as well as all atoms of the CO_2 monomer have diffuse functions, will be denoted as local-cc-pV*XZ* (la*XZ*). Such a selective removal of basis functions at the X = D level removes linear dependencies that prevent some CCSD(T) calculations from converging, reduces the cost of the CCSD(T) computation 5- to 10-fold depending on symmetry, and retains the accuracy of the full aDZ basis set.[49] It should be noted that the presence of diffuse functions on atoms closest to the interacting partner is absolutely crucial for saturating the dispersion energy. Therefore, in calculations of this kind,[49] the la*XZ* scheme of augmentation outperforms the "calendar" basis sets[59] for which diffuse functions are removed from all atoms in the same manner. The notation *method*/(*basis*1,*basis*2) denotes that the correlation energy has been obtained from the values in bases (*basis*1) and (*basis*2) using the standard X^{-3} extrapolation[60] for a given method. The SCF interaction energy is taken from the larger of (*basis*1,*basis*2) and not extrapolated.

The DFT functionals employed were the generalized gradient approximations (GGAs) BLYP,[61,62] BP86,[61,63] PBE,[64] and B97[23] (Grimme's reparameterization of Becke's original B97 functional, denoted B970 herein); the hybrid-GGAs B3LYP,[65,66] PBE0,[67,68] and B970;[69] the interaction-optimized functionals dlDF[31] (with the -D_{as} dispersion expression from ref 70), ωB97X-D,[29] M05-2X,[28] and M06-2X;[30] the nonlocal functional VV10;[33] the range-separated functionals LC-ωPBE and LC-ωPBE0;[71] and the double-hybrid B2PLYP[34] approach. The DFT functionals were selected on the basis of previous performance for methane−nanotube complexes[14] and from the top performers in a recent NCI benchmarking study of DFT functionals,[36] ensuring that if available both the hybrid and nonhybrid forms were computed. All DFT results were computed with MOLPRO except for the ωB97X-D, LC-ωPBE, and LC-ωPBE0 functionals (computed with the PSI4 code)[72] and the VV10 functional (treated using QCHEM).[73] The MOLPRO program was locally modified to support the B97 and dlDF-D_{as} functionals. The range-separation parameters ω in the LC-ωPBE and LC-ωPBE0 calculations were kept at their originally recommended values of 0.4[71] and 0.3 bohr^{-1}, respectively.

The density functionals were augmented by two kinds of dispersion corrections. The first was Grimme's atom-pairwise dispersion expression in the -D2[23] and -D3[24] variants. The -D2 correction and the four variants of the -D3 correction (with either Chai−Head-Gordon[29] or Becke−Johnson (BJ) damping[74] and with or without the three-body term -$E^{(3)}$) were computed using Grimme's DFT-D3 program V3, revision 2. The second kind, the density-dependent dispersion correction (dDsC) of Steinmann and Corminboeuf,[27,75] was computed using a modified version of the GAMESS software package.[76]

The MP2 and DFT computations utilized density fitting.[77,78] All calculations employed the counterpoise correction for basis set superposition error[79,80] unless explicitly stated otherwise. Statistical quantities used in this paper are mean unsigned relative errors (MURE), mean unsigned errors (MUE), and maximum unsigned errors (max UE).

Similar to ref 14, we consider two separate classes of carbon nanotube fragments. The first is constructed by adding additional layers of perifused benzene rings around a central benzene. This is denoted C_n, where n is the number of additional layers around the center so that benzene corresponds to C_0, coronene is C_1, circumcoronene is C_2, etc. The second scheme is created by slicing a carbon nanotube perpendicular to its principal axis to create full toroidal models. These models are denoted T_n, where n relates to the number of benzene rings across its length. Specifically, the number of benzene rings along the nanotube axis is the same for the C_n and T_n models. Both models are shown in Figure 1.

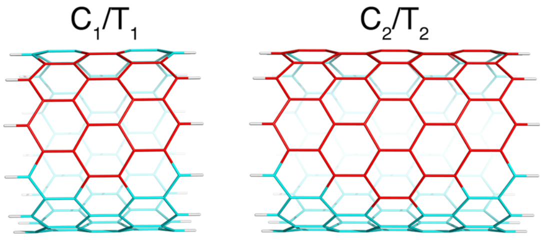

Figure 1. Illustration of the definition of the (circum)-coronene (C_n, red) and toroidal (T_n, teal) nanotube fragments cut from a (12,0) nanotube.

Model zigzag (k,0) or armchair (k,k) nanotube[11] fragments were constructed by first generating large nanotube geometries with the TubeGen program;[81] the desired fragments were then cut out of larger nanotubes. When large C_n fragments are carved out of nanotubes with a small diameter, the C_n fragment wraps around, resulting in a short toroidal fragment, as demonstrated in ref 14. Cleaved carbon−carbon bonds were capped with hydrogen atoms at a C−H bond length of 1.0845 Å. The benzene, naphthalene, pyrene, and CO_2 geometries were optimized at the MP2/aTZ level of theory. The value z will always represent the distance between the carbon of the CO_2 molecule and the surface of the PAH or carbon nanotube fragment, as defined by the cylinder on which all carbons from a nanotube lie.

■ RESULTS AND DISCUSSION

Benchmark Construction and Accuracy. To determine the best method to estimate the CCSD(T)/CBS results for the CO_2−PAH models, we first selected a series of planar PAHs: benzene, naphthalene, and pyrene. For each of these complexes, CCSD(T) can be computed in at least the aTZ basis set for symmetric C_{2v} geometries. In each case, the global minimum is a structure where the CO_2 molecule is parallel to the PAH surface and the carbon of the CO_2 molecule is directly over a carbon−carbon bond (Figure 2). This orientation will be called parallel and denoted as ||. To explore the interaction energy dependence on the orientation of the CO_2 molecule, the configuration where CO_2 is perpendicular to the PAH plane will also be considered; it will be denoted as perpendicular, or ⊥. This orientation is not a local minimum but rather a saddle point on the full six-dimensional PES. Therefore, only the three dimensions that define the position of the CO_2 molecule over the PAH plane are optimized for the ⊥ geometries. We consider additional high-symmetry C_{2v} geometries where the CO_2 molecule is located over the center of the PAH; these orientations will be labeled as centered or abbreviated as C. The minimum CO_2 position for each complex was optimized at the MP2/aTZ level, and then the distance z was reoptimized using the composite MP2/(aQZ,a5Z)+ΔCCSD(T)/aDZ approach because MP2 yields configurations that are too close to the PAH plane. The resulting minima are displayed in Figure 2.

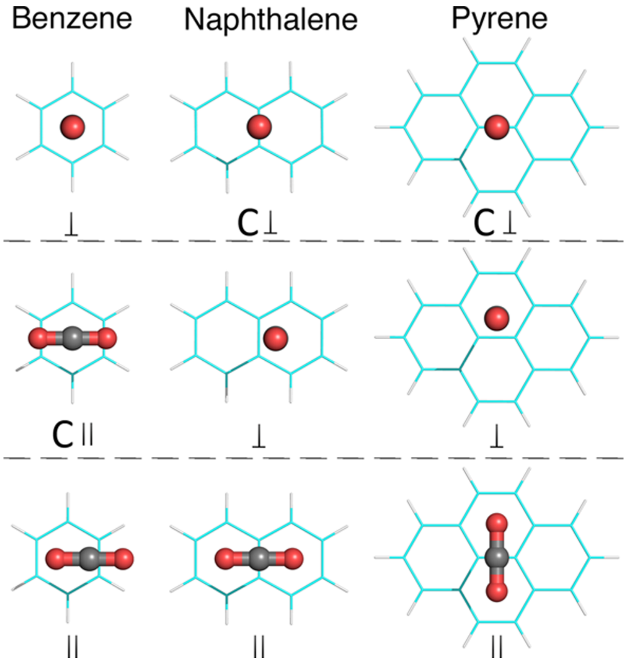

Figure 2. Minimum geometries for the CO_2−PAH complexes as found in the text.

The eight complexes for which CCSD(T)/aTZ could be computed (all structures from Figure 2, except for the ⊥ CO_2−pyrene system) will be denoted as the "minimum PAH benchmark". A comprehensive set of MP2, MP2-F12, CCSD(T), and CCSD(T)-F12 results were obtained for this minimum PAH benchmark test set. Comparing the (aQZ,a5Z) extrapolated MP2 and MP2-F12 interaction energies for the eight dimers shows a maximum difference of only 0.005 kcal/mol. Because the MP2-F12 energies become very costly to compute in large basis sets for the pyrene and coronene complexes, all MP2 values shown here were obtained from conventional calculations. Following previous works for weak interaction energies, the explicitly correlated ΔCCSD(T) results will be taken from the CCSD(T)-F12a and CCSD(T**)-F12b calculations.[55,82] The other two possibilities, CCSD(T**)-F12a and CCSD(T)-F12b, are significantly less accurate, as illustrated in Table S1 of the Supporting Information.

It was previously shown that extrapolating ΔCCSD(T) from the aDZ and aTZ bases does not always improve the value of this correction compared to the nonextrapolated aTZ result because of nonmonotonic convergence patterns.[83] Interestingly, for the ⊥ CO_2−benzene complex, the ΔCCSD(T**)-F12b correction also has a nonmonotonic convergence pattern with the results for the (aDZ, aTZ, aQZ) basis sets amounting to (0.408, 0.395, 0.403) kcal/mol, respectively. Accordingly, no

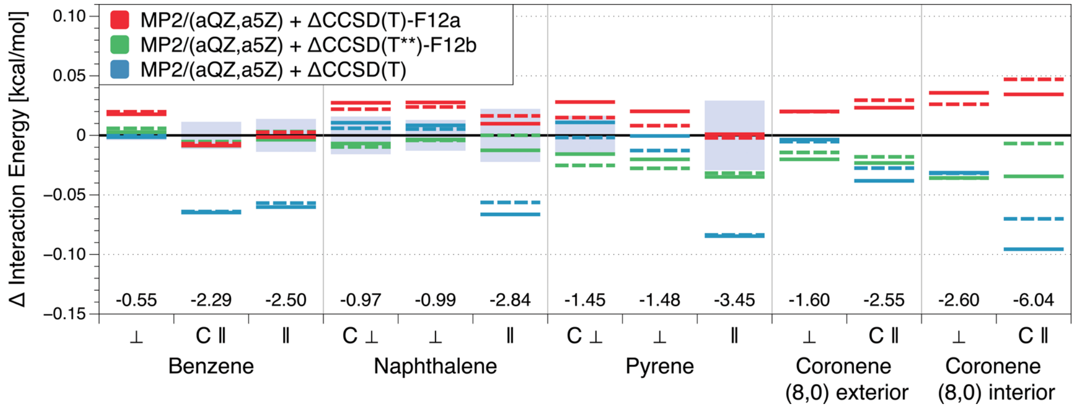

Figure 3. Differences between various CCSD(T)/CBS interaction energy estimates, with the ΔCCSD(T) term computed in the aDZ (solid lines) and laDZ (dashed lines) bases. If the benchmark cannot be calculated in at least the aTZ basis, then the average between MP2/(aQZ,a5Z)+ΔCCSD(T)-F12a/aDZ and MP2/(aQZ,a5Z)+ΔCCSD(T**)-F12b/aDZ was taken as the zero line, and no uncertainty was assigned. Otherwise, the benchmark was computed as described in the text, and the light-blue shaded regions represent the uncertainty of the benchmark value. The numbers along the horizontal axis give benchmark interaction energies in kilocalories per mole.

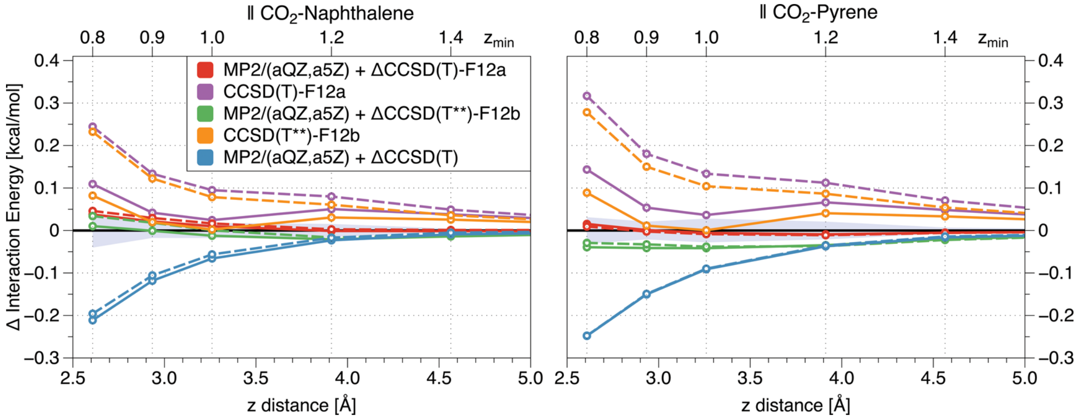

Figure 4. Comparison of the conventional and explicitly correlated composite MP2/CBS+ΔCCSD(T) schemes for the ∥ CO_2−naphthalene (benchmark: MP2/(aQZ,a5Z) + ΔCCSD(T)-F12avg/aTZ) and ∥ CO_2−pyrene (benchmark: MP2/(aQZ,a5Z) + ΔCCSD(T)-F12avg/laTZ) complexes. Solid lines represent the ΔCCSD(T) correction in the aDZ basis set, whereas the dashed lines represent ΔCCSD(T) in the laDZ basis set. The blue region is the uncertainty range of the benchmark.

conventional or explicitly correlated ΔCCSD(T) correction will be extrapolated. The benchmark interaction energy is then either MP2/(aQZ,a5Z)+ΔCCSD(T)-F12a/aXZ or MP2/(aQZ,a5Z)+ΔCCSD(T**)-F12b/aXZ, where X = Q for the two C_{2v} CO_2−benzene complexes and X = T for all other systems. Because these two methods never differ by more than 0.018 kcal/mol at the minimum for X = T, the simple average of the two values is taken as the benchmark and denoted MP2/(aQZ,a5Z)+ΔCCSD(T)-F12avg/aXZ. The uncertainty of this benchmark is estimated as

$$\begin{aligned}\sigma = {} & |\mathrm{MP2(aQZ,\ a5Z)} - \mathrm{MP2/(aTZ,\ aQZ)}| \\ & + |\Delta\mathrm{CCSD(T)\text{-}F12avg/a}X\mathrm{Z} \\ & - \Delta\mathrm{CCSD(T)\text{-}F12avg/(a(}X-1\mathrm{)Z,\ a}X\mathrm{Z)}| \qquad (2)\end{aligned}$$

For larger systems when CCSD(T)/aTZ is not feasible, the ΔCCSD(T) correction can be computed using any combination of ΔCCSD(T), ΔCCSD(T)-F12a, or ΔCCSD(T**)-F12b with either the laDZ or aDZ basis, retaining a MURE under 1.6% on the minimum PAH benchmark test set. To elucidate the trends exhibited by the small-basis ΔCCSD(T) corrections, the absolute deviations between various variants and the benchmark are shown in Figure 3. When the ΔCCSD(T) correction is computed using conventional CCSD(T), the performance is quite good for the ⊥ CO_2 configurations; however, conventional CCSD(T) appears to overbind the ∥ CO_2 configurations in every case shown. Figure 3 also demonstrates that the MP2/(aQZ,a5Z)+ΔCCSD(T)-F12a/aDZ approach tends to underbind, whereas MP2/(aQZ,a5Z)+ΔCCSD(T**)-F12b/aDZ usually overbinds slightly. Furthermore, for all complexes except the ∥ CO_2−coronene (8,0) interior system (a CO_2−coronene complex curved to the shape of an (8,0) nanotube, vide supra), the difference between the laDZ and aDZ basis sets in the ΔCCSD(T) and ΔCCSD(T)-F12 corrections does not exceed 0.018 kcal/mol. For the ∥ CO_2−coronene (8,0) interior complex, which is the worst case for the laDZ basis set because there are more coronene carbon atoms close to CO_2, the ΔCCSD(T) difference between the laDZ and aDZ basis sets is at most 0.034 kcal/mol and, in relative terms, is offset by the deeper minima for the interior complexes. By averaging the ΔCCSD(T)-F12a and ΔCCSD(T**)-F12b values, the MURE with respect to the minimum PAH benchmark is reduced to 0.7% for both the aDZ and laDZ bases.

To understand the performance of different composite methods as a function of the intermolecular z distance, the ∥ CO_2−naphthalene and ∥ CO_2−pyrene complexes were investigated at 0.8, 0.9, 1.0, 1.2, and 1.4 times the minimum distance (z_{min}), as shown in Figure 4. Both the benchmark value and its uncertainty are calculated in the same fashion as for the minima. Because of the cost of computing CCSD(T)/aTZ for the ∥ CO_2−pyrene complex, the benchmark ΔCCSD(T) correction was reduced to CCSD(T)-F12avg/laTZ. At the ∥ CO_2−pyrene minimum, the difference between ΔCCSD(T)-F12avg/laTZ and ΔCCSD(T)-F12avg/aTZ amounts to 0.007 kcal/mol or 0.2%. The benchmark uncertainty was computed using the laDZ and laTZ bases in a way analogous to eq 2.

Figure 4 shows that the CCSD(T)-F12a and CCSD(T**)-F12b results without the supplement of an MP2/CBS term are excellent at the minima; however, at both shorter and longer range the accuracy is somewhat diminished. In addition, the truncation of the aDZ basis set to laDZ has a much larger impact on the entire CCSD(T)-F12 interaction energy than on the ΔCCSD(T)-F12 term. The conventional ΔCCSD(T) correction in Figure 4 has a larger deviation at short range, emphasizing the need for larger basis sets in this regime. When the ΔCCSD(T) energy is computed using either conventional or explicitly correlated methods, the pruned laDZ values are nearly identical (within a few hundredths of kcal/mol) to the aDZ values for both naphthalene-CO_2 and pyrene-CO_2. The MP2/(aQZ,a5Z)+ΔCCSD(T)-F12a and MP2/(aQZ,a5Z)+ΔCCSD(T**)-F12b methods differ by at most 0.05 kcal/mol or 1.1% for the ∥ CO_2−pyrene complex at $0.8z_{\mathrm{min}}$ and neither variant is consistently better than the other. Consequently, the benchmark will always be the average of these two values. Using the composite MP2/(aQZ, a5Z) + ΔCCSD(T)-F12avg/laDZ level of theory, one can expect a MURE of 1% (a MUE of 0.03 kcal/mol) at the minimum and distances longer than the minimum, and a MURE of 2% (a MUE of 0.06 kcal/mol) at distances shorter than the minimum compared to our best CCSD(T)/CBS estimate.

Benchmark Data Set for CO_2−Curved Coronene. The benchmark set of C_1 (coronene) sized nanotube fragments was created by choosing the (5,5), (6,6), (7,7), (8,0), (10,0), and (12,0) nanotubes in addition to flat graphene. The (5,5) and (8,0) nanotubes are the smallest for which a CO_2 molecule can fit inside a carbon nanotube (have an attractive interaction energy) as determined using an MP2/aDZ calculation with a large T_2 fragment (Figure 1). For each of the CO_2−C_1 fragment complexes, the ⊥ and ∥ configurations (on both exterior and interior, except for flat graphene) were optimized using MP2/aTZ. The ⊥ structure always optimized over the central benzene ring, and the ∥ configuration always ended up over a carbon−carbon bond. It should be noted that the lowest-energy ∥ configuration for a zigzag nanotube has C_1 symmetry. In such a case, the geometry was twisted to an adjacent, more symmetric minimum, see Figure 5. An additional "centered ∥" C_{2v} position was also calculated where CO_2 is shifted so that it is directly over the central benzene ring (Figure 5). As before, the MP2/aTZ method predicts the CO_2 molecule to be too close to the PAH plane; however, optimizing the z distance with a coupled-cluster method is not feasible. On the other hand, the B3LYP-D3/aDZ functional was found to recapture the z_{min} distance of the nine complexes in Figure 2 to within 0.02 Å with respect to the MP2/(aQZ,a5Z)+ΔCCSD(T)/aDZ results. For comparison, the MP2/aTZ level of theory recovers the z_{min} distance to within 0.12 Å. Therefore, the z distances of all CO_2−C_1 structures were optimized with B3LYP-D3/aDZ. The minimum distance z_{min} was then multiplied by 0.8, 0.9, 1.0, 1.2, and 1.4 for a total of 195 geometries. A comparison between MP2/(aTZ,aQZ) and MP2/(aQZ,a5Z) for 5 random geometries each at $0.8z_{\mathrm{min}}$, z_{min}, and $1.4z_{\mathrm{min}}$ results in a MUE of 0.01 kcal/mol (max UE 0.03 kcal/mol) and a MURE of 0.8%. Because the MP2/a5Z computations become very expensive for this large system, it is beneficial to reduce the size of the basis sets used in the extrapolation with little loss in accuracy. As a result, the 195 benchmark geometries were investigated using the MP2(aTZ,aQZ)+ΔCCSD(T)-F12avg/laDZ and MP2-(aTZ,aQZ)+ΔCCSD(T)/laDZ levels of theory.

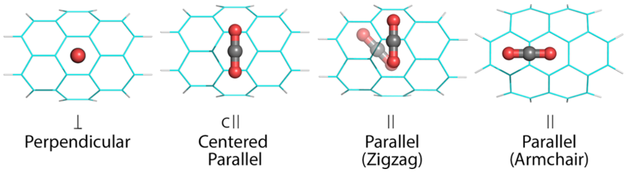

Figure 5. Model configurations for the C_1 fragment−CO_2 complexes. Note that unlike both the ⊥ and C ∥ configurations, the lowest-energy ∥ configuration is different for armchair and zigzag nanotubes. The semitransparent CO_2 molecule on the ∥ zigzag nanotube represents the global minimum, whereas the fully opaque CO_2 is the lowest-energy C_{2v} structure included in our benchmark set.

As can be seen in Table 1, the range of interaction energies provided by the benchmark is quite broad, resulting in a comprehensive data set to test various DFT methods; however, there is some difficulty finding a single metric that describes how well a given method does overall. The mean unsigned error (MUE) does well when all values are of similar magnitude; however, a 0.1 kcal/mol deviation at long range (−0.3 kcal/mol, 30% error) is much more grievous than at short range (12.2 kcal/mol, 0.8% error). On the other hand, the unsigned relative error (URE) is meaningful across the entire energy surface except near to where the potential crosses zero at short range. In the latter case, smaller reference values cause such points to be weighted disproportionately high. To reduce this issue, an upper weight limit was introduced, leading to a weighted mean unsigned relative error (wMURE).

Table 1. Mean, Minimum, and Maximum Values of the CO_2−C_1 Fragment Benchmark Interaction Energies at Different $x\cdot z_{\mathrm{min}}$ Separations (kcal/mol)

x	mean	max	min
0.8	4.59	12.17	0.46
0.9	−2.45	−0.58	−5.33
1.0	−3.43	−1.60	−6.02
1.2	−2.14	−0.82	−4.18
1.4	−1.09	−0.29	−2.35

$$\mathrm{wMURE} = \mathrm{mean}\left(\left|\frac{E - E_{\mathrm{ref}}}{E_{\mathrm{weight}}}\right|\right)\cdot 100\%,$$

$$E_{\mathrm{weight}} = \begin{cases} |E_{\mathrm{ref}}| & z \geq z_{\mathrm{min}} \\ \max\{|E_{\mathrm{ref}}|, E_{\mathrm{mask}}\} & z < z_{\mathrm{min}} \end{cases} \qquad (3)$$

The algorithm of eq 3 masks the points closest to zero on the repulsive wall so that very large weights do not occur there. As shown in Table 1, the potential crosses zero between $0.8z_{\mathrm{min}}$

Table 2. Statistics of the Wavefunction-Based Interaction Energies Compared to the MP2/(aTZ,aQZ)+ΔCCSD(T)-F12avg/laDZ Benchmark Sorted by Overall wMURE[a]

	$z < z_{\min}$		$z \geq z_{\min}$	overall	
	MURE	wMURE	wMURE ≡ MURE	MURE	wMURE
MP2/(aTZ,aQZ)+ΔCCSD(T**)-F12b/laDZ	1.72	1.25	1.11	1.35	1.17
MP2/(aTZ,aQZ)+ΔCCSD(T)-F12a/laDZ	1.72	1.25	1.11	1.35	1.17
MP2/(aTZ,aQZ)+ΔCCSD(T)/laDZ	5.77	4.41	0.85	2.82	2.28
SCS-MP2/(aTZ,aQZ)	4.27	3.35	2.37	3.13	2.76
SCS-MP2/(aDZ,aTZ)	9.98	7.33	2.61	5.56	4.50
CCSD(T**)-F12b/laDZ	8.60	5.72	4.10	5.90	4.75
SCS-MP2/aQZ	11.46	8.55	3.27	6.55	5.38
CCSD(T)-F12a/laDZ	12.03	8.22	6.32	8.61	7.08
SCS-MP2/aTZ	26.89	19.77	4.76	13.61	10.77
SCS-MP2/aDZ	69.81	51.69	9.76	33.78	26.54
CCSD(T)/laDZ	88.31	63.78	14.41	43.97	34.16
MP2/aDZ	70.92	48.54	27.17	44.67	35.72
MP2/(aTZ,aQZ)	148.05	105.36	36.38	81.05	63.97

[a] All MURE and wMURE values have been computed on the 195 CO_2-C_1 (coronene) configurations and are given in percent.

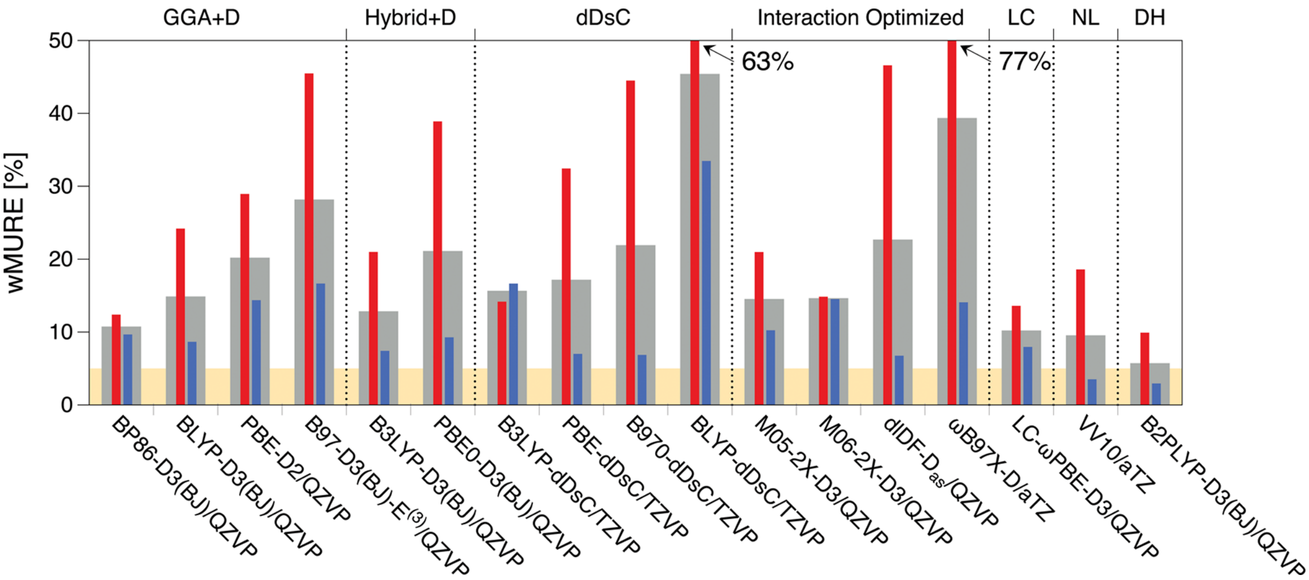

Figure 6. Performance of each density functional in the largest basis set computed (CP-corrected) combined with the best atom-pairwise dispersion term (if applicable). The large gray bars represent the overall wMURE, the smaller red and blue bars represent preminimum and postminimum wMURE, respectively. LC, NL, and DH correspond to long range corrected (range-separated), nonlocal, and double-hybrid functionals, respectively. The target accuracy level of 5% has been shaded in yellow.

and $0.9z_{\min}$. Because the uncertainty in the benchmark for these points is approximately 0.1 kcal/mol and our target accuracy is approximately 5%, a mask value of $E_{\text{mask}} = 2.0$ kcal/mol appears optimal. Taking the worst offender out of our data set (the interior (8,0) ⊥ configuration at $0.8z_{\min}$, with a CCSD(T)/CBS value of 0.46 kcal/mol), an absolute error of 0.1 kcal/mol leads to a URE of 22% or a weighted URE of 5%, bringing the latter value in line with our stated expectations. It should be noted that the weighting of eq 3 typically does not change the ordering of the best methods compared to MURE, but leads to more meaningful error values.

The optimal DFT variant should have consistent accuracy across the entire potential energy surface. To examine if this is the case, the overall MURE and wMURE is divided into two regimes; the "preminimum" part includes the points at $0.8z_{\min}$ and $0.9z_{\min}$, whereas the "postminimum" set includes the points at $z_{\min}$, $1.2z_{\min}$, and $1.4z_{\min}$. Table 2 lists the MURE and wMURE values of different benchmark variants. As can be seen from this table, wMURE does not radically change the ordering of the methods compared to MURE. For $z \geq z_{\min}$, where we can expect MP2/(aTZ,aQZ)+ΔCCSD(T)/laDZ to perform equally well as the benchmark, it is good to see an agreement of better than 1%. For the $z < z_{\min}$ points, we see a deviation of the conventional and explicitly correlated ΔCCSD(T) corrections. Additionally, the CCSD(T)-F12 results without an MP2/CBS term deviate by more than 8% for the preminimum points, indicating that the inclusion of the MP2/(aTZ,aQZ) term is highly beneficial. Somewhat surprisingly, the SCS-MP2/(aTZ,aQZ) and SCS-MP2/(aDZ,aTZ) calculations perform well, with overall wMURE's of 2.8 and 4.5%, respectively. Simply taking the SCS-MP2/aDZ energy is quite inaccurate, with an overall wMURE of 26.5%, indicating that an extrapolation to the CBS limit is absolutely crucial for this method. Table 2 also demonstrates the overbinding of

MP2 at the CBS limit. In addition, the MP2/aDZ result demonstrates that the cancellation of errors between the MP2 overbinding and basis set incompleteness effects is not satisfactory, leading to an overall wMURE of 35.7%.

Performance of Different DFT Variants. From the perspective of DFT calculations for larger nanotube models, the best-case scenario would be a GGA functional (N^3 scaling) that could reproduce CCSD(T)-quality benchmarks in either the SVP or aDZ basis set. Although this is a fairly tall order, it has happened before in our methane-nanotube study: we demonstrated that the B97-D3(BJ)/SVP functional reproduced the CCSD(T)-quality benchmarks with excellent accuracy.[14] To assess which DFT methods can reproduce the CCSD(T)-level benchmark interaction energies for the 195 CO_2−C_1 fragment complexes, a wide spectrum of functionals was tested.

The performance of all DFT functionals in the largest basis sets computed, with the CP correction, is shown in Figure 6. The dDsC results could not be computed in the QZVP basis set as density fitting is not available for this correction. Comparing all four functional and dDsC combinations between the TZVP and QZVP results for the six CO_2 − benzene and CO_2 − naphthalene minima shows a maximum deviation of 2%, indicating that this reduction in basis set does not significantly alter the results. It should be noted that each DFT+D method in Figure 6 is augmented by its best atom-pairwise dispersion variant as determined by wMURE.

The best DFT method is B2PLYP-D3(BJ)/QZVP with an overall wMURE of 5.7% (preminimum 9.9%, postminimum 2.9%); however, when the size of the basis set is reduced to aDZ, the wMURE becomes 10.2% (preminimum 22.1%, postminimum 2.3%). Although the postminimum accuracy remains very good, the preminimum accuracy diminishes strongly in the smaller basis set. This is somewhat expected as basis set incompleteness errors are much more pronounced in the MP2 correlation energy than in the Kohn−Sham energy; therefore, it is not a surprise that the double-hybrid functional demonstrates a different convergence pattern than standard GGA or hybrid-GGA methods. This deficiency at short range makes the B2PLYP-D3(BJ) functional unsuitable for computing an entire energy surface in the aDZ basis set; however, the QZVP accuracy is quite good. Although B2PLYP/QZVP is feasible for molecules up to the C_2 size (54 carbon atoms), the N^5 scaling of this method makes a large number of geometries impractical to compute.

The second best DFT method, $\mathrm{VV10}/_{\mathrm{aTZ}}^{\mathrm{CP}}$, has an overall wMURE of 9.5%. Although this functional has excellent accuracy at long range (postminimum 3.5% wMURE), the accuracy at short range is significantly diminished (preminimum 18.6% wMURE). Reduction of the aTZ basis set to aDZ only increases the overall wMURE of the functional to 9.8% (preminimum 19.3%, postminimum 3.4%), indicating a more typical DFT convergence pattern. However, similar to B2PLYP, this short range deviation from the benchmark makes the VV10 functional unsuitable for computing an entire potential energy curve. The comparison in Figure 6 demonstrates the importance of both the ΔCCSD(T)-F12 term and the use of wMURE over MURE at short range. The conventional MP2/CBS+ΔCCSD(T) interaction energy is too negative at short range which exacerbates the error of the too positive DFT functionals. At the same time, the use of wMURE over MURE prevents large contributions from small values on the repulsive wall. For example, the top performer, B2PLYP-D3(BJ)/QZVP, has a preminimum wMURE of 9.9% when compared to the MP2/(aTZ,aQZ)+ΔCCSD(T)-F12avg/laDZ benchmark; however, when compared to the MP2/(aTZ,aQZ)+ΔCCSD(T)/laDZ values, the preminimum wMURE is 14.5% (a preminimum MURE of 27.8%).

So far we have considered only CP-corrected functionals in the largest basis sets. The primary reason behind this is that CP-corrected DFT energies are much less dependent on the basis set than non-CP-corrected energies.[36] For example, taking $\mathrm{PBE\text{-}D3}/_{\mathrm{QZVP}}^{\mathrm{CP}}$ as the reference, $\mathrm{PBE\text{-}D3}/_{\mathrm{SVP}}^{\mathrm{CP}}$ has a wMURE of 5.7% (MUE 0.21 kcal/mol) compared to $\mathrm{PBE\text{-}D3}/_{\mathrm{SVP}}^{\mathrm{NoCP}}$ which has a wMURE of 47.4% (MUE of 1.6 kcal/mol). Because the choice of the basis set, and of the CP correction or lack thereof, has a greater effect on the DFT interaction energy at short range than at long range, it is inevitable that some combination of a smaller basis set and the lack of the CP correction will lead to an improved accuracy; however, this effect should not be relied upon as it is accidental in nature. The best non-CP-corrected DFT+D variant in any basis, when compared to the 195 CO_2−C_1 fragment benchmark results, is $\mathrm{M05\text{-}2X\text{-}D3\text{-}E^{(3)}}/_{\mathrm{aTZ}}^{\mathrm{No\,CP}}$ with a wMURE of 6.7%; however, the reduction of this basis to aDZ yields a wMURE of 25.4%. Conversely, $\mathrm{BP86\text{-}D3(BJ)}/_{\mathrm{aTZ}}^{\mathrm{CP}}$ has a wMURE of 10.6%, whereas $\mathrm{BP86\text{-}D3(BJ)}/_{\mathrm{aDZ}}^{\mathrm{CP}}$ has a wMURE of 10.7%, demonstrating that a reduction in basis set size when the DFT functional is computed in the CP-corrected way has a negligible effect on the interaction energy. The performance of each functional paired with each basis set, CP or non-CP corrected, and with each dispersion expression, can be found in the Supporting Information.

Examining all of the functionals in Figure 6, we observe that the postminimum wMURE is generally much lower than the preminimum wMURE. This is true for all functionals except for BP86-D3(BJ), B3LYP-dDsC, and M06-2X-D3. For every functional except M06-2X-D3, the interaction energy is always too positive for the preminimum points. The reasons for this behavior may lie both in the DFT part and in the dispersion part. In the first case, it has been observed before that the exchange energy from common GGA functionals is too repulsive for overlapping density tails compared to exact exchange[84−86] which is related to the incorrect asymptotics of the exchange-correlation potential.[87] A remedy to this problem exists in a form of range-separated hybrid functionals[88−90] and range separation has been observed to mimic dispersion at short range[86] by virtue of a decrease in exchange energy. In the latter case, as the results in Figure 6 show, the dispersion terms in the currently available variants (-D2, -D3, -dDsC, -D_{as}, VV10) are quite accurate asymptotically, but their damping at short range might be the problem: in fact, the sign of the DFT+D errors suggests that the dispersion term is consistently overdamped. The damping of an atom-pairwise dispersion correction needs to account for two effects: the physical charge-overlap effects on dispersion energy and the switch-off of dispersion at short range to eliminate double counting between the DFT part and the dispersion part. Although the charge-overlap effects are rigorously taken into account by symmetry-adapted perturbation theory (SAPT),[91−93] the damping functions designed to fit SAPT dispersion, whereas highly useful in combination with dispersion-free methods such as HF[70] or XPol,[94,95] are not suitable for DFT+D unless an additional, functional-dependent switching function is used to remove double counting. Instead, most standard DFT+D variants use a single damping-switching function that is selected and validated empirically. Interestingly, the dDsC dispersion expression, although designed specifically to cover a wider range of intermolecular separations through the use of separate damping and switching functions,[27,96] does not exhibit better performance at short range except for the accidental high accuracy of CP-uncorrected B3LYP-dDsC/TZVP with an overall wMURE of 6.3%. The overdamping of dispersion will be addressed in more detail later; right now, we will focus on the overestimation of exchange energy.

Role of Exact Exchange and Range Separation. Taking the PBE functional family as an example, the balance between DFT and HF exchange can be varied both globally (from PBE via PBE0 to HFPBE, that is, pure HF exchange and PBE correlation) and locally (using the range-separated functionals LC-ωPBE[71] and LC-ωPBE0). Although range separation lowers the short range interaction energies, it is not a substitute for dispersion: all of the PBE-based approaches require the +D term even for qualitative accuracy. As seen in Figure 6, LC-ωPBE-D3 does lead to better accuracy at short range than PBE-D3 and PBE0-D3 (-D2 happens to be the most accurate dispersion counterpart to PBE), however, the improvement is not completely satisfactory, and the short range interaction energies are still too high. This situation is illustrated in Table 3 which, unlike the rest of the text, lists mean errors (ME) (computed with signs) with respect to benchmark for points at $0.8z_{\rm min}$, $0.9z_{\rm min}$, and $z_{\rm min}$ separately. It should be noted that although the -D3 and -D3(BJ) parameters are available for the LC-ωPBE functional, to our knowledge, such parameters have not been optimized for either HFPBE or LC-ωPBE0. The values of the -D3 and -D3(BJ) parameters for these functionals utilized in Table 3 (which are given in the Supporting Information) have been optimized by us on the union of the S22+ and S66+ databases (that is, the subsets of the S22 × 5[37] and S66 × 8[97] databases, respectively, corresponding to the intermolecular separations larger or equal to the van der Waals minimum distances) using the QZVP basis set (the further details of the optimization procedure are the same as in the next section. Although the fitting set differs from the actual set used for the optimization of -D3 and -D3(BJ) by Grimme,[24,74] we verified that Grimme's parameters for both PBE, PBE0, and LC-ωPBE would be nearly optimal for the union of the S22+ and S66+ sets (the MURE values for PBE-D3, PBE0-D3, and LC-ωPBE-D3 in the QZVP basis are 12.0, 10.2, and 5.8%, respectively, compared to the optimal, refitted values of 9.0, 8.1, and 5.3%, respectively). Therefore, the -D3 and -D3(BJ) expressions optimized in this way should be just as sufficient, or just as insufficient, at short range as the ones involving parameters optimized according to Grimme's original algorithm. The results in Table 3 show that an increased fraction of the HF exchange, included either globally or with range separation, does decrease the interaction energy at short range, bringing it closer to the CCSD(T)-level benchmark. However, the overestimation of the short range interaction energies remains substantial: manipulating the HF exchange is no substitute for including atom-pairwise dispersion. The inclusion of the -D3 or -D3(BJ) dispersion term reduces the short range errors significantly, although the interaction energies remain too high (with an exception of HFPBE-D3 which is, in turn, quite inaccurate at long range as shown in the next section). Range separation clearly improves the performance of PBE and PBE0 at short range, bringing the mean error at $0.8z_{\rm min}$ down from 1.5−2.5 to 0.5−0.8 kcal/mol. Thus, the overestimation of short range interaction energies is relieved, but not completely removed, by range separation; the preminimum wMURE of the LC-ωPBE-D3/QZVP approach is still 13.6% as shown in Figure 6. Apparently, the short range DFT+D insufficiencies cannot be fully overcome by modifying the DFT part alone.

Table 3. Mean Errors (Calculated with Signs, in Kilocalories Per Mole) of the Functionals from the PBE Family Relative to the Benchmark CO_2−C_1 Interaction Energies Obtained for the Subsets of the Benchmark Data Corresponding to $0.8z_{\rm min}$, $0.9z_{\rm min}$, and $z_{\rm min}$[a]

method	$0.8z_{\rm min}$	$0.9z_{\rm min}$	$z_{\rm min}$
PBE	7.40	5.55	3.88
PBE0	6.83	5.26	3.81
HFPBE	4.68	4.19	3.53
LC-ωPBE	6.47	5.20	3.93
LC-ωPBE0	6.38	5.17	3.93
PBE-D3	2.52	1.20	0.32
PBE0-D3	1.77	0.88	0.35
HFPBE-D3	−0.76	−0.30	0.28
LC-ωPBE-D3	0.57	0.23	0.21
LC-ωPBE0-D3	0.77	0.44	0.37
PBE-D3(BJ)	1.89	1.08	0.41
PBE0-D3(BJ)	1.53	0.85	0.30
HFPBE-D3(BJ)	0.12	0.18	0.11
LC-ωPBE-D3(BJ)	0.54	0.23	−0.03
LC-ωPBE0-D3(BJ)	0.61	0.42	0.20

[a] The QZVP basis set was used, and the CP correction was applied. The -D3 and -D3(BJ) parameters for the HFPBE and LC-ωPBE0 functionals were optimized on the combined S22+ and S66+ databases as described in the text.

We conclude that no method tested is both computationally tractable and accurate enough for computing a large number of points on a CO_2−nanotube fragment potential energy surface.

Refitting DFT+D. As previously noted, the DFT+D values are universally too large at short range. Although, as discussed above, this effect might be partially due to an overestimation of the DFT exchange energy, at least part of the problem comes from the overdamping of dispersion. Because Grimme's -D dispersion correction is an a posteriori term, refitting the damping parameters is a computationally inexpensive task and a relatively simple exercise compared to, say, refitting the range separation parameter ω or some other parameters in the density functional. It should be noted that the sole nonlocal functional tested, VV10, has a superior accuracy at long range compared to any GGA+D or hybrid GGA+D combination employed. Because the default damping parameter was utilized for VV10, refitting this parameter would most likely shore up the short range deficiencies. However, as this parameter must be changed before the VV10 computation, the cost of refitting would be many times that of Grimme's atom-pairwise dispersion term and refitting VV10 was not pursued. Three separate fitting forms were utilized, including the so-called "zero damping" or Chai−Head-Gordon (CHG) damping form,[24,29] which has two parameters s_8 and $s_{r,6}$ (the $s_{r,8}$ values are held constant at 1), represented as

$$E_{\rm disp}^{\rm CHG} = -\frac{1}{2}\sum_{A\neq B}\sum_{n=6,8} s_n \frac{C_n^{AB}}{r_{AB}^n}\frac{1}{1+6(r_{AB}/(s_{r,n}R_0^{AB}))^{-\alpha_n}} \tag{4}$$

The α_n parameters are set to 14 and 16 for α_6 and α_8, respectively, and are not adjusted.

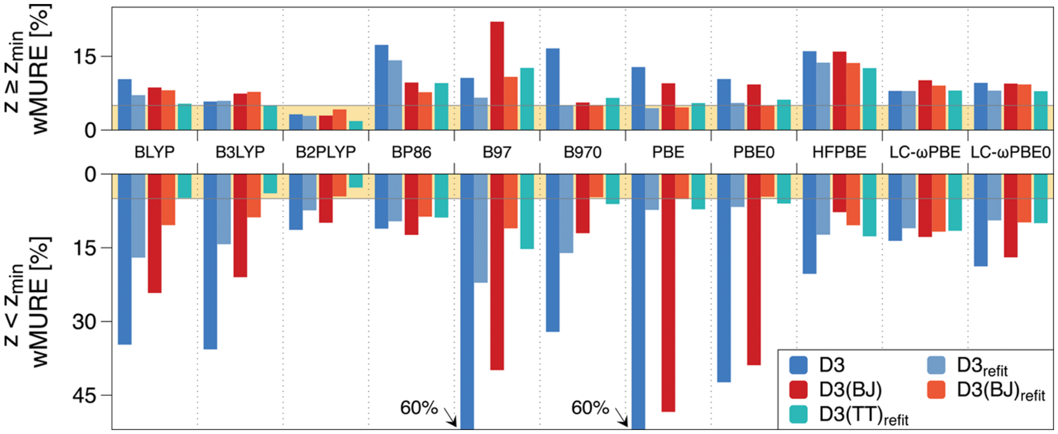

Figure 7. Performance of different DFT-D3, DFT-D3(BJ), and DFT-D3(TT) variants, with original and refitted damping parameters, on the 195 CO_2-C_1 geometries. In each case, the DFT part is computed in the QZVP basis set and includes the CP correction. The yellow range represents the target mean accuracy of 5%. Grimme's damping parameters are not available for the B970, HFPBE, and LC-ωPBE0 functionals; in these cases, the nonrefitted values shown here were obtained by us using the combination of the S22+ and S66+ databases (see text for details).

The Becke–Johnson (BJ) damping,[74,98] with three parameters s_8, α_1, and α_2, is represented as

$$E_{\text{disp}}^{\text{BJ}} = -\frac{1}{2}\sum_{A\neq B}\sum_{n=6,8} s_n \frac{C_n^{AB}}{r_{AB}^n + (\alpha_1 R_0^{AB} + \alpha_2)^n} \qquad (5)$$

The Tang and Toennies (TT)[99] damping, with two parameters s_8 and d_{TT}, has the form

$$E_{\text{disp}}^{\text{TT}} = -\frac{1}{2}\sum_{A\neq B}\sum_{n=6,8} s_n \frac{C_n^{AB}}{r_{AB}^n} f_{\text{TT},n-1}\left(\frac{r_{AB}\cdot d_{\text{TT}}}{R_0^{AB}}\right) \qquad (6)$$

$$f_{\text{TT},n}(x) = 1 - \text{e}^{-x}\sum_{m=0}^{n}\frac{x^m}{m!} \qquad (7)$$

Note that the TT damping function is evaluated as $f_{\text{TT},n-1}(x)$ so that $\lim_{r_{AB}\to 0} f_{\text{TT},n-1}(r_{AB})/r_{AB}^n$ is not zero at short range but rather a constant value reflecting a more physical picture (similar to the BJ damping).

The R_0^{AB} value for the CHG damping comes from the original -D3 work,[24] whereas for the BJ damping, the R_0^{AB} value is computed as $R_0^{AB} = (C_8^{AB}/C_6^{AB})^{1/2}$. For the TT damping, both forms of R_0^{AB} were tried; the R_0^{AB} used in CHG damping yields more accurate results and was universally employed for all TT damping expressions. The s_6 parameter is always set to unity except for the B2PLYP double hybrid functional, for which the recommended value of 0.64[24] was employed. Note that the adjustment of the s_8 scaling factor for the C_8^{AB}/r_{AB}^8 terms is absolutely crucial for the performance of the -D3 correction, both original and refitted; the price one has to pay is a functional-dependent value of the second leading asymptotic constant C_8. Similarly, although an inclusion of adjustable C_{10}^{AB}/r_{AB}^{10} terms could further improve the refit, we elected not to do so because the molecular C_{10} constants determined by fitting to short range data would bear no connection to the correct long range behavior of dispersion. In one case (the PBE functional), the best fit (a wMURE of 4.4% on the 195 CO_2-C_1 structures) of the CHG damping expression resulted in an unphysical, negative value of the factor s_8; we discarded this fit in favor of the second best one (a wMURE of 5.6%), for which s_8 is reasonable. Interestingly, for the BJ damping, eq 5, most of our best fits employ negative values of the α_2 parameter. Although such values were disallowed in the original parameter fit,[74] they do not lead to any unphysical behavior as long as the expression $(\alpha_1 R_0^{AB} + \alpha_2)$ remains far from zero for all values of R_0^{AB} that can be attained in real molecular systems (the range of the R_0^{AB} values between different types of atoms is quite limited). In our calculations, $(\alpha_1 R_0^{AB} + \alpha_2)$ is never close to zero, so we accepted the optimized expressions with negative α_2.

The fitting procedure utilizes the 195 CO_2-C_1 benchmark geometries. All functionals were fitted using the largest basis set computed, QZVP. The nonlinear parameters were selected to minimize the weighted root-mean-square error, represented as

$$\text{Error} = \sqrt{\text{mean}\left(\frac{(E - E_{\text{ref}})^2}{E_{\text{weight}}^2}\right)} \qquad (8)$$

where the weight is identical to the weighting function of wMURE (eq 3). The linear parameter, s_8, was fitted via weighted linear least-squares at each nonlinear iteration with the same weight as above. The refitted parameters for each functional and damping expression can be found in Table S2 of the Supporting Information.

Performance of the Refitted DFT+D Approaches. As can be seen from Figure 7, refitting the damping parameters greatly enhances the accuracy of DFT+D methods, particularly for the preminimum set of points. For each functional, there is at least one fitting form that provides an overall wMURE of under 11%. It is of interest that different fitting forms work better for different functional families. For example, the -D3(TT)$_{\text{refit}}$ terms work best for the BLYP family of functionals (BLYP, B3LYP, and B2PLYP), whereas for PBE and PBE0, all fitting forms work nearly equally well.

The two best refitted GGA+D functionals are PBE-D3(BJ)$_{\text{refit}}$/QZVP with a wMURE of 4.8% and BLYP-D3(TT)$_{\text{refit}}$/QZVP with a wMURE of 5.2%. Up to this point, all data provided has been shown at the largest basis sets possible; however, for fragments larger than coronene only basis sets up to aDZ can be used, and for fragments C_3 or larger only the SVP basis set can be used because of linear dependencies. As shown in Table 4 in case of the BLYP-D3(TT) and PBE-D3(BJ) functionals with parameters refitted using the QZVP basis, all basis sets aDZ and larger, when CP-corrected, give values within 0.7% wMURE of each other,

Table 4. wMURE of the Two Best Refitted DFT+D GGA Functionals BLYP-D3$(TT)_{refit}$ and PBE-D3$(BJ)_{refit}$ Compared to the 195 CO_2−C_1 Benchmark Interaction Energies[a]

	CP BLYP-D3$(TT)_{refit}$			CP PBE-D3$(BJ)_{refit}$		
basis	$z < z_{min}$	$z \geq z_{min}$	overall	$z < z_{min}$	$z \geq z_{min}$	overall
SVP	8.8	10.0	9.5	11.0	8.2	9.3
aDZ	6.1	5.8	5.9	5.3	4.9	5.1
TZVP	6.2	5.3	5.7	6.4	4.9	5.5
aTZ	5.0	5.3	5.2	5.1	4.6	4.8
QZVP	4.9	5.4	5.2	5.1	4.6	4.8
	no-CP BLYP-D3$(TT)_{refit}$			no-CP PBE-D3$(BJ)_{refit}$		
basis	$z < z_{min}$	$z \geq z_{min}$	overall	$z < z_{min}$	$z \geq z_{min}$	overall
SVP	109.6	46.9	72.0	95.2	31.7	57.1
aDZ	38.5	26.6	31.4	46.1	34.0	38.9
TZVP	12.2	11.7	11.9	12.0	10.7	11.2
aTZ	15.6	12.9	14.0	15.0	13.7	14.2
QZVP	6.9	6.9	6.9	5.9	5.9	5.9

[a] The basis sets are ordered by the number of basis functions per carbon atom.

whereas a downgrade to the SVP basis set roughly doubles the wMURE. For the non-CP corrected results, any basis set smaller than QZVP quickly diverges from the best result, making the CP correction essential. Although it is possible to fit to results in any basis set, CP- or non-CP corrected, the optimal parameters obtained without the CP correction would not be transferable to any other basis set because of the poor stability of the non-CP results.

To explore how well the new coronene-refitted DFT+D models perform for PAHs both smaller and larger than coronene, two new benchmark sets were developed. First, the C_{2v} minima for benzene (⊥ and C ||), naphthalene (C ⊥ and ||), and pyrene (C ⊥ and ||) were shifted to 0.8, 0.9, 1.0, 1.2, and 1.4 times the minimum distance for a total of 10 geometries per PAH; the benchmark interaction energies for these geometries were then computed at the MP2/(aQZ, a5Z)+ΔCCSD(T)-F12avg/aDZ level of theory. The $1.4z_{min}$ ⊥ CO_2−benzene benchmark value is very small (−0.004 kcal/mol) and was removed from the data set to avoid overweighting of this point. Second, although CCSD(T) in any reasonable basis set is not feasible for a C_2 fragment, two lower scaling methods, SCS-MP2/(aDZ,aTZ) and B2PLYP-D3$(TT)_{refit}$/QZVP, exhibit an excellent accuracy for the CO_2−C_1 benchmark set with a wMURE of 4.5 and 2.2%, respectively. Following the language of ref 100, we will name the SCS-MP2/(aDZ,aTZ) and B2PLYP-D3$(TT)_{refit}$/QZVP levels of theory our "silver standards". The (12,0) C_2 fragment was chosen for the C_2 benchmark because linear dependencies preclude the computation of MP2/aTZ for flat graphene-like C_2 fragments. For the CO_2−C_2 (12,0) complex, the minimum positions for the ⊥, C ||, and || orientations were found for both interior and exterior geometries at the PBE-D3$(BJ)_{refit}$/aDZ level of theory. Starting from these minimum geometries, the z distance was again multiplied by 0.8, 0.9, 1.0, 1.2, and 1.4 for a total of 15 interior and 15 exterior geometries. These structures were then computed at both the SCS-MP2/(aDZ,aTZ) and B2PLYP-D3$(TT)_{refit}$/QZVP levels of theory. For the CO_2−C_2 (12,0) complex, it is unclear which of the two approaches should be a better benchmark; in this case, we will display the wMURE values with respect to both SCS-MP2/(aDZ,aTZ) and B2PLYP-D3$(TT)_{refit}$/QZVP and refer to them as a range of accuracy of a given DFT+D approach.

The wMURE values at different fragment sizes for the best CO_2−benzene GGA+D (PBE-D2/aDZ), the best CO_2−C_1 GGA+D (BP86-D3(BJ)/aDZ), the two best CO_2−C_1 refitted GGA+D functionals (BLYP-D3$(TT)_{refit}$/aDZ and PBE-D3$(BJ)_{refit}$/aDZ), the two best CO_2−C_1 refitted hybrid GGA+D functionals (B970-D3$(BJ)_{refit}$/aDZ and B3LYP-D3$(TT)_{refit}$/aDZ), and the two silver standards (B2PLYP-D3$(TT)_{refit}$/QZVP and SCS-MP2/(aDZ,aTZ)) are shown in Figure 8. It is encouraging to see that the two silver standards deviate from each other by only 3.4% on the average for the CO_2−(12,0) C_2 benchmark. In addition, the wMURE of both silver standards is below 5.5% for PAHs the size of pyrene and C_1. Thus, a similar performance for CO_2−C_2 should be expected.

Ideally, the performance of the best DFT+D functional would be transferable between models of different sizes; however, Figure 8 demonstrates that this is rarely the case.

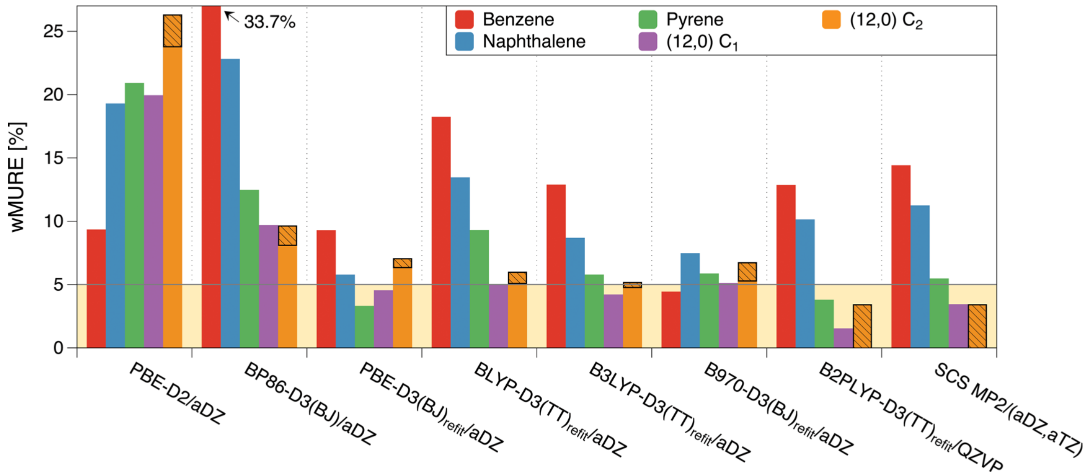

Figure 8. Top performing DFT functionals combined with the best (original or refitted) +D terms for five separate CO_2−PAH complexes. Benchmark values and geometries are as described in the text. Because no higher-level benchmark is available for the circumcoronene (C_2) complexes, a range of wMURE values based on the comparison to the two silver standards, B2PLYP-D3$(TT)_{refit}$/QZVP and SCS-MP2/(aDZ,aTZ), is indicated by the shading.

Choosing a DFT+D functional on the basis of the performance on the small CO_2−benzene complex (PBE-D2/aDZ) yields good results for this complex (wMURE 9.4%), whereas for the larger (12,0) C_2 system, the wMURE increases to 23.8−26.3%. Conversely, when the DFT+D functional is chosen on the basis of the CO_2−C_1 benchmark (BP86-D3(BJ)/aDZ), the performance for interior and exterior (12,0) C_2 complexes is quite good (a wMURE of 8.1−9.6%); however, the wMURE for the CO_2−benzene dimer is 33.7%. Interestingly, the size dependence is not limited to DFT+D functionals and can be seen in our silver standards as well, again highlighting the need for CCSD(T)-level benchmarks.

Examining the B2PLYP, B3LYP, BLYP, BP86, B97, PBE0, and PBE functionals with the -D3 and -D3(BJ) dispersion expressions, we see that refitting for the CO_2−C_1 complex improves the CO_2−benzene performance in every single case. For example, the PBE-D3(BJ)/aDZ functional has a wMURE of 15.9%, whereas PBE-D3(BJ)$_{\text{refit}}$/aDZ has a wMURE of 8.4% for CO_2−benzene. It should be noted that not all functionals see such a large improvement: in the worst case, PBE0-D3/aDZ has a wMURE of 13.7%, whereas PBE0-D3$_{\text{refit}}$/aDZ has a wMURE of 13.2%. Thus, refitting using the largest PAH possible universally improves the results for smaller PAHs.

One could ask whether the refitted damping parameters obtained by us are transferable to any other weakly interacting systems, for example, to the popular databases of noncovalent interaction energies such as S22 × 5^{37} and S66 × $8.^{97}$ These databases cover a wide range of hydrogen-bonded, dispersion-bonded, and mixed interactions and encompass both the long range and the region around the van der Waals minimum. The shortest intermolecular distances in S22 × 5 and S66 × 8 are 0.9 times the minimum separation and still correspond to negative interaction energies. Thus, these databases do not sample the mildly repulsive region of the interaction as broadly as our CO_2−C_1 benchmark set. However, the accuracy of several standard DFT+D approaches has been found to deteriorate already at the shortest separations from S22 × 5^{37} in accordance with the findings of this work. Therefore, the combination of the S22 × 5 and S66 × 8 sets provides a stringent test of whether -D3$_{\text{refit}}$ is applicable to general weakly interacting systems as readily as the original -D3. To this end, we computed the MURE values for the refitted DFT+D approaches (using the QZVP basis set and including the CP correction) on the union of the S22 × 5 and S66 × 8 databases, comparing them to the corresponding unrefitted DFT+D. The resulting MURE values are collected in Table 5. Interestingly, for the original -D3 approach (eq 4), the accuracy of the original and refitted dispersion expressions is very similar; depending on a functional, refitting leads to either a minor improvement or a minor worsening. This result is very promising; apparently, by fitting our damping parameters to a very specific class of systems, we have not sacrificed the robustness of the -D3 correction. The same cannot be said about the BJ damping form (except for the B2PLYP functional); refitting its damping parameters for the CO_2−C_1 data significantly decreases the accuracy for the S22 × 5 and S66 × 8 databases, indicating that the -D3(BJ)$_{\text{refit}}$ expression, unlike -D3$_{\text{refit}}$, is not transferable to other systems. The accuracy of the DFT-D3(TT)$_{\text{refit}}$ approaches on the S22 × 5 and S66 × 8 sets is also unsatisfactory (although better than that of DFT-D3(BJ)$_{\text{refit}}$), advising against the use of the TT damping parameters fitted to the CO_2−C_1 data for other classes of interacting systems.

Table 5. Mean Unsigned Relative Errors (in Percent) for Different Density Functionals Augmented by the Original (Refs 24 and 74) and Refitted (Using Our 195 CO_2−C_1 Benchmark Geometries) Atom-Pairwise Dispersion Corrections, Averaged over the Combined S22 × 5^{37} and S66 × 8^{97} Datasets[a]

functional	-D3	-D3$_{\text{refit}}$	-D3(BJ)	-D3(BJ)$_{\text{refit}}$	-D3(TT)$_{\text{refit}}$
BLYP	10.7	9.1	6.8	29.0	13.4
B3LYP	10.5	10.3	4.9	28.1	14.9
B2PLYP	7.9	5.9	6.8	6.7	7.0
BP86	13.6	12.0	12.4	68.3	13.3
B97	9.1	11.2	13.4	40.4	18.7
B970	9.9	13.7	6.4	31.3	21.5
PBE	15.9	14.1	10.8	33.9	20.1
PBE0	13.4	13.3	9.6	42.3	17.4
HFPBE	18.0	17.2	15.1	28.6	21.6
LC-ωPBE	6.3	8.1	7.7	21.2	10.8
LC-ωPBE0	7.9	9.7	5.7	23.3	12.7

[a] The QZVP basis set and CP correction were used for all DFT calculations.

Nanotube Fragments. On the basis of the results in Figure 8, the PBE-D3(BJ)$_{\text{refit}}$ approach, providing a fairly consistent accuracy for nanotube models of different sizes, is the best candidate to explore the interaction energy behavior for larger nanotube fragments. Using the density-fitted MOLPRO code, fragments as large as C_3 (up to approximately 100 carbon atoms) can be computed in the aDZ basis set. If the basis set is reduced to SVP, then larger C_4 and T_2 fragments can be computed (up to approximately 180 carbon atoms). As shown in Table 4, the downgrade from PBE-D3(BJ)$_{\text{refit}}$/aDZ to PBE-D3(BJ)$_{\text{refit}}$/SVP increases the wMURE of this method from 5.1 to 9.3% for the CO_2−C_1 complexes. Because the purpose here is mainly to explore the dependence of the interaction energy on the size of the nanotube fragment, rather than an accurate value of the interaction energy itself, this is an acceptable approximation.

The global-minimum CO_2 positions for the nanotube fragments were optimized at the BLYP-D3(TT)$_{\text{refit}}$/aDZ level (PBE-D3(BJ)$_{\text{refit}}$/aDZ geometries would be similar) for all zigzag and armchair nanotubes with diameters between 4 and 15 Å at both the C_1 and C_2 level. Because the computations are density fitted, these geometry optimizations are no longer constrained by symmetry; however, the reoptimized minimum CO_2−C_1 geometries were similar to those of Figure 5. In addition, the interior geometries were constrained so that the z distance could not exceed the radius of the nanotube. Because geometry optimizations for fragments larger than C_2 are not practical, the C_2 geometry was used for all larger nanotube models.

Figure 9 shows the results of the PBE-D3(BJ)$_{\text{refit}}$/SVP calculations for the largest fragments possible. The number of carbon atoms in the toroidal fragments grows as the nanotube diameter increases; thus, it is not always possible to compute the T_1 and T_2 models. However, the C_n sizes are constant, so it is always possible to compute a C_4 fragment in the SVP basis set.

For exterior positions, the C_1, C_2, and C_3 fragments capture, on the average, 88.9, 96.7, and 99.0%, respectively, of the interaction energy compared to the most complete C_4 fragment for 18 nanotubes in Figure 9. For the deepest interior minimum, the (5,5) nanotube, the coronene-like C_1, C_2, and

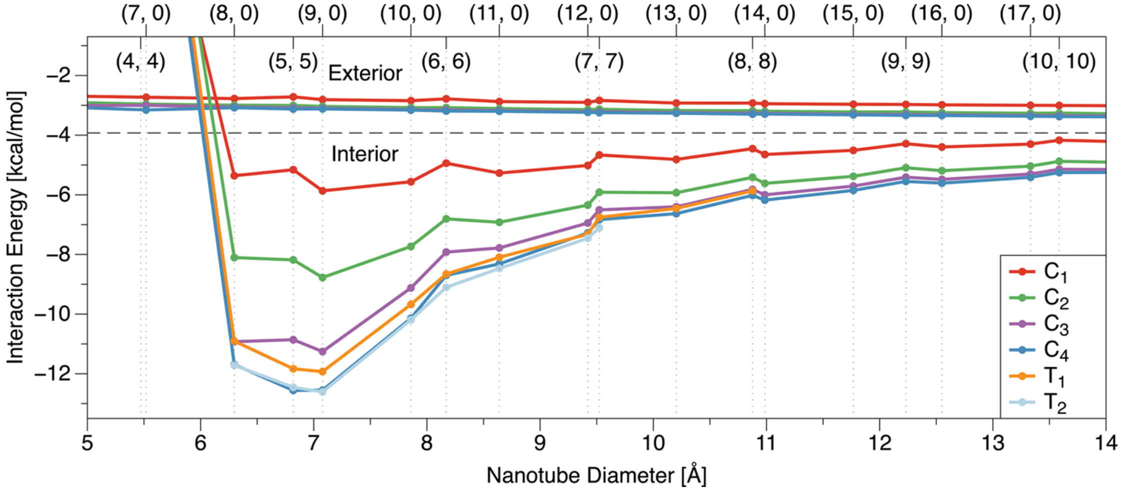

Figure 9. || CO_2−nanotube fragment interaction energy at the minimum computed at the PBE-D3(BJ)$_{refit}$/SVP level as a function of fragment size and nanotube diameter. The dashed line is from a CO_2−flat (graphene-like) C_4 PBE-D3(BJ)$_{refit}$/SVP computation. The exterior and interior minimum geometries for each nanotube were optimized using BLYP-D3(TT)$_{refit}$/aDZ for the C_1 and C_2 fragments as described in the text.

C_3 fragments capture 41.1, 65.1, and 86.5%, respectively, of the interaction energy compared to the largest fragment (C_4), whereas the toroidal T_1 and T_2 fragments capture 94.1 and 99.2%, respectively, of the C_4 result. The relatively poor performance of the C_1 and C_2 fragments for interior sites is due to the greater number of carbon atoms in close proximity to the CO_2 molecule in a complete nanotube. In addition, this simple geometric picture explains why the interior site interaction energy is so much larger than that for exterior sites. This behavior has been seen before for the methane−nanotube system;[14] however, the salient point is that very large (150 carbon atoms) fragments are required to fully saturate the interior interaction energy, whereas for exterior sites, smaller C_2 fragments (54 carbon atoms) are sufficient.

On the basis of the results in Figure 9, for exterior sites we recommend the PBE-D3(BJ)$_{refit}$/aDZ level of theory computed at the CO_2−C_2 fragment size. Adding the error from the smaller C_2 fragment size and the error of the refitted functional, we arrive at an accuracy of approximately 8%. For interior sites, we recommend the PBE-D3(BJ)$_{refit}$/SVP level of theory computed at the CO_2−T_2 fragment size for nanotubes smaller than 9 Å in diameter; for larger nanotubes, we recommend the CO_2−C_3 model. For interior sites, we expect an accuracy of approximately 10%. Our best interaction energy estimates for a CO_2 molecule bound to a carbon nanotube can be found in Figure S2 in the Supporting Information.

It should be noted that our estimates involve a pairwise additive treatment of dispersion that might not be adequate for the asymptotic constants between extended nanostructures.[101−103] While it is not entirely clear how system size affects the damping functions (which, as shown here, have their own issues) and the interaction energies at finite distances, and although no performance decrease of pairwise-additive DFT+D is observed for models as large as circumcoronene (as compared to wave function-based results; for example, SCS-MP2), further studies that explicitly include dispersion nonadditivity are required to unambiguously determine adsorption energies on extended nanostructures.

■ CONCLUSIONS

As the first step toward constructing a more accurate interaction potential between CO_2 and carbon nanotubes, we benchmarked a wide range of CO_2−PAH complexes with the PAH size ranging from benzene (6 carbon atoms) to circumcoronene (54 carbon atoms). Our composite MP2/CBS+ΔCCSD(T)-F12avg/laDZ benchmark interaction energies are accurate to 3% or better, as demonstrated for the benzene, naphthalene, and pyrene complexes at different orientations and distances. This composite method was then applied for 195 configurations of the largest fragment feasible at this level, the CO_2−curved coronene complex, and a variety of novel dispersion including DFT functionals were benchmarked. The results indicate that although the accuracy of these methods at the minimum and longer distances is quite good, the results at ranges shorter than the minimum distance deviate strongly from the benchmark. To overcome this short range deficiency, the damping parameters of Grimme's -D3 dispersion term were refitted to reproduce the CO_2−C_1 benchmark. This refitting resulted in several highly accurate DFT+D functionals such as B2PLYP-D3(TT)$_{refit}$ and PBE-D3(BJ)$_{refit}$, with errors (wMURE) on the CO_2−C_1 benchmark set as low as 2.2%.

The B2PLYP-D3(TT)$_{refit}$/QZVP and SCS-MP2/(aDZ,aTZ) levels of theory were found to be acceptable silver standards for the large CO_2−C_2 complexes because their errors on both the CO_2−pyrene and CO_2−C_1 benchmarks were below 5.5%. In addition, these two methods agree to 3.4% on the average for the CO_2−C_2 interaction energies. The DFT+D interaction energy dependence on the PAH size, from the smallest CO_2−benzene complex to the CO_2−C_2 dimer, was explored. On the basis of the accuracy trends as functions of the fragment size, PBE-D3(BJ)$_{refit}$ was chosen as the best functional. To further explore the size dependence of the interaction energy, the PBE-D3(BJ)$_{refit}$/SVP level of theory was used to investigate complexes involving fragments up to T_2 and C_4. For exterior sites, C_2-sized fragments are sufficient to fully converge the interaction energy, whereas for interior sites, large T_2 or C_3 fragments are required. Using the best combination of a DFT+D approach, basis set, and fragment size, we can recover the interaction energy between a CO_2 molecule and a carbon nanotube to within 10%.

DOI: 10.1021/jp512926n
J. Phys. Chem. C 2015, 119, 4934−4948

The primary effect that hinders the performance of standard functionals for the CO_2−PAH complexes is the overdamping of dispersion. Interestingly, this overdamping is seen for Grimme's atom-pairwise dispersion, the -dDsC correction, the -D_{as} correction to dlDF, and the nonlocal VV10 functional, indicating that the damping issue may apply to all current dispersion forms that require empirical damping parameters. While the -D3 damping parameters that were fitted specifically for the CO_2−PAH systems perform similarly to Grimme's original parameters on the S22 × 5 and S66 × 8 benchmark sets, the performance of the CO_2−PAH-refitted BJ damping parameters is significantly worse than that of Grimme's original values. Therefore, the refitted parameters should not be treated as new, improved general-purpose values. Instead, they demonstrate that standard damping forms may not be sufficient to overcome the short range DFT+D deficiencies over different classes of complexes. A new approach is needed to develop a transferable dispersion expression, and work in this direction is in progress in our group.

ASSOCIATED CONTENT

Ⓢ Supporting Information

Performance statistics for all DFT variants, dispersion corrections, and basis sets, refitted -D3 damping parameters, and Cartesian geometries and benchmark interaction energies for the complexes studied in this work. This material is available free of charge via the Internet at http://pubs.acs.org.

AUTHOR INFORMATION

Corresponding Author

*Phone: +1 334 844 7522. E-mail: patkowsk@auburn.edu.

Notes

The authors declare no competing financial interest.

ACKNOWLEDGMENTS

This research was supported by the Donors of the American Chemical Society Petroleum Research Fund, the NSF CAREER award CHE-1351978, and startup funding from Auburn University. We thank Dr. Clemence Corminboeuf for valuable discussions and Dr. Mike Schmidt for his assistance with the GAMESS calculations.

REFERENCES

(1) Lu, C.; Bai, H.; Wu, B.; Su, F.; Hwang, J. F. Comparative Study of CO_2 Capture by Carbon Nanotubes, Activated Carbons, and Zeolites. *Energy Fuels* **2008**, *22*, 3050−3056.

(2) Samanta, A.; Zhao, A.; Shimizu, G. K. H.; Sarkar, P.; Gupta, R. Post-Combustion CO_2 Capture Using Solid Sorbents: A Review. *Ind. Eng. Chem. Res.* **2012**, *51*, 1438−1463.

(3) Liu, Y. Y.; Wilcox, J. CO_2 Adsorption on Carbon Models of Organic Constituents of Gas Shale and Coal. *Environ. Sci. Technol.* **2011**, *45*, 809−814.

(4) Kowalczyk, P.; Furmaniak, S.; Gauden, P. A.; Terzyk, A. P. Optimal Single-Walled Carbon Nanotube Vessels for Short-Term Reversible Storage of Carbon Dioxide at Ambient Temperatures. *J. Phys. Chem. C* **2010**, *114*, 21465−21473.

(5) Lithoxoos, G. P.; Labropoulos, A.; Peristeras, L. D.; Kanellopoulos, N.; Samios, J.; Economou, I. G. Adsorption of N_2, CH_4, CO and CO_2 Gases in Single Walled Carbon Nanotubes: A Combined Experimental and Monte Carlo Molecular Simulation Study. *J. Supercrit. Fluids* **2010**, *55*, 510−523.

(6) Rahimi, M.; Singh, J. K.; Babu, D. J.; Schneider, J. J.; Müller-Plathe, F. Understanding Carbon Dioxide Adsorption in Carbon Nanotube Arrays: Molecular Simulation and Adsorption Measurements. *J. Phys. Chem. C* **2013**, *117*, 13492−13501.

(7) Bucior, B. J.; Chen, D.-L.; Liu, J.; Johnson, J. K. Porous Carbon Nanotube Membranes for Separation of H_2/CH_4 and CO_2/CH_4 Mixtures. *J. Phys. Chem. C* **2012**, *116*, 25904−25910.

(8) Liu, H.; Cooper, V. R.; Dai, S.; Jiang, D. Windowed Carbon Nanotubes for Efficient CO_2 Removal from Natural Gas. *J. Phys. Chem. Lett.* **2012**, *3*, 3343−3347.

(9) Kauffman, D. R.; Star, A. Carbon Nanotube Gas and Vapor Sensors. *Angew. Chem., Int. Ed.* **2008**, *47*, 6550−6570.

(10) Kong, J.; Franklin, N. R.; Zhou, C. W.; Chapline, M. G.; Peng, S.; Cho, K. J.; Dai, H. J. Nanotube Molecular Wires as Chemical Sensors. *Science* **2000**, *287*, 622−625.

(11) Britz, D. A.; Khlobystov, A. N. Noncovalent Interactions of Molecules with Single Walled Carbon Nanotubes. *Chem. Soc. Rev.* **2006**, *35*, 637−659.

(12) Georgakilas, V.; Otyepka, M.; Bourlinos, A. B.; Chandra, V.; Kim, N.; Kemp, K. C.; Hobza, P.; Zboril, R.; Kim, K. S. Functionalization of Graphene: Covalent and Non-Covalent Approaches, Derivatives and Applications. *Chem. Rev.* **2012**, *112*, 6156−6214.

(13) Giacinto, P.; Bottoni, A.; Calvaresi, M.; Zerbetto, F. $Cl^{(-)}$ Exchange S_N2 Reaction inside Carbon Nanotubes: C-H···π and Cl···π Interactions Govern the Course of the Reaction. *J. Phys. Chem. C* **2014**, *118*, 5032−5040.

(14) Smith, D. G. A.; Patkowski, K. Toward an Accurate Description of Methane Physisorption on Carbon Nanotubes. *J. Phys. Chem. C* **2014**, *118*, 544−550.

(15) Raghavachari, K.; Trucks, G. W.; Pople, J. A.; Head-Gordon, M. A 5th-Order Perturbation Comparison of Electron Correlation Theories. *Chem. Phys. Lett.* **1989**, *157*, 479−483.

(16) Řezáč, J.; Hobza, P. Describing Noncovalent Interactions beyond the Common Approximations: How Accurate Is the "Gold Standard," CCSD(T) at the Complete Basis Set Limit? *J. Chem. Theory Comput.* **2013**, *9*, 2151−2155.

(17) Smith, D. G. A.; Jankowski, P.; Slawik, M.; Witek, H. A.; Patkowski, K. Basis Set Convergence of the Post-CCSD(T) Contribution to Noncovalent Interaction Energies. *J. Chem. Theory Comput.* **2014**, *10*, 3140−3150.

(18) Schütz, M.; Manby, F. R. Linear Scaling Local Coupled Cluster Theory with Density Fitting. Part I: 4-External Integrals. *Phys. Chem. Chem. Phys.* **2003**, *5*, 3349−3358.

(19) Schütz, M.; Yang, J.; Chan, G. K.; Manby, F. R.; Werner, H.-J. The Orbital-Specific Virtual Local Triples Correction: OSV-L(T). *J. Chem. Phys.* **2013**, *138*, 054109.

(20) Riplinger, C.; Sandhoefer, B.; Hansen, A.; Neese, F. Natural Triple Excitations in Local Coupled Cluster Calculations with Pair Natural Orbitals. *J. Chem. Phys.* **2013**, *139*, 134101.

(21) Voloshina, E.; Usvyat, D.; Schütz, M.; Dedkov, Y.; Paulus, B. On the Physisorption of Water on Graphene: a CCSD(T) Study. *Phys. Chem. Chem. Phys.* **2011**, *13*, 12041−12047.

(22) Yang, J.; Hu, W.; Usvyat, D.; Matthews, D.; Schütz, M.; Chan, G. K. Ab Initio Determination of the Crystalline Benzene Lattice Energy to Sub-kilojoule/mole Accuracy. *Science* **2014**, *345*, 640−643.

(23) Grimme, S. Semiempirical GGA-Type Density Functional Constructed with a Long-Range Dispersion Correction. *J. Comput. Chem.* **2006**, *27*, 1787−1799.

(24) Grimme, S.; Antony, J.; Ehrlich, S.; Krieg, H. A Consistent and Accurate Ab Initio Parametrization of Density Functional Dispersion Correction (DFT-D) for the 94 Elements H-Pu. *J. Chem. Phys.* **2010**, *132*, 154104.

(25) Tkatchenko, A.; Scheffler, M. Accurate Molecular Van Der Waals Interactions from Ground-State Electron Density and Free-Atom Reference Data. *Phys. Rev. Lett.* **2009**, *102*, 073005.

(26) Becke, A. D.; Johnson, E. R. A Unified Density-Functional Treatment of Dynamical, Nondynamical, and Dispersion Correlations. *J. Chem. Phys.* **2007**, *127*, 124108.

(27) Steinmann, S. N.; Corminboeuf, C. Comprehensive Benchmarking of a Density-Dependent Dispersion Correction. *J. Chem. Theory Comput.* **2011**, *7*, 3567−3577.

(28) Zhao, Y.; Schultz, N. E.; Truhlar, D. G. Design of Density Functionals by Combining the Method of Constraint Satisfaction with Parametrization for Thermochemistry, Thermochemical Kinetics, and Noncovalent Interactions. *J. Chem. Theory Comput.* **2006**, *2*, 364−382.

(29) Chai, J.-D.; Head-Gordon, M. Long-Range Corrected Hybrid Density Functionals with Damped Atom-Atom Dispersion Corrections. *Phys. Chem. Chem. Phys.* **2008**, *10*, 6615−6620.

(30) Zhao, Y.; Truhlar, D. G. The M06 Suite of Density Functionals for Main Group Thermochemistry, Thermochemical Kinetics, Noncovalent Interactions, Excited States, and Transition Elements: Two New Functionals and Systematic Testing of Four M06-Class Functionals and 12 Other Functionals. *Theor. Chem. Acc.* **2008**, *120*, 215−241.

(31) Pernal, K.; Podeszwa, R.; Patkowski, K.; Szalewicz, K. Dispersionless Density Functional Theory. *Phys. Rev. Lett.* **2009**, *103*, 263201.

(32) Dion, M.; Rydberg, H.; Schröder, E.; Langreth, D. C.; Lundqvist, B. I. Van der Waals Density Functional for General Geometries. *Phys. Rev. Lett.* **2004**, *92*, 246401.

(33) Vydrov, O. A.; van Voorhis, T. Nonlocal van der Waals Density Functional: The Simpler the Better. *J. Chem. Phys.* **2010**, *133*, 244103.

(34) Grimme, S. Semiempirical Hybrid Density Functional with Perturbative Second-Order Correlation. *J. Chem. Phys.* **2006**, *124*, 034108.

(35) Zhang, Y.; Xu, X.; Goddard, W. A., III Doubly Hybrid Density Functional for Accurate Descriptions of Nonbond Interactions, Thermochemistry and Thermochemical Kinetics. *Proc. Natl. Acad. Sci. U.S.A.* **2009**, *106*, 4963−4968.

(36) Burns, L. A.; Vazquez-Mayagoitia, A.; Sumpter, B. G.; Sherrill, C. D. Density-Functional Approaches to Noncovalent Interactions: A Comparison of Dispersion Corrections (DFT-D), Exchange-Hole Dipole Moment (XDM) Theory, and Specialized Functionals. *J. Chem. Phys.* **2011**, *134*, 084107.

(37) Gráfová, L.; Pitoňák, M.; Řezáč, J.; Hobza, P. Comparative Study of Selected Wave Function and Density Functional Methods for Noncovalent Interaction Energy Calculations Using the Extended S22 Data Set. *J. Chem. Theory Comput.* **2010**, *6*, 2365−2376.

(38) Lechner, C.; Sax, A. F. Adhesive Forces Between Aromatic Molecules and Graphene. *J. Phys. Chem. C* **2014**, *118*, 20970−20981.

(39) Cinke, M.; Li, J.; Bauschlicher, C. W., Jr.; Ricca, A.; Meyyappan, M. CO_2 Adsorption in Single-Walled Carbon Nanotubes. *Chem. Phys. Lett.* **2003**, *376*, 761−766.

(40) Torrisi, A.; Mellot-Draznieks, C.; Bell, R. G. Impact of Ligands on CO_2 Adsorption in Metal-Organic Frameworks: First Principles Study of the Interaction of CO_2 with Functionalized Benzenes. I. Inductive Effects on the Aromatic Ring. *J. Chem. Phys.* **2009**, *130*, 194703.

(41) Besnard, M.; Cabaço, M. I.; Talaga, D.; Danten, Y. Raman Spectroscopy and Ab Initio Investigations of Transient Complex Formation in CO_2-Benzene Mixtures. *J. Chem. Phys.* **2008**, *129*, 224511.

(42) Chen, L.; Cao, F.; Sun, H. Ab Initio Study of the π-π Interactions Between CO_2 and Benzene, Pyridine, and Pyrrole. *Int. J. Quantum Chem.* **2013**, *113*, 2261−2266.

(43) Witte, J.; Neaton, J. B.; Head-Gordon, M. Assessing Electronic Structure Approaches for Gas-Ligand Interactions in Metal-Organic Frameworks: The CO_2-Benzene Complex. *J. Chem. Phys.* **2014**, *140*, 104707.

(44) Zhao, J.; Buldum, A.; Han, J.; Lu, J. P. Gas Molecule Adsorption in Carbon Nanotubes and Nanotube Bundles. *Nanotechnology* **2002**, *13*, 195−200.

(45) Quiñonero, D.; Frontera, A.; Deyà, P. M. Feasibility of Single-Walled Carbon Nanotubes as Materials for CO_2 Adsorption: A DFT Study. *J. Phys. Chem. C* **2012**, *116*, 21083−21092.

(46) Mackie, I. D.; DiLabio, G. A. CO_2 Adsorption by Nitrogen-Doped Carbon Nanotubes Predicted by Density-Functional Theory with Dispersion-Correcting Potentials. *Phys. Chem. Chem. Phys.* **2011**, *13*, 2780−2787.

(47) Umadevi, D.; Sastry, G. N. Molecular and Ionic Interaction with Graphene Nanoflakes: A Computational Investigation of CO_2, H_2O, Li, Mg, Li^+, and Mg^{2+} Interaction with Polycyclic Aromatic Hydrocarbons. *J. Phys. Chem. C* **2011**, *115*, 9656−9667.

(48) Lee, K.-J.; Kim, S.-J. Theoretical Investigation of CO_2 Adsorption on Graphene. *Bull. Korean Chem. Soc.* **2013**, *34*, 3022−3026.

(49) Smith, D. G. A.; Patkowski, K. Interactions between Methane and Polycyclic Aromatic Hydrocarbons: A High Accuracy Benchmark Study. *J. Chem. Theory Comput.* **2013**, *9*, 370−389.

(50) Werner, H.-J.; Knowles, P. J.; Knizia, G.; Manby, F. R.; Schütz, M.; Celani, P.; Korona, T.; Lindh, R.; Mitrushenkov, A.; Rauhut, G. et al. *MOLPRO, a general purpose quantum chemistry program package*, version 2012.1; University College Cardiff Consultants: Cardiff, U.K., 2012. http://www.molpro.net (accessed June 2, 2014).

(51) Grimme, S. Improved Second-Order Møller−Plesset Perturbation Theory by Separate Scaling of Parallel- and Antiparallel-Spin Pair Correlation Energies. *J. Chem. Phys.* **2003**, *118*, 9095−9102.

(52) Adler, T. B.; Knizia, G.; Werner, H.-J. A Simple and Efficient CCSD(T)-F12 Approximation. *J. Chem. Phys.* **2007**, *127*, 221106.

(53) Knizia, G.; Adler, T. B.; Werner, H.-J. Simplified CCSD(T)-F12 Methods: Theory and Benchmarks. *J. Chem. Phys.* **2009**, *130*, 054104.

(54) Marchetti, O.; Werner, H.-J. Accurate Calculations of Intermolecular Interaction Energies Using Explicitly Correlated Coupled Cluster Wave Functions and a Dispersion-Weighted MP2 Method. *J. Phys. Chem. A* **2009**, *113*, 11580−11585.

(55) Marshall, M. S.; Sherrill, C. D. Dispersion-Weighted Explicitly Correlated Coupled-Cluster Theory [DW-CCSD(T**)-F12]. *J. Chem. Theory Comput.* **2011**, *7*, 3978−3982.

(56) Dunning, T. H., Jr. Gaussian-Basis Sets for Use in Correlated Molecular Calculations. 1. The Atoms Boron through Neon and Hydrogen. *J. Chem. Phys.* **1989**, *90*, 1007−1023.

(57) Kendall, R. A.; Dunning, T. H., Jr.; Harrison, R. J. Electron Affinities of the 1st-Row Atoms Revisited - Systematic Basis Sets and Wave Functions. *J. Chem. Phys.* **1992**, *96*, 6796−6806.

(58) Weigend, F.; Ahlrichs, R. Balanced Basis Sets of Split Valence, Triple Zeta Valence and Quadruple Zeta Valence Quality for H to Rn: Design and Assessment of Accuracy. *Phys. Chem. Chem. Phys.* **2005**, *7*, 3297−3305.

(59) Papajak, E.; Leverentz, H. R.; Zheng, J.; Truhlar, D. G. Efficient Diffuse Basis Sets: cc-pVxZ+ and maug-cc-pVxZ. *J. Chem. Theory Comput.* **2009**, *5*, 1197−1202.

(60) Halkier, A.; Helgaker, T.; Jørgensen, P.; Klopper, W.; Koch, H.; Olsen, J.; Wilson, A. K. Basis-Set Convergence in Correlated Calculations on Ne, N_2, and H_2O. *Chem. Phys. Lett.* **1998**, *286*, 243−252.

(61) Becke, A. D. Density-Functional Exchange-Energy Approximation with Correct Asymptotic Behavior. *Phys. Rev. A* **1988**, *38*, 3098−3100.

(62) Lee, C.; Yang, W.; Parr, R. G. Development of the Colle-Salvetti Correlation-Energy Formula into a Functional of the Electron Density. *Phys. Rev. B* **1988**, *37*, 785−789.

(63) Perdew, J. P. Density-Functional Approximation for the Correlation Energy of the Inhomogeneous Electron Gas. *Phys. Rev. B* **1986**, *33*, 8822−8824.

(64) Perdew, J. P.; Burke, K.; Ernzerhof, M. Generalized Gradient Approximation Made Simple. *Phys. Rev. Lett.* **1996**, *77*, 3865−3868.

(65) Becke, A. D. Density-Functional Thermochemistry. 3. The Role of Exact Exchange. *J. Chem. Phys.* **1993**, *98*, 5648−5652.

(66) Stephens, P. J.; Devlin, F. J.; Chabalowski, C. F.; Frisch, M. J. Ab-Initio Calculation of Vibrational Absorption and Circular-Dichroism Spectra Using Density-Functional Force-Fields. *J. Phys. Chem.* **1994**, *98*, 11623−11627.

(67) Adamo, C.; Barone, V. Toward Reliable Density Functional Methods without Adjustable Parameters: The PBE0 Model. *J. Chem. Phys.* **1999**, *110*, 6158−6170.

(68) Ernzerhof, M.; Scuseria, G. E. Assessment of the Perdew−Burke−Ernzerhof Exchange-Correlation Functional. *J. Chem. Phys.* **1999**, *110*, 5029−5036.

(69) Becke, A. D. Density-Functional Thermochemistry. 5. Systematic Optimization of Exchange-Correlation Functionals. *J. Chem. Phys.* **1997**, *107*, 8554−8560.

(70) Podeszwa, R.; Pernal, K.; Patkowski, K.; Szalewicz, K. Extension of the Hartree−Fock Plus Dispersion Method by First-Order Correlation Effects. *J. Phys. Chem. Lett.* **2010**, *1*, 550−555.

(71) Vydrov, O. A.; Scuseria, G. E. Assessment of a Long-Range Corrected Hybrid Functional. *J. Chem. Phys.* **2006**, *125*, 234109.

(72) Turney, J. M.; Simmonett, A. C.; Parrish, R. M.; Hohenstein, E. G.; Evangelista, F. A.; Fermann, J. T.; Mintz, B. J.; Burns, L. A.; Wilke, J. J.; Abrams, M. L.; et al. Psi4: An Open-Source *Ab Initio* Electronic Structure Program. *WIREs Comput. Mol. Sci.* **2012**, *2*, 556−565.

(73) Shao, Y.; Fusti-Molnar, L.; Jung, Y.; Kussmann, J.; Ochsenfeld, C.; Brown, S. T.; Gilbert, A. T. B.; Slipchenko, L. V.; Levchenko, S. V.; O'Neill, D. P.; et al. Advances in Methods and Algorithms in a Modern Quantum Chemistry Program Package. *Phys. Chem. Chem. Phys.* **2006**, *8*, 3172−3191.

(74) Grimme, S.; Ehrlich, S.; Goerigk, L. Effect of the Damping Function in Dispersion Corrected Density Functional Theory. *J. Comput. Chem.* **2011**, *32*, 1456−1465.

(75) Steinmann, S. N.; Corminboeuf, C. A Generalized-Gradient Approximation Exchange Hole Model for Dispersion Coefficients. *J. Chem. Phys.* **2011**, *134*, 044117.

(76) Schmidt, M. W.; Baldridge, K. K.; Boatz, J. A.; Elbert, S. T.; Gordon, M. S.; Jensen, J. H.; Koseki, S.; Matsunaga, N.; Nguyen, K. A.; Su, S.; et al. General Atomic and Molecular Electronic Structure System. *J. Comput. Chem.* **1993**, *14*, 1347−1363.

(77) Werner, H.-J.; Manby, F. R.; Knowles, P. J. Fast Linear Scaling Second-Order Møller−Plesset Perturbation Theory (MP2) Using Local and Density Fitting Approximations. *J. Chem. Phys.* **2003**, *118*, 8149−8160.

(78) Polly, R.; Werner, H.-J.; Manby, F. R.; Knowles, P. J. Fast Hartree−Fock Theory Using Local Density Fitting Approximations. *Mol. Phys.* **2004**, *102*, 2311−2321.

(79) Boys, S. F.; Bernardi, F. Calculation of Small Molecular Interactions by Differences of Separate Total Energies - Some Procedures with Reduced Errors. *Mol. Phys.* **1970**, *19*, 553−566.

(80) van Duijneveldt, F. B.; van Duijneveldt-van de Rijdt, J. G. C. M.; van Lenthe, J. H. State-of-the-Art in Counterpoise Theory. *Chem. Rev.* **1994**, *94*, 1873−1885.

(81) Frey, J. T.; Doren, D. J. *TubeGen* 3.4; University of Delaware: Newark DE, 2011. http://turin.nss.udel.edu/research/tubegenonline.html.

(82) Patkowski, K. Basis Set Converged Weak Interaction Energies from Conventional and Explicitly Correlated Coupled-Cluster Approach. *J. Chem. Phys.* **2013**, *138*, 154101.

(83) Marshall, M. S.; Burns, L. A.; Sherrill, C. D. Basis Set Convergence of the Coupled-Cluster Correction, $\delta_{\mathrm{MP2}}^{\mathrm{CCSD(T)}}$: Best Practices for Benchmarking Non-Covalent Interactions and the Attendant Revision of the S22, NBC10, HBC6, and HSG Databases. *J. Chem. Phys.* **2011**, *135*, 194102.

(84) Henderson, T. M.; Janesko, B. G.; Scuseria, G. E. Generalized Gradient Approximation Model Exchange Holes for Range-Separated Hybrids. *J. Chem. Phys.* **2008**, *128*, 194105.

(85) Steinmann, S. N.; Wodrich, M. D.; Corminboeuf, C. Overcoming Systematic DFT Errors for Hydrocarbon Reaction Energies. *Theor. Chem. Acc.* **2010**, *127*, 429−442.

(86) Seth, M.; Ziegler, T.; Steinmetz, M.; Grimme, S. Modeling Transition Metal Reactions with Range-Separated Functionals. *J. Chem. Theory Comput.* **2013**, *9*, 2286−2299.

(87) Tozer, D. J.; Handy, N. C. Improving Virtual Kohn−Sham Orbitals and Eigenvalues: Application to Excitation Energies and Static Polarizabilities. *J. Chem. Phys.* **1998**, *109*, 10180−10189.

(88) Leininger, T.; Stoll, H.; Werner, H.-J.; Savin, A. Combining Long-Range Configuration Interaction with Short-Range Density Functionals. *Chem. Phys. Lett.* **1997**, *275*, 151−160.

(89) Tawada, Y.; Tsuneda, T.; Yanagisawa, S.; Yanai, T.; Hirao, K. A Long-Range-Corrected Time-Dependent Density Functional Theory. *J. Chem. Phys.* **2004**, *120*, 8425−8433.

(90) Gerber, I. C.; Ángyán, J. G. Hybrid Functional with Separated Range. *Chem. Phys. Lett.* **2005**, *415*, 100−105.

(91) Jeziorski, B.; Moszynski, R.; Szalewicz, K. Perturbation Theory Approach to Intermolecular Potential Energy Surfaces of van der Waals Complexes. *Chem. Rev.* **1994**, *94*, 1887−1930.

(92) Szalewicz, K.; Patkowski, K.; Jeziorski, B. Intermolecular Interactions via Perturbation Theory: from Diatoms to Biomolecules. *Struct. Bonding (Berlin, Ger.)* **2005**, *116*, 43−117.

(93) Hohenstein, E. G.; Sherrill, C. D. Wavefunction Methods for Noncovalent Interactions. *WIREs Comput. Mol. Sci.* **2012**, *2*, 304−326.

(94) Lao, K. U.; Herbert, J. M. Accurate Intermolecular Interactions at Dramatically Reduced Cost: XPol+SAPT with Empirical Dispersion. *J. Phys. Chem. Lett.* **2012**, *3*, 3241−3248.

(95) Lao, K. U.; Herbert, J. M. An Improved Treatment of Empirical Dispersion and a Many-Body Energy Decomposition Scheme for the Explicit Polarization Plus Symmetry-Adapted Perturbation Theory (XSAPT) Method. *J. Chem. Phys.* **2013**, *139*, 034107.

(96) Steinmann, S. N.; Csonka, G.; Corminboeuf, C. Unified Inter- and Intramolecular Dispersion Correction Formula for Generalized Gradient Approximation Density Functional Theory. *J. Chem. Theory Comput.* **2009**, *5*, 2950−2958.

(97) Řezáč, J.; Riley, K. E.; Hobza, P. S66: A Well-balanced Database of Benchmark Interaction Energies Relevant to Biomolecular Structures. *J. Chem. Theory Comput.* **2011**, *7*, 2427−2438.

(98) Johnson, E. R.; Becke, A. D. A Post-Hartree−Fock Model of Intermolecular Interactions. *J. Chem. Phys.* **2005**, *123*, 024101.

(99) Tang, K. T.; Toennies, J. P. An Improved Simple Model for the van der Waals Potential Based on Universal Damping Functions for the Dispersion Coefficients. *J. Chem. Phys.* **1984**, *80*, 3726−3741.

(100) Parker, T. M.; Burns, L. A.; Parrish, R. M.; Ryno, A. G.; Sherrill, C. D. Levels of Symmetry Adapted Perturbation Theory (SAPT). I. Efficiency and Performance for Interaction Energies. *J. Chem. Phys.* **2014**, *140*, 094106.

(101) Misquitta, A. J.; Spencer, J.; Stone, A. J.; Alavi, A. Dispersion Interactions between Semiconducting Wires. *Phys. Rev. B* **2010**, *82*, 075312.

(102) Dobson, J. F. Dispersion and Induction Interactions of Graphene with Nanostructures. *Surf. Sci.* **2011**, *605*, 1621−1632.

(103) Gobre, V. V.; Tkatchenko, A. Scaling Laws for Van der Waals Interactions in Nanostructured Materials. *Nat. Commun.* **2013**, *4*, 2341.

Appendix E

Limits of accuracy of the -D3 dispersion correction to Density Functional Theory at all length scales

Limits of accuracy of the -D3 dispersion correction to Density Functional Theory at all length scales

Daniel G. A. Smith,[1, a] Lori A. Burns,[2, b] Konrad Patkowski,[1, c] and C. David Sherrill[2, 3, d]

[1] *Department of Chemistry and Biochemistry, Auburn University, Auburn, AL 36849*

[2] *Center for Computational Molecular Science and Technology, School of Chemistry and Biochemistry, Georgia Institute of Technology, Atlanta, GA 30332-0400*

[3] *School of Computational Science and Engineering, Georgia Institute of Technology, Atlanta, GA 30332-0400*

(Dated: 21 October 2015)

Since the original fitting of Grimme's atom-pairwaise -D3 damping parameters, the number and quality of benchmark intermolecular interaction energies has increased significantly. Current benchmark sets such as S22x5, NBC10, and CH_4·PAH are extended to shorter ranges in order to fully capture the van der Waals well. Conventional benchmark sets, which focus on near-minima, lack overall diversity in the types of interactions captured; these datasets are augmented by modern sets, such as SSI, which are composed of interactions gleaned from crystal data and contain no such minima-focused bias. The resulting testing and a validation set provides a balanced description of distances, both shorter and longer than the minima, and covers the entire range of interaction types. The original training set damping parameters had 130 datapoints. The new training set contains 1,526 datapoints. Both the new and old DFT-D3 damping parameters were tested against a new validation set containing 6,825 datapoints.

---

[a] Electronic mail: dsmith@auburn.edu

[b] Electronic mail: lori.burns@gatech.edu

[c] Electronic mail: patkowsk@auburn.edu

[d] Electronic mail: sherrill@gatech.edu

I. INTRODUCTION

Dispersion-including density functional theory (DFT) methods have become integral to the evaluation of intermolecular interaction energies and potential energy surfaces. Numerous studies have shown that often these methods obtain impressive accuracies at the van der Waals minima, with average errors down to about 0.2 kcal/mol (0.8 kJ/mol) in some cases.[1] However, it is important to note that the accuracy near the minima is not always representative of the accuracy across the entire potential energy surface.[1–4]

Databases of accurate noncovalent interactions have been an invaluable source of data for assessing the performance of both established approaches and new approximations. The early databases[5–7] focused on the van der Waals minimum structures. However, it was realized shortly thereafter[8] that a good performance of a DFT-based approach at the minimum does not necessarily translate to a similar performance at other intermolecular separations, for example, semilocal functionals, even when parametrized for noncovalent interactions,[9,10] cannot reproduce the correct long-range behavior of interaction energy. Therefore, nearly all newer databases[2,11,12] are composed of radial curves passing through the van der Waals minimum. Only few benchmark studies[13] have included non-minimum angular configurations of interacting monomers, but there is a multitude of complete PES data for small complexes to assess the accuracy of DFT-based approaches at non-minimum orientations.

While density functionals that include nonlocal dispersion, either in an atom-pairwise form[14–16] or through a nonlocal correlation functional,[17,18] perform generally quite well at long range (the leading asymptotic constants C_6 are usually accurate to better than 10%), at distances slightly shorter than the van der Waals minimum the accuracy of DFT deteriorates quickly. Large errors of DFT-D2[19] at center-of-mass minimum separations (R_{eq}) have been observed already in Ref. 2, however, these issues went relatively unnoticed by the general community. Recently, two of us[4] performed extensive benchmark calculations of complexes involving carbon dioxide and coronene-sized models of graphene and carbon nanotubes at distances down to $0.8 \cdot R_{\mathrm{eq}}$, observing a dramatic drop in DFT accuracy at short range. Ref. 4 attributed the short-range issues to two sources: the overestimation of exchange due to incorrect asymptotic behavior of the exchange-correlation potential and the inadequacy of damping functions commonly used in atom-pairwise dispersion expressions. As evidenced by the long-range corrected functional LC-ωPBE[20] performing only somewhat better than standard functionals, the second issue is likely more important. It should be noted that the errors of DFT-based approaches become quite severe already at distances around $0.8 - 0.9 \cdot R_{\mathrm{eq}}$, where the interaction energies are either still negative or only slightly positive (up to, say, 10 kcal/mol). Such mildly repulsive configurations are probed in molecular dynamics simulations at standard conditions of temperature and pressure and the errors of DFT at this range are likely to adversely influence the resulting quantities such as spectra and virial coefficients. Moreover, a vastly different accuracy at different R leads to highly inaccurate gradients of the intermolecular potential (forces).[21]

The availability of multiple benchmark NCI databases including radial curves, along with the increase in computer power, has made it possible to evaluate and optimize DFT-based approaches on a much larger scale, up to exploring complete DFT parameter spaces of a given size.[22,23] Moreover, the very recent development of the SSI benchmark database by two of us and collaborators[24] extends the available benchmark set far beyond the global-minimum angular orientations with favorable electrostatics. Therefore, we are now in a much better position to revisit the parameter selection in the original DFT-D3[14] and DFT-D3(BJ)[25] approaches. That still requires an extension of several existing benchmark databases to shorter distances, and we performed such an extension in the present work.

For intermolecular interactions the ultimate DFT method would reproduce CCSD(T) quality results at both short-range and long-range distance for a very diverse set of interactions. Therefore, all benchmark databases utilized must be computed at the CCSD(T) silver standard of Ref. 43 ($\approx$5% accuracy) or better, dissociation curves must contain at least one positive point on the repulsive wall (HBC6 excepted on this point since it would exhibit double-minimum potentials) and extend past the van der Waals minima, and the databases taken together must represent a diverse set as demonstrated by SAPT theory. Upon selection of databases to be used in the testing and validation sets, it was discovered that many of the established databases themselves do not meet these requirements.

Often benchmark sets that include dissociation curves are created by first finding the global or local minima of a dimer. Then more points are created by changing the distance between the molecules by a fraction of the reduced distance $z = \frac{R}{R_{eq}}$. These types of databases will be denoted "minima cross section" and comprise all databases employed in this study except for SSI, BBI, and Water2510. Selection of the correct set of z distance is of utmost importance to capture accurately the shape of the potential energy curve. For

TABLE I. Datasets utilized in the training and validation sets.

Database	Points	Curves	Largest[f]	Reference	Description
Training	**1526**	**114**			
$CO_2 \cdot$ PAH	249	45	27	4	CO_2 with PAHs the size of benzene through coronene and curved coronene
HBC6[b]	118	6	6	26 and 27	dissociation curves of doubly hydrogen-bonded bimolecular complexes
NBC10ext[b]	195	10	12	27 and 28	dissociation curves of dispersion-bound bimolecular complexes
S22×7[b,c]	154	22	19	29	dissociation curves for a balanced mix of hydrogen bonded and dispersion bonded complexes
SSI500	500	[a]	20	24	a subset of 500 molecules from SSI
X31×10[d]	310	31	18	30	dissociation curves of organic halides, halohydrides, and halogens
Validation	**6773**	**148**			
ACHC	54	6	19	31	rise, twist, slide, shift, roll, and tilt of adenine:cytosine nucleobase step
BBI	100	[a]	10	24	peptide backbone-backbone complexes
$C_2H_4 \cdot$ PAH	75	15	26	32	ethene with curved coronene
$CH_4 \cdot$ PAH[b]	405	45	25	3 and 33	methane with PAHs the size of benzene through coronene and curved coronene
$CO_2 \cdot$ NPHAC	96	16	27	34	CO_2 with nitogen-doped polyheterocyclic aromatic compounds (N-PHAC)
S66×10[b]	660	66	16	35	dissociation curves for a balanced mix of biomolecule NCI bonding motifs
SSI	[e]2873	[a]	21	24	peptide sidechain-sidechain complexes
Water2510	2510	[a]	2	36–38	water PES
Thermochemistry	**52**				
CONF[c]	52	[a]	20	39–42	The ACONF, CYCONF, PCONF, and SCONF-A datasets.

[a] Database does not contain curves.

[b] Database was extended to shorter ranges.

[c] Database was recomputed at a higher level of theory.

[d] The X40×10 database with iodine containing complexes removed.

[e] SSI contains 3380 bimolecular complexes. The stated figure is less 500 from the SSI500 fitting subset and 7 for which GGA functionals do not reliably converge.

[f] Largest refers to the largest number of heavy atoms in the dataset.

example, the S22×5 database's z distance was originally selected as 0.9, 1.0, 1.2, 1.5, and 2.0. The long range is well covered by this selection of z; however, short range is inadequate: for z=0.9, only one curve has a positive point on the repulsive wall. Extending this benchmark to z=0.8, there are 11 curves with positive points on the repulsive wall. Finally, at z=0.7 all curves contain points that are positive on the repulsive wall. This problem is not isolated to the S22×5 database, in total the S22×5 (S22×7), S66×8 (S66×10), NBC10 (NBC10ext), and CH_4·PAH datasets sets were extended to shorter ranges for this Letter, new names are denoted in parenthesis.

To examine the diversity requirement, SAPT[44,45] was computed for all datasets and the results were plotted using "ternary" diagrams that represent the nature of an intermolecular interaction by relative contributions from the three attractive SAPT components: electrostatics, induction, and dispersion.[46] Examining Figure 1 the “minima cross section” ternary plot demonstrates that this type of dataset only explores the dispersion and electrostatically bound region. While this bound region can be argued to be the most important it can be seen clearly that the SSI and Water2510 sets explore a more diverse set of interaction archetypes. The lack of points that contain purely induction (top right corner of a ternary diagram) is considered quite satisfactory as only pathological systems such as $H^{+}\cdot$ LiH can be found in this region.

The original -D3 training set contained 130 separate datapoints broken into 72 intermolecular interactions (for which SAPT can be computed) and 58 thermochemistry based datapoints. 5are comprised of the S22 and S22+ sets (S22x7 at z=1.0, 1.2, 1.5) and are plotted in Figure 1 in comparison to the current training set. The S22+ dataset has no points shorter than the minima (a region where damping will play a much greater role), and the original benchmark values did not meet the CCSD(T) silver standard. The quality, diversity, and range of the new training set for intermolecular interactions has been significantly improved compared to the of original training dataset. As thermochemistry data is not the focus of the current work, the CONF dataset, which represents 52 of the 58 datapoints in the original training dataset, will only be used as a metric to ensure that this type of data is not radically skewed by the refitting.

The fitting forms utilized are as follows:

The Becke-Johnson (BJ) damping[47,48] with three parameters s_8, α_1, and α_2 is:

$$E_{\text{disp}}^{\text{BJ}} = -\frac{1}{2}\sum_{A\neq B}\sum_{n=6,8} s_n \frac{C_n^{AB}}{r_{AB}^n + (\alpha_1 \cdot R_0^{AB} + \alpha_2)^n} \tag{1}$$

The “zero damping” or Chai-Head-Gordon (CHG) damping form[49,50],

$$E_{\text{disp}}^{\text{CHG}} = -\frac{1}{2}\sum_{A\neq B}\sum_{n=6,8} s_n \frac{C_n^{AB}}{r_{AB}^n}\frac{1}{1+6(r_{AB}/(s_{r,n}R_0^{AB}) + R_0^{AB}\beta)^{-\alpha_n}}, \tag{2}$$

which has three parameters s_8, $s_{r,6}$, and β (the $s_{r,8}$ values are held constant at 1). The α_n parameters are set to 14 and 16 for α_6 and α_8, respectively, and not adjusted. The β parameter is introduced to CHG damping in this paper to give the same number of fitting parameters as BJ damping.

The training and validation databases cover a large range of interaction energies making a weight like mean unsigned error heavily favor the complexes with large interaction energies.

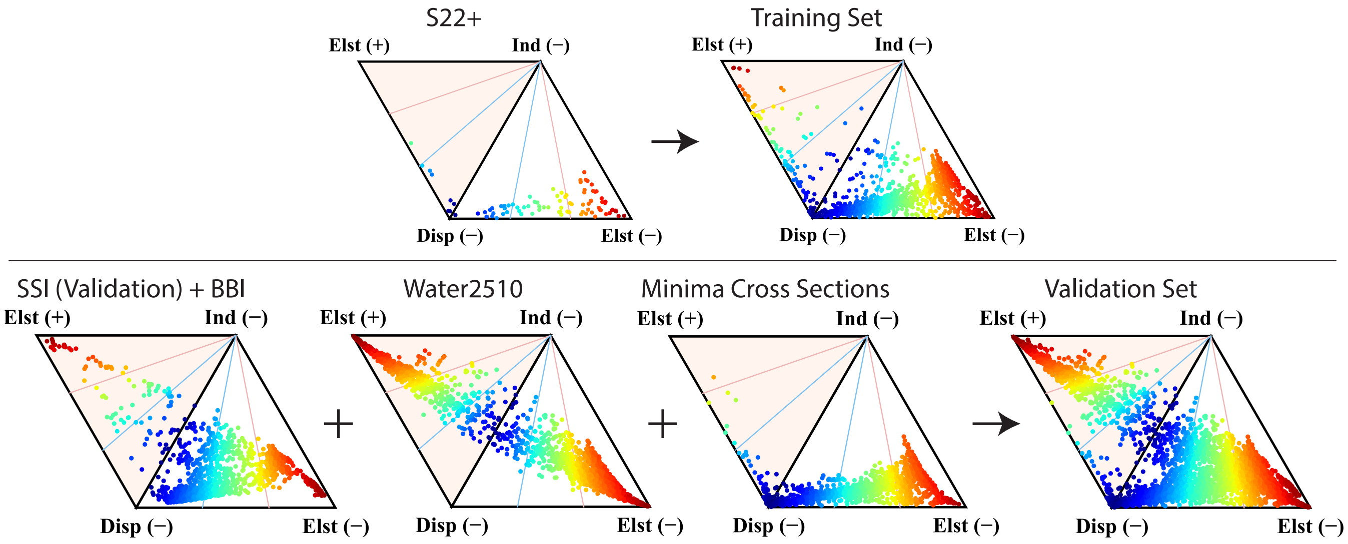

FIG. 1. Top Panel: Ternary diagram comparison between the original -D3 fitting set and the current fitting set. Bottom Panel: Ternary diagram breakdown of the three major categories of points included in the validation set.

A statistical quantity like the mean unsigned relative error would be a better metric to measure the overall accuracy; however, this methodology quickly runs into singularities at short range when the PES crosses the zero line or at long range where the interaction energy is very small. To circumvent this issue a capped relative error (CRE) is introduced where the weight is capped at a certain value. Unfortunately, as in Ref. 4 a singular value is not appropriate for the entire database. Instead, this cap needs to have a functional form to take into account the large range of interaction energies.

$$\mathrm{CRE} = \left(\frac{E - E_{\mathrm{ref}}}{E_{\mathrm{weight}}}\right) \cdot 100\%, \quad E_{\mathrm{weight}} = \max\{|E_{\mathrm{ref}}|, \frac{\xi |E_{\mathrm{ref-eq}}|}{z^3}\} \tag{3}$$

ξ is a flexible dimensionless parameter that determines the severity of the capping. In this paper a value of 0.2 was selected, as it represents a good balance between the number of points capped and singularity avoidance. At this weight only 10% of the values had their weights altered, with an average difference between the benchmark and capped value of 0.25 kcal/mol. For the SSI and BBI datasets, complete curves are not available and a simple cap of 0.5 kcal/mol was used; this value was chosen because it damps a similar percentage of overall points (7%). Variations of the CRE also include capped unsigned relative error (CURE) and mean capped unsigned relative error (MCURE).

For overall statistical quantities, each database is weighted equally, except for the SSI

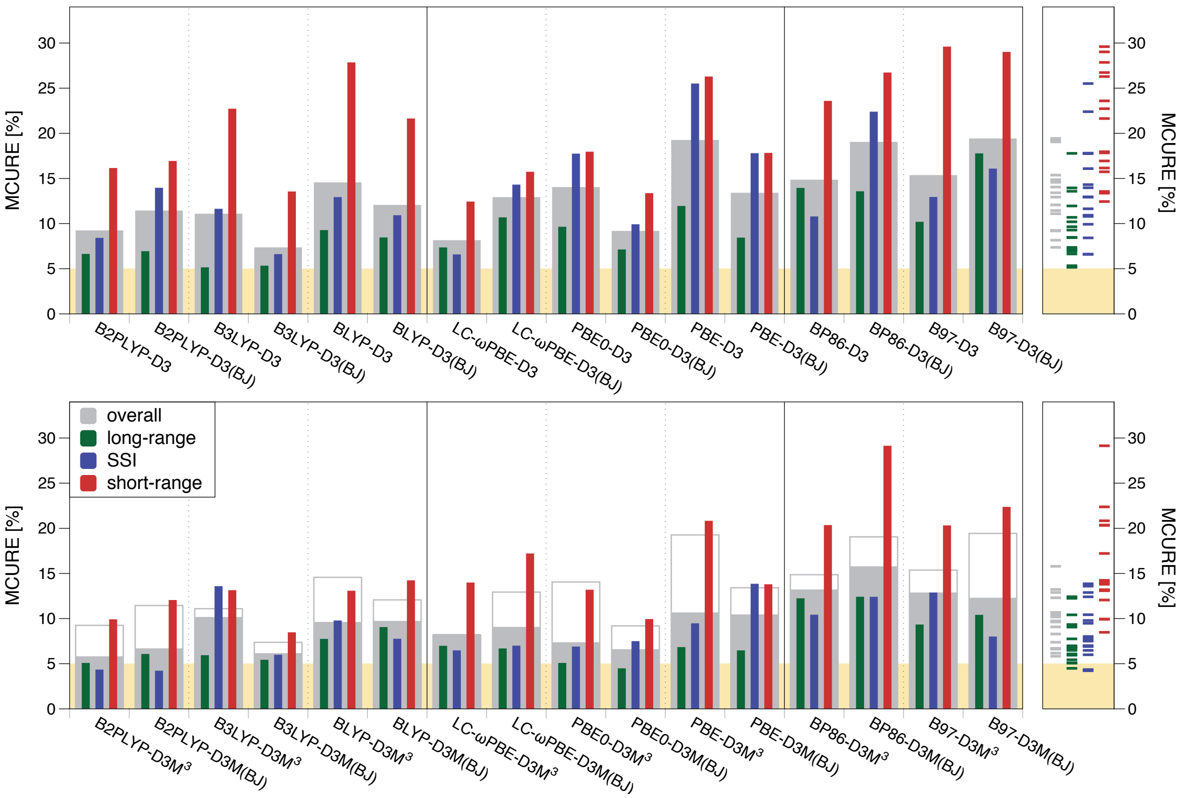

FIG. 2. Top Panel: All functionals utilizing the original damping parameters. Bottom Panel: All functionals utilizing the new damping parameters the light grey outlines represent the MCURE of the original damping parameters. The right hand panels gives the spread of MCURE values for all functionals.

database which will always contribute $\frac{1}{3}$ to the overall statistic. This was done so that the different number of points in each dataset does not implicitly weight the datasets and the relative importance of the SSI dataset is always represented. All damping parameters were fit to the training set and all statistical quantities are on the validation set. Additional statistics can be found in the SI.

In Figure 2 the MCURE is shown for all functionals with original damping parameters. The diversity in the statistics between functionals and damping forms is quite striking, especially for the SSI and short-range quantities. For this large dataset it is apparent that long-range DFT+D is overall quite excellent, often with 10% MCURE and at worst case 18% MCURE for the B97-D3(BJ) functional. However, accuracy radically deteriorates at short range for all functionals with a best case scenario of 12% for LC-ωPBE-D3 and worst case of 29% for B97-D3. Interestingly, it was reported that short-range inaccuracies in DFT+D

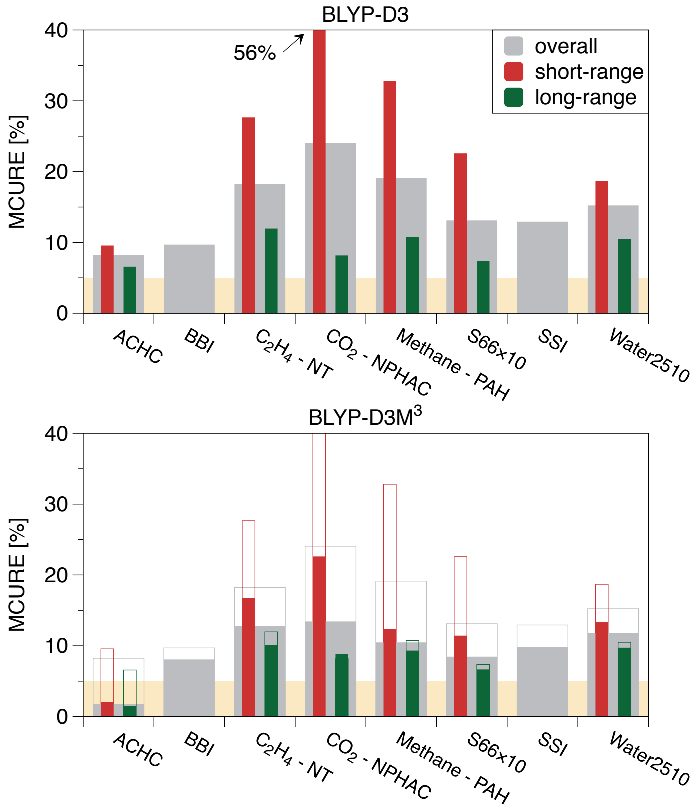

FIG. 3. Performance per validation dataset for the BLYP-D3 and BLYP-D3M methods.

were due to KS exchange being too repulsive.

After refitting it can be seen that the overall MCURE for every functional either improved or, for one case, LC-ωPBE-D3M^3, did not change. The long-range accuracies are now much more consistent with errors between 4 and 11%. As the C_6 coefficients used in the dispersion term are only accurate to about 10%, the overall performance at long range is quite satisfactory. The accuracies for the SSI dataset is also increased significantly. Before refitting errors ranged from 5 to 26% and now only range from 4 to 14%. The reduction in short-range MCURE is not always guaranteed; for the LC-ωPBE and BP86 functional, the error becomes worse by several percent. However, for the B2PLYP, B3LYP, and BLYP series, short range errors significantly improve from 14 to 28% before refitting down to 8 to 14% after refitting. The most notable single functional improvement comes from the refitting of the popular PBE-D3 method, for which the overall MCURE went from 19% to 10% and the MCURE for the SSI validation set went from 26% to 9%.

Quantities shown in Figure 2 represent a overview of the statistics. To obtain a better understanding of the improvement per dataset the MCURE for each dataset is shown in

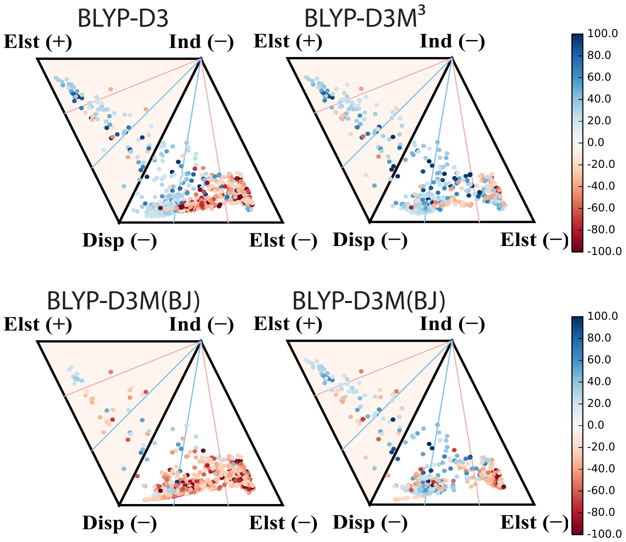

FIG. 4. Capped relative error (signed) for the BLYP functional for both CHG and BJ damping before and after the fitting for points at the minimum separation and shorter in addition to the SSI dataset. Red represents overbound DFT-D3 energies while blue represents underbound DFT-D3 energies. Errors within ±20% are not shown for clarity.

Figure 3. The BLYP-D3 functional was chosen as it represents a reasonable middle ground in terms of overall improvement. Figure 3 demonstrates that the accuracy per dataset can vary dramatically, especially at short range. After the refitting, we can observe that the accuracy per dataset is much more even and the largest outliers have been brought more in line with the remaining dataset.

To examine the fundamental limits of current damping forms Figure 4 shows CRE per datapoint. For zero damping, dispersion dominated systems are typically underbound while electrostatically bound systems are overbound. Interestingly, the zero refitting appears to fix the electrostatically bound systems while the errors remain relatively unchanged for dispersion bound systems. The overlapping too low and too systems for the refitted results suggest that even if more complex damping forms were utilized that take into account the types of interaction little improvement would be seen. This would appear to indicate that increasingly complex damping forms are not an avenue of research worth pursuing.

As this refitting is clearly one that favors intermolecular interactions, the CONF datasets was used to ensure that refitting does not significantly impact thermochemistry. Across all functionals and damping forms, the refitted parameters only worsen the CONF dataset by

2% on the average. For the worst case scenario: B97-D3(BJ) compared to B97-D3M(BJ) the CONF MCURE worsens by 8% (26 to 34%, respectively). This demonstrates that, at least for the CONF dataset, damping forms and values have a much smaller impact on intramonomer dispersion.

As was previously noted, all DFT values were computed with the CP correction in the QZVP basis set. As such, the underlying DFT should always be computed as close to the basis limit as possible. Compared to the CP corrected QZVP computation the MCURE only deviates by 1-2% when the basis is reduced to CP aDZ. However, when the basis is reduced to non-CP QZVP, the MCURE deviates by 2-4% and 45-60% for non-CP aDZ. Therefore, the basis for CP computations must be of at least aDZ quality and for non-CP of QZVP quality. Otherwise, basis set superpositions errors will become a much greater source of error than the quality of the dispersion contribution itself.

In summary, we have demonstrated that current “minima cross section” benchmarks do not fully explore the van der Waals well at short range and do not have enough diversity to adequately describe all interactions in either protein-protein interaction or even a water dimer potential energy surface. Current benchmark sets have been extended to satisfy the former requirement and novel benchmark sets such as SSI were utilized to satisfy the later. The original DFT-D3 damping parameters were not fit to short-range points and subsequently do poorly in this region compared to long-range points. Refitting can reduce DFT-D3 errors by up to half and in general greatly reduces the large variability between functional selection. We recommend avoiding the BP86 and B97 functionals and advocate the use of B3LYP-D3M(BJ) as the best overall functional.

COMPUTATIONAL METHODS

All computations were performed using the MOLPRO[51] 2012 and PSI4[52] suite of *ab initio* quantum chemistry programs. The B2PLYP,[53] B3LYP,[54,55] BLYP,[56,57] BP86,[56,58] PBE0,[59,60] LC-ωPBE,[20] PBE,[61] and B97[19] functionals were utilized. The def2-QZVP[62] and aug-cc-pVDZ[63,64] (hereafter shortened to QZVP and aDZ, respectively) basis sets were utilized. Unless otherwise stated all computation are counterpoise corrected[65,66] and utilized the QZVP basis set. Density fitting was utilized for all DFT computations.[67,68]

ASSOCIATED CONTENT

AUTHOR INFORMATION

ACKNOWLEDGMENTS

D.G.A.S and K.P are supported by the Donors of the American Chemical Society Petroleum Research Fund, the NSF CAREER award CHE-1351978, and the startup funding from Auburn University. L.A.B. and C.D.S. are supported by a grant provided by the United States National Science Foundation (Grant No. CHE-1300497). Computational Molecular Science and Technology is funded through a NSF CRIF award (Grant No. CHE-0946869) and by Georgia Institute of Technology.

REFERENCES

[1] L. A. Burns, A. Vazquez-Mayagoitia, B. G. Sumpter, and C. D. Sherrill, J. Chem. Phys. **134**, 084107 (2011).

[2] L. Gráfová, M. Pitoňák, J. Řezáč, and P. Hobza, J. Chem. Theory Comput. **6**, 2365 (2010).

[3] D. G. A. Smith and K. Patkowski, J. Phys. Chem. C **118**, 544 (2014).

[4] D. G. A. Smith and K. Patkowski, J. Phys. Chem. C **119**, 4934 (2015).

[5] Y. Zhao and D. G. Truhlar, J. Phys. Chem. A **109**, 5656 (2005).

[6] Y. Zhao and D. G. Truhlar, J. Chem. Theory Comput. **1**, 415 (2005).

[7] P. Jurečka, J. Šponer, J. Černý, and P. Hobza, Phys. Chem. Chem. Phys. **8**, 1985 (2006).

[8] C. D. Sherrill, T. Takatani, and E. G. Hohenstein, J. Phys. Chem. A **113**, 10146 (2009).

[9] Y. Zhao, N. E. Schultz, and D. G. Truhlar, J. Chem. Theory Comput. **2**, 364 (2006).

[10] Y. Zhao and D. G. Truhlar, Theor. Chem. Acc. **120**, 215 (2008).

[11] K. S. Thanthiriwatte, E. G. Hohenstein, L. A. Burns, and C. D. Sherrill, J. Chem. Theory Comput. **7**, 88 (2011).

[12] J. Řezáč, K. E. Riley, and P. Hobza, J. Chem. Theory Comput. **7**, 2427 (2011).

[13] J. C. Faver, M. L. Benson, X. He, B. P. Roberts, B. Wang, M. S. Marshall, M. R. Kennedy, C. D. Sherrill, and K. M. Merz, Jr., J. Chem. Theory Comput. **7**, 790 (2011).

[14] S. Grimme, J. Antony, S. Ehrlich, and H. Krieg, J. Chem. Phys. **132**, 154104 (2010).

[15] A. D. Becke and E. R. Johnson, J. Chem. Phys. **127**, 124108 (2007).

[16] A. Tkatchenko and M. Scheffler, Phys. Rev. Lett. **102**, 073005 (2009).

[17] M. Dion, H. Rydberg, E. Schröder, D. C. Langreth, and B. I. Lundqvist, Phys. Rev. Lett. **92**, 246401 (2004).

[18] O. A. Vydrov and T. Van Voorhis, J. Chem. Phys. **133**, 244103 (2010).

[19] S. Grimme, J. Comput. Chem. **27**, 1787 (2006).

[20] O. A. Vydrov and G. E. Scuseria, J. Chem. Phys. **125**, 234109 (2006).

[21] C. Lechner and A. F. Sax, J. Phys. Chem. C **118**, 20970 (2014).

[22] N. Mardirossian and M. Head-Gordon, J. Chem. Phys. **140**, 18A527 (2014).

[23] N. Mardirossian and M. Head-Gordon, J. Chem. Phys. **142**, 074111 (2015).

[24] J. C. Faver, L. A. Burns, C. D. Sherrill, and K. M. Merz Jr., "Assessing modeling errors with the biomolecular fragment database," *in preparation*.

[25]S. Grimme, S. Ehrlich, and L. Goerigk, J. Comput. Chem. **32**, 1456 (2011).

[26]K. S. Thanthiriwatte, E. G. Hohenstein, L. A. Burns, and C. D. Sherrill, J. Chem. Theory Comput. **7**, 88 (2011).

[27]M. S. Marshall, L. A. Burns, and C. D. Sherrill, J. Chem. Phys. **135**, 194102 (2011).

[28]L. A. Burns, Á. Vázquez-Mayagoitia, B. G. Sumpter, and C. D. Sherrill, J. Chem. Phys. **134**, 084107 (2011).

[29]L. Gráfová, M. Pitoňák, J. Řezáč, and P. Hobza, J. Chem. Theory Comput. **6**, 2365 (2010).

[30]J. Řezác, K. E. Riley, and P. Hobza, J. Chem. Theory Comput. **8**, 4285 (2012).

[31]T. M. Parker and C. D. Sherrill, J. Chem. Theory Comput. **11**, 4197 (2015).

[32]S. Li and K. Patkowski, unpublished .

[33]D. G. A. Smith and K. Patkowski, J. Chem. Theory Comput. **9**, 370 (2013).

[34]S. Li, D. G. A. Smith, and K. Patkowski, Phys. Chem. Chem. Phys. **17**, 16560 (2015).

[35]J. Řezáč, K. E. Riley, and P. Hobza, J. Chem. Theory Comput. **7**, 2427 (2011).

[36]R. Bukowski, K. Szalewicz, G. C. Groenenboom, and A. van der Avoird, Science **315**, 1249 (2007).

[37]R. Bukowski, K. Szalewicz, G. C. Groenenboom, and A. van der Avoird, J. Chem. Phys. **128**, 094313 (2008).

[38]D. G. A. Smith and K. Patkowski, unpublished .

[39]D. Gruzman, A. Karton, and J. M. L. Martin, J. Phys. Chem. A **113**, 11974 (2009).

[40]J. J. Wilke, M. C. Lind, I. H. F. Schaefer, A. G. Császár, and W. D. Allen, J. Chem. Theory Comput. **5**, 1511 (2009).

[41]D. Reha, H. Valdes, J. Vondrášek, P. Hobza, A. Abu-Riziq, B. Crews, and M. S. de Vries, Chem. Eur. J. **11**, 6803 (2005).

[42]L. Goerigk and S. Grimme, J. Chem. Theory Comput. **6**, 107 (2010).

[43]L. A. Burns, M. S. Marshall, and C. D. Sherrill, J. Chem. Phys. **141**, 234111 (2014).

[44]B. Jeziorski, R. Moszyński, and K. Szalewicz, Chem. Rev. **94**, 1887 (1994).

[45]E. G. Hohenstein and C. D. Sherrill, WIREs Comput. Mol. Sci. **2**, 304 (2012).

[46]N. J. Singh, S. K. Min, D. Y. Kim, and K. S. Kim, J. Chem. Theory Comput. **5**, 515 (2009).

[47]E. R. Johnson and A. D. Becke, J. Chem. Phys. **123**, 024101 (2005).

[48]S. Grimme, S. Ehrlich, and L. Goerigk, J. Comput. Chem. **32**, 1456 (2011).

[49] J. Chai and M. Head-Gordon, Phys. Chem. Chem. Phys. **10**, 6615 (2008).

[50] S. Grimme, J. Antony, S. Ehrlich, and H. Krieg, J. Chem. Phys. **132**, 154104 (2010).

[51] H.-J. Werner, P. J. Knowles, G. Knizia, F. R. Manby, M. Schütz, P. Celani, T. Korona, R. Lindh, A. Mitrushenkov, G. Rauhut, K. R. Shamasundar, T. B. Adler, R. D. Amos, A. Bernhardsson, A. Berning, D. L. Cooper, M. J. O. Deegan, A. J. Dobbyn, F. Eckert, E. Goll, C. Hampel, A. Hesselmann, G. Hetzer, T. Hrenar, G. Jansen, C. Köppl, Y. Liu, A. W. Lloyd, R. A. Mata, A. J. May, S. J. McNicholas, W. Meyer, M. E. Mura, A. Nicklass, D. P. O'Neill, P. Palmieri, D. Peng, K. Pflüger, R. Pitzer, M. Reiher, T. Shiozaki, H. Stoll, A. J. Stone, R. Tarroni, T. Thorsteinsson, and M. Wang, Molpro, version 2012.1, a package of ab initio programs, 2012, see http://www.molpro.net (accessed June 2, 2014).

[52] J. M. Turney, A. C. Simmonett, R. M. Parrish, E. G. Hohenstein, F. A. Evangelista, J. T. Fermann, B. J. Mintz, L. A. Burns, J. J. Wilke, M. L. Abrams, N. J. Russ, M. L. Leininger, C. L. Janssen, E. T. Seidl, W. D. Allen, H. F. Schaefer, R. A. King, E. F. Valeev, C. D. Sherrill, and T. D. Crawford, WIREs Comput. Mol. Sci. **2**, 556 (2012).

[53] S. Grimme, J. Chem. Phys. **124**, 034108 (2006).

[54] A. D. Becke, J. Chem. Phys. **98**, 5648 (1993).

[55] P. J. Stephens, F. J. Devlin, C. F. Chabalowski, and M. J. Frisch, J. Phys. Chem. **98**, 11623 (1994).

[56] A. D. Becke, Phys. Rev. A **38**, 3098 (1988).

[57] C. Lee, W. Yang, and R. G. Parr, Phys. Rev. B **37**, 785 (1988).

[58] J. P. Perdew, Phys. Rev. B **33**, 8822 (1986).

[59] C. Adamo and V. Barone, J. Chem. Phys. **110**, 6158 (1999).

[60] M. Ernzerhof and G. E. Scuseria, J. Chem. Phys. **110**, 5029 (1999).

[61] J. P. Perdew, K. Burke, and M. Ernzerhof, Phys. Rev. Lett. **77**, 3865 (1996).

[62] F. Weigend and R. Ahlrichs, Phys. Chem. Chem. Phys. **7**, 3297 (2005).

[63] T. H. Dunning Jr., J. Chem. Phys. **90**, 1007 (1989).

[64] R. A. Kendall, T. H. Dunning Jr., and R. J. Harrison, J. Chem. Phys. **96**, 6796 (1992).

[65] S. F. Boys and F. Bernardi, Mol. Phys. **19**, 553 (1970).

[66] F. B. van Duijneveldt, J. G. C. M. van Duijneveldt-van de Rijdt, and J. H. van Lenthe, Chem. Rev. **94**, 1873 (1994).

[67] H. Werner, F. R. Manby, and P. J. Knowles, J. Chem. Phys. **118**, 8149 (2003).

[68] R. Polly, H.-J. Werner, F. R. Manby, and P. J. Knowles, Mol. Phys. **102**, 2311 (2004).